

Luminosity control and beam orbit stability with beta star leveling at LHC and HL-LHC

THÈSE N° 7338 (2016)

PRÉSENTÉE LE 30 NOVEMBRE 2016
À LA FACULTÉ DES SCIENCES DE BASE
LABORATOIRE DE PHYSIQUE DES ACCÉLÉRATEURS DE PARTICULES
PROGRAMME DOCTORAL EN PHYSIQUE

ÉCOLE POLYTECHNIQUE FÉDÉRALE DE LAUSANNE

POUR L'OBTENTION DU GRADE DE DOCTEUR ÈS SCIENCES

PAR

Arkadiusz Andrzej GORZAWSKI

acceptée sur proposition du jury:

Prof. H. M. Rønnow, président du jury
Prof. L. Rivkin, Dr J. Wenninger, directeurs de thèse
Dr R. Tomas, rapporteur
Dr R. Jacobsson, rapporteur
Dr M. Aiba, rapporteur



ÉCOLE POLYTECHNIQUE
FÉDÉRALE DE LAUSANNE

Suisse
2016

Success consists of going from failure to failure without loss of enthusiasm.
— Winston Churchill

To my wife...

Acknowledgements

Firstly, I would like to express my sincere gratitude to my advisor Prof. Lenny Rivkin for accepting me for the doctoral program under his laboratory. A big "thank you" goes for him for an excellent contact and help throughout the courses I took outside the EPFL.

I owe deepest gratitude to my CERN supervisor Dr. Jörg Wenninger. For his endless passion in explanations and discussions about the accelerator matters and not only. For his effort in channeling my ideas towards the right direction and for the support in the endless review process of my write-ups including this thesis. Thank you!

This work could be carried out thanks to the support of CERN and EPFL, thanks to that I could attend many topical schools that were organized all around the world and eventually I substantially enriched my knowledge about the accelerator physics.

I would like to show my gratitude to my LHC–OP colleagues: Belen, Delphine, Giulia, Lene, Laurette, Maria, Michaela, Reyes, Verena, Andrea, Georges–Henry, Guy, Jörg, Kajetan, Lasse, Michi, Mirko, Matteo, Rosano, Ron, Tobias and Sylvia with Mike. Thank you all for a warm welcome at the beginning of my doctoral appointment and for all nice professional and private moments throughout it.

I am grateful to the people from BE–ABP group, Dr. Tatiana Pieloni, Dr. Rogelio Tomás Garcia, Dr. Bernhard Holzer and Dr. Werner Herr for interesting discussions, ideas and inputs at various stages of this thesis.

I would like to show my gratitude to experiments contact persons, Dr. A. Dabrowski, Dr. W. Kozański and Dr. R. Jacobsson for their support and help in getting non–standardized data from the detectors data storage.

It is a pleasure to thank my former section TE–MPE–MS, for Dr. Markus Zerlauth, Dr. Kajetan Fuchsberger, Jean–Christophe Garnier and Maxime Audrain for a great discussions and always positive attitude with all the projects that we had done together and that are still in use! Thank you goes to TE–MPE–EE section, as the group in which I started my CERN journey, Knud Dahlerup–Petersen, Gert–Jan Coelingh and Bozidhar Panev for great discussions throughout my time at CERN.

I am grateful to my Polish friends: Alicja and Mateusz, Justyna and Adam, Ania and Paweł, Zaneta and Czesiek, Julia and Mariusz, Karolcia and Piotr, Ewelina and Mateusz, Kinga and

Acknowledgements

Łukasz and Tomuś with whom all I started my journey at CERN, with whom I shared all the nice moments during thesis time when not working on it. Thanks guys! I would not come so far if I were without you.

I would like to thank again to my office mate and a good friend Dr. Kajetan Fuchsberger for all great discussions we had. Often, having so different opinions at the start of the conversation we always found a way to converge. Thank you goes for a strong support throughout the thesis time. And even before, as he managed to reinforce me with my plan to start my doctorate studies.

Last but not least, a big "thank you" goes to my wife Basia and my kids Karolina and Tymek. Thank you for understanding of some of my renouncement and all the busy days and weeks that I have spent in the office. To my parents Ania and Andrzej and my brother Adam for that they always supported me in my career.

For all of you that were not listed above but our ways somehow crossed during my studies, Thank you all.

Geneva, 7 October 2016

A. G.

Abstract

This thesis describes the wide subject of the luminosity leveling and its requirements for the LHC and the HL-LHC. We discuss the advantages and disadvantages of different leveling methods focusing the thesis on the β^* leveling technique. We review the beams offset build-up due to the environmental (i.e. natural ground motion) and mechanical (i.e. moving quadrupole) sources. We quantify the instrumentation requirements for the reliable and reproducible operation with small offsets at the interaction points. Last but not least, we propose a novel method for the beam offset stabilization at the collision point based on the feedback from the luminosity.

Key words: luminosity leveling, LHC, HL-LHC, orbit correction, orbit stabilization, offset correction, feedback.

Résumé

Le sujet de cette thèse est le nivellement de la luminosité pour le LHC et le HL-LHC. Nous discutons les avantages et les inconvénients de différentes méthodes de nivellement en nous focalisant sur la technique de nivellement par β^* . Nous analysons les sources de perturbations d'orbites provenant de l'environnement (mouvements du sol) et de causes mécaniques (mouvements de quadrupoles) pouvant nuire au bon fonctionnement du nivellement. Nous quantifions les exigences de l'instrumentation pour un fonctionnement fiable et reproductible du nivellement de la luminosité en respectant les tolérances sur les écarts des faisceaux au points de collision. Finalement nous proposons un nouveau procédé pour la stabilisation du faisceau aux points de collision à l'aide d'une technique de stabilisation de la luminosité.

Mots clefs : le nivellement de la luminosité, LHC, HL-LHC, correction d'orbites, stabilisation d'orbit, correction d'offset au points de collision.

Zusammenfassung

Diese Doktorarbeit betrachtet verschiedene Aspekte der Luminositätsnivellierung am CERN Large Hadron Collider (LHC) und High Luminosity LHC (HL-LHC). Unterschiedliche Nivellierungstechniken werden verglichen, wobei der Schwerpunkt der Arbeit auf der Veränderung der Strahlgröße am Interaktionspunkt (β^* levelling) liegt. Störungsquellen, die die Strahlposition (und folglich die Nivellierung) beeinflussen können, werden im Detail analysiert. Mithilfe von Simulationen und Experimenten werden daraus Anforderungen an die Strahlinstrumentierung abgeleitet, die sicherstellen, dass die Luminosität risikolos nivelliert werden kann. Abschließend wird eine neuartige Methode vorgestellt, die während der Nivellierung einsetzbar ist um die Strahlen an den Kollisionen zentriert zu halten und somit einen reproduzierbaren Prozess ermöglicht.

Stichwörter: Luminositätsnivellierung, LHC, HL-LHC, Orbitkorrektur, Orbitstabilisierung, Offsetkorrektur, Strahlorbitfeedback

Motivation

The first 2 years of physics production at the Large Hadron Collider (LHC) in 2011 and 2012 were highly successful despite the lower energy thanks to the large amount of integrated luminosity. The discovery of the Higgs particle was possible thanks to this outstanding performance of the LHC collider and its injectors with a limited but still record-breaking energy of 4 TeV.

The need for ever increasing luminosity will be satisfied in the coming years by a succession of upgrades on the injectors (LIU, LHC Injector Upgrade project) and the LHC itself with the High Luminosity-LHC (HL-LHC) project. With these performance upgrades, the LHC will be able to discover new rare and heavy particles or push up their mass bounds.

Needs

During the very successful LHC run in 2012 two important issues have been encountered with the very bright beams used in that year. These issues will be further amplified in the future with the upcoming upgrades and will have to be mastered during future LHC operation.

The first limitation encountered in 2012 with the bright proton beams is the event *pile-up* observed in the detectors. The event *pile-up* corresponds to the number of simultaneous particle interactions that are recorded in the same bunch crossing. The maximum *pile-up* that is acceptable for the high luminosity experiments ATLAS and CMS is ≈ 40 (design ≈ 20). This issue will remain valid for the HL-LHC despite detector performance increases because the beam brightness will be much higher than it is nowadays.

The second limitation for bright beams are collective effects, and the associated beam instabilities. The high brightness beams must be stabilized with a mixture of active transverse feedback and of passive *Landau damping*. The main ingredient of the *Landau damping* mechanism is the tune spread. At the LHC some tune spread is provided by the octupole magnets but it is limited by their strength. Already at 4 TeV the octupoles were operated very close to their maximum current. At injection energy (450 GeV) the effectiveness of the octupole magnets is sufficient to prevent instabilities. However, when reaching top energy (6.5 TeV) their efficiency drops as the beam size is shrinking due to the relativistic Lorentz contraction. At the LHC it was realized that the head-on beam-beam interaction is the largest and most efficient source of *Landau damping*.

Acknowledgements

Cures

The excessive event *pile-up* may be controlled by *luminosity leveling*: the luminosity is deliberately reduced to an acceptable level and maintained at this level until the intensity of the beams has sufficiently decayed. Such an operation mode provides constant luminosity over many hours and very stable operating conditions for the experiments. *Luminosity leveling* by β^* adjustment (" β^* leveling") is one of the preferred techniques that will be explored in this thesis from the operational point of view.

Performing some of the high energy optics manipulations (β -squeeze) with colliding beams ("*collide and squeeze*") is very similar to β^* leveling and provides the required beam stabilization with the beam-beam effect.

Both of these processes however, imply increased operational complexity. To preserve head-on collisions, the orbit stability and the orbit corrections may pose a series of challenges that have to be solved regarding operation with changing optics. This is discussed in this thesis.

Structure and content of this document

The first two chapters (Chapter 1: Summary of accelerator physics and Chapter 2: LHC and the CERN accelerator complex) are intended to be an introduction to some general accelerator physics concepts and to the the CERN accelerator complex, including of course the LHC.

Operational scenarios (involving the *luminosity leveling*) for LHC Run 2 and Run 3 are presented in Chap. 3 for LHC and HL-LHC. Different *luminosity leveling* techniques are described in this section, with emphasis on β^* leveling. Requirements and preparations needed for the implementation of the method are discussed and treated in the following chapters of the document.

Chapter 4 describes and analyses the orbit drifts at the LHC. A way to use this measurement to characterize elements misalignment is shown. Beam orbit during the long stable beam periods is presented, highlighting the production disturbances related to the orbit stability at the interaction point. The squeeze process is the most delicate part of the nominal LHC (and later HL-LHC) cycle particularly in terms of orbit control. A model of the beam orbit and of the feedback system in the squeeze is presented and discussed in Chap. 5. Requirements on the beam instrumentation and on the reproducibility of the beam position monitors are also presented. Chapter 6 discusses experiments on collide and squeeze performed in the context of this thesis. The first successful experiment on collide and squeeze is presented.

The last chapter (Chapter 7: IP orbit stabilization with luminosity), reviews and presents a novel method for the beam collision stabilization. The method is presented with the first experimental results for the LHC beams.

This dissertation will close with conclusions presented in Chapter 8.

Acronyms and Abbreviations

- ALICE** A Large Ion Collider Experiment. 27, 28, 43, 44
- ATLAS** A Toroidal LHC ApparatuS. xxi, 13, 21, 25, 28, 44–46, 63, 70, 87, 108
- BBQ** Base Band Tune. 31, 32
- BCM** Beam Current Monitor. 30
- BCT** Beam Current Transformer. 95
- BLM** Beam Loss Monitor. 30
- BPM** Beam Position Monitor. 30–32, 56, 76, 77, 81, 82, 87, 95, 107, 111, 118, 120
- BSRT** Beam Synchrotron light Telescope. 30, 93
- CMS** Compact Muon Solenoid. xxi, 13, 25, 44–46, 87, 95
- COD** Orbit correction dipole. 32, 55, 75, 78, 82
- DOROS** Diode ORbit and Oscillation System. 31, 87, 89, 111, 118, 120, *Glossary*: DOROS
- EV** Eigenvalue. 10, 75, 77, 80, 81
- HO** The head-on interaction. 18, 19, 41, 106, 121, *Glossary*: head-on
- HOBB** HO Beam beam interaction. 43, *Glossary*: head-on
- IP** Interaction Point. 7, 35, 63, 70, 73, 76–78, 80, 85, 87, 95, 107, 111, 120, 124, *Glossary*: interaction point
- IR** Interaction Region. 56, 95, 115, *Glossary*: interaction region
- LHC** The Large Hadron Collider. xi–xiv, xvii, xviii, xxi, xxii, 11, 13, 14, 23–28, 32–34, 37, 38, 40, 43–47, 50, 54–70, 73, 74, 78, 81, 84, 121, 124, 131, 137, 138, 140
- LHCb** LHC beauty experiment. 13, 27, 28, 43, 44, 46, 47, 87

Acronyms and Abbreviations

LR Long range. 18, 19, 121, 122, *Glossary*: long range

LRBB LR Beam beam interaction. 47, *Glossary*: long range

MCBX The common vacuum chamber COD. xxi, 29, 30, 32, 56, 75, 77, 81

MD Machine Development. 85, 87, 92, 106, 124

OFB Orbit Feedback System. 32, 56, 57, 59, 75, 80, 141

SVD Singular–Value–Decomposition. 10, 78, 82, 141, *Glossary*: Singular–Value–Decomposition

TCT Tertiary collimators, located upstream of each inner triplet. 29, 87

WPS Wire Position System. 64, 68

WS Wire scanner. 30, 93

Glossary

β^* leveling An operation scheme where the luminosity is adjusted (leveled) by a change of the beam size at the collision point during the stable beams. 48

betatron function The function that describes the focusing properties of the machine. xvii, 3, 4, 7, 34, 50, 56, 95

bunch Set of particles oscillating around the same longitudinal fixed point inside one RF bucket. 12

collide and squeeze An operation scheme where the betatron squeeze is performed with colliding beams. 48, 49, 75, 87, 106

crossing angle The non zero angle between the beams at the IP that is used to separate the beams and avoid parasitic collisions at the long range encounters. 18, 39, 41, 87, 90, 95

dispersion function The function that relates the displacement of an off-momentum particle with respect to the ideal particle as a function of a momentum offset. 4, 25

DOROS A Diode ORbit and Oscillation System. An enhanced sensitivity BPM electronics with a beam position resolution with a μ -meter resolution. 31

drift (orbit drift) An undesired increase in beam separation at the interaction point. 63, 100, 107, 111, 117

head-on Beam beam head-on interactions between bunches in the IPs. 16, 38

hourglass effect Longitudinal variation of the beam size around the interaction point due to the position dependence of the betatron function at the waist. xviii, xxi, 13, 50–52

interaction point A place in a collider ring where head-on collisions are expected to occur, usually the center of the experiment. xvii, 12, 28, 86

interaction region A place in a collider ring where different interactions can occur (head-on or long range) due to the shared vacuum chamber between two beams or if single beam considered a place with beam interactions like beam diagnostics or injection/extraction activities. 56, 80

Glossary

- Landau damping** A stabilizing mechanism related to the frequency spread between the oscillating particles. 21, 41, 107, 117
- long range** Interaction of the beams by the beam–beam force in locations where the beams are separated by certain distance (no overlap). 18
- luminosity** The quantity that measures the ability of a particle accelerator to produce the required number of interactions. 1, 115, 117
- luminosity leveling** A dynamic adjustment (usually reduction) of the luminosity to adapt the luminosity to the experimental constraints. 37, 47
- luminosity optimization** (or luminosity scan) A process to determine the maximum value of achievable luminosity by moving beams in separation and crossing plane with modest steps. 88
- orbit** (beam orbit) The closed trajectory of the traveling particles. 1, 20, 55, 56, 68, 71, 74, 87, 115, 116, 119
- orbit bump** An intentional local orbit often used to guide the beam at the IRs. 38
- pile-up** Simultaneous interaction during a bunch crossing at the IP. When the *pile-up* is too large (>50) the data processing and reconstruction degrades. xxi, 13, 37, 44–47, 52
- quench** An accidental transition of a super-conducting material to the normal conductivity state. 31
- response matrix** A matrix that relates the beam response (eg. orbit) to a machine parameter changes (e.g. orbit correctors). The matrix depends on the machine optics. 7, 9
- Singular-Value-Decomposition** An algebraic algorithm that decomposes a matrix to identify its eigenvalues and eigenmodes. It is frequently used for linear optimization or fitting problems. 10
- squeeze** The operational phase during which the optics of the machine is modified, such as to reduce the beam size at the interaction points. 62, 73, 81, 85, 92
- train** (or bunch train) a set of bunches that are injected together into the LHC. 18, 20, 121
- TWISS** a set of optics parameters describing the beam ellipse in the phase space. 6

List of symbols

α_u	The Courant–Snyder parameter, $\alpha_u = -\frac{1}{2} \frac{d\beta_u}{ds}$
β_r	The relativistic factor, $\beta_r = \frac{v}{c}$
β_u	The Courant–Snyder parameter, the betatron function for the plane u
β^*	The beta function value at the center of the IP
D_u	The linear dispersion for the plane u
ε_{un}	The normalized emittance, $\varepsilon_{un} = \varepsilon_u \gamma_r \beta_r$
ε_u	The beam emittance for the plane u
Φ	The Piwinski angle, $\Phi = \frac{\phi \sigma_z}{2\sigma_x^*}$
ϕ	Total crossing angle, <i>Glossary</i> : crossing angle
γ_r	The Lorentz factor, $\gamma_r = \frac{1}{\sqrt{1-\beta_r^2}}$
γ_u	The Courant–Snyder parameter, $\gamma_u = \frac{1+\alpha_u^2}{\beta_u}$
k	The quadrupole gradient
λ_i	The eigenvalue EV
\mathcal{L}	Luminosity
$\overline{\mathcal{L}_\phi}$	The normalized scan luminosity, see. Sec. 7.1
μ	The event <i>pile-up</i>
μ_u	The betatron phase advance in the plane u
Q_u	Machine tune for the plane u
Q'_u	The effective chromaticity for the plane u
ρ	The bending radius of the machine (of the main dipole)
r_0	The classical particle radius

Glossary

σ_u	The beam size for the plane u
σ_u^*	The beam size at the center of the IP for the plane u
θ	The dipolar kick from the COD
u, u'	The position and the angle in the plane u
ξ_u	The natural chromaticity, proportionality factor between momentum offset and tune change
ξ_{bb}	The beam–beam parameter
x, y	Horizontal and vertical coordinates
x', y'	Horizontal and vertical angles with respect to the beam traveling direction

Contents

Acknowledgements	iii
Abstract (English/ Français/ Deutsch)	v
Motivation	xi
Acronyms and Abbreviations	xii
Glossary	xiv
List of symbols	xvi
List of figures	xxiii
List of tables	xxvii
1 Summary of accelerator physics	1
1.1 Basics of accelerator physics	1
1.1.1 Transverse beam dynamics	2
1.1.2 The closed orbit	7
1.1.3 Main source of perturbations	9
1.1.4 Global orbit correction	9
1.1.5 Longitudinal beam dynamics	11
1.2 Collider luminosity	12
1.2.1 Collider performance	12
1.2.2 Integrated luminosity	13
1.2.3 Pile-up	13
1.3 Multi particle effects, beam instabilities and mitigations	14
1.3.1 Instability mitigation	15
1.3.2 Beam-beam effects	16
2 LHC and the CERN accelerator complex	23
2.1 LHC injector complex	23
2.2 The Large Hadron Collider	23
2.2.1 Magnets	24
2.3 LHC insertion regions	25

Contents

2.3.1	Interaction points	25
2.3.2	Cleaning regions	28
2.4	Orbit correction	29
2.5	Beam instrumentation	30
2.5.1	Beam position monitors	30
2.5.2	Beam loss monitors	31
2.6	LHC feedback systems	32
2.7	LHC operation	33
2.7.1	The cycle	33
2.7.2	LHC Run definition	34
2.7.3	Accelerator controls system	35
3	Luminosity leveling at LHC and HL-LHC	37
3.1	Luminosity leveling and pile-up limits	37
3.2	Available luminosity leveling methods	38
3.2.1	Beam offsets at the IP	38
3.2.2	Piwinski angle	39
3.2.3	Crab cavities	40
3.2.4	Beam size change – via β^*	41
3.3	Experience with the offset leveling in LHCb and ALICE	43
3.4	Leveling scenario for LHC Run 2 and Run 3	44
3.4.1	The LHC beams	46
3.4.2	Scenario of β^* leveling for LHCb in Run 2	46
3.4.3	Scenario for ATLAS and CMS for (Run 2) and Run 3	47
3.4.4	Overview of β^* leveling scenarios	48
3.5	Collide and squeeze	48
3.6	β^* leveling scenarios for the HL-LHC	50
3.6.1	HL-LHC Base line	50
3.6.2	ATS optics challenges	53
3.7	β^* leveling "a la carte"	53
3.8	Conclusions	54
4	Orbit drifts at LHC	55
4.1	Source of perturbations	55
4.2	Reference orbit and correction strategy	56
4.3	Bare orbit	56
4.3.1	Quadrupole misalignment and r.m.s. orbit perturbation	57
4.4	LHC orbit during cycle	59
4.4.1	Run 1 (2011-2012)	59
4.4.2	Run 2 (2015)	59
4.4.3	Specific patterns in the correction solutions	62
4.5	LHC orbit drifts during stable beams in 2015	63
4.5.1	The orbit drifts	63

4.5.2	Localization of the drift source	63
4.5.3	Reconstruction of the orbit from the positioning system	66
4.6	Observations in 2016	70
4.7	Conclusions	71
5	Orbit perturbations during the squeeze	73
5.1	The squeeze process at the LHC	73
5.2	Orbit perturbations	74
5.2.1	Beam position and separation at the IP	75
5.3	IP orbit drifts during the squeeze	75
5.3.1	Impact of BPM errors on the corrections	77
5.3.2	Correction solutions patterns	78
5.4	LHC Orbit feedback configuration	80
5.5	IP orbit drifts at the HL-LHC machine	80
5.5.1	Impact of BPM error on the correction	82
5.6	Conclusions	84
6	Experiments on collide and squeeze	85
6.1	MD results and long term stability validation	85
6.1.1	Orbit control	87
6.1.2	Collimators and beam losses	87
6.1.3	Beam position at the IP	87
6.1.4	Long term stability	92
6.1.5	Beam emittance evolution	93
6.2	Measurement of the crossing angle	95
6.3	Conclusions	97
7	IP orbit stabilization with luminosity	99
7.1	Feedback on the special luminosity modulation	99
7.1.1	Scan phases	99
7.1.2	Scan description and analysis	100
7.1.3	Luminosity rate and scan properties	105
7.2	Experimental validation of the stabilization method	106
7.2.1	Validation scenarios and assumptions	106
7.2.2	Tests without collisions	107
7.2.3	First experimental tests	108
7.2.4	Second experimental test	111
7.2.5	Summary of the experiments and remarks for future tests	117
7.3	Optimization scans with high luminosity	117
7.4	Beam position tracking during the scans	118
7.5	Bunch train behavior under stabilization scan	121
7.6	Conclusion and Outlook	124

Contents

8 Summary and outlook	125
Appendices	129
A Multi-orbit calculation framework	131
A.1 Idea and main concepts	131
A.2 Structure of the framework	132
A.3 Symmetrical patterns in correction solutions	134
A.4 Orbits in squeeze calculation	135
B Tensorics	137
B.1 The idea behind the need	137
B.2 Tensors and their language	138
B.3 Fields, operations and fluent API	139
C LHC analysis and operation tools	141
C.1 Orbit correction and eigenvalues	141
C.2 Conceptual design for the leveling service	141
C.3 Generation of spiral scans	142
C.4 Initial finding of the collisions	143
C.5 Luminosity data with higher rate	144
C.6 Luminosity leveling predictor	147
C.7 Bunch by Bunch orbit with LR interactions: TRAIN	148
Bibliography	151
Curriculum Vitae	159

List of Figures

1.1	The co-rotating coordinate system used to describe the trajectory of the particles when discussing beam dynamics. We use the x and y to describe transverse horizontal and vertical coordinates.	1
1.2	Example of the horizontal and vertical betatron functions.	4
1.3	The origin of the natural chromaticity and the use of sextupole magnets to compensate it [1].	5
1.4	Phase space ellipse.	6
1.5	Three different types of the orbit bumps.	8
1.6	The beam–beam force is represented here as a closed orbit shift (Δu) normalized to the r.m.s. beam size σ	17
1.7	Head–on (HO) and Long–range (LR) interactions in the presence of an external crossing angle	18
1.8	LHC tune footprints for head–on (HO) collisions only (blue region) and with long–range (LR) interactions.	18
1.9	The beam–beam force derivative as a function of beam separation.	19
1.10	Bunch by bunch separations at the IP due to the LR interactions at the IPs as function of the bunch slot for two selected batches of 72 bunches.	20
1.11	The orbit displacement along the trains.	21
2.1	CERN accelerator complex [29].	24
2.2	The aerial (a) view of the LHC (yellow) and of its four detectors. In blue the SPS accelerator and in red the PS. (b) illustrates the schematic view of the LHC with its sectors, octants and insertion regions [30].	25
2.3	The LHC main bending magnet and the tunnel. [30]	27
2.4	The LHC’s regular lattice cell consists of a focusing quadrupole (MQ), three dipoles (MBA, MBB), defocusing quadrupole and another three dipoles. The total length of the cell is 106.90 m [31].	27
2.5	Schematic layouts of the LHC interaction points [11].	28
2.6	The LHC collimation hierarchy.	29
2.7	Control theory feedback loop.	32
2.8	Standard LHC cycle.	33
3.1	Beam offset leveling.	39

List of Figures

3.2	Crossing angle reduction factor.	40
3.3	Sketch of the HO restoring process in the four dimensional space, using the crab cavities.	40
3.4	Proposed β^* leveling implementation.	41
3.5	Example of fully operational luminosity leveling by offset in the separation plane of LHCb [54].	43
3.6	An LHC Run 1 instability example, when some of the bunches (without HO collisions in IR1 and IR5) are drastically loosing intensity, courtesy X.Buffat [57].	44
3.7	Event pile-up for the LHC experiments.	45
3.8	Luminosity leveling scenarios for LHCb.	48
3.9	Scenarios for ATLAS/CMS experiments for bright beams.	49
3.10	The hourglass effect illustrated as a transverse beam size variation around the IP for a different LHC and HL-LHC optics configuration for design bunch length of $\sigma_z=7.7$ cm.	51
3.11	Pile-up at the HL-LHC IPs.	51
3.12	Luminosity leveling scenarios for ATLAS/CMS for the HL-LHC.	52
3.13	Betatron function with ATS optics from an experiment.	53
4.1	Distribution of the orbit r.m.s. for 100 simulated machines, for the LHC Run 1 and Run 2	58
4.2	Bare orbit r.m.s. evolution during LHC Run 1.	60
4.3	The extrapolation (from the period of fills 2800–2980) of the maximum orbit r.m.s. growth.	61
4.4	Bare orbit r.m.s. evolution during LHC Run 2 (2015).	61
4.5	Example of the correction patterns appearing in the OFB real time channel. . .	62
4.6	Measured and bare orbit r.m.s. during fill 4402.	64
4.7	The triplet layout on the right side of LHC point 8. The colored marks (A,B) represent the positions of the WPS sensors.	65
4.8	The LHC triplet movement on the left and right side of points 8 (top row), during 24h period before the start of the Technical Stop 1.	65
4.9	Comparison of the observed bare orbit r.m.s. evolution (obtained from unfolding corrections) and the simulation based on the recorded triplet movements. . . .	66
4.10	The triplet alignment before the main perturbation.	67
4.11	Reconstrucion of orbit perturbation in fills 4538 and 4540.	68
4.12	HL-LHC response for the triplet movement as observed in 2015 in the LHC. . .	68
4.13	Triplet thermal shield.	69
4.14	One of the main ingredients for the cryostat movements.	69
4.15	Fill 4947 r.m.s. bare orbit evolution.	70
5.1	The time evolution of the β^* in the LHC IPs.	73
5.2	Example of the parabolic segments in the functions to ensure that the gradient and current derivations with time are zero at the matched points.	74

5.3	The beam separation is calculated from the adjacent BPMs using equations 5.2 and 5.3.	75
5.4	The beam separation at the IPs at the final point of the squeeze with ideal BPMs.	76
5.5	Beam separation at the IPs at the final point of the squeeze with real BPMs. . .	77
5.6	Optimization trims for LHC in 2012.	78
5.7	Impact of the BPM errors on the beam separation in beam sigma at the IP . . .	79
5.8	Example of accumulated correction solutions obtained after 14 squeeze steps.	79
5.9	Average separation at the IP at the end of the squeeze as a function of a number of eigenvalues used for correction (BPM errors of 20 μm). A broad <i>minimum</i> is present around 440 values	80
5.10	The beam separation at the IPs at the final point of the squeeze with ideal BPMs.	81
5.11	The beam separation at the IPs at the final point of the squeeze with real BPMs.	82
5.12	Impact of the BPM errors on the beam separation in beam sigma at the IP as a function of the number of EVs used in the correction. The top row illustrates the mean values obtained in the calculations while the bottom shows the maximum values obtained. Simulations done for ATS optics with $\beta^*=10$ cm. (a) and (b) represent the mean value, (c) and (d) represent the max value	83
6.1	The evolution of the luminosity and of β^* for the 3 colliding IPs during MD sessions in 2015.	86
6.2	The reference orbit concept.	88
6.3	The evolution of the beam position wrt to the center of the collimator.	89
6.4	Evolution of the luminosity and of the beam offset at IP5 interpolated from the DOROS data.	89
6.5	Comparison of the evolution of the beam offsets tracked by DOROS with the offsets reconstructed from the luminosity optimization scans in IP1 and IP5. .	90
6.6	Evolution of the beam positions at the ATLAS (top left) and CMS (top right) IPs obtained by extrapolation of the DOROS data along the fill 4604.	91
6.7	The absolute value for the horizontal separation knob.	92
6.8	The evolution of the beam separation trims as a function of the time along the squeeze w.r.t. the settings established in August (fill 4295).	92
6.9	The evolution of the emittance of the two bunches of each beam during the squeeze of fills 4292 and 4604.	94
6.10	Reconstructed geometric factor (F) in IP1 based on the recorded luminosity data along the squeeze.	96
6.11	Crossing angle at IP1 in 2015.	96
7.1	Positions of the beams in the x-y plane during the scan.	100
7.2	The time evolution of the trajectories (Eq. 7.2) for the horizontal (blue) and the vertical plane (red).	101
7.3	Simulated horizontal (x) and vertical (y) trajectories (top row) and simulated (noisy) luminosity measurement computed from the beam separation during the scans.	104

List of Figures

7.4	Simulated fit result (for ν_{Δ} and α) and its error as a function of the luminosity rate.	105
7.5	Traces of the beam movement measured by the standard LHC BPMs installed next to the Q1 quadrupole.	108
7.6	Luminosity data recorded at 3 Hz in IP1 during fills 4292 (a) and 4295 (b).	109
7.7	Example of a scan test with Beam 1 (b) in IP1 with 3 Hz data.	109
7.8	Examples of the scan test results of Beam 1 in IP8 with 10 Hz data.	110
7.9	The IP1 3 Hz luminosity data for fills 4603 (left) and 4604 (right).	112
7.10	IP1 scan results for fill 4603.	113
7.11	IP1 scan results for fill 4604.	114
7.12	IP8 high rate luminosity data during fill 4603.	115
7.13	The IP8 scan results.	116
7.14	Example of a scan at high luminosity with a reduced scan radius.	118
7.15	The expected and recorded (DOROS extrapolation) beam movement at the IP.	118
7.16	Beam position at IP1 and IP5 during rotation scans.	119
7.17	The beam–beam kick and the associated closed orbit shift at the IP for the beam emittance of $2.5 \mu\text{m}$	120
7.18	The correlation between the moving and static beam during a scan.	121
7.19	Bunch by bunch offsets in the crossing (top) and the separation (bottom) planes at IP5.	122
7.20	Offsets induced due to the deliberate separation required by the scan.	123
A.1	Result of the pattern search task. Most of the build structures appear in the same configuration that points to the static origin for this phenomena.	135
C.1	Eigenvalue spectrum for LHC Beam 2.	142
C.2	LUMI-SCAN Knob example for the Beam1 in IP1.	143
C.3	<i>Generation Application</i> main panel.	143
C.4	The actual functions (horizontal–darker and vertical–lighter LUMI scans) that were used for the optimiation scan tests.	144
C.5	Example for finding collisions for a given initial separation based on a spiral scan.	145
C.6	Finding collisions with a <i>spiral scan</i> (seen as a black line in the right bottom part, here in "rectangular form") on April 8th 2016 when establishing first collisions after the winter stop in 2015/2016.	146
C.7	Principle of the LHCb luminosity data transmission.	146
C.8	Result panel of the luminosity leveling tool.	147
C.9	Cover page of the TRAIN repository https://gitlab.cern.ch/agorzaws/train	148
C.10	Structure of the TRAIN data flow. Input files marked in red. The middle state result/input files in blue.	149

List of Tables

1.1	Main multipolar components and their effect on the beam.	2
2.1	Selected LHC parameters. A complete list as well as the detailed explanation of the physical meaning can be found in [11].	26
2.2	Parameters of the LHC orbit correctors. The MCB correctors are installed in the arcs, all other types are distributed over the insertions. The MCBX type correctors are installed on the vacuum chamber that is common for both beams [11, Tab. 7.15, 8.17, 8.19, 8.23]. Types: SC – super conducting, NC – normal conducting, T – super conductor type, (*) – it is the gap height.	30
2.3	Summary on the LHC runs. In bold the years of operation data used in this thesis. In italic forecast–ed dates [41]. A Long Shutdown (LS) typically lasts 18–36 months.	34
3.1	Typical pile–up limit values and expected leveled luminosity (given in $\text{cm}^{-2}\text{s}^{-1}$) in the LHC experiments for different time periods [45, 43]. DR – Design Report. (*) – 2808 bunches design brightness, (**) – ≈ 2500 bunches, Run 2 brightness (see Tab. 3.3).	38
3.2	Overview of luminosity control methods.	42
3.3	LHC beam overview with peak pile–up for high (ATLAS and CMS) and medium luminosity (LHCb) experiments. Cases that exceed the allowed pile–up limits are highlighted in bold. Pile–up values are calculated for a bunch length of $\sigma_z = 10$ cm with cross section of $\sigma_p = 82$ mb and crossing angle $\phi/2 = 145 \mu\text{rad}$ ($\phi/2 = 185 \mu\text{rad}$ for LHC 2016). Acronyms: INJ–Injection, FT– Flat top and SB– Stable beams, DR – Design report.	46
3.4	Summary on the leveling times and the required number of β^* points for different implementations and operation scenarios. When two leveling methods are mixed, separation leveling is used first, followed by β^* leveling. Leveling types: d –offset and β^* leveling.	49
3.5	Summary of HL–LHC beams [41] with associated peak pile–up ($\sigma_p = 82\text{mb}$) for high luminosity IPs (ATLAS and CMS). The pile–up is calculated for a nominal bunch length of $\sigma_z = 7.7$ cm, crossing angle of $\phi/2 = 180 \mu\text{rad}$ (restored with CCs) and includes the hourglass effect. (*) this is a theoretical value for the LHC beam for this β^*	52

List of Tables

4.1	Estimate of the r.m.s. element misalignment and the corresponding orbit r.m.s. The estimates are valid for the injection optics.	58
4.2	Estimates of the r.m.s. orbit growth for LHC Run 1 and Run 2 and corresponding estimated quadrupole misalignment.	60
4.3	Details of selected LHC fills in 2015, used for further analysis. SB – Stable Beams.	63
5.1	The influence of the initial misalignment and BPM errors on the end of squeeze (collision optics) beam separation d_{IP} for the LHC.	78
5.2	The influence of the initial misalignment and BPM errors on the end of squeeze (collision optics) beam separation d_{IP} for the HL-LHC.	82
6.1	Measured normalized emittances for the squeeze of fill 4604.	93
6.2	The half-crossing angle estimate obtained from this collide and squeeze (C and S) MD are compared to the design values as well as to the values measured with K-Modulation [87]. No usable data was recorded in IP5.	95
7.1	The settings for IP1, IP5 and IP8 scans executed in the fills 4292, 4295, 4603 and 4604. The difference in the scan radius between the generated and used scan is due the fact that the actual emittance was much smaller than the value that was used for the generation. The last column represents the artificial separation at the end of the scan. Values in bold are normalized to the actual emittance. . . .	106
7.2	List of scans performed during the MD blocks. SB – Stable Beams.	107
7.3	The scans performed during MD2 and their results. For IP8 data (ST#1) due to the noise on the recorded signal it was impossible to finalize the analysis. . . .	108
7.4	Scan parameters of second tests and results. (<i>n/a</i>) is for the scans disturbed by the orbit drifts that occurred in IP8, see details in Sec 7.2.4.2.	111
7.5	Expected kicks (θ_{bb}) and orbit displacements (u_{bb}) at the IP due to the beam-beam effect for $\beta^* = 80$ cm at 6.5 TeV for a selection of beam separations and an emittance of $\varepsilon = 2 \mu\text{m}$	120

1 Summary of accelerator physics

This first chapter recalls basics of accelerator physics. We start with some principles of beam dynamics and introduce the concept of luminosity. This chapter closes with a discussion of the main causes and possible mitigation of beam instabilities. The reader will find here a review of literature in a shortened way with no detailed derivations, since those can be found in most accelerator physics textbooks such as [1, 2, 3, 4] often quoted in this document. Some of the examples are related to the Large Hadron Collider (LHC) that is discussed later in Chap. 2.

1.1 Basics of accelerator physics

To describe particles traveling in an accelerator, a co-moving coordinate system is introduced (see Fig. 1.1). It is defined with respect to the nominal design orbit which describes the closed trajectory of an ideal particle in the machine. The transverse axes are denoted by the symbols

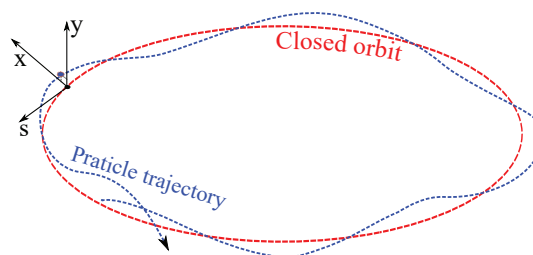


Figure 1.1 – The co-rotating coordinate system used to describe the trajectory of the particles when discussing beam dynamics. We use the x and y to describe transverse horizontal and vertical coordinates.

x and y and describe the radial (horizontal) plane, respectively the perpendicular (vertical) plane. The global coordinate s defines the zero position of the co-moving coordinate system along the design orbit with respect to an arbitrary location in the global reference frame.

1.1.1 Transverse beam dynamics

1.1.1.1 Linear equations of motion

The motion of particles in an accelerator is mostly determined by the electric \vec{E} and magnetic \vec{B} fields. The momentum \vec{p} changes due to the Lorentz force as:

$$\frac{d\vec{p}}{dt} = q(\vec{E} + \vec{v} \times \vec{B}), \quad (1.1)$$

where q is the particle charge and \vec{v} its velocity. If the magnetic field vector \vec{B} is orthogonal to the particle momentum \vec{p} , the equilibrium of the Lorentz force and centrifugal force leads to the definition of the beam rigidity $B\rho$:

$$B\rho = \frac{p}{q}, \quad (1.2)$$

with ρ the bending radius and $B = |\vec{B}|$ and $p = |\vec{p}|$. The magnetic field in the vicinity of the origin can be expanded into multipoles¹:

$$B_y(x) = B_{y0} + \frac{\partial B_y}{\partial x} x + \frac{1}{2!} \frac{\partial^2 B_y}{\partial x^2} x^2 + \frac{1}{3!} \frac{\partial^3 B_y}{\partial x^3} x^3 + \dots \quad (1.3)$$

Normalizing the magnetic field to the magnetic rigidity (Eq. 1.2) we obtain the magnetic field expressed as an infinite sum of multipolar elements:

$$\frac{q}{p} B_y(x) = \frac{1}{\rho} + kx + \frac{1}{2!} mx^2 + \frac{1}{3!} ox^3 + \dots \quad (1.4)$$

where k is a quadrupole component, m is a sextupole component and o is an octupole component. The notations and the effects of each multipole are listed in Table 1.1. If we

Multipole	Parameter	Unit	Effect on the beam
Dipole	$\frac{1}{\rho}$	1/m	bending
Quadrupole	k	T/m ²	focusing
Sextupole	m	T/m ³	chromatic correction
Octupole	o	T/m ⁴	amplitude detuning

Table 1.1 – Main multipolar components and their effect on the beam.

restrict the expression to quadrupole fields and we keep only the leading terms of Eq. 1.4, then

¹here we consider only the vertical component of the magnetic field B_y , the horizontal B_x develops in the same way.

Eq. 1.1 can be rewritten as a differential equation of motion [1, Sec. 3.2]:

$$\boxed{\begin{aligned} x''(s) + k_x(s) \cdot x(s) &= \frac{1}{\rho(s)} \frac{\Delta p}{p} \\ y''(s) + k_y(s) \cdot y(s) &= 0, \end{aligned}} \quad (1.5)$$

where $\frac{\Delta p}{p}$ denotes the momentum offset relative to the reference momentum and s the longitudinal position within the ring. Equations 1.5 are Hill's type differential equations. The gradients k_x and k_y are related to the strength of the quadrupolar fields $K(s)$ and to the term $\frac{1}{\rho^2}$, stemming from the dipolar fields:

$$\begin{aligned} k_x &= \frac{1}{\rho^2} - K(s) = \frac{1}{\rho^2} + \frac{1}{B\rho} \frac{\partial B_y}{\partial x} \\ k_y &= K(s) = \frac{1}{B\rho} \frac{\partial B_x}{\partial y}. \end{aligned} \quad (1.6)$$

1.1.1.2 Beta function and dispersion

The equations of motion (Eq. 1.5) for the horizontal and vertical planes are independent if no coupling term is considered. Both planes can then be treated separately. The following discussion considers one plane denoted as u , which applies to the horizontal or to the vertical plane. The homogeneous part of these equations (i.e. without $\frac{\Delta p}{p}$) can be solved with Floquet's Theorem [5]. The solution is given by:

$$\boxed{u_\beta(s) = \sqrt{\varepsilon_u \beta_u} \cos(\mu_u(s) + \mu_u(s_0))}, \quad (1.7)$$

with the initial conditions ε_u and $\mu_u(s_0)$, s_0 denotes an arbitrary but fixed longitudinal position in the ring or the starting point in a transfer line, β_u is the so-called *betatron function* for the plane u which is by definition always positive and ε_u is the *transverse emittance* for the plane u .

The betatron function at a collision point(*) is usually denoted as β_u^* .

The betatron phase μ_u for the plane u is related to the betatron function via

$$\mu_u = \int_{s_0}^s \frac{ds}{\beta_u(s)}. \quad (1.8)$$

As indicated by Eq. 1.5, the trajectories of particles with non-zero momentum deviations $\frac{\Delta p}{p}$ are modified by dipolar fields. A linear ansatz can be made for the solution of the in-homogeneous

Chapter 1. Summary of accelerator physics

equation:

$$u(s) = u_\beta(s) + D_u(s) \frac{\Delta p}{p}, \quad (1.9)$$

where $u(s)$ denotes the transverse position, $D_u(s)$ the (linear) *dispersion function* at the s coordinate, u_β the solution of the homogeneous Hill's equation (betatron oscillation, Eq. 1.7). Figure 1.2 illustrates the beta function and the dispersion function for an accelerator cell and for a section of a ring.

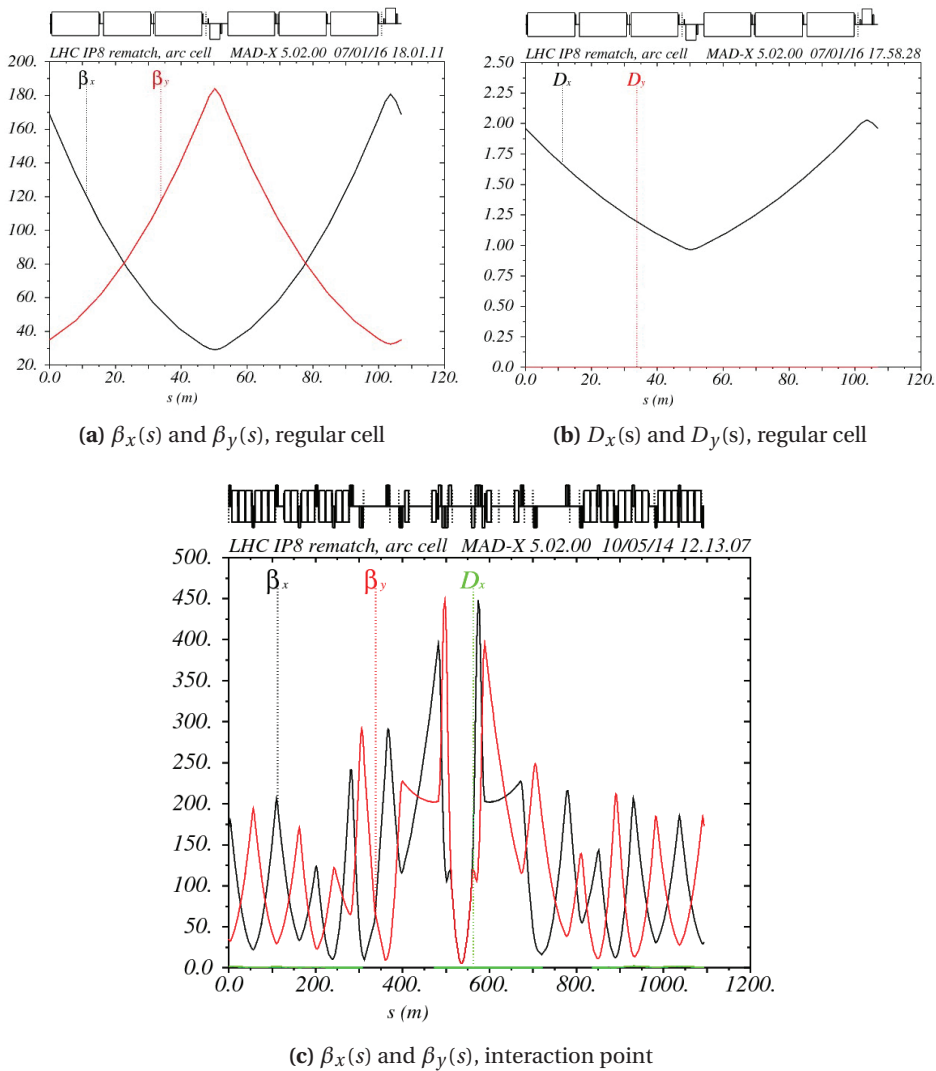


Figure 1.2 – Example of the horizontal and vertical betatron functions (a) and dispersion function (b) evolution along the s coordinate in the regular an LHC arc lattice. (c) evolution of the betatron functions around the LHC interaction point. The beam waist at $s \approx 550$ m corresponds to the interaction point.

1.1.1.3 Tune and chromaticity

The particle trajectory has an oscillatory behavior as indicated by Eq. 1.7. These transverse oscillations are called *betatron oscillations*, since they were first observed in betatron accelerators [1, Sec. 1.3.8]. In a ring, the number of betatron oscillations per revolution is called the *tune*. For the plane u the *tune* Q_u of an accelerator can be calculated from the phase advance and thus from the betatron function by:

$$Q_u = \frac{1}{2\pi} (\mu_u(s+C) - \mu_u(s)) = \frac{1}{2\pi} \oint_C \frac{ds}{\beta(s)}, \tag{1.10}$$

where C is the accelerator circumference.

Chromaticity and its correction Combining Eq. 1.2 and Eq. 1.6 shows that the strength $K(s)$ of quadrupole fields is inversely proportional to the particle momentum. This results in a momentum dependence of the tune. In a linear approximation, the natural *chromaticity* ξ_u is defined as a proportionality factor between momentum offset and tune change:

$$\Delta Q_u = \xi_u \cdot \frac{\Delta p}{p}. \tag{1.11}$$

In order to reduce the tune spread induced by the energy spread and to avoid certain instabil-

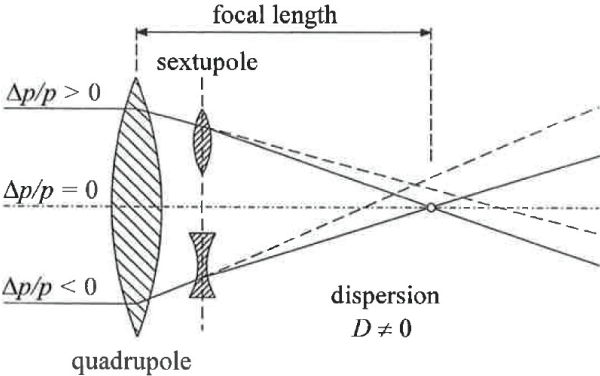


Figure 1.3 – The origin of the natural chromaticity and the use of sextupole magnets to compensate it [1].

ities (see Sec. 1.3), sextupole magnets are installed in locations of non-vanishing dispersion to correct the natural chromaticity of a machine. Figure 1.3 illustrates the principle of chromaticity correction. The effective chromaticity is given by:

$$Q'_u = \frac{\Delta Q}{\frac{\Delta p}{p}}. \tag{1.12}$$

1.1.1.4 Beam emittance and the beam size

For each transverse plane u , every particle in a storage ring follows an ellipse in phase space (u, u') which is described by the so-called Courant-Snyder invariant a , which is defined by

$$a_u = \gamma_u u^2 + 2\alpha_u u u' + \beta_u u'^2, \quad (1.13)$$

where u' defines the beam angle with respect to the beam direction. The area of the ellipse

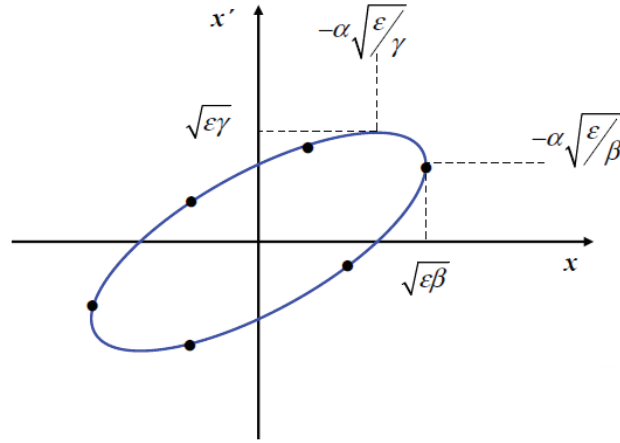


Figure 1.4 – Phase space ellipse.

(Fig. 1.4) is given by πa_u . The functions α and γ are (together with β) the so-called Courant-Snyder functions which are defined for each plane [6]. The parameters α , β and γ are usually called TWISS parameters. For a particle beam which consists of many particles with a certain distribution in phase space, each particle follows its own Courant-Snyder ellipse within the distribution. As a characteristic property of such a beam, the so-called *transverse emittance* ϵ for the plane u is defined by:

$$\epsilon_u = \sqrt{\langle u^2 \rangle + \langle u'^2 \rangle - \langle uu' \rangle}. \quad (1.14)$$

During the acceleration, the longitudinal momentum is increased while the transverse momentum is not affected. Thus u' , the angle between particle trajectory and design trajectory, decreases. Therefore, the transverse emittance decreases according to Eq. 1.14. This effect is called *adiabatic damping* [6, Sec. 3.d]. For that reason, a more convenient quantity for the operation of a proton storage ring is the *normalized emittance* ϵ_n which is defined for the plane u as

$$\epsilon_{un} = \epsilon_u \gamma_r \beta_r, \quad (1.15)$$

where γ_r and β_r are the relativistic Lorentz factors. The normalized emittance may be used to compare the emittance along an accelerator chain or between different hadron colliders. The

r.m.s. transverse beam size for plane u along the accelerator is given by:

$$\sigma_u(s) = \sqrt{\varepsilon_u \beta_u(s) + \left(D_u(s) \frac{\Delta p}{p}\right)^2} \quad (1.16)$$

where $\beta_u(s)$ is the betatron function and $D_u(s)$ is the dispersion at coordinate s . Usually the dispersion is brought close to zero in the insertion (straight) regions therefore the beam size σ_n^* at an interaction point IP is given by:

$$\sigma_u^* = \sqrt{\frac{\varepsilon_{un} \beta_u^*}{\gamma_r \beta_r}}. \quad (1.17)$$

As shown in Fig. 1.2c, the smallest beam size is obtained at the waist of the beta function.

Matched optics A matched betatron function with desired β^* values in each collision point, desired tune and natural chromaticity defines a so called machine *optics* that consists of a well defined and self consistent set of magnet strengths needed to obtain the desired parameters.

1.1.2 The closed orbit

As shown in Eq. 1.1 a transverse magnetic field leads to a particle trajectory change. The ideal particle will follow a particular trajectory, which closes on itself after one revolution. This trajectory is called the *closed orbit*. Without derivation (see for example [7]) we present the relation for the orbit change Δu at the position j , resulting from a dipolar kick θ at the position i for the plane u . For a ring this is given by

$$\Delta u_j = R_{ji} \theta_{ui}, \quad (1.18)$$

where

$$R_{ji} = \frac{\sqrt{\beta_j \beta_i} \cos(|\mu_i - \mu_j| - \pi Q)}{2 \sin(\pi Q)}, \quad (1.19)$$

is the element² of the linearized response matrix. β and μ correspond to the beta function and the phase advance at the locations of the observation point j and the kick i . Q is the machine tune.

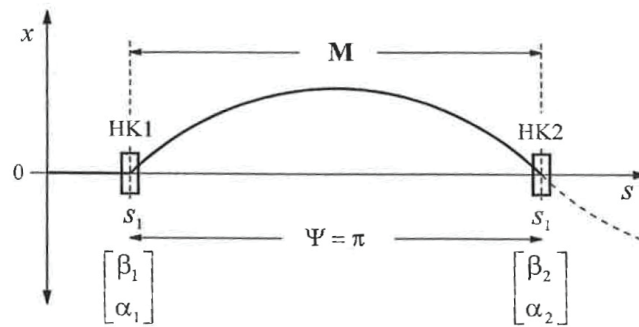
Orbit bumps

An orbit bump is a local excursion of the beam in the x or y plane. In order to control the transverse beam position at specific locations, for example at the collision points, several

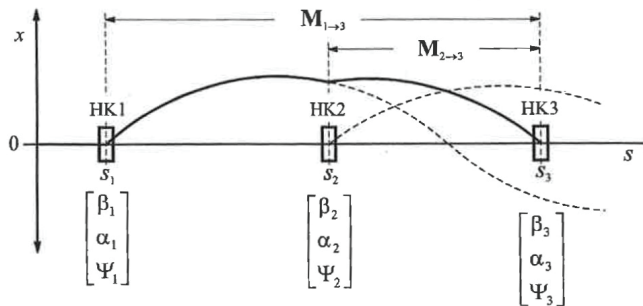
²here we omit the u denotation, but both planes get the R respectively.

Chapter 1. Summary of accelerator physics

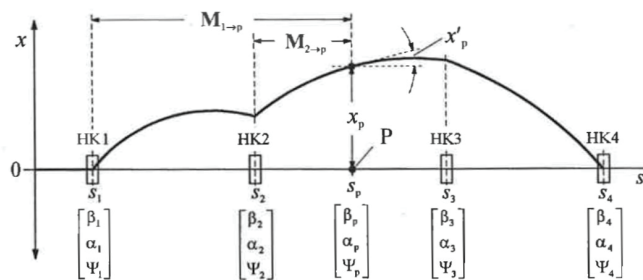
types of orbit bumps can be constructed. The most commonly used four corrector bump (along with two other options) is shown in Fig. 1.5 [1]. While the bump with two correctors (Fig. 1.5a) works only for phase advance of $n\pi$, the three corrector (Fig. 1.5b) option overcomes this limitation but does not provide a control over the angle at the target location. Figure 1.5c illustrates the four corrector bump, which provides control over both u and u' at the desired place.



(a) 2 corrector bump



(b) 3 corrector bump



(c) 4 corrector bump

Figure 1.5 – Three different types of the orbit bumps. Only the bump using four correctors (c) gives full control (u and u') at the desired point P [1].

1.1.3 Main source of perturbations

The majority of closed orbit perturbations originates from quadrupole misalignments. Their impact is discussed later in this document (see Chaps. 4 and 5).

A quadrupole displaced by δ_u introduces a dipole kick θ_Q that is proportional to its focusing strength k and its length l :

$$\theta_Q = kl \cdot \delta_u. \quad (1.20)$$

Using Eq. 1.18, the orbit displacement at the observation point j , due to N misaligned quadrupoles is given by:

$$\Delta u_j = \sum_{i=1}^N R_{Q_{ji}} \cdot \delta_{ui} \quad (1.21)$$

where $R_{Q_{ij}} = R_{ij} k_i l_i$ is the response matrix element for the j -th observation point (for example a beam position monitor) and i -th quadrupole of length l_i and strength k_i .

1.1.4 Global orbit correction

Orbit correction is one of the fundamental processes used for beam control in accelerators. Whether steering beams into collision for high-energy physics, steering photon beams in a synchrotron light source or positioning a beam on target for medical applications, it is essential to control the beam trajectory (transfer line) or orbit (synchrotron).

In linear approximation, the orbit change $\Delta \vec{u}$ at N monitors is related to the kicks $\Delta \vec{\theta}$ at M dipole correctors by the response matrix \mathbf{R} :

$$\Delta \vec{u} = \mathbf{R} \cdot \Delta \vec{\theta} \quad (1.22)$$

$$\begin{pmatrix} \Delta u_1 \\ \Delta u_2 \\ \Delta u_3 \\ \vdots \\ \Delta u_N \end{pmatrix} = \begin{pmatrix} R_{11} & R_{12} & R_{13} & \cdots & R_{1M} \\ R_{21} & R_{22} & R_{23} & \cdots & R_{2M} \\ R_{31} & R_{32} & R_{33} & \cdots & R_{3M} \\ \vdots & \vdots & \vdots & \ddots & \vdots \\ R_{N1} & R_{N2} & R_{N3} & \cdots & R_{NM} \end{pmatrix} \begin{pmatrix} \Delta \theta_1 \\ \Delta \theta_2 \\ \Delta \theta_3 \\ \vdots \\ \Delta \theta_M \end{pmatrix} \quad (1.23)$$

The response matrix \mathbf{R} depends on the machine optics, its elements are described by Eq. 1.19. Let us consider a measured orbit as \vec{u}_m . The goal of the orbit correction is to find kicks $\Delta \vec{\theta}_c$ such as to minimize the r.m.s. orbit:

$$\|\vec{u}_m + \mathbf{R} \vec{\theta}_c\|^2 = \min. \quad (1.24)$$

Chapter 1. Summary of accelerator physics

Equation 1.23 must be inverted to obtain the required corrector settings $\vec{\theta}_c$. If \mathbf{R} is a square and invertible matrix then $\vec{\theta}_c = -\mathbf{R}^{-1}\vec{u}_m$. In the general case the Singular-Value-Decomposition algorithm (SVD) [8] may be used to decompose a non-square ($N \times M$) matrix \mathbf{R} into the following form:

$$\mathbf{R} = \mathbf{U} \cdot \lambda \cdot \mathbf{V}^T, \quad (1.25)$$

where λ is a diagonal matrix of M eigenvalues (EV, λ_i) with $U^T U = I$ and $V V^T = V^T V = I$:

$$\lambda = \begin{pmatrix} \lambda_1 & 0 & \cdots & 0 \\ 0 & \lambda_2 & \cdots & 0 \\ \vdots & \vdots & \ddots & \vdots \\ 0 & 0 & \cdots & \lambda_M \end{pmatrix} \quad (1.26)$$

The solution minimizing the residual orbit error (in the least square sense) is obtained from the SVD decomposition as:

$$\vec{\theta}_c = \mathbf{V} \lambda^{-1} \mathbf{U}^T \vec{u}_m, \quad (1.27)$$

where \vec{u}_m is a measured orbit perturbation and \mathbf{V} , \mathbf{U} and λ are the result of the SVD operation on the initial \mathbf{R} matrix.

Another popular correction algorithm is MICADO [9] (*MINimisation des Carres de Distorsions d'Orbite*). Contrary to the SVD correction, this method performs an iterative search over all the available correctors, selecting at each step the one that is the most effective to reduce the r.m.s. For a non-singular matrix \mathbf{R} the two methods converge differently but the solution with the smallest r.m.s. is the same in both cases. The main difference comes from the fact that MICADO adds correctors one by one, it can be used to correct with fewer but stronger kicks as compared to SVD that always uses all correctors [10, Sec. 4.7.3]. When the response matrix is accurate, a correction with a small number of correctors can be used to localize the source of the perturbation (see example in Sec. 4.5).

1.1.5 Longitudinal beam dynamics

Equation 1.1 shows that acceleration can be provided by an electric field. The fields that can be used for beam acceleration are of two types: DC acceleration structures and radio-frequency (RF) cavities. DC acceleration is typically used for low energy accelerators. An RF acceleration cavity generates a longitudinal electric field at an RF frequency ω_{RF} . The energy gain (ΔE) per passage through a cavity gap is given by:

$$\Delta E = qV_0 \sin(\omega_{\text{RF}} t + \phi_s), \quad (1.28)$$

where V_0 defines the effective peak accelerating voltage. ϕ_s is the phase of the particle with respect to the RF field. For the special case of $\phi_s = 0$, the particle maintains its energy constant turn after turn. For $\pi > \phi_s > 0$, the particle is accelerated, while if $2\pi > \phi_s > \pi$, the particle is decelerated.

The particle that circulates with a constant phase ϕ_s turn after turn is known as the synchronous particle. The particles in the beam, due to the finite energy spread, perform oscillations in the longitudinal plane ($\Delta\phi - \frac{\Delta p}{p}$) around the stable ϕ_s . Similarly to the transverse motion, the number of those oscillations per turn is called synchrotron tune (Q_s) with values much lower than the betatron tune.

To ensure that the particles always see an accelerating voltage when they transit the RF cavity, the frequency of the electric field has to be an integer multiple of the machine revolution frequency. Each period of the electric field defines a *RF bucket* that may hold a particle bunch. The total number of buckets (harmonic number of the RF system) is given by:

$$h = \frac{f_{\text{RF}}}{f_{\text{rev}}}, \quad (1.29)$$

where f_{RF} is frequency of the RF system and f_{rev} is the revolution frequency. Total number of bunches in the machine is limited by h and depends on the desired bunch spacing. The LHC RF frequency is 400 MHz and a bucket corresponds to 2.5 ns. The total number of available buckets is 35640. For a design bunch spacing of 25 ns, the maximum number of bunches is 3564. In reality, due to the injection and dump kicker gaps, the maximum number of bunches is only 2808 [11].

The proton bunch length depends on the rf-wavelength and on the longitudinal emittance. The longitudinal emittance is proportional to the product of energy spread and bunch length. The bunch length and the energy spread may be controlled through the RF voltage $\sigma_s \propto \frac{1}{\sqrt{V_{\text{RF}}}}$ [2, Sec. 8.3.2].

1.2 Collider luminosity

1.2.1 Collider performance

For a physical process p with a cross-section σ_p , the number of events per unit time $\frac{dR_p}{dt}$ is given by

$$\frac{dR_p}{dt} = \mathcal{L} \times \sigma_p. \quad (1.30)$$

The factor \mathcal{L} is called the luminosity. It is measured in $[\text{cm}^{-2}\text{s}^{-1}]$ and characterizes the particle collider performance.

To compute the luminosity, let us consider two particle beams. The distribution of particles in a single bunch, centred around a longitudinal fixed point s_0 is given by $\rho(\vec{x}, s_0)$. For each bunch crossing, the luminosity is given by the convolution of the distributions of the two beams labelled (1) and (2)[12]:

$$\mathcal{L} = N_1 N_2 f_{rev} \iiint_{-\infty}^{\infty} \rho_1(\vec{x}, s_0) \rho_2(\vec{x} - s_0) dx dy ds. \quad (1.31)$$

N_1, N_2 denote for the number of particles in the bunch of beam 1(2). We will assume that the beams have identical orbits, emittance and optics and that the beam sizes are constant over the interaction region. For Gaussian distributions in all degrees of freedom, the luminosity \mathcal{L}_b from any bunch pair colliding in the center of the interaction point is given by:

$$\mathcal{L}_b = \frac{N_1 N_2 f_{rev} \gamma_r}{4\pi \sqrt{\beta_x^* \varepsilon_x} \sqrt{\beta_y^* \varepsilon_y}} \times R(\phi, d), \quad (1.32)$$

$\beta_{x,y}^*$ is the (horizontal/vertical) betatron function at the interaction point and $\varepsilon_{x,y}$ is the normalized beam emittance, f_{rev} is the revolution frequency, γ_r the relativistic factor and $R(\phi, d)$ is the reduction factor for the geometric overlap. The maximum luminosity at the interaction point for round beams ($\beta_x^* = \beta_y^*$) follows from Eq. 1.32:

$$\mathcal{L}_{IP} = \frac{N_1 N_2 n_{IP} f_{rev} \gamma_r}{4\pi \beta^* \varepsilon}, \quad (1.33)$$

where n_{IP} denotes for the number of bunch-pairs colliding at the IP. For beams colliding with a transverse offset d and a finite angle ϕ (the crossing angle) the luminosity becomes:

$$\mathcal{L}_{IP} = \frac{N_1 N_2 n_{IP} f_{rev} \gamma_r}{4\pi \beta^* \varepsilon} \times F(\phi) \times D(d) \times W(\phi, d). \quad (1.34)$$

$F(\phi)$ stands for a correction factor for the crossing angle ϕ and $D(d)$ is a transverse separation factor. Both terms can be considered as reduction factors. $W(\phi, d)$ is the additional reduction

when both ϕ and d are present at the same time [12, Sec 6.2]. The expressions for the two factors are:

$$D(d) = \exp\left(-\frac{|\vec{d}|^2}{4\sigma^{*2}}\right), \quad (1.35)$$

$$F(\phi) = \frac{1}{\sqrt{1 + \left(\frac{\sigma_z}{\sigma^*} \tan\left(\frac{\phi}{2}\right)\right)^2}}, \quad (1.36)$$

where $|\vec{d}|$ is the transverse separation of two beams, σ^* is the transverse beam size ($\sqrt{\frac{\beta^* \epsilon_n}{\gamma_r \beta_r}}$) at the iteration point and σ_z is the bunch length. Both factors $D(d)$ and $F(\phi)$ are ≤ 1 and can be used to adjust ("lower") the luminosity (see Chap. 3). The assumption of a constant beam size over the bunch length breaks down when β^* is comparable to the bunch length (hourglass effect) [12, Sec 6.1]. There exists no analytic formula for the general case in the simultaneous presence of the hourglass effect, crossing angle and transverse offset. In that case the overlap integral has to be evaluated numerically.

1.2.2 Integrated luminosity

The integrated luminosity measured in [cm^{-2}] and given by

$$\mathcal{L}_{\text{int}} = \int_0^T \mathcal{L}(t) dt, \quad (1.37)$$

is the main performance parameter of a collider. $\mathcal{L}_{\text{int}} \times \sigma_p$ gives the number of events for a process p that have been produced over a time interval T (Eq. 1.30).

1.2.3 Pile-up

An important parameter that affects the quality of the recorded luminosity at the LHC is the *event pile-up*, the number of simultaneous particle interactions during one bunch crossing. A high event pile-up complicates the physics analysis and degrades the data quality for certain types of physics channels. The event pile-up μ is directly proportional to the luminosity per bunch crossing \mathcal{L}_b (see Eq. 1.32) and is given by:

$$\mu = \mathcal{L}_b \times \sigma_p, \quad (1.38)$$

where σ_p is the total cross section for proton-proton interactions at the LHC, $\sigma_p = 70$ to 110 mbarn³. For the 2015 peak LHC luminosity, the expected pile-up for the ATLAS/ CMS experiments is around 20. For the LHCb experiment the peak pile-up is around 12, while a maximum of 2 can be accepted by experiment. The pile-up management is one of the key issues for the

³barn = 10^{-28} m^2 , given that for the LHC the energy span is 450 GeV – 7 TeV

LHC (run 2 and run 3) and the HL-LHC operation and will be discussed later in this document (Chap. 3).

1.3 Multi particle effects, beam instabilities and mitigations

In the previous section we discussed the single particle motion. In a real accelerator many particles are stored together. Their mutual interactions play an important role and often limit the beam intensity. In the LHC the number of particles per beam ranges between 10^9 and few 10^{14} charges, grouped in up to ≈ 2800 bunches. In the presence of many particles, various collective effects can be observed due to the interaction of the beam with its surroundings (vacuum chamber, cavities, etc.) or with other particles of the same or of the counter rotating beam. Collective effects may be classified into the following categories:

- incoherent effects where the impact of the collective effect is different for each particle,
- coherent effects for which the particles of a beam are affected in a collective manner,
- single beam effects that do not depend on the presence of the second beam,
- two-beam effects that are due to the mutual interaction of the two counter rotating beams.

Intra-Beam Scattering (IBS) is an important incoherent effect at the LHC. IBS leads to emittance growth at all energies, but is more important at injection. It can affect very severely high brightness beams if the injection period is too long [13].

A good example for a coherent collective instability is the head-tail instability [2, Sec. 19.5]. This instability arises from the continuous exchange of the head and tail particles and their influence via their wake fields (the electro-magnetic – EM) perturbation represented in time domain [4, Chap. 2]) on the transverse motion. Instabilities may occur in both the vertical and the horizontal planes depending on the transverse wakes [14]. Above transition energy ($\eta_c < 0$) the beam becomes unstable for negative chromaticity. This is one of the reasons for the insertion of sextupole magnets to compensate for the naturally negative chromaticity of the FODO lattice.

Multi bunch instabilities driven by the wake fields from one bunch to another are another type of single beam collective effects. Such instabilities are mainly driven by high cavity quality factor (Q) or narrow-band impedances like those encountered in accelerating cavities. These effects may be mitigated at the design level by minimizing the machine impedance and therefore increasing the rise time of the instabilities [2, Sec. 19.6].

At the LHC another critical single beam collective effect is the electron cloud effect. The e-cloud effect depends strongly on the distance between consecutive bunches due to the fact that one bunch passing the vacuum chamber attracts the electrons liberated from the surface

1.3. Multi particle effects, beam instabilities and mitigations

of the chamber. Those electrons are accelerated towards the opposite (or adjacent) wall by the electric field of the bunch and create secondary emission electrons. The formation of the electron clouds depends strongly on the secondary emission yield (SEY) of electrons from the vacuum chamber. In the presence of electron clouds the bunches at the trailing edge of the bunch trains are most severely affected (tune shifts, head–tail type instability) in the vertical plane [15].

At the LHC e–clouds are mitigated by so–called "scrubbing runs". During such periods the highest possible intensity is accumulated at injection. The electron bombardment of the vacuum chamber by the electrons from the e–cloud leads to a progressive reduction of the SEY [16].

The last type of collective effects, where two beams interact with each other is described in section 1.3.2.

Tune spread The spread of tunes among the particles of a bunch has an important role for the development of collective instabilities. In the ensemble of the particles, the distribution of the tunes is given by the tune spread. Larger tune spread increases the threshold for inducing collective oscillations or instabilities but may lead to lifetime reduction when some particles encounter resonances. A trade–off is required between maximizing the tune spread and poorer tune diagnostics and lifetimes (see Sec. 2.5) [17].

1.3.1 Instability mitigation

1.3.1.1 Active mitigation

To actively mitigate instabilities, as a first step the coherent motion of the beams must be observed at a position monitor that should have the highest possible resolution. A feedback loop may be built with a fast kicker (electrostatic pickups) capable of acting on the bunches with the shortest possible time delay. Such a transverse feedback can be used to fight the coherent motion induced by instabilities as long as the rise time is not too short. At the LHC the transverse damper (ADT) provides this functionality. More details may be found in [18, 19].

1.3.1.2 Passive mitigation

Working point As a passive measure, the choice of the working point parameters Q and Q' may mitigate the onset of instabilities, for example positive chromaticity to avoid the head–tail instability.

Landau damping In the particle distribution (i.e. beam bunch) where a wake force excites a number of collective waves and displaces them from the equilibrium position, an energy

exchange between the particles and the wave occurs. It results in growth in amplitude for some waves and damping for others. The larger the spread in the oscillation frequency is, the more effective is the energy transfer from the coherent mode to the incoherent motion. This process provides damping and is commonly referred to as *Landau damping* [10, Sec. 2.4.11]. Damping is however only provided if the coherent oscillation modes frequency is within the incoherent (tune) frequency spectrum of the beam. The head-on (HO) beam-beam interaction between the two beams of a collider is a very effective source of *Landau damping*. At the LHC it is by far the most effective source. In the absence of collisions octupoles provide *Landau damping* (for example during the LHC ramp and squeeze). At the LHC for the brightness beams, the octupoles combined with the transverse feedback may however not be sufficient to stabilize the beams [20].

1.3.2 Beam-beam effects

When two beams cross each other at a collision point, the particles in each beam feel the EM field of the counter rotating beam. The kick $\Delta\vec{u}'$ due to the EM field depends on the transverse distance \vec{d}_u to the center of the opposite beam accordingly to:

$$\Delta\vec{u}' = -\frac{2N_p r_0}{\gamma_r} \frac{\vec{d}_u}{|\vec{d}_u|^2} \left[1 - \exp\left(-\frac{|\vec{d}_u|^2}{2\sigma_u^2}\right) \right] . \quad (1.39)$$

Here r_0 is the classical particle radius, N_p the number of particles in the opposing bunch, γ_r the Lorentz factor, $|\vec{d}_u|$ the separation between the beams and σ_u is the beam size in the u -th plane.

1.3.2.1 Beam-beam parameter and tune effects

In general pushing the luminosity by increasing the number of particles N_p and reducing the beam size σ_u , $\mathcal{L} \propto \frac{N_p}{\sigma_u^2} n_b$, also increases the beam-beam interaction because:

$$\Delta\vec{u}' \propto \frac{N_p}{\sigma_u^2} . \quad (1.40)$$

For small amplitudes, $\vec{d}_u < \sigma_u$, as show in Fig. 1.6, the beam-beam force (F) (Eq. 1.39) can be linearized as:

$$F \propto -\xi_{bb} d , \quad (1.41)$$

with the so called *beam-beam parameter* ξ_{bb} , given by

$$\xi_{bb} = \frac{N_p r_0 \beta^*}{4\pi \gamma_r \sigma^2} = \frac{N_p r_0}{4\pi \gamma_r \varepsilon} , \quad (1.42)$$

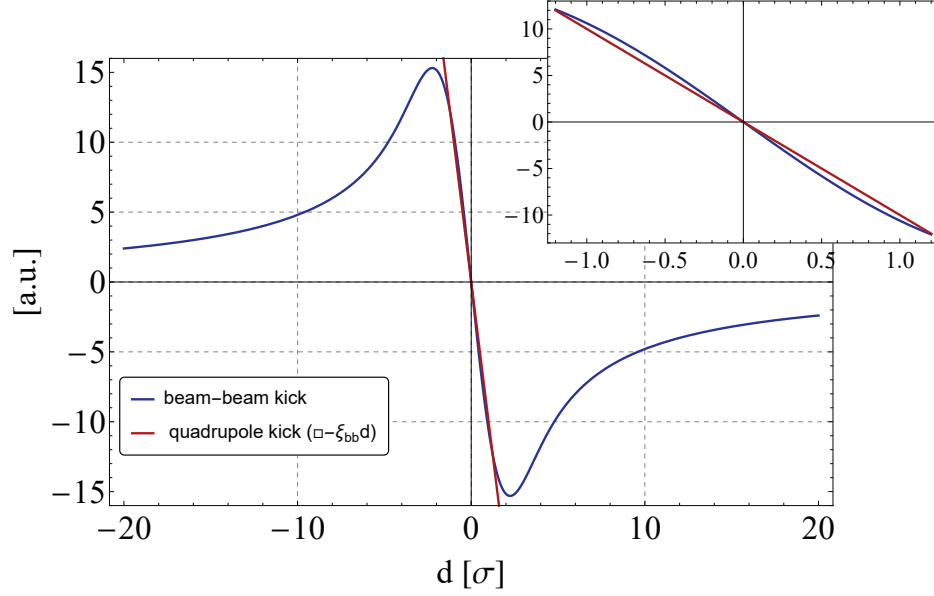


Figure 1.6 – The beam–beam force is represented here as a closed orbit shift (Δu) normalized to the r.m.s. beam size σ . This example corresponds to $N_p = 1.15e11$, $\gamma_r = 6927$, $\sigma = 18\mu\text{m}$ and $\beta^* = 0.8\text{ m}$. Within the range $-1.5\sigma \leq d \leq 1.5\sigma$ the force is linear and corresponds to a defocusing quadrupole for equally charged beams. For larger amplitudes one enters the strongly non–linear domain of the force.

which depends only on the beam brightness $\frac{N_p}{\varepsilon}$ but not on β^* for round beams and no crossing angle.

From Eq. 1.41 we observe that the resulting force acts on the beam as a quadrupole magnet (see Eq. 1.4) and therefore generates a tune shift. The focal length of this quadrupole f is inversely proportional to ξ_{bb} :

$$\frac{1}{f} = \frac{\Delta u'}{u} = \frac{N_p r_0}{\gamma_r \sigma^2} = \frac{\xi_{bb} 4\pi}{\beta^*} . \quad (1.43)$$

The design LHC beam–beam parameter is $\xi = 0.0037$ per IP without crossing angle⁴. In 2012, when LHC was operated with higher intensities (1.7×10^{11} ppb at 50 ns), ξ_{bb} reached a value of 0.009 per IP.

1.3.2.2 Crossing angle

A head–on (HO) collision corresponds to the situation where the two beams collide with each other (without offset if possible). At the LHC the two beams share the same vacuum chamber in a 140 m long common region around the interaction point (IP). In order to avoid parasitic

⁴ with crossing angle design value is $\approx \xi = 0.0034$, the one obtained in 2012 is 0.007

HO collision a crossing angle ϕ is introduced at the collision point. Figure 1.7 illustrates the HO and the long range (LR) interaction for a bunch train. Introducing the crossing angle leads to a \mathcal{L} reduction through the form factor ($F(\phi)$, see Eq. 1.36) and therefore reduces the maximum obtainable luminosity, but it is unavoidable at the LHC where almost 2800 bunches grouped in bunch trains are stored.

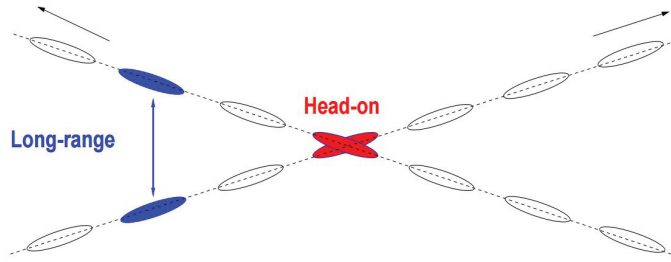


Figure 1.7 – Head-on (HO) and Long-range (LR) interactions in the presence of an external crossing angle. Its geometrical implications and the resulting luminosity deterioration are discussed in Sec 1.2.1. Courtesy W. Herr [21].

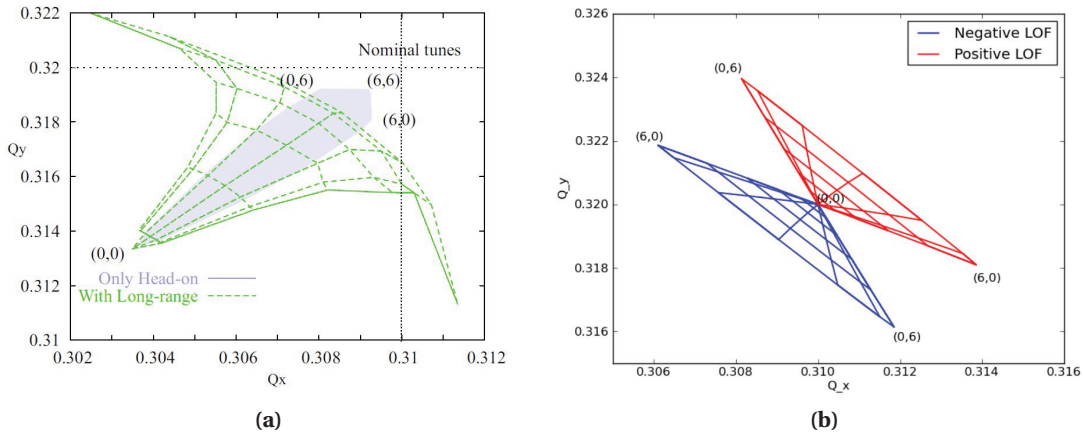


Figure 1.8 – LHC tune footprints for head-on (HO) collisions only (blue region) and with long-range (LR) interactions (a) and for octupoles with both polarities (b). For (a) the maximum tune shift that is observed at (0,0) corresponds to small amplitude particles. For particles at large amplitudes (0,6), (6,6), (6,0) the tune shift is much smaller (Courtesy S.White [22]). Case (b) illustrates situation for octupoles where the tune shifts are largest for the large amplitude particles (Courtesy X. Buffat [23]).

Detuning with amplitude Due to the non-linearity of the beam-beam force, the tune shift is maximum for small amplitude particles, whereas the tune shift vanishes for large amplitude particles. This is clearly visible in Fig. 1.8a on the HO foot-print (blue region) where the

1.3. Multi particle effects, beam instabilities and mitigations

particles at '0' amplitude exhibit the largest tune shift. Figure 1.9a illustrates the force that is responsible for that effect. The opposite situation occurs for the long range (LR) interactions where the large amplitude particles feel the largest tune shifts while small amplitude do not experience almost no tune shift (see Fig. 1.9b).

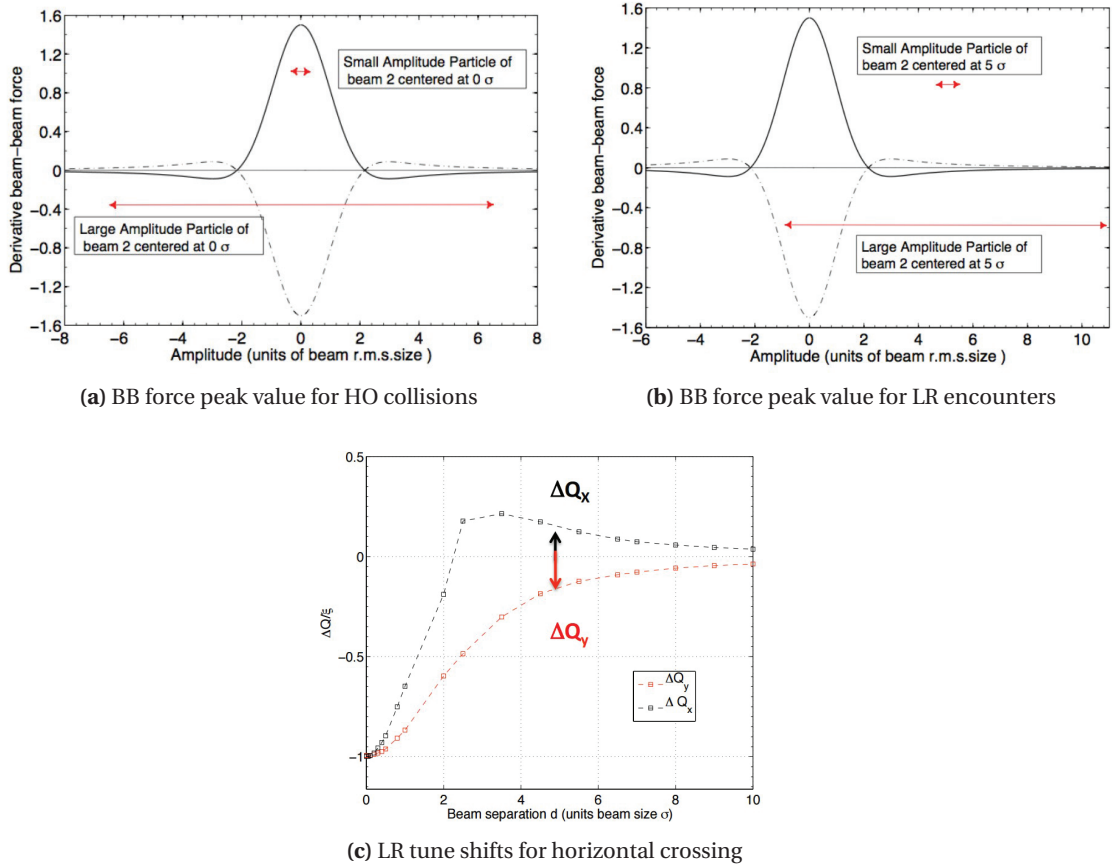


Figure 1.9 – The beam–beam force derivative as a function of beam separation which is proportional to the tune shift, and how it affects the second beam due to the HO interaction (a) and LR interaction (b). (c) illustrates the tune shifts for the plane of separation (black) and for the crossing plane (red). Courtesy T. Pieloni [24].

Moreover the LR interaction in one plane introduces the tune shifts in both planes (see Fig. 1.9c) with positive and negative directions due to the slope of the driving force. Since this effect could introduce asymmetric tune changes a passive compensation with alternating crossing planes in two IPs is used at the LHC [25, Sec. 5.4]. The compensation is achieved with horizontal crossing at the CMS experiment and vertical crossing at the ATLAS experiment (see Sec. 2.3.1).

1.3.2.3 Orbit effects and luminosity

A non-zero beam-beam deflection affects the closed orbit. For an offset d at an encounter the orbit change $\Delta u(d)$ at the location of the kick (IP) is given by:

$$\Delta u(d) = \frac{\beta_u \Delta u'(d)}{2 \tan(\pi Q_u)}, \tag{1.44}$$

where $u'(d)$ is the beam-beam kick, β_u is the beta function at the IP.

For a machine that operates with bunch trains (like the LHC), an additional complication arises. The bunches at the ends of the trains have fewer LR encounters, therefore their closed orbit differs from the ones in the middle of the train since the beam-beam kicks are not identical for all bunches.

Figure 1.10 illustrates the simulated bunch to bunch offsets at the IP as a function of the bunch slot number. Clear signatures of the LR interaction (of the total number of them) are visible at both ends of the train.

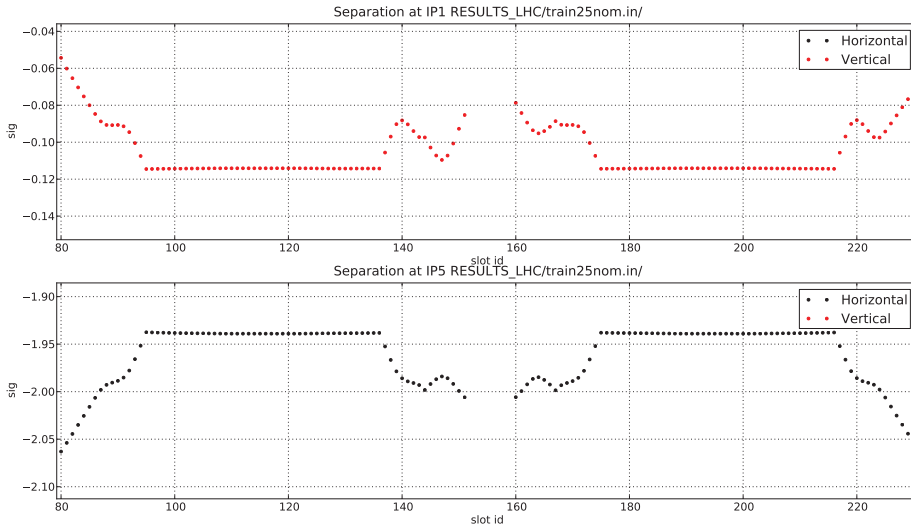


Figure 1.10 – Bunch by bunch separations at the IP due to the LR interactions at the IPs as function of the bunch slot for two selected batches of 72 bunches.

Missing LR interactions (start and end of the train are the most affected parts) lead to a transverse separation between the bunches and to a (small) reduction of the luminosity (see Eq. 1.34 and Fig. 1.11) due to the transverse offsets at the IP.

1.3. Multi particle effects, beam instabilities and mitigations

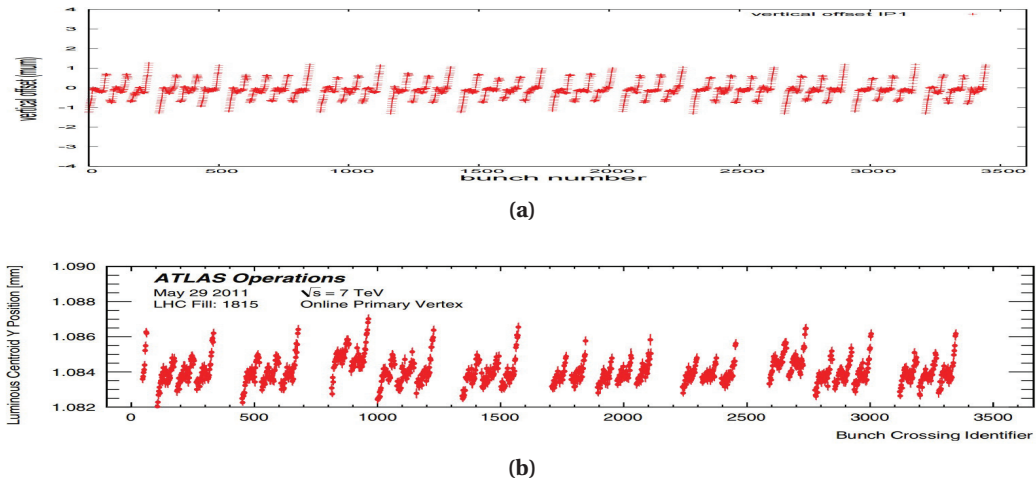


Figure 1.11 – (a) The orbit displacement along the trains. The start and the end of each train visibly differs from the middle of the train due to the LR interaction [26]. (b) The measured ATLAS luminous regions centers (bunch by bunch) illustrates the effect [27].

1.3.2.4 Stability criterion

For colliding beams almost all Landau damping against any possible collective effects comes from HO collisions. Operation with a small transverse separation at the IP reduces the tune spread and therefore the stability margins with respect to instabilities. For the LHC a series of simulations and experiments were conducted. As a result, it was observed that a separation of $1-1.5\sigma$ is the most delicate regime for ensuring sufficient damping. Consequently the time spent with such a separation should be minimized [20, 28] to ensure beam stability.

2 LHC and the CERN accelerator complex

CERN (*Conseil Européen pour la Recherche Nucléaire*) is the largest particle accelerator facility in the world, hosting more than 13 000 visiting scientists and engineers and more than 2200 staff employees. It is located between the French and Swiss borders within the canton of Geneva. An introduction to the LHC, its injector complex and its relevant systems is given in this chapter.

2.1 LHC injector complex

The laboratory halls and underground structures of CERN host the world's largest accelerator complex (see Fig. 2.1). The main focus of the CERN accelerators is to provide beams of protons and heavy ions. The protons for the LHC are obtained by heating up a hydrogen gas until it becomes a plasma and then by separating protons with an electric field in the source. The particles are then guided through a series of accelerating structures that compose a linear accelerator (LINAC2). At the exit of LINAC2 the protons have an energy of 50 MeV. The PS booster, the first of a series of synchrotrons, accelerates the proton beam to 1.4 GeV. As a next step, the Proton Synchrotron (PS) accelerates the beam up to 26 GeV. In the PS 6 bunches injected from the booster are split into 72 bunches. The splitting mechanism splits the initial 6 bunches into 18 at low energy, and later at top energy (26 GeV) the operation is repeated twice with a split factor of 2. Up to 4 trains of 72 bunches (the result of four PS cycles) are transferred into the Super Proton Synchrotron (SPS) and further accelerated up to 450 GeV, the injection energy of the LHC. The beam is then transferred to the LHC through two transfer lines (TI2 and TI8).

2.2 The Large Hadron Collider

The LHC is installed inside the former 27 km long LEP (Large Electron–Positron collider) tunnel. It is located at an average depth of 100 m below the surface. Figure 2.2b presents a schematic view of the LHC. The beams travel in opposite directions: Beam 1 travels clockwise

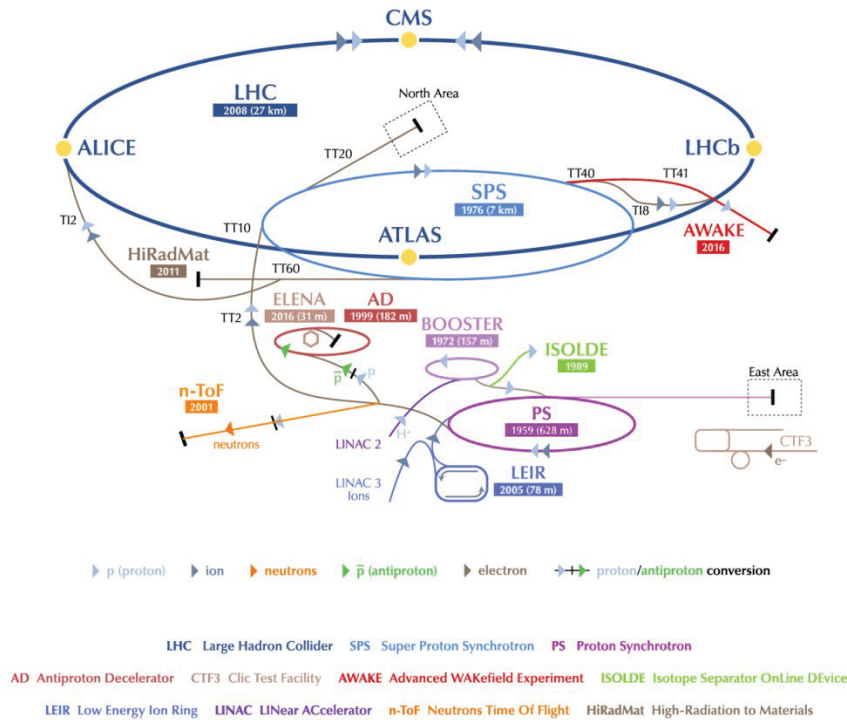


Figure 2.1 – CERN accelerator complex [29].

and Beam 2 counter-clockwise. To accelerate and collide particles of the same charge the dipole fields must point in opposite directions and the beams are kept separated in most parts of the machine. The eight arc sections (octants) occupy most of the ring whereas insertion regions are located in the middle of each octant. More details on the LHC insertion regions are presented in Sec. 2.3. Table 2.1 summarizes some LHC parameters.

2.2.1 Magnets

As has been discussed in Sec. 1.1, a dipole field orthogonal to the traveling direction is required to guide charged particles on a circular path. The LHC consists of 1232 main dipole magnets (see Fig. 2.3), each of them deflecting the beam by $\frac{2\pi}{1232} = 5.1$ mrad. To provide the focusing, 396 quadrupole magnets are installed around the ring in the arc. The regular arc lattice is built using standard cells composed of six dipoles and two quadrupoles as illustrated in Fig. 2.4. To achieve the high magnetic fields required to reach an energy of 7 TeV, the magnets are based on super-conducting technology. Nb-Ti is used as superconductor in the LHC magnets. Main dipoles and main quadrupoles can be fed with a current of up to 13 000 A. Due to the high inductance (in the dipole case $L=15.4$ H) the stored magnetic energy in the dipole magnets is 8.8 GJ. A Quench Protection (QPS) and Energy Extraction (EE) system are protecting the magnets against damage in the event of a transition from the superconducting to the normal

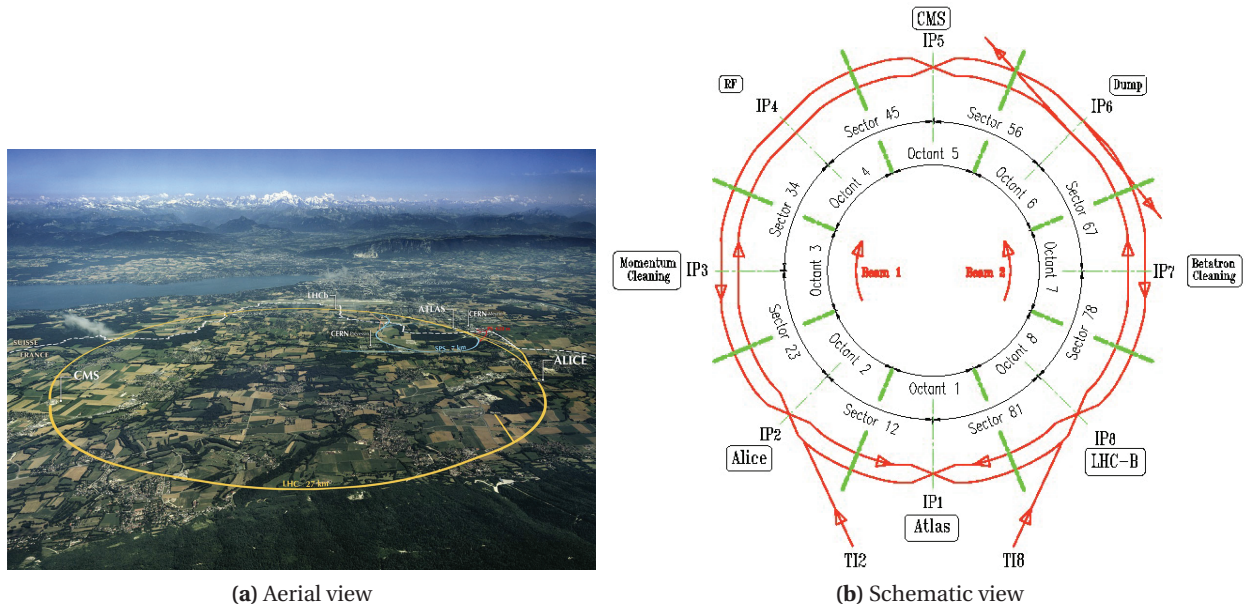


Figure 2.2 – The aerial (a) view of the LHC (yellow) and of its four detectors. In blue the SPS accelerator and in red the PS. (b) illustrates the schematic view of the LHC with its sectors, octants and insertion regions [30].

conducting state. The QPS and EE are also the last line of defense against particle losses (see Sec. 2.5).

2.3 LHC insertion regions

As we discussed in the Sec. 1.1.1.4, the dispersion function is brought close to zero in most insertion regions (IR), therefore all octants have an arc–insertion transition with a so called dispersion suppressors. Four out of eight insertions are dedicated to the experiments (IR1, IR2, IR5 and IR8). Two insertions are for the beam cleaning system (IR3 and IR7), one for accelerating cavities and beam instrumentation (IR4) and a last one for the beam dumping system (IR6).

2.3.1 Interaction points

IR1 and IR5 The two high luminosity insertions IR1 and IR5 are hosting the ATLAS and CMS experiments. These experiments are designed for a peak luminosity of $\approx 10^{34} \text{cm}^{-2} \text{s}^{-1}$. Figure 2.5a shows a schematic overview of the ATLAS insertion, the CMS insertion is similar. The two beams are initially separated, they are brought together by the D1 and D2 dipole magnets into the common vacuum chamber. Whereas the typical average beam size in the arcs is $\approx 200\text{-}300 \mu\text{m}$ the role of the *final focus triplet* (Q1, Q2 and Q3) is to lower the beam size

Chapter 2. LHC and the CERN accelerator complex

parameter		injection	collision	
			design	Run 2
GENERAL				
Ring circumference	[m]		26658.883	
Number of collision points			4	
Number of main dipole magnets			1232	
Length of main dipole magnets	[m]		14.3	
Bending radius	[m]		2808.95	
Main dipole field	[T]	0.535	8.33	8.11
RF System				
Revolution frequency	[kHz]		11245	
RF frequency	[MHz]		400.8	
Harmonic number			35640	
Total RF Voltage	[MV]	8	16	12
BEAM				
Number of particles per bunch			$1.15 \cdot 10^{11}$	
Number of bunches			2808	2760
Proton momentum	[GeV/c ²]	450	7000	6500
Lorentz factor γ_r		479	7461	6927
Transverse normalized emittance ϵ_n	[μ mrad]	3.5	3.75	3.5
Longitudinal emittance	[eVs]	1.0	2.5	1.89
Circulating current	[A]		0.582	0.57
Stored energy	[MJ]	23.3	362	340
LATTICE (Run 2)				
Horizontal tune Q_x		64.28	64.31	
Vertical tune Q_y		59.31	59.32	
Maximum dispersion in the arc	[m]		2.018(H), 0.0(V)	
Minimum H dispersion in the arc	[m]		0.951	
Maximum β in the arc	[m]		177(H), 180(V)	
Minimum β in the arc	[m]		30(H), 30(V)	
β^* in IP1 and IP5	[m]	11	0.55	0.8/0.4
β^* in IP2	[m]	10	0.5(Pb) 10(p)	0.8(Pb) 10(p)
β^* in IP8	[m]	10	3	3

Table 2.1 – Selected LHC parameters. A complete list as well as the detailed explanation of the physical meaning can be found in [11].

to around 10–20 μ m at the IP. For the HL–LHC upgrade the triplet aperture will be increased to be able to lower β^* (respectively the beam size) further in order to boost the peak luminosity. A partial compensation of long range beam–beam tune spread (see Sec. 1.3.2.1) is obtained by crossing the beams in different planes between those two points, namely vertical in IR1 and horizontal in IR5.

The accelerator device installed closest to the IP is the TAS absorber that intercepts together with the TAN absorber that is installed further downstream, the debris created by the primary

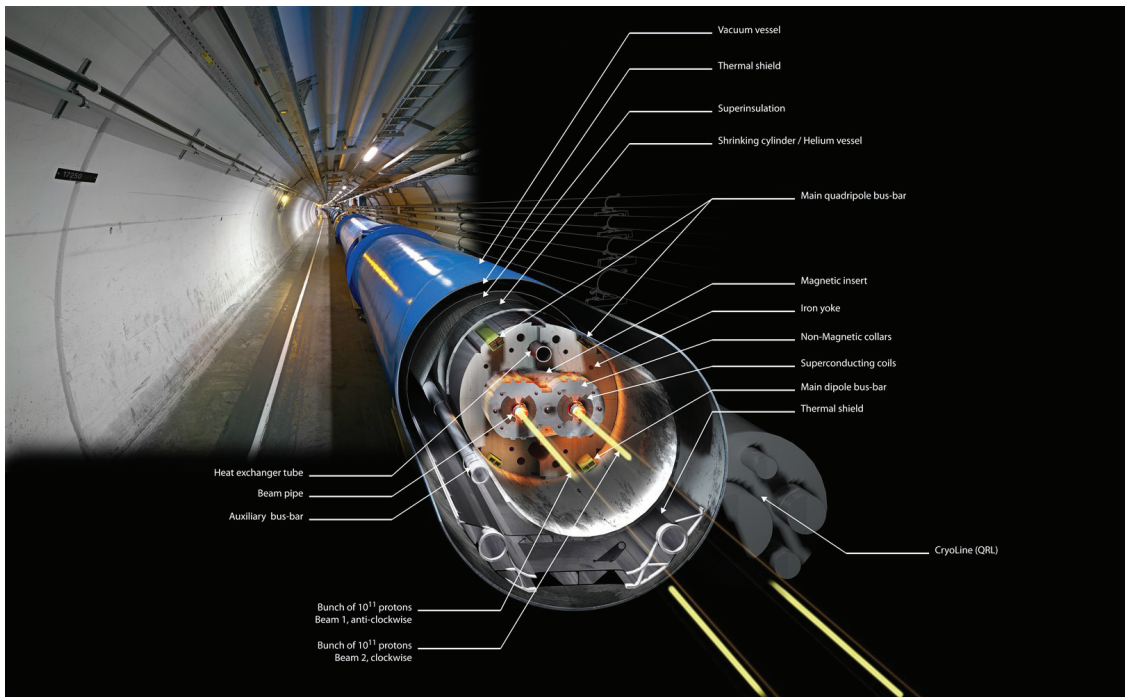


Figure 2.3 – The LHC main bending magnet and the tunnel. [30]

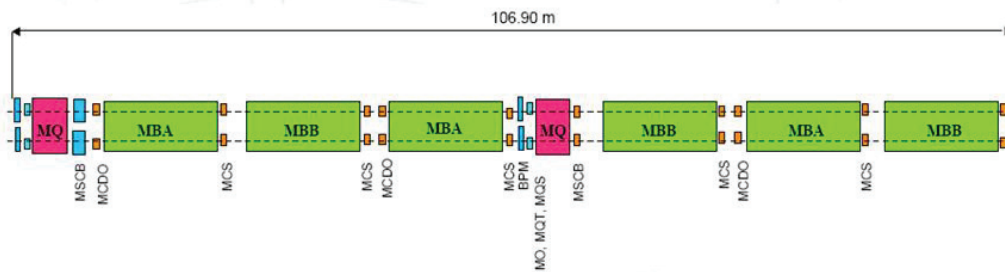


Figure 2.4 – The LHC's regular lattice cell consists of a focusing quadrupole (MQ), three dipoles (MBA, MBB), defocusing quadrupole and another three dipoles. The total length of the cell is 106.90 m [31].

collisions that emerge along the beam axis.

IR2 and IR8 The ALICE and LHCb experiments are hosted in the insertions IR2 and IR8 respectively. Their schematic layouts are shown in Fig. 2.5b and Fig. 2.5c. To avoid LR encounters the beams cross horizontally in IR8 and vertically in IR2. The injection devices for Beam 1 and the end of the TI2 transfer line are installed in IR2. The same applies for Beam 2 and TI8 in IR8.

Chapter 2. LHC and the CERN accelerator complex

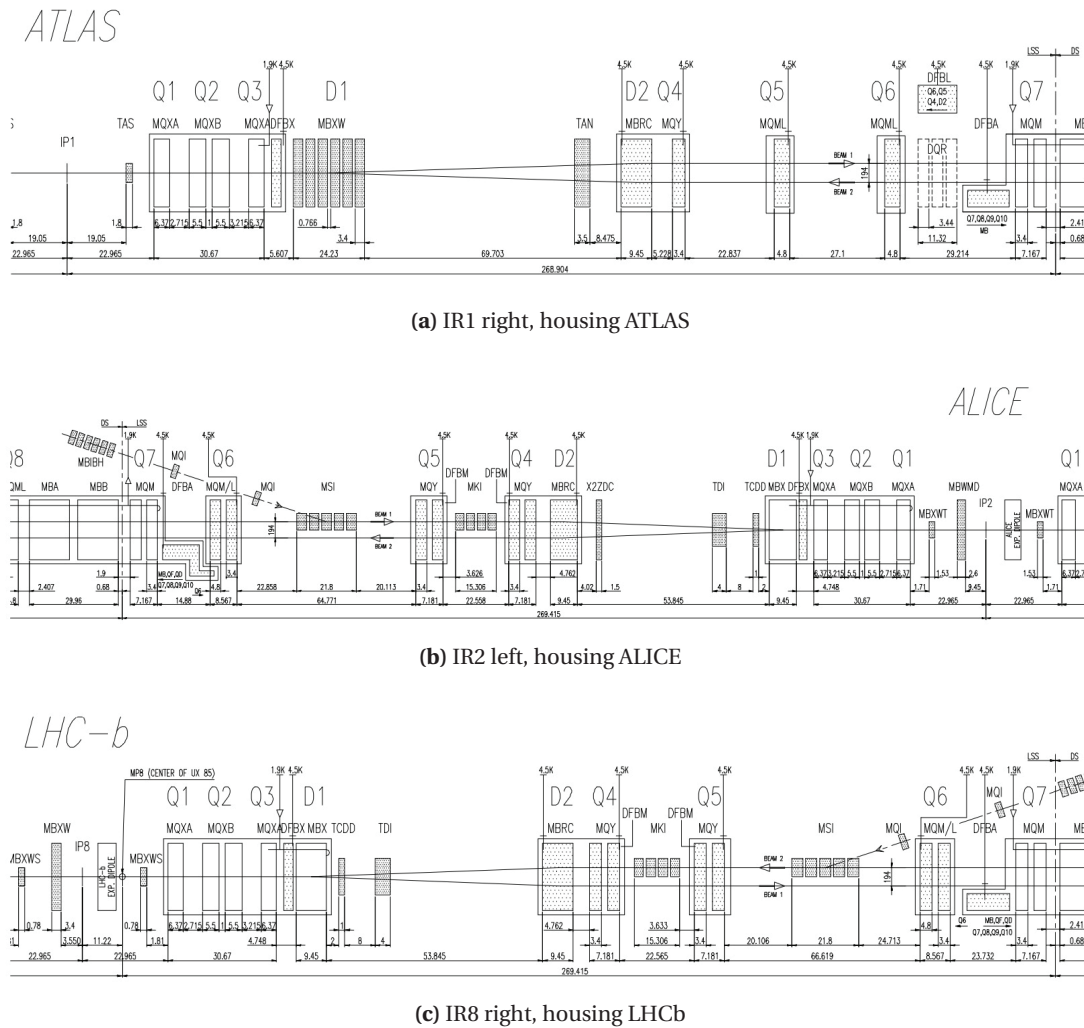


Figure 2.5 – Schematic layouts of the LHC interaction points [11]. The layout of IR5 is similar to IR1 (a). The distances in the longitudinal coordinate are given in meters and the nominal temperatures of the magnet cold masses in Kelvin. The layouts of IR2 (b) and IR8 (c) include the injection devices of the transfer lines TI2 (IR2) and TI8 (IR8).

2.3.2 Cleaning regions

Particle losses are unavoidable during normal operation (for example due to the instabilities, tails, orbit perturbations). To ensure the coexistence of beams with few hundreds of MJ of stored energy and superconducting magnets that may quench due to energy depositions of few mJ/cm^2 , over 99.9% of the particles lost from the beam must be intercepted. A complex 4 stage collimation system with over 100 collimators is installed in the LHC to intercept particles that drift to large amplitudes. Most of the collimators have movable jaws that can be adjusted to the required position around the beam. Figure 2.6 shows all stages of the cleaning system.

The primary (TCP) and secondary (TCS) collimators are installed in IR7 (betatron cleaning)

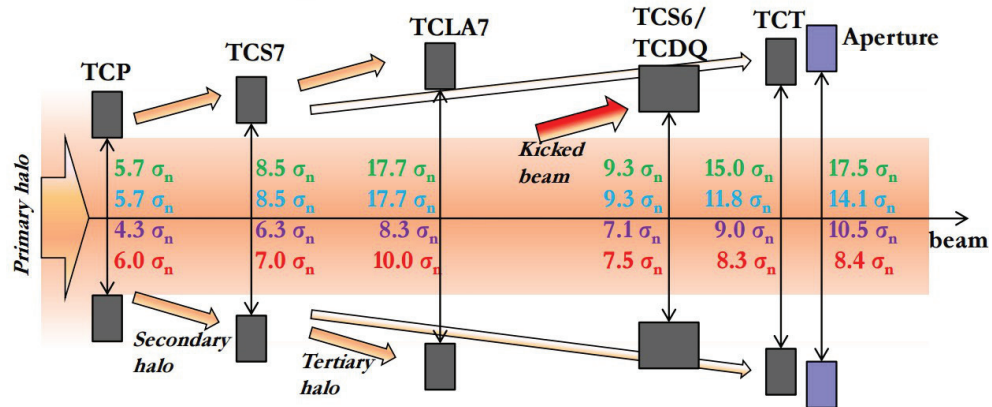


Figure 2.6 – The LHC collimation hierarchy. The beam sizes σ corresponds to $\epsilon_n = 3.5 \mu\text{m}$. Colors of the limits corresponds to settings and red is the nominal configuration for $\beta^* = 0.55 \text{ m}$ and energy of 7 TeV. Courtesy R. Bruce [32].

and IR3 (off-momentum cleaning). In order to clean off-momentum particles IR3 is the only insertion with significant dispersion.

To intercept large beam losses due to the equipment failures, some collimators are strategically positioned around the ring in order to intercept the particles, thus serving as a protection for other critical, mostly superconducting, elements.

Tertiary collimators (TCTs) are installed in all experimental IRs to protect the triplet quadrupoles against quenching and damage. The betatron function varies by orders of magnitude at the TCTs when optics is changed at the IPs. Their gaps size has to track such optics changes, and the centers of the collimators have to track the associated orbit changes.

2.4 Orbit correction

Orbit correctors are installed next to the quadrupoles to compensate misalignments and adjust the beam orbit. The majority of the LHC orbit correctors (1012 out of 1060) are installed on a single beam vacuum chamber. They affect only one beam and provide therefore independent steering of Beam 1 and Beam 2. With a few exceptions in IR3 and IR7 the correctors are superconducting magnets. A group of 48 superconducting orbit correctors (MCBX) is installed in the common vacuum chambers around IP1, IP2, IP5 and IP8. Their fields are affecting both beams, but in opposite directions. Parameters of both families are listed Table. 2.2.

	unit	MCB (H,V)	MCBC (H,V)	MCBY (H,V)	MCBW (H,V)	MCBX H V	
Type		SC	SC T2	SC T2	NC	SC T4	
Overall length	[mm]	1260	1100	1100	1700	730	
Magnetic length	[mm]	647	904	899	1700	450	480
Inner coil diameter	[mm]	56	56	70	52(*)	90	
Nominal strength	[T]	2.90	3.11	3.0	1.1	3.35	3.26
Nominal current	[A]	55	100	88	550	550	
Total number		752	168	76	16	48	
Integrated dipole strength	[Tm]	1.9	2.81	2.70	1.87	1.51	1.56
Maximum kick at 450 GeV	[mrad]	1.25	1.8	1.8	1.26	1	
Maximum kick at 7 TeV	[μ rad]	80	120	115	81	67	

Table 2.2 – Parameters of the LHC orbit correctors. The MCB correctors are installed in the arcs, all other types are distributed over the insertions. The MCBX type correctors are installed on the vacuum chamber that is common for both beams [11, Tab. 7.15, 8.17, 8.19, 8.23]. Types: SC – super conducting, NC – normal conducting, T – super conductor type, (*) – it is the gap height.

2.5 Beam instrumentation

The quality of the beam instrumentation installed around the LHC is critical to ensure smooth operation and high performance. The following subsections will cover only the operation of the main beam instruments: the beam position monitors (BPM), beam current monitors (BCM) and the beam loss monitors (BLM). Profile measurements like Wire Scanner (WS) and Beam Synchrotron Light Telescope (BSRT) are briefly mentioned in the following chapters when needed. More detailed discussions and explanations on the instrumentation can be found in [7, 33].

2.5.1 Beam position monitors

A charged particle travelling along the vacuum chamber induces image charges on the wall due to Gauss law. This image charge can be measured for example on electrostatic pick-ups that are inserted in the vacuum chamber wall. To first approximation, the beam position u can be obtained with the following formula:

$$u = \frac{d}{4} \frac{V_1 - V_2}{V_1 + V_2} \quad (2.1)$$

where d is the distance between the pickup electrodes, and V_1 and V_2 are the voltages measured on the electrodes. The measurement (Eq. 2.1) is normalized to be independent of the beam intensity. In general a higher order polynomial must be used to reconstruct the position from V_1 , V_2 [34, 35].

2.5.1.1 Tune measurement

The fractional part of the betatron tune (see Sec. 1.1.1.3) is measured by observing the beam oscillation on a position pickup. At the LHC a diode-based high resolution measurement system, the Base-Band Q (BBQ) system [36] provides measurements for most beam types. This is an advantage for a hadron machine where external excitation generally induces emittance growth due to the absence of synchrotron radiation [1, Chap. 6]. Natural oscillations are sufficiently large to provide a signal for the BBQ systems. The quality may however be affected by (high) chromaticity or octupoles.

2.5.1.2 Standard LHC BPM system

The LHC beam position monitor system consists of 2140 measurement channels that depend on an extensive acquisition chain of 1070 monitors, 3820 electronic cards distributed along the LHC underground tunnel and about 1070 additional digital post-processing cards located in surface buildings. In the first years of operation the reproducibility of the measurements was affected by the temperature drifts in the electronics racks ($20 \mu\text{m} / ^\circ\text{C}$) but even then the majority of the channels were showing a resolution of less than $10 \mu\text{m}$ for beams with many bunches [37]. After Long Shutdown 1 (see. 2.7.2), the drifts were reduced with improved control of the rack temperature and additional cooling.

The overall BPM resolution is proportional to the mechanical aperture of the monitor (see Eq. 2.1) and the resolution of the induced voltage measurement. For the BPMs installed in the common region for both beams the resolution is $20 \mu\text{m}$. Since the precision is at the same level as the IP beam size it is difficult to track the IP position with sufficient accuracy.

2.5.1.3 DOROS – high resolution BPM system

Based on the LHC tune measurement system (BBQ), a high resolution (down to $1 \mu\text{-meter}$) orbit measurement electronics was developed. For the first part of LHC Run 2, IP1 and IP5 were equipped with this DOROS (Diode ORbit and Oscillation System) electronics [38, 39]. The DOROS electronics was installed on the Q1 quadrupole that is closest to the IP, in parallel to the standard BPM (BPMSW) electronics. The aim of this installation was the demonstration of tracking the IP position with $\mu\text{-meter}$ resolution. After the winter technical stop (2015/2016), the LHC will restart with all four experiments equipped with the high resolution beam position measurement. More detailed discussion on the usage and quality of this data is held in Sec. 7.4.

2.5.2 Beam loss monitors

The loss of a very small fraction of the circulating beam may induce a quench of the superconducting magnets or even physical damage to machine components. The measurement principle is based on the detection of secondary shower particles using ionization chambers

[11, Sec. 13.3.1]. About 4000 monitors observe losses at likely loss location, predicted by particle tracking and shower simulation codes. The detection of lost particles allows protection of the equipment against quenches and damage by generating a beam dump trigger when the losses exceed predefined thresholds. In addition to the quench prevention and damage protection, the loss detection allows the observation of local aperture restrictions, orbit distortions, beam oscillations and particle diffusion, etc.

2.6 LHC feedback systems

In the LHC, two independent feedback systems are used to control the tune (QFB) and the orbit (OFB) in order to ensure smooth operation [40]. Both systems operate in a closed loop mode (see. Fig. 2.7) with 12.5 Hz (OFB) and 4 Hz (QFB) loop periods. The advantage of this solution (over i.e. feed forward) is that even in the presence of the errors (input measurements, controller's, actuators) the corrections tends to converge.

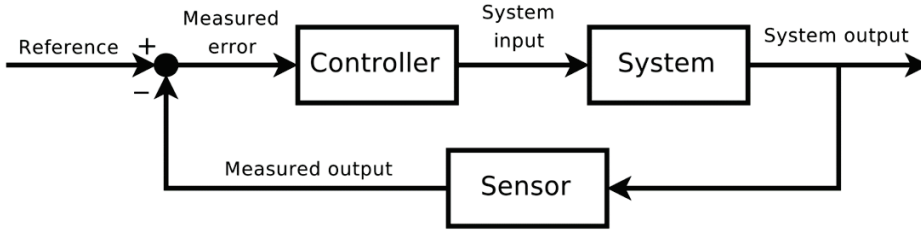


Figure 2.7 – Control theory feedback loop. In the LHC (system) the tune feedback (QFB) measures via BBQ and acts via tuning quadrupole magnets. Orbit feedback (OFB) measures via BPMs and acts via CODs.

Tune feedback The QFB operates with the horizontal and vertical tunes of both beams obtained from the BBQ systems (4 inputs in total). It acts on the beams through 32 tuning quadrupole magnet circuits (MQTs) [11, Sec. 7.6.3] with a total number 32 circuits to control.

Orbit feedback The OFB operates with the position data of over 2000 standard LHC BPMs and acts on around 1000 correctors¹ listed in Tab. 2.2. The OFB is typically operated with damping times of 5–20 seconds that are adequate for LHC operation. The OFB is using a Proportional Integral (PI) Controller with gains K_i and K_p to feedback on the orbit. The control equation is given by:

$$\vec{u}_i = \vec{u}_{i-1} + K_p [\mathbf{R} \cdot (\vec{\theta}_{i-1} - \vec{\theta}_{i-2})] + K_i T_s [\mathbf{R} \cdot \vec{\theta}_{i-1}] \quad (2.2)$$

¹It is 1028(BPMs) and 528(CODs) for given plane for both beam due to the orbit correction coupling via MCBX correctors installed in the shared vacuum chamber

Here \vec{u} is the total orbit shift at step i , $\vec{\theta}_i$ is the deflection to correct the full perturbation at step i and T_s is the loop period. Values of the gains K_i and K_p are set such that around 5% of the perturbation is corrected over one second.

2.7 LHC operation

The LHC as a collider is a machine with a long cycle time. Because the energy of beam injection and physics production differ, the beams must first be injected, then accelerated to the target energy before collisions can be provided to the experiments. When the beam intensities have degraded, the beams are dumped, the machine is set back to the injection and the cycle restarts. At the LHC one full machine cycle is called a fill and is associated with an unique fill number.

2.7.1 The cycle

The standard LHC cycle is illustrated in Fig. 2.8. The main phases are described below.

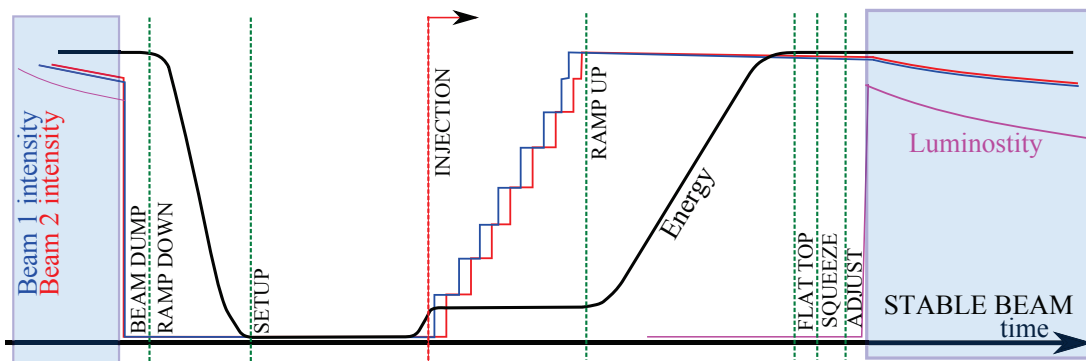


Figure 2.8 – Standard LHC cycle. The blue region corresponds to the STABLE BEAMS production phase. The remaining TURNAROUND TIME consist of the phases, here listed in the logical order (from the left): BEAM DUMP, RAMP DOWN, SETUP, INJECTION, RAMP, FLAT TOP, SQUEEZE and ADJUST.

INJECTION The injection phase begins with the injection of a low intensity probe bunch to adjust the beam parameters (tune, chromaticity, orbit). Once good conditions are established, the nominal beam is injected in trains of varying length from the SPS. The duration of this phase depends on the total number of bunches and the quality of the beams.

RAMP Once the machine is filled, the beam energy is increased to its target value during this phase. This phase has a fixed length for a given target energy, to reach 6.5 TeV takes 20 minutes.

Chapter 2. LHC and the CERN accelerator complex

SQUEEZE During this phase the betatron function at the interaction points (β^*) is adjusted from the value at the flat top to its target value for collisions. A smooth and step-wise optics change is applied, details will be presented later. This phase, like the ramp, has a fixed duration.

ADJUST Up to this point the two LHC beams were kept separated at the IPs. During the ADJUST phase the beams are brought into collision, and the final beam parameter optimizations are performed.

STABLE BEAMS is the luminosity production phase that can last more than 20 hours. During that phase the beams are maintained in stable collision for the experiments, only minor adjustments are made to the beam parameters in this phase.

The LHC cycle has additional phases that occur after **STABLE BEAMS**:

BEAM DUMP This is the shortest phase of the LHC cycle. It takes only one turn of the beam around the accelerator to execute it. Circulating stored beam is safely dumped into the absorber block.

RAMP DOWN The magnet currents are brought down to their injection values (450 GeV). During this phase other equipment are prepared for injection.

2.7.2 LHC Run definition

LHC time line is divided into so called LHC runs. Table 2.3 summarizes past, present and future runs. **This thesis will focus on the data from Run 1 and the first year of Run 2.** Each individual Run year ends with Year End Technical Stop (YETS)² that usually lasts around 3 months.

#	energy	years	ends with
Run 1	3.5 TeV 4 TeV	2008 – 2011 2012 – 2013 (Q1)	LS1
Run 2	6.5 TeV	2015 (Q2) – 2018	LS2
Run 3	6.5 TeV	2021 – 2023	LS3
Run 4 HL-LHC	7 TeV	2026 Q2 –	

Table 2.3 – Summary on the LHC runs. In bold the years of operation data used in this thesis. In italic forecast-ed dates [41]. A Long Shutdown (LS) typically lasts 18–36 months.

²or in some cases Extended YETS

2.7.3 Accelerator controls system

To overcome the complexity of the operation the LHC has a dedicated control system. The central part of the configuration management is the so-called LHC Software Architecture (LSA) that has different layers of services to control the machine. Together with a timing and synchronization system, the simultaneous powering of more than 1600 electrical circuits, RF systems, etc. is guaranteed [42].

Beam Process A beam process is a container for settings (circuits, collimators) associated to any of the machine cycle phases (see Sec. 2.7.1). Each physical quantity (i.e. beam position or tune) is abstracted and represented units, later is translated into the field gradient and only then to the current that is sent to the power converters. The settings are generated from matched optics and energy. The continuity of the functions is ensured by interpolation rules. Smoothing of functions is introduced to match the power converter acceleration and ramp rates.

Knob To simplify the operation, a concept of *knobs* was introduced. A knob is an abstract layer that allows to modify multiple parameters together with a fixed relation. This allows to produce a tune or chromaticity change, or a bump to shift the beam position at the IP. Knobs often group different subsystems and allow to change them consistently. This allows operation using physical quantities and not with individual magnet strengths.

3 Luminosity leveling at LHC and HL-LHC

This chapter is focused on luminosity leveling including its operational aspects. The first part of this chapter reviews possible leveling methods. The second part is focused on the proposed operational scenarios for the LHC and for the HL-LHC. The proposals are supported by some operational solutions.

3.1 Luminosity leveling and pile-up limits

To maximize the LHC physics output, neither the peak instantaneous luminosity (Eq. 1.34) nor the integrated luminosity (Eq. 1.37) alone are good figures of merit. Although the push for higher luminosity is realized by lowering β^* and by increasing the LHC beam brightness (ϵ_n and N , listed later in Tab. 3.3), the usable instantaneous luminosity is limited by the number of interactions per bunch crossing (pile-up) that each experiment is able to cope with.

Instrumental limitations or damage may appear when the instantaneous luminosity exceeds design limits of some detectors types. Gaseous detectors for example, may be damaged by sparking due to the excessive ionization [43, 44]. Operation at excessive luminosity may lead to faster detector ageing, scaling directly with both the instantaneous and integrated luminosity. This can lead to increased downtime and reduce the overall efficiency.

With increased instantaneous luminosity and event pile-up, the performance of some sub-detectors degrades with out-of-time pile-up called *spill-over*. A spill-over, effectively introduces uncorrelated hits on subsequent bunch crossings and therefore degrades the resolution.

Due to the increased combinatorics (of increasing pile-up) the off-line data analysis time increases almost exponentially [43].

Finally, at increasing pile-up interesting physics events are accompanied by a rising number of bias events. They impact the physics resolutions (i.e. tagging, vertexing, tracking, etc.) due to poorer background correction and poorer signal quality [43].

Detector limits breakdown

Each LHC experiment has its own pile-up limit, and **it is the aim of luminosity leveling to stabilize the \mathcal{L} at or below the pile-up value**. Table 3.1 summarizes pile-up limits for all four LHC experiments.

	ATLAS/CMS	LHCb	ALICE
LHC DR 7 TeV	20 (1×10^{34})*	1.6 (4×10^{32})	$\ll 1$ (1×10^{30})
LHC Run 2 6.5 TeV	40 (2×10^{34})**	2 (6×10^{32})	0.01 (2×10^{30})
HL-LHC DR 7 TeV	130 (5×10^{34})	8 (4×10^{33})	0.06 (4×10^{30})

Table 3.1 – Typical pile-up limit values and expected leveled luminosity (given in $\text{cm}^{-2}\text{s}^{-1}$) in the LHC experiments for different time periods [45, 43]. DR – Design Report. (*) – 2808 bunches design brightness, (**) – ≈ 2500 bunches, Run 2 brightness (see Tab. 3.3).

3.2 Available luminosity leveling methods

The four main methods of luminosity control will now be discussed. Techniques that affect the luminosity of all experiments at the same time have been omitted, for example RF coggling [46] and bunch length change [47] since those cannot be used to adjust luminosities individually for each experiment as required at LHC.

3.2.1 Beam offsets at the IP

The simplest method for controlling the luminosity is to separate the beams transversely at the interaction point. We consider first the case with a separation in the plane orthogonal to the crossing plane. Equation 1.35 for a round beams shows that by introducing such a separation the luminosity reduction follows the curve shown in Fig. 3.1a. This method provides a continuous and wide range of reduction factors, its implementation is very simple in operation by offsetting the beams with local orbit bumps around the target collision point.

The main drawback of the method is related to transverse beam stability. Bunches that are not colliding head-on do not profit from the Landau damping and are more vulnerable to collective instabilities as described in Sec. 1.3 and later in Sec. 3.3.

Offsetting the beams in the crossing plane also allows adjusting the luminosity. It shifts the longitudinal center of the luminous region depending on the crossing angle and the beam emittance. Figure 3.1b illustrates the shift, the dashed lines show the luminous region and the geometrical crossing point with HO collision while the solid lines show the luminous region and the geometrical crossing point in LHCb with the Run 2 beam parameters and a shift of one sigma per beam [43]. This method **is not favoured by the experiments due to the longitudinal shift of the luminous region**.

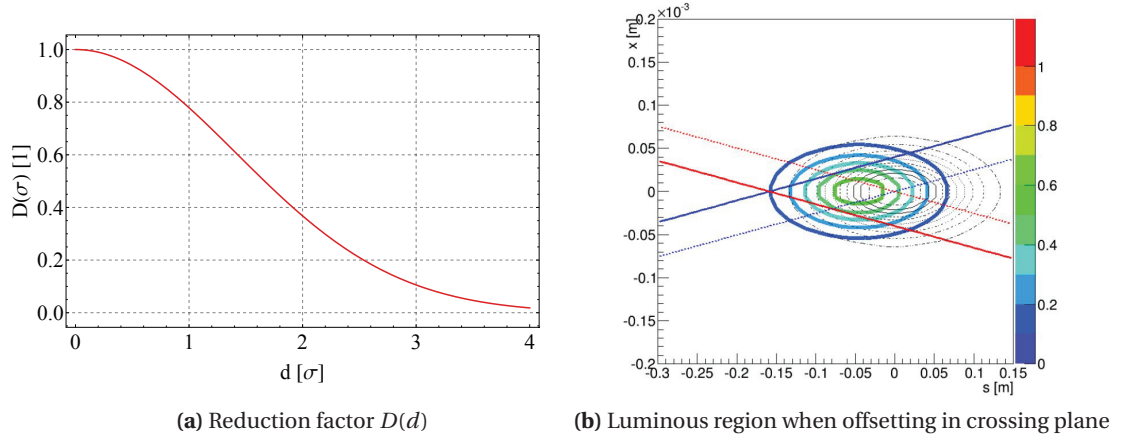


Figure 3.1 – Beam offset leveling. (a) The reduction factor as a function of the offset in the plane that is orthogonal to the crossing. (b) Shift of the luminous region when offsetting in the crossing plane. Courtesy R.Jacobsson [43].

3.2.2 Piwinski angle

The geometric factor in the equation of luminosity (see Eq. 1.36) depends on the crossing angle ϕ , the longitudinal (σ_z) and transverse σ_x^* beam sizes:

$$L(\Phi) = \frac{1}{\sqrt{1 + \Phi^2}} \quad (3.1)$$

For a small crossing angles, the *Piwinski angle* Φ is given by:

$$\Phi = \frac{\phi \sigma_z}{2\sigma_x^*} \quad (3.2)$$

The luminosity may be controlled in two ways:

- through the bunch length
- through the crossing angle

Controlling the luminosity through the bunch length affects all experiments at the same time. The range is also limited by the RF bucket size (larger σ_z) and longitudinal instabilities and beam induced heating (shorter σ_z).

The crossing angle allows in principle to control \mathcal{L} independently for each experiment. The range however, is limited by the long range beam–beam separation required to ensure good beam lifetimes (smaller crossing angle) and by the mechanical aperture (larger crossing angle).

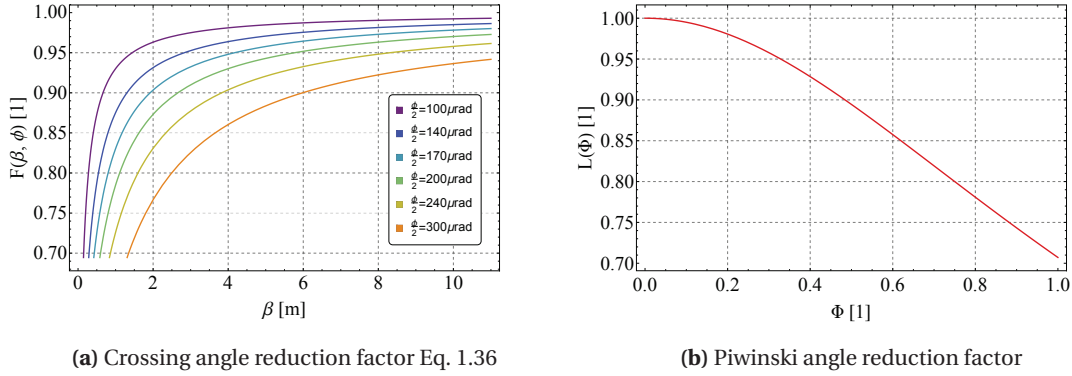


Figure 3.2 – Crossing angle reduction factor (a) and the effective beam overlap reduction factor (b).

3.2.3 Crab cavities

The Crab Crossing Scheme (CCS) [48] is designed to overcome the luminosity loss coming from the large crossing angle and Piwinski angle (see previous section). Introduction of the crossing angle in the LHC is responsible for around 18% luminosity loss for design beam parameters while for the HL-LHC the loss reaches 70%¹. The luminosity loss may be recovered and controlled with *crab cavities* (CC)[49]. The CCs are installed before and after the interaction point and provide local control at a given IP. The CCs provide a transverse RF kick to head and tail of the bunches to restore HO collisions at the IP as illustrated in Fig. 3.3. Figure 3.2a show the loss factor depending on the initial crossing angle and β^* value.

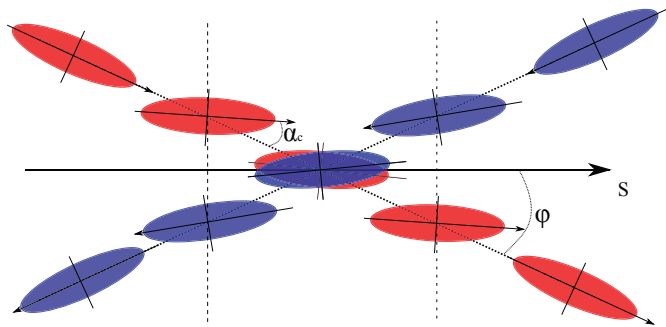


Figure 3.3 – Sketch of the HO restoring process in the four dimensional space, using the crab cavities.

The CC can be used not only to restore HO collisions but also to control the luminosity with partial or even deliberate luminosity reduction [50]. As this method requires installation of the new hardware, it is only considered for the HL-LHC upgrade.

¹this is bare value calculated for no compensations given from CCs

3.2.4 Beam size change – via β^*

Another way for controlling the pile-up is to change the beam size of the colliding beam through β^* . This technique has the advantage that it does not affect the beam-beam parameter since the beams remain head-on and ξ_{bb} is independent of β^* for round beams. Landau damping from the HO collisions is therefore preserved [51].

During a change of β^* the optics of the entire interaction region and long straight section is affected. The gradient changes in the quadrupoles require adjustments of the crossing angle shapes and lead to orbit changes due to feed-down from the beam offsets in the quadrupoles (due to misalignments). As a consequence the beam orbit must be stabilized during such a leveling process by an active orbit feedback system, that drives the orbit correctors as the optics changes. This effect is discussed more in details in Chap. 5 of this thesis. The tertiary collimators have to follow the orbit and beam size change at their locations.

The currently favored leveling scheme consists in moving step wise from one matched optics point to the next, each matched optics corresponding to a certain β^* value. The luminosity evolution will remain very smooth provided the change in β^* is small enough. Figure 3.4 illustrates luminosity evolution in time, with alternation of upward steps (change of β^*) and luminosity decay.

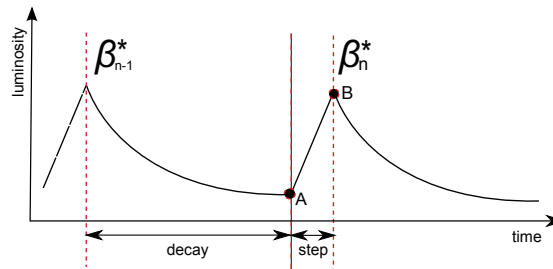


Figure 3.4 – Proposed β^* leveling implementation: a step in \mathcal{L} due to a change of β^* is followed by a period of luminosity decay. The process is repeated at regular intervals.

Optics imperfections that are present in the machine induce betatron function changes around the entire machine at each β^* leveling step. This may lead to cross-talk between the leveled IP and the others experiments [52]. To limit such a cross-talk, a very accurate optics correction has to be established for β^* leveling.

Table 3.2 presents an overview of the four leveling methods that have been discussed.

	Offset control	Crab crossing	Piwiński angle	β^*
Reduction	$D(d) = \exp\left(-\frac{ d ^2}{4\sigma^{*2}}\right)$	$F(\phi) = \frac{1}{\sqrt{1 + \left(\frac{\sigma_x}{\sigma^*} \tan\left(\frac{\phi}{2}\right)\right)^2}}$	$L(\Phi) = \frac{1}{\sqrt{1 + \Phi^2}}$	$B(\beta^*) = \frac{F(\beta^*, \phi)}{\beta^*}$
Range	local	local	global/local	local
Advantages	<ul style="list-style-type: none"> • Easy to implement (local orbit bumps) • Provides a large and continuous range of reduction 	<ul style="list-style-type: none"> • Allows for complete cancellation of the crossing angle effect 	<ul style="list-style-type: none"> • Easy to implement (σ_z or ϕ change) 	<ul style="list-style-type: none"> • Provides constant ξ_{bb} along the fill • For smaller values ensures better beam lifetime [53]
Disadvantages	<ul style="list-style-type: none"> • ξ_{bb} is not constant along the fill • Reduced beam stability (loss of Landau damping) 	<ul style="list-style-type: none"> • Requires dedicated elements • ξ_{bb} is not constant 	<ul style="list-style-type: none"> • Affects all IPs in case of σ_z change • Limited by aperture and LRBB separation for ϕ changes 	<ul style="list-style-type: none"> • Requires accurate orbit control with less than 1σ of accuracy • Currently only possible with predefined discrete β^* values • Changes of β^* in one point may cause perturbations of β^* in the other experiments

Table 3.2 – Overview of luminosity control methods.

3.3 Experience with the offset leveling in LHCb and ALICE

During LHC Run 1 and Run 2, leveling by transverse offset (in the separation plane) was used every fill for the ALICE and LHCb experiments. Figure 3.5 illustrates the luminosity evolution during stable beams in fill 2651. The luminosity was adjusted to the LHCb target (with pile-up ≈ 2) via leveling in separation plane.

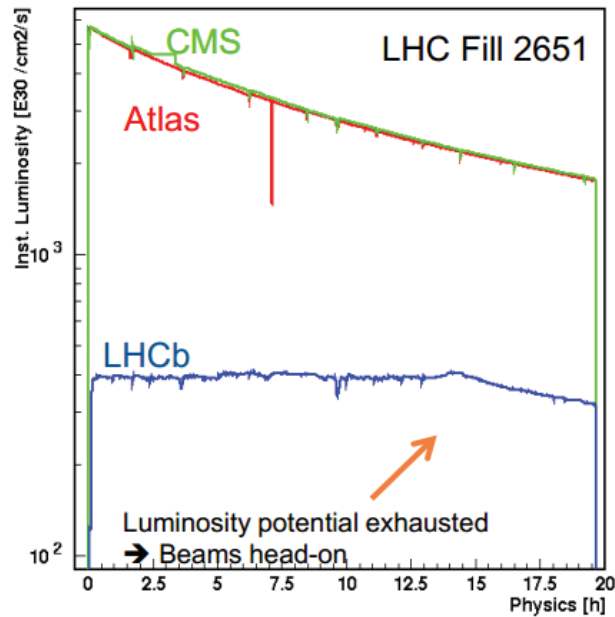


Figure 3.5 – Example of fully operational luminosity leveling by offset in the separation plane of LHCb [54].

The LHC high intensity beams are stabilized by a transverse feedback and by Landau damping from octupoles and from HOBB collisions as explained in the previous chapter. Since bunches colliding with offsets have less Landau damping, it was suspected that collision offsets may be the cause of some instability observed [55]. Such offsets are introduced for offset leveling in ALICE&LHCb or for luminosity optimizations when two beams are scanned transversely one against the other [56]. For these reasons, offset leveling cannot be applied at all LHC collision points at the same time [57], at least not for very bright beams.

In principle it can be envisaged to enforce that every bunch collides in ATLAS and CMS to profit from Landau damping by HOBB. As this constraint penalizes LHCb and/or ALICE, there is generally the desire to maintain some 'private' bunches that collide only in LHCb or ALICE. Furthermore the experiments often request non-colliding bunches for background studies. Such bunches can potentially become unstable, loose intensity or grow in emittance. Figure 3.6 illustrates the loss of the intensity for bunches that are only colliding in IP8 with transverse offset.

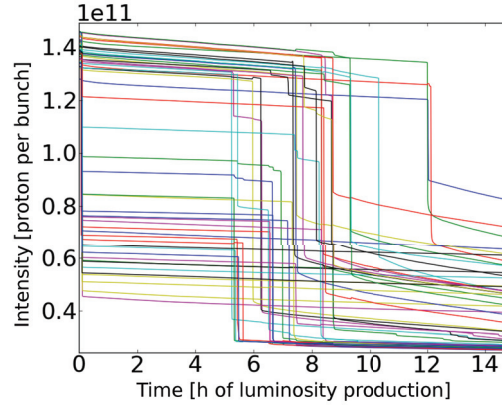


Figure 3.6 – An LHC Run 1 instability example, when some of the bunches (without HO collisions in IR1 and IR5) are drastically losing intensity, courtesy X.Buffat [57].

3.4 Leveling scenario for LHC Run 2 and Run 3

After the long shutdown (LS1) the LHC resumed beam operation in 2015 at an energy of 6.5 TeV. The LHC high luminosity experiments ATLAS and CMS can cope with a maximum average pile-up of 50 and a time-averaged pile-up (μ) of **30 to 40**. The medium luminosity experiment LHCb operates at a maximum pile-up of $\mu \approx 1.6$ and the low pile-up experiment ALICE with $\mu \approx 0.01$.

After LS1 the LHC was restarted with 25 ns bunch spacing, with a relaxed $\beta^* = 0.8$ m and $\frac{\phi}{2} = 145 \mu\text{rad}$ in ATLAS and CMS. The beam parameters of $N_b \approx 1.2 \times 10^{11}$ ppb and $\varepsilon_n \approx 3.5 \mu\text{m}$ were close to the nominal values. With this configuration the pile-up did not exceed ≈ 20 for ATLAS and CMS. LHCb and ALICE were both leveled by offset, LHCb to $\mathcal{L} \approx 5 \times 10^{32}$ ($\mu \approx 1.6$) and ALICE to $\mathcal{L} \approx 10^{30}$ ($\mu \approx 0.01$).

In 2016 β^* was lowered to 0.4 m with a crossing angle $\frac{\phi}{2} = 185 \mu\text{rad}$. With standard beam parameters the luminosity reaches $1\text{-}1.2 \times 10^{34} \text{ cm}^{-2}\text{s}^{-1}$ which is close to design. It is expected that no leveling will be required up to long shutdown 2 (LS2). With the injector upgrades (LIU) planned during LS2, leveling will however be mandatory in LHC Run 3 (2021 and later).

Figure 3.7 summarizes accessible parameter space (ε_n and N_p) and associated pile-up values for all LHC experiments in different optics configurations.

The following simulations are based on a software tool that models the main ingredients defining the luminosity evolution, namely the proton burn-off (based on operational data from LHC Run 1) and the emittance growth (two models: from 2012 and 2015). The tool evaluates the leveling times and assesses the need for β^* steps to ensure the desired luminosity 'smoothness'. More details can be found in App. C.6.

3.4. Leveling scenario for LHC Run 2 and Run 3

50 ns bunch spacing A step back to 50 ns bunch spacing and higher bunch brightness would require leveling for ATLAS and CMS from beginning of each fill since the **pile-up reaches 80** for the lowest β^* and brightest beams (see Tab.3.3). It is estimated that a leveling is necessary for the first **three hours** of collision phase to limit the pile-up. This case is currently unlikely since operation with 25 ns in 2015 and 2016 did not pose significant problems.

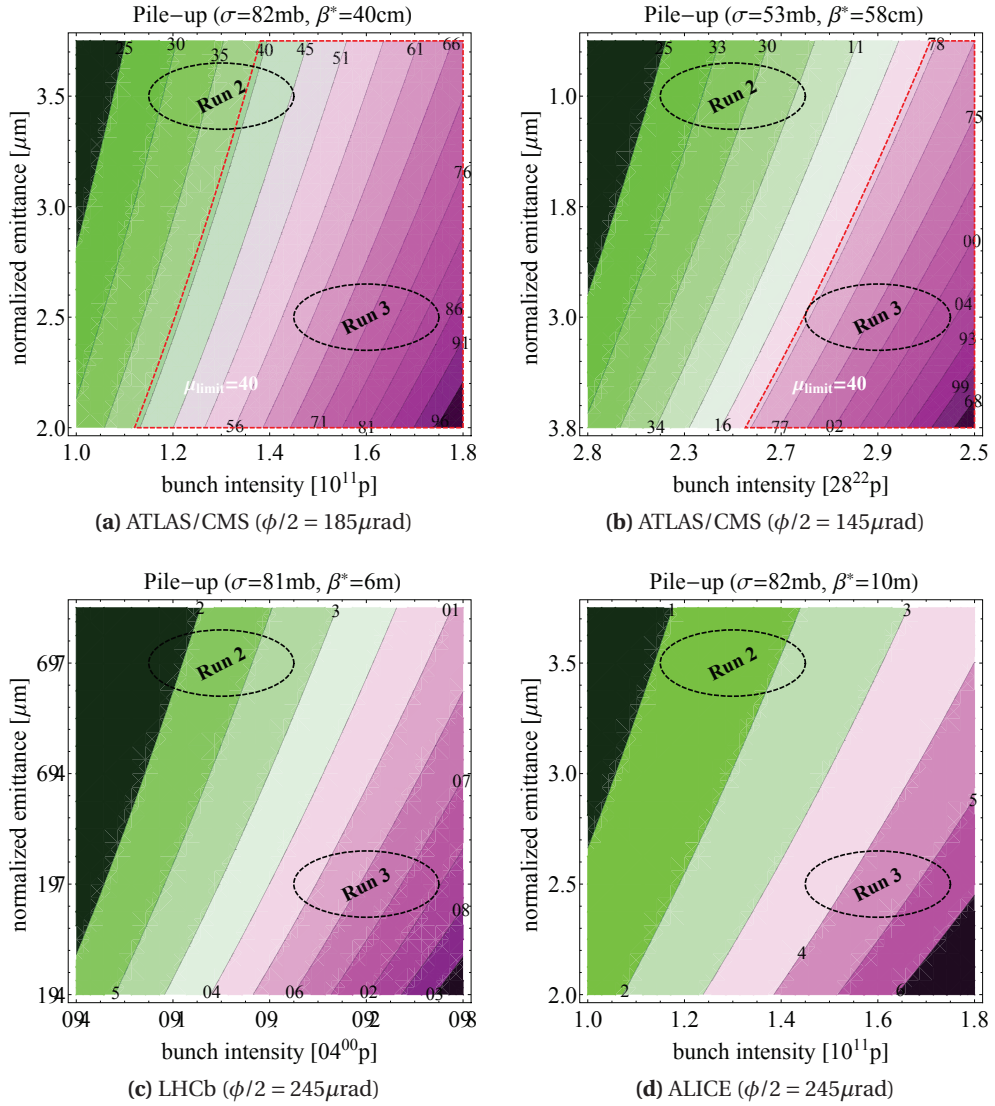


Figure 3.7 – Event pile-up for the LHC experiments (distinguished by achievable β^* at the IP) over a wide parameter space (ϵ_n and N_p). A bunch length of 10 cm was assumed. The pile-up limit is marked for ATLAS and CMS. ALICE and LHCb require leveling for any of the parameter (see Tab.3.1).

3.4.1 The LHC beams

Various types of beams may be used in the LHC. For luminosity production however, only few types are considered. During LHC Run 1 50ns bunch spacing was used to boost luminosity and avoid delays due to electron cloud scrubbing [58]. As from the restart in 2015 only 25 ns configurations were used in operation. Table 3.3 summarizes the main beam types. Whereas the STANDARD beam type undergoes the normal PS bunch splitting, the other two schemes, Bunch Compression Merging Scheme (BCMS) and eight bunches four empty (8b+4e) slots, provide higher brightness and reduced electron cloud activity [59]. They require different treatment in the PS resulting in a lower total number of bunches.

LHC configuration beam type	DESIGN 7 TeV	Run 1 4 TeV	Run 2 6.5 TeV			
	DESIGN	STANDARD	STANDARD	STANDARD	BCMS	8b+4e
spacing [ns]	25	50	50	25		
N_b [e11]	1.15	1.7	1.7	1.2	1.3	1.8
# bunches/ PS batch	72	36	36	72	48	48
max # bunches	2808	1374	1374	2786	2540	1968 ²
ϵ_n at INJ [$\mu\text{m rad}$]	3.5	2.5	1.7	2.5	1.4	2.4
ϵ_n at FT [$\mu\text{m rad}$]	3.75	3.0	2.5	3.0	2.5	3.0
LHCb pile-up μ [1]						
$\beta^*=10\text{ m}$	1.5	2.3	5.1	2.5	3.7	7
$\beta^*=3\text{ m}$	5	10	15	8	11	21
ATLAS/CMS pile-up μ [1]						
$\beta^*=0.8\text{ m}$ (LHC 2015)	n/a	n/a	47	40	33	50
$\beta^*=0.65\text{ m}$ (LHC 2012)	n/a	42	55	27	38	62
$\beta^*=0.55\text{ m}$ (LHC DR)	20	n/a	56	31	42	72
$\beta^*=0.4\text{ m}$ (LHC 2016)	n/a	n/a	77	38	52	80

Table 3.3 – LHC beam overview with peak pile-up for high (ATLAS and CMS) and medium luminosity (LHCb) experiments. Cases that exceed the allowed pile-up limits are highlighted in bold. Pile-up values are calculated for a bunch length of $\sigma_z=10\text{ cm}$ with cross section of $\sigma_p=82\text{ mb}$ and crossing angle $\phi/2=145\mu\text{rad}$ ($\phi/2=185\mu\text{rad}$ for LHC 2016). Acronyms: INJ–Injection, FT– Flat top and SB– Stable beams, DR – Design report.

3.4.2 Scenario of β^* leveling for LHCb in Run 2

Although offset leveling provides an efficient way to level luminosity in LHCb, a scenario was defined that would allow to test β^* leveling operationally at LHCb to gain experience with that technique for HL-LHC.

The LHCb experiment operates at a typical pile-up of $\mu \approx 1.6$. Due to aperture and practical constraints the largest usable β^* is 10 m, the value that is also used at injection. For such a β^*

²This limited filling scheme is only considered when a limitation related to the electron cloud will play a role.

the max pile-up may reach up to $\mu=7$. It is therefore not possible to perform pure luminosity leveling only with β^* (see Tab.3.4) starting from $\beta^*=10$ m. The location of the injection devices in the proximity of the experiment dictates certain aperture limits. Those limits imply $\beta^*=10$ m at injection. For a scenario of pure β^* leveling, it would have been possible *a priori* [60] to de-squeeze the beam to $\beta^*=20$ m (see Fig. 3.8b) between injection and collisions. However, with this solution the LRBB separation criterion would not be met due to the limited separation for the closest LR encounters next to the IP. Consequently such a scenario had to be rejected.

Therefore, some offset leveling is required. It was simulated that **the offset leveling time will last up to 6 h for each fill** (if bright beams are used). To limit the influence and the possible operation complications of the leveling by β^* it was also considered to squeeze LHCb to 8 m before going into collisions. That extends the period of the offset luminosity leveling to maximum of 8 h.

As the process is based on a step-wise change of β^* at the collision point a smooth luminosity can only be delivered with small β^* steps. To fulfill the experiment wish to stabilize the luminosity within 5%, it was calculated, that for the LHCb case until 5 m the steps can be made **every 50 cm and later until 3 m every 25 cm. A total of 20 β^* points are required to cover the β^* range of 10 m to 3 m and ensure that the luminosity remains within $\pm 5\%$ of the average value.**

The commissioning procedure implies careful optics and orbit corrections to keep the beams head-on during each step. The optics must be corrected such that it minimizes the perturbation of β^* in IR1 and IR5. Performing β^* leveling in LHCb may not be transparent to the ATLAS and CMS luminosity. In case of imperfect optics corrections variation of the recorded luminosity in IR1 and IR5 are expected to happen. All necessary corrections to compensate such perturbations must be included in the commissioning phase but residual errors may remain. The time needed for the commissioning was estimated to 4 shifts [61].

Figure 3.8 presents the luminosity and β^* evolution for selected scenarios of LHCb offset and β^* leveling, simulated for different LHC beams. Details of the scenarios are listed in the summary Tab. 3.4.

3.4.3 Scenario for ATLAS and CMS for (Run 2) and Run 3

A priori there is no need for the luminosity leveling for both ATLAS and CMS experiments for design beam parameters. However, since for Run 2 β^* was already lowered to 40 cm in 2016 and there are plans to push the beam brightness, some operation scenarios may require short periods of leveling if the experiments are not ready to deal with pile-up above the design value.

Figure 3.9 illustrates the pushed scenario for which the leveling will need to be done with several steps.

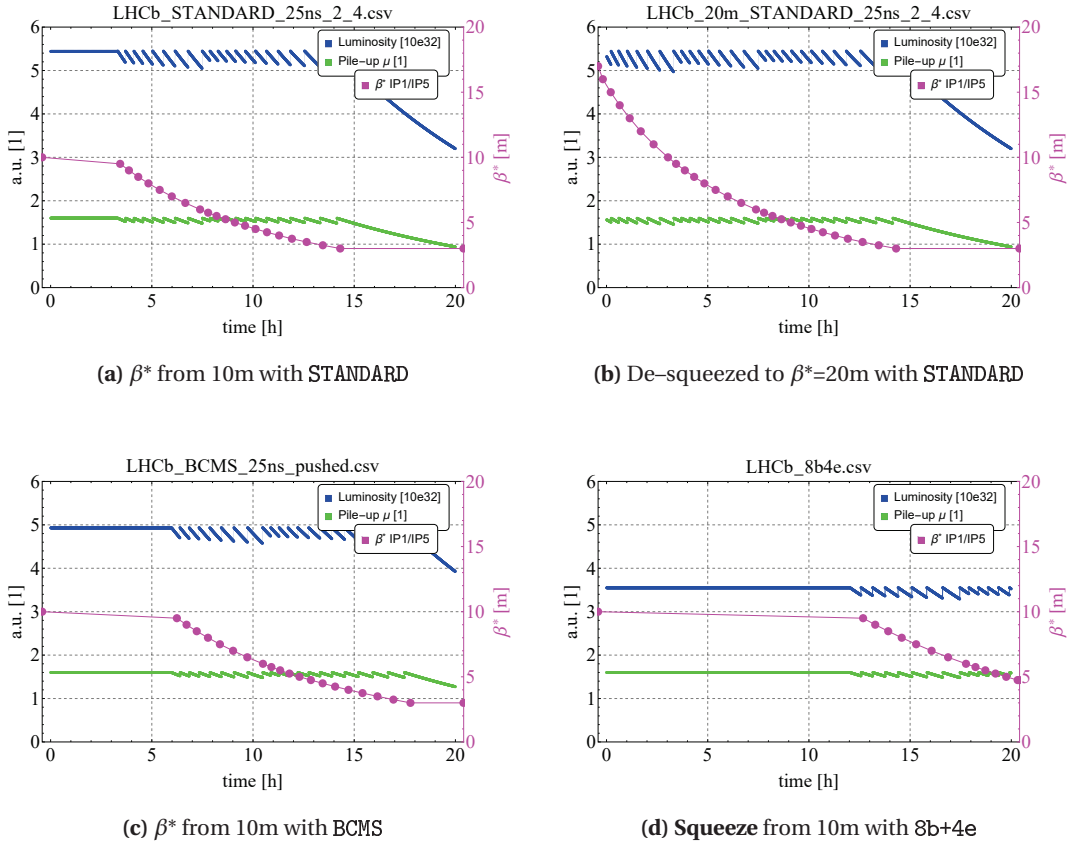


Figure 3.8 – Luminosity leveling scenarios for LHCb with the STANDARD, BCMS and 8b4e beam types (see Tab. 3.3). (a) illustrates the mixture of the offset leveling and β^* leveling scenario. (b) assumes that a β^* of 20 m could be used as starting value. (c) and (d) are the scenarios of mixed leveling methods for BCMS and 8b4e beams.

3.4.4 Overview of β^* leveling scenarios

Table 3.4 summarizes leveling times, number of β^* points and required separation range in order to level the LHC experiments with bright beams.

3.5 Collide and squeeze

In 2012 for the very bright 50 ns beams ($N=1.7 \times 10^{11}$ p/b) the situation in terms of beam stability was so critical [62] that a *collide and squeeze* (C&S) scheme was considered as a solution to mitigate the beam instabilities.

The aim of β^* leveling, as described before, is to provide a smooth and stable (with respect to beam instabilities) leveling of the luminosities. Conceptually a β^* leveling step consists of an

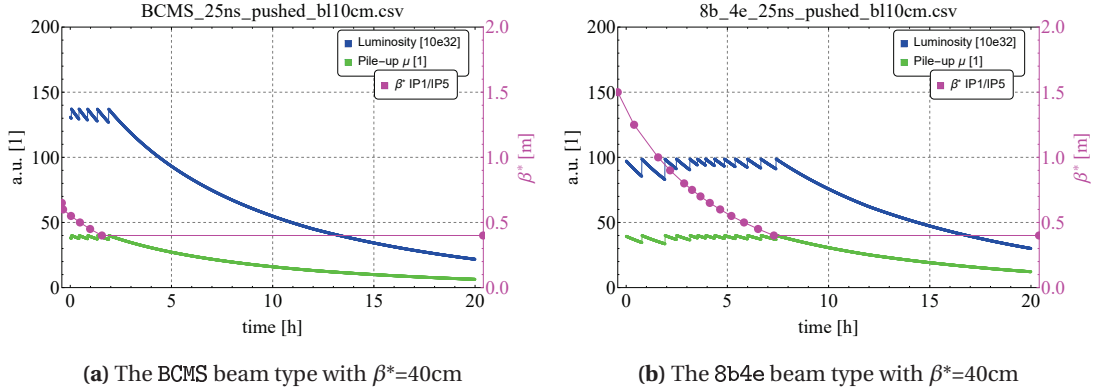


Figure 3.9 – Scenarios for ATLAS/CMS experiments for bright BCMS (a) and 8b4e (b) beam types (see Tab. 3.3) with Run 2 pushed $\beta^*=40\text{cm}$.

type (n/ϵ_n)	leveling type	total time [h] (offset time [h])	β^* start [m] (# points)	separation d [σ]
ATLAS/CMS $\beta^* = 40\text{cm}$				
BCMS (1.3e11/2.5 μm)	β^*	0.8 (0)	0.5 (#3)	n/a
BCMS (1.3e11/2.5 μm)	d	0.8(0.8)	0	0.7
8b4e (1.8e11/2.5 μm)	β^*	3.8 (0)	0.8 (#9)	n/a
8b4e (1.8e11/2.5 μm)	d	3.8(3.8)	0	1.4
LHCb $\beta^* = 10\text{m}$				
STANDARD (1.2e11/3.0 μm)	$d + \beta^*$	10(0.5)	10 (#22)	1.0
BCMS (1.3e11/2.5 μm)	$d + \beta^*$	15(5)	10 (#22)	1.6
8b4e (1.8e11/2.5 μm)	$d + \beta^*$	20(8.5)	10 (#22)	2.0
LHCb $\beta^* = 20\text{m}$				
STANDARD (1.2e11/3.0 μm)	$d + \beta^*$	14(0)	17 (#28)	n/a
BCMS (1.3e11/2.5 μm)	$d + \beta^*$	15.5(0.3)	#all	0.3
8b4e (1.8e11/2.5 μm)	$d + \beta^*$	20(3.2)	#all	1.2

Table 3.4 – Summary on the leveling times and the required number of β^* points for different implementations and operation scenarios. When two leveling methods are mixed, separation leveling is used first, followed by β^* leveling. Leveling types: d –offset and β^* leveling.

optics squeeze step performed with colliding beams while experiments are taking data.

The traditional method of operating LHC, as it is practiced today, consists of first performing the optics squeeze to the smallest β^* , and then to collide the beams. In some situations the beams may be so unstable during the squeeze that only head-on beam-beam collisions may provide sufficient Landau damping. In that case the concept of *collide and squeeze*, where two beams are brought into collision before the optics squeeze, may be considered. Conceptually the collide and squeeze is identical to a series of β^* leveling steps executed as

a continuous sequence. Clearly since the optics change spanned by the C&S is much larger than a β^* leveling step, such a process is more delicate to control, in particular because the orbit stability requirements in terms of beam size remain identical.

While the first attempts of the experimental validation of the C&S were performed already in 2012 [63, 64, 65], the results of experiments performed in 2015 in the frame of this work presented in Chap. 6 of this thesis [66, 67, 68].

3.6 β^* leveling scenarios for the HL-LHC

3.6.1 HL-LHC Base line

For the LHC luminosity upgrade HL-LHC (from 2025) [69] luminosity leveling by β^* is part of the operational baseline. Therefore an extended learning period will be needed to master the process and study in more details the stability criteria in terms of the orbit reproducibility, margin on beam offsets etc. A few additional effects have to be considered for a detailed luminosity leveling description and requirements.

3.6.1.1 Geometric factor reduction restoration

As the HL-LHC will operate with a total crossing angle $\phi = 585 \mu\text{rad}^3$ and $\beta^* \approx 10 \text{ cm}$ a compensation is needed to restore the large luminosity reduction due the geometric factor (see Sec. 1.36). As described earlier crab cavities (CC, see Sec.3.2.3) will be used to compensate the effect of the large crossing angle. During the first part of the LHC upgrade with the CC at their nominal voltage, the overall reduction due to the resulting angle (ϕ_{cc}) will be restored to the LHC level with $F(\phi_{cc}) \approx 0.81$ [41] (uncompensated $F(\phi) \approx 0.20$).

3.6.1.2 Hour glass effect

Additionally, when β^* approaches a value similar to the bunch length σ_z (see later with ATS optics, Sec. 3.6.2), the previously omitted *hourglass effect* must be taken into account. The betatron function $\beta(s)$ in a drift space varies with the distance s to the minimum (β^*):

$$\beta(s) = \beta^* \left(1 + \frac{s^2}{\beta^{*2}} \right) \quad (3.3)$$

Figure 3.10 illustrates the variation of the transverse beam size with respect to the distance from the IP for different β^* values. The luminosity reduction due to the hourglass effect remains below 1% for the nominal LHC $\beta^*=0.55 \text{ m}$. For the HL-LHC case ($\beta^*=0.15 \text{ m}$) the effect reaches a level of 5%.

³uncompensated

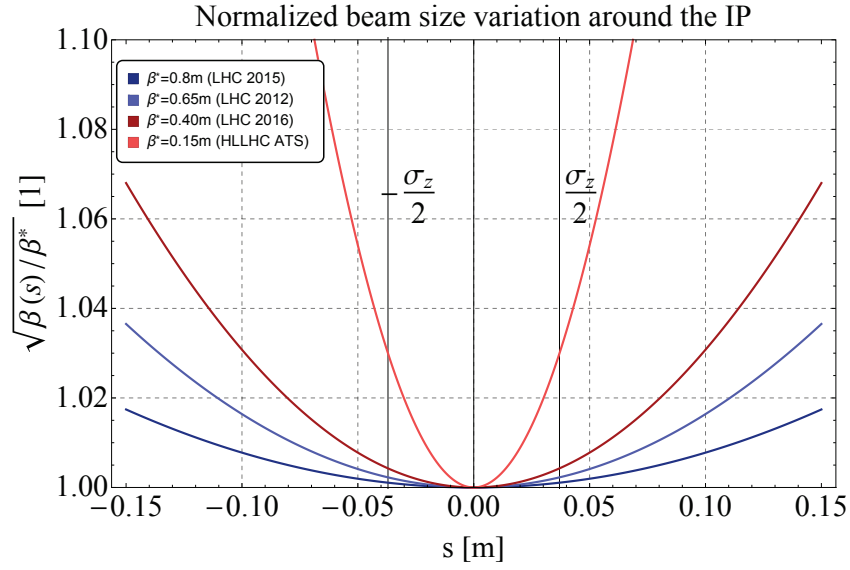


Figure 3.10 – The hourglass effect illustrated as a transverse beam size variation around the IP for a different LHC and HL-LHC optics configuration for design bunch length of $\sigma_z=7.7$ cm.

3.6.1.3 Leveling requirements

Figure 3.11 and Tab. 3.5 presents scenarios for beam parameters that may be used in the HL-LHC [41]. The scenarios for the DESIGN beam are presented in Fig. 3.12. The leveling scenarios

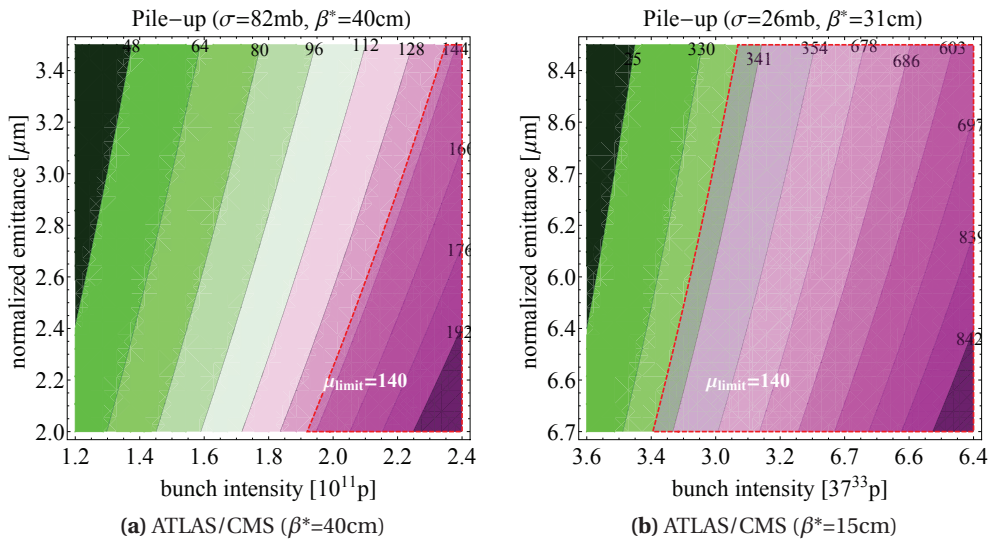


Figure 3.11 – Pile-up at the HL-LHC IPs (distinguished by achievable β^* at the IP) over a wide parameter space (ϵ_n and N_p). The values correspond to a bunch length of $\sigma_z=7.7$ cm and a half-crossing angle $\phi/2 = 180 \mu\text{rad}$.

Chapter 3. Luminosity leveling at LHC and HL-LHC

takes into account the hourglass effect and assume a design bunch length of $\sigma_z = 7.7$ cm. When comparing Fig. 3.12a to Fig. 3.12b we see that in order to correctly smooth the luminosity (jump $\leq 5\%$) the β^* step must be ≈ 1 cm. For DESIGN beam parameters the total leveling time

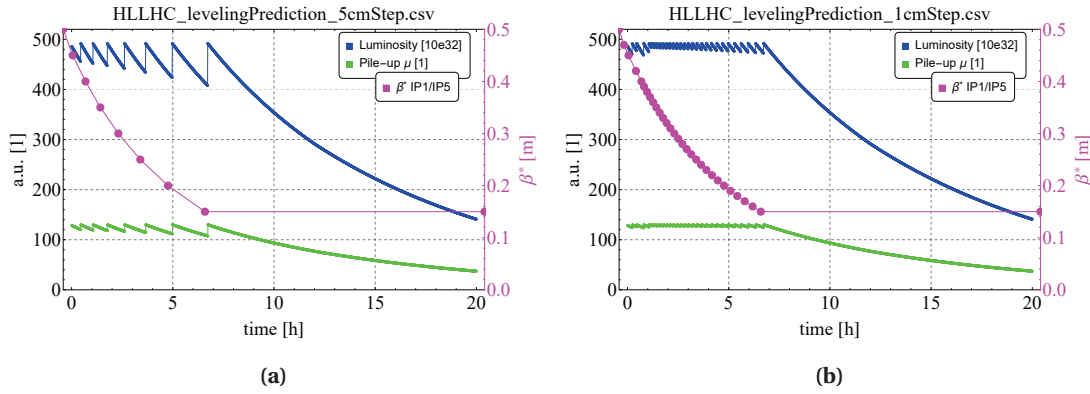


Figure 3.12 – Luminosity leveling scenarios for ATLAS/CMS for 5 cm β^* steps (a) and for 1 cm β^* steps (b) for a 8b+e4 beam type (see Tab. 3.5) based on a maximum pile-up $\mu=130$.

will reach **6.7 hours** while for the increased brightness 8b4e beam leveling times can reach up to **8.2 hours**.

HL-LHC configuration	LHC	HL-LHC		
	7 TeV			
beam type	DESIGN	DESIGN	BCMS	8b+4e
spacing [ns]	25			
N_b [e11]	1.15	2.2	2.2	2.3
max # bunches	2808	2736	2592	1968 ⁴
ε_n at FT [$\mu\text{m rad}$]	3.75	2.5	2.5	2.2
ATLAS/CMS pile-up μ [1]				
$\beta^*=0.4$ m	30	110	110	140
$\beta^*=0.15$ m	65*	280	280	340

Table 3.5 – Summary of HL-LHC beams [41] with associated peak pile-up ($\sigma_p = 82\text{mb}$) for high luminosity IPs (ATLAS and CMS). The pile-up is calculated for a nominal bunch length of $\sigma_z = 7.7$ cm, crossing angle of $\phi/2=180 \mu\text{rad}$ (restored with CCs) and includes the hourglass effect. (*) this is a theoretical value for the LHC beam for this β^* .

⁴This limited filling scheme is only considered when a limitation related to the electron cloud will play a role.

3.6.2 ATS optics challenges

The Achromatic Telescopic Squeeze (ATS) scheme was adopted for HL-LHC to boost the minimum β^* using the matching quadrupoles in adjacent IRs (i.e. IR 2/8 for IR1 and IR 4/6 for IR5) [70]. As shown in Fig. 3.13 this scheme affects the magnet gradients in adjacent octants and requires special attention for orbit stability since the locality of the squeeze is broken.

While the orbit effects will be discussed in Chap. 5 we focus here on the conceptual solution for the operation. The change of the matching quadrupole gradients in the adjacent IPs (see Fig. 3.13b) may significantly reduce the options for the leveling method in IP2 and IP8. Therefore, the required luminosity leveling is only applicable for the IP1 and IP5 at the same time. The two remaining experiments will be leveled with a transverse offset.

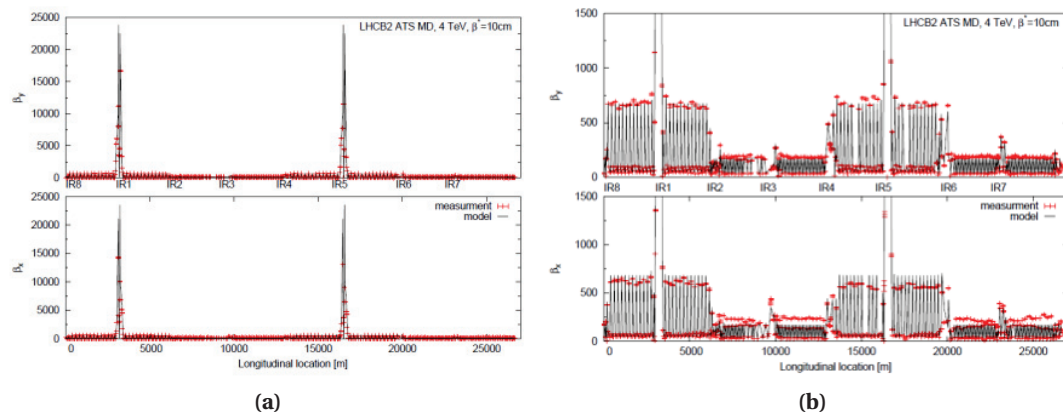


Figure 3.13 – Betatron function with ATS optics from an experiment at 4 TeV in 2012. The top row corresponds to the vertical, bottom row to the horizontal plane. (a) display of the betatron function along the ring, with peaks reaching 25 km in triplets around two high lumi IPs. (b) same display with a zoom that shows the arc betatron function reaches 800 m (where $\hat{\beta} = 180\text{ m}$ for the regular arc). Courtesy S.Fartoukh [71].

3.7 β^* leveling "a la carte"

An ultimate solution for a β^* leveling would be an independent (i.e. between the interaction points) and flexible (no predefined optics matched points) schema. This however requires a significant re-design of the control system as compared to the current LHC including more dynamic optics correction procedure. For example the currently applied global optics corrections may not be used for such a scheme.

3.8 Conclusions

We studied the advantages and disadvantages of the different luminosity leveling methods. For β^* leveling, an excellent orbit stability at the IP is required in order to maintain HO collisions and profit from the main advantage of this technique, namely the strong Landau damping.

We have studied the scenario where LHCb would be used as a target experiment to gain experience with β^* leveling. While for Run 2 it is not the case for the LHC machine, some scenarios might allow up to **10 hours** of β^* leveling per fill.

The two LHC high luminosity experiments (ATLAS/CMS) will not require leveling before LS2, however some extreme brightness beam scenarios may trigger the need already in 2017 up to **4 hours** of β^* leveling per fill.

Since in 2015 no instabilities were observed during the squeeze (similar to those observed for high brightness beams in 2012), **collide and squeeze is very likely not required during Run 2.**

The **HL-LHC will require the leveling in the high luminosity experiments** for up to **5 hours** (for design parameters) and up to **8 hours** for brighter beams, during which an orbit stability is required.

β^* leveling is a baseline for the HL-LHC to obtain adjustable luminosity, therefore in the following chapters of this thesis we will evaluate the influence of the following issues:

- The impact of ground motion and other sources of beam orbit variation on the orbit reproducibility at the interaction point for collide and squeeze and for β^* leveling.
- The impact of optics changes during β^* leveling or collide and squeeze for the beam offsets at the IP.
- Configurations of the LHC orbit feedback system that are optimized for β^* leveling.

4 Orbit drifts at LHC

This chapter discusses the LHC beam orbit perturbations and their causes. The analysis of the orbit perturbations is used to quantify the machine misalignment and its evolution over time. The disturbing mechanical problems of the LHC inner triplets that are affecting the orbit stability is reviewed.

4.1 Source of perturbations

As pointed out in Sec. 1.1.3, the main source of beam orbit perturbations comes from the quadrupole misalignments. The misalignment sources may be grouped into the following three categories:

1. Environmental sources, such as natural ground motion and tides. The perturbations are propagated down to the beam mainly through the quadrupole displacements.
2. Machine-inherent sources, such as decay and snap-back of the superconducting circuits [61], the flow of the super-fluid and fluid helium in the cryostat (see. Sec 4.5) or changes of the optics as performed in the betatron squeeze (see Chap. 5).
3. Equipment failures, such as loss of an orbit correction dipole (COD).

In this chapter, we will discuss the environmental and machine-inherent sources. Coping with equipment failures is a machine protection issue.

Even if the orbit is initially corrected, with time the ground motion generates some additional misalignment as described by Eq. 4.1:

$$\Delta u_j = \sum_{i=0}^N R_{Q_{ij}} \cdot \Delta \delta_{ui} \quad (4.1)$$

where $\Delta \delta_{ui}$ is the change in misalignment and $R_{Q_{ij}}$ is the response matrix element as described in Sec. 1.1.2. One can immediately see that the strength of the perturbation is proportional to

the optics functions at the source and at the observer. A higher betatron function implies a higher amplitude of the perturbation.

4.2 Reference orbit and correction strategy

During *beam commissioning* a flat reference orbit is established at an early stage. This reference orbit is used as base for the entire LHC machine cycle and for the duration of a run (≈ 1 year). The correction is made using a maximum number of corrector magnets including the correctors in the common vacuum chamber (MCBX), in order to achieve the best correction of the initial misalignments. The number of eigenvalues is cut off by trial and error at the point where the corrector kick strength starts to increase by a significant amount without gain in orbit quality, typically ≈ 460 out of 520 eigenvalues are used at this stage. Since the singular eigenvalues usually correspond to local solutions around the IRs, it is the strength of the correctors between the Q6 magnets on either sides of the interaction region (IR) that tends to diverge. After correction the typical orbit r.m.s. ranges between **0.25 mm** and **0.35 mm** [72].

Such manual corrections are performed first at injection, and later during the commissioning of the flat top and the squeeze. Once the reference is established at injection, the orbits in all other phases are corrected to that target (crossing bumps and separation bumps are added as required on top of the reference orbit).

When the first manual setting up is done, correction of the orbit through each cycle is performed automatically by the LHC Orbit Feedback (OFB) [73, 74]. The OFB applies corrections at 12.5 Hz with a typical bandwidth of ≤ 0.1 Hz. For feedback operation the number of eigenvalues is limited to ≈ 440 to avoid problems with BPM errors and noise in the IRs leading to excessive deflections through the singular eigenvalues. This effect will be highlighted by the simulations presented in the following chapter (e.g. Sec. 5.3.1).

Furthermore the so-called 'common' correctors in the triplet regions (MCBX), 3 on each side of every IP, are excluded from the on-line OFB correction. The reason for this is due to the QPS that is protecting those corrector magnets. The QPS severely limits the acceleration ($\frac{dI}{dt^2}$) and ramp rates ($\frac{dI}{dt}$). Exceeding these limitations provokes 'false' QPS triggers, leading to premature beam aborts [74]. This problem does not exist for the other correctors that are self-protected (no QPS). As we will see later, the absence of the MCBX correctors (24 in total per plane) has a significant impact on the orbit correction quality around the IPs.

4.3 Bare orbit

There is no direct way to measure the quadrupole misalignments but it may be estimated from the orbit corrections. As described in Sec. 2.6 the correction of the orbit at LHC is standing on two pillars:

- pre-defined settings and functions of the orbit correctors established during commissioning and periodically updated
- real-time corrections by the OFB to compensate dynamic effects that are non-reproducible as well as all perturbations that have occurred since the functions were updated (see previous item)

At regular time intervals, the latest real-time corrections are collected and added to the pre-defined settings (feed-forward). The procedure ensures that the OFB corrections remain small, and increase the chances of beam survival in case of the OFB stops by accident.

If one calculates the orbit response for the inverse corrections (either from the OFB real time channel (RT) or from the base setting functions (BC)), the orbit will be as described by the Eq. 4.2:

$$\vec{u}_{\text{raw}} = (\vec{u}_c - \vec{u}_c^{\text{ref}}) - \mathbf{R} \cdot (\vec{\theta}_{\text{FB}} - \vec{\theta}_{\text{FB}}^{\text{ref}}) \quad (4.2)$$

where u_c is the actual corrected orbit, \mathbf{R} is the current optics response matrix and θ_{FB} is the setting of the feedback system. In order to see the actual influence of the feedback corrections, the reference was set to the moments where an accumulated RT correction was incorporated (feed forward) into the base correction, therefore, only a net correction was used for calculation. The result of the calculation (unfolding orbit) is called *bare orbit*.

The algorithm to perform this calculation for multiple orbits was implemented in the `MultiOrbitCalculationFramework` (see Appendix A.2) where manipulations may be performed on multiple orbits.

4.3.1 Quadrupole misalignment and r.m.s. orbit perturbation

The average misalignment of the machine elements can be estimated by unfolding the effect of all orbit corrector deflections for a given LHC closed orbit and comparing it to simulations with misaligned machines. Figure 4.1 shows the r.m.s. orbit obtained by unfolding the corrections¹ from the all orbits recorded at injection for the 2012 and 2015 runs. For a given plane and beam, the distributions are quite narrow (see Figs. 4.1b and 4.1c). The evolution of the misalignments over a year is therefore small compared to the initial offsets.

The average r.m.s. is equal to $u_{\text{rms}} \approx 10$ mm with values ranging from 5 mm to 15 mm. Figure 4.1 shows the simulated orbit r.m.s. obtained for a misalignment of $\delta_Q^{\text{rms}} = 100 \mu\text{m}$. The average orbit r.m.s. is $u_{\text{rms}} \approx 3$ mm. Assuming all perturbations are due to quadrupoles misalignment and comparing the two numbers one can estimate the typical LHC misalignment to $\delta_{\text{rms}}^{\text{LHC Run 1}} \approx 300 \mu\text{m}$. This is summarized in the Table 4.1. The small reduction of the r.m.s. in 2015 with respect to the 2012 may be due to the machine realignment performed in 2014.

¹ To estimate the *bare orbit* it is sufficient to invert the total correction (base correction summed with the real time feedback actions) that is applied.

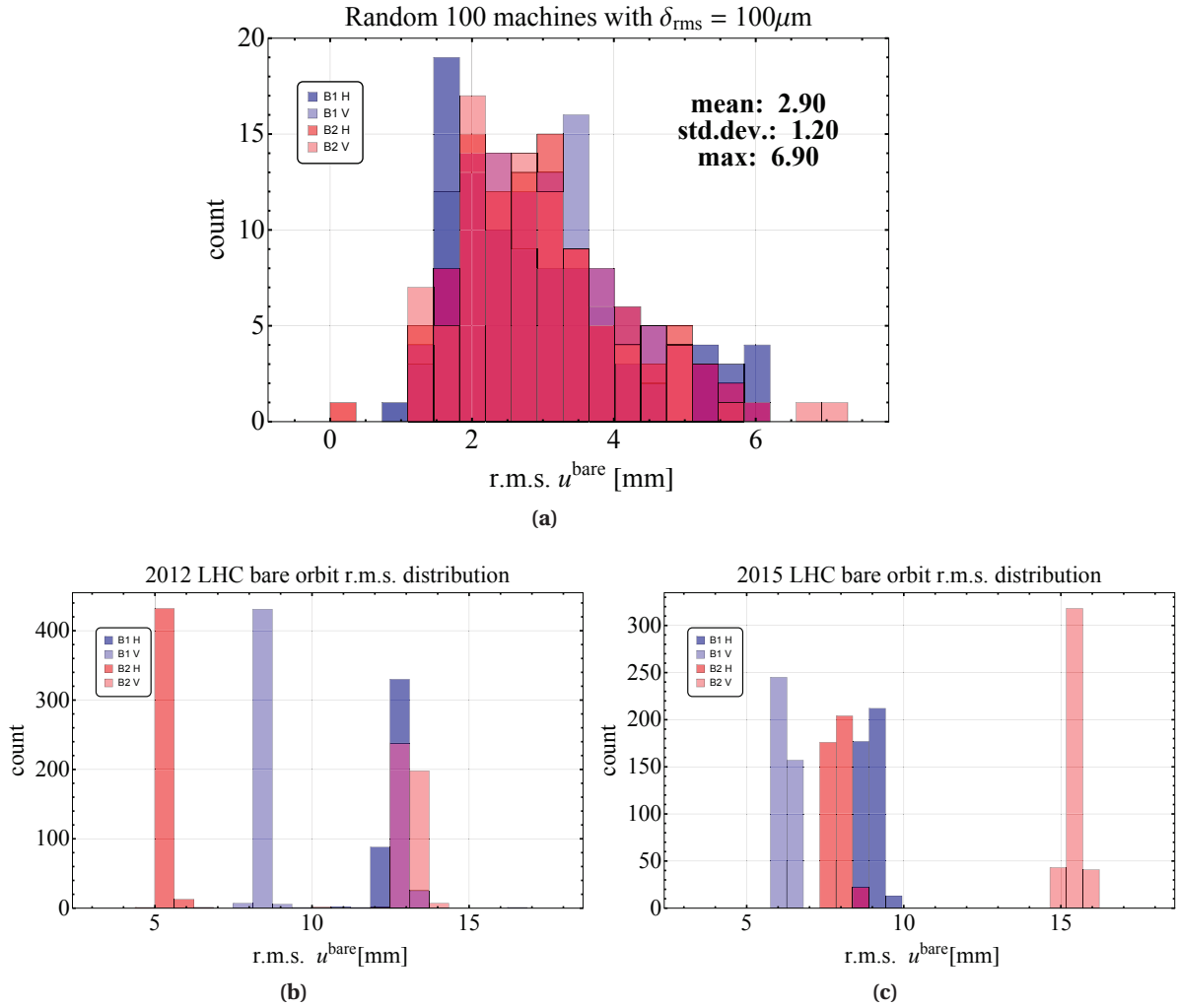


Figure 4.1 – (a) Distribution of the orbit r.m.s. for 100 simulated machines for a r.m.s. quadrupole misalignment of $\delta_Q = 100\ \mu\text{m}$. (b) and (c) present distributions of the bare orbits at injection obtained by unfolding all corrections for 2012 fills (448) and for 2015 fills (403) respectively.

Initial misalignment		orbit perturbation r.m.s.
$\delta_Q = 100\ \mu\text{m}$	\Rightarrow	$u_{rms} \approx 3\text{mm}$
$\delta_Q^{\text{LHC 2012}} \approx 300\ \mu\text{m}$	\Leftarrow	$u_{rms}^{\text{LHC 2012}} \approx 10\text{mm}^2$
$\delta_Q^{\text{LHC 2015}} \approx 270\ \mu\text{m}$	\Leftarrow	$u_{rms}^{\text{LHC 2015}} \approx 9\text{mm}^3$

Table 4.1 – Estimate of the r.m.s. element misalignment and the corresponding orbit r.m.s. The estimates are valid for the injection optics.

²estimated by unfolding all corrections at injection optics, data set of 448 elements

³estimated by unfolding all corrections at injection optics, data set of 403 elements

4.4 LHC orbit during cycle

As described in Sec. 2.7 the LHC cycle is divided into specific phases. The following sections will focus on three moments⁴ of the LHC cycle:

1. The start of RAMP, with injection optics (ATLAS/CMS $\beta^*=11$ m, LHCb/ALICE $\beta^*=10$ m), with:
 - (a) **438** orbits for 2012 run
 - (b) **463** orbits for 2015 run
2. The start of FLATTOP (=end of RAMP), with injection optics (ATLAS/CMS $\beta^*=11$ m, LHCb/ALICE $\beta^*=10$ m), with:
 - (a) **372** orbits for 2012 run
 - (b) **371** orbits for 2015 run
3. The start of ADJUST (just before colliding the beams), with collision optics, with:
 - (a) **310** orbits for 2012 run (ATLAS/CMS $\beta^*=0.65$ m, LHCb $\beta^*=3$ m and ALICE $\beta^*=10$ m)
 - (b) **243** orbits for 2015 run (ATLAS/CMS $\beta^*=0.8$ m, LHCb $\beta^*=3$ m and ALICE $\beta^*=3$ m)

For each of the listed moments a calculation to obtain the bare orbit (see Sec. 4.3) without the OFB real time corrections was performed to assess the evolution of the r.m.s. misalignment.

4.4.1 Run 1 (2011-2012)

Figure 4.2 illustrates the evolution of the unfolded orbit r.m.s. as a function of the fill number in different moments of the cycle. The dips that are visible in the evolution (e.g. around fills 2806 and 2980) are related to the feed forward incorporation of the accumulated real time corrections into the base correction. In these points the reference for the calculations (see Eq. 4.2) was reset.

From the periods of growth (Fig. 4.2 highlighted in green) one can estimate the maximum r.m.s. orbit perturbation evolution as listed in the summary Tab. 4.2. Figure 4.3 illustrates the period with a largest growth during LHC Run 1 (2012). The most active plane (Beam 1, vertical) reached an r.m.s. orbit growth rate of around **1 mm per month** (see Fig. 4.3). **These values will be used later as a reference for the maximum environmental input to the r.m.s. perturbation.**

4.4.2 Run 2 (2015)

A similar analysis was performed for the beginning of Run 2 in 2015. Figure 4.4 illustrates the evolution of the orbit perturbation along the year. No growth can be extracted from the

⁴moments refer to 1 minute after declaring given beam mode

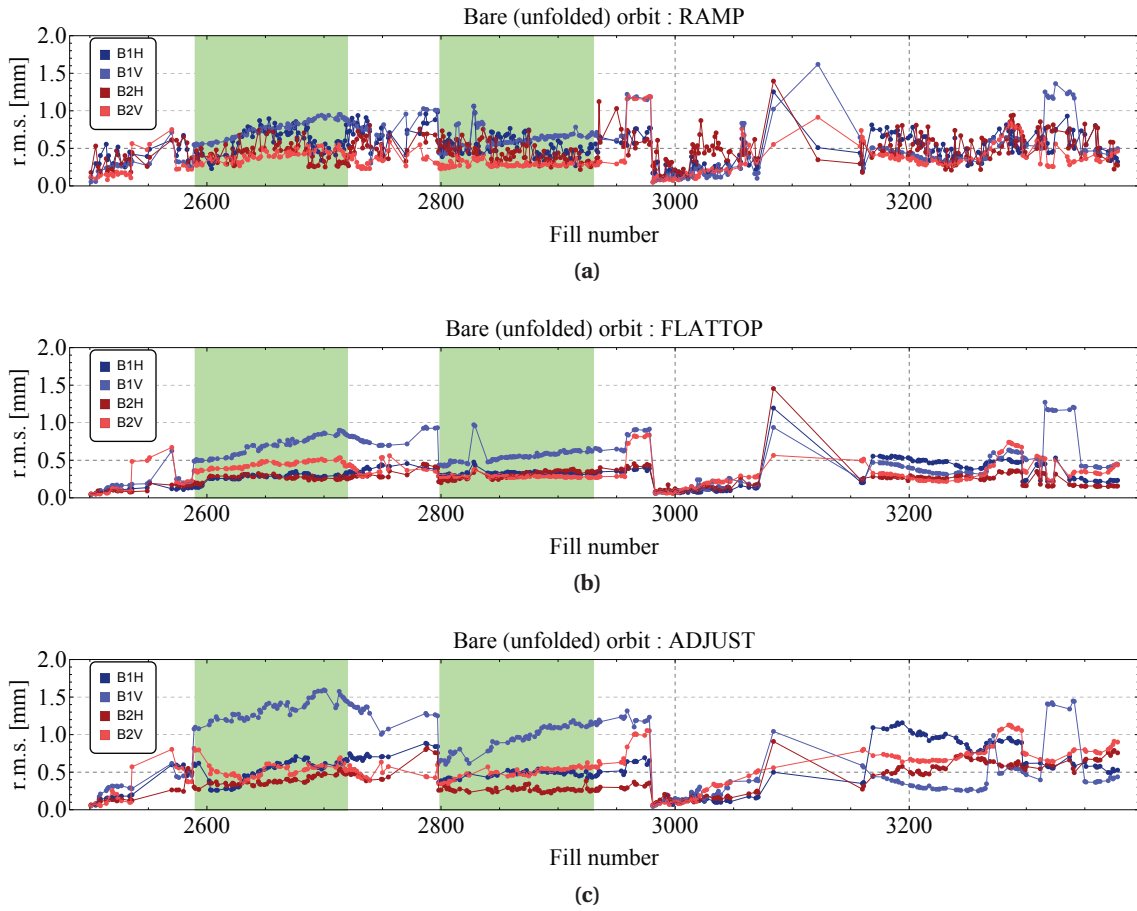


Figure 4.2 – Bare orbit r.m.s. evolution during LHC Run 1 (2011–2012) for: (a) one minute after the start of RAMP, (b) one minute after the start of FLATTOP, (c) one minute after the end of SQUEEZE. In green, isolated periods of stable orbit growths.

optics	r.m.s. growth [$\mu\text{m}/\text{day}$]		misalignment [$\mu\text{m}/\text{day}$]	
	2012	2015	2012	2015
FLATTOP	15	n/a	0.3	n/a
ADJUST	33	15	0.3	0.15

Table 4.2 – Estimates of the r.m.s. orbit growth for LHC Run 1 and Run 2 and corresponding estimated quadrupole misalignment.

data because the orbit is very stable in the production phases, however one can quantitatively see that again, the vertical plane of Beam 1 is the most active. Jumps are however observed after the technical stop periods and different LHC beam commissioning like electron cloud scrubbing runs [58] or medium and large β^* optics [61]. Periods highlighted in red were affected by the mechanical issues in the inter triplet in IP8 (see later in Sec. 4.5). The period highlighted in green was used to estimate a possible growth rate as listed in Tab. 4.3.

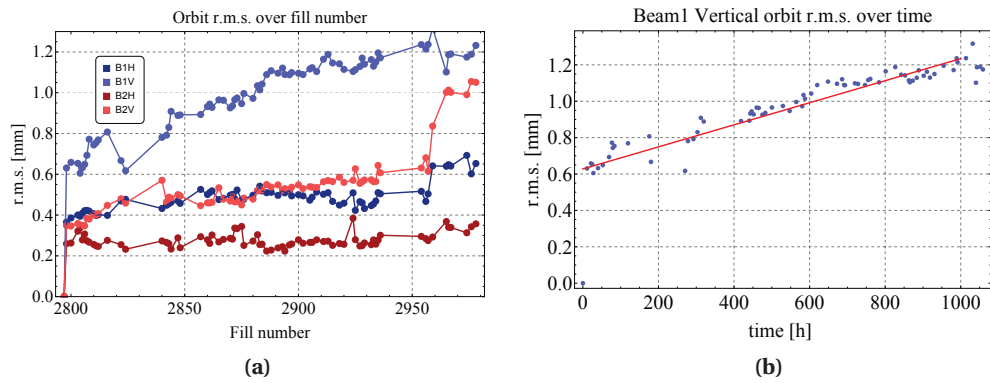


Figure 4.3 – The extrapolation (from the period of fills 2800–2980) of the maximum orbit r.m.s. growth.

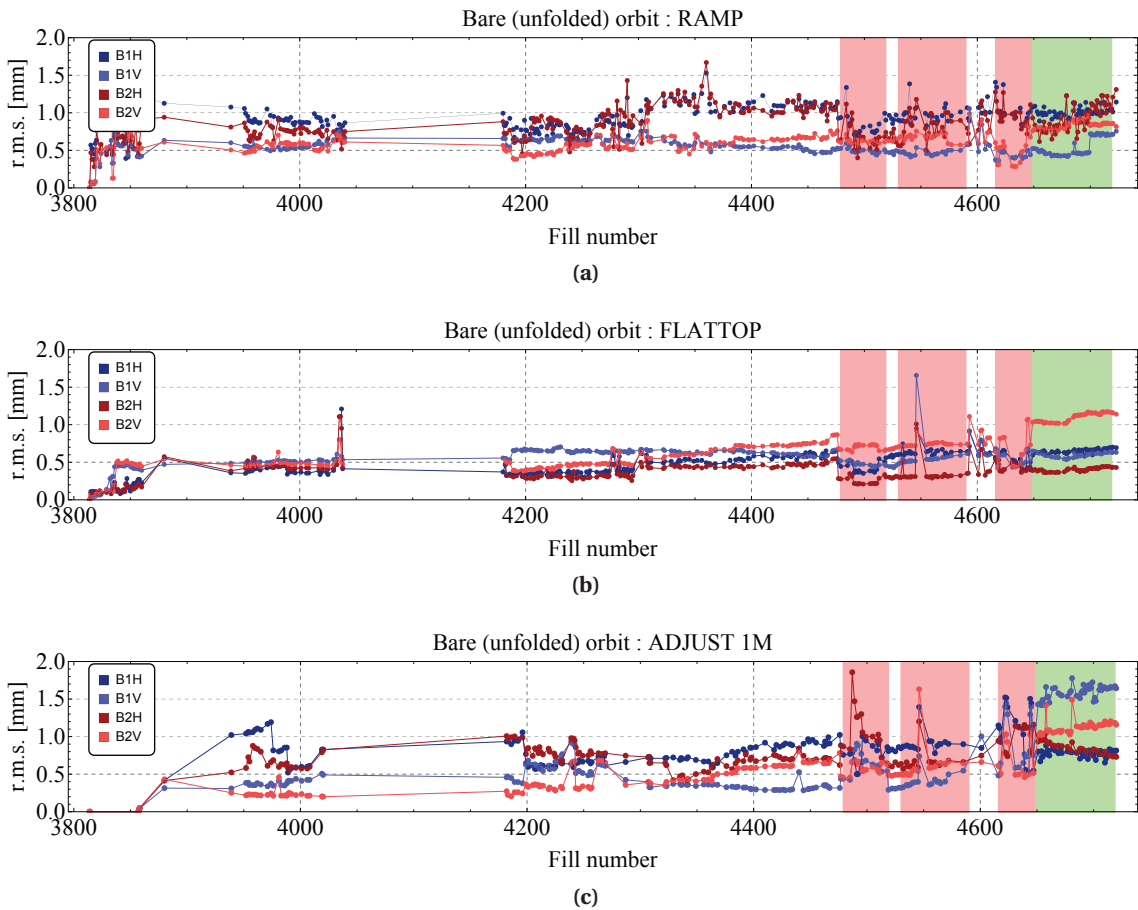


Figure 4.4 – Bare orbit r.m.s. evolution during LHC Run 2 (2015) for: (a) one minute after the start of RAMP, (b) one minute after the start of FLATTOP, (c) one minute after the end of SQUEEZE. In green, isolated periods of stable orbit growths. In red periods of increased activity in IR8, see Sec. 4.5.

4.4.3 Specific patterns in the correction solutions

During the LHC Run 1, some puzzling structures appeared in the corrections applied by the orbit feedback system. Examples for those structures are shown in Fig. 4.5. The structures appeared as "correction" bumps next to IR1 and IR5.

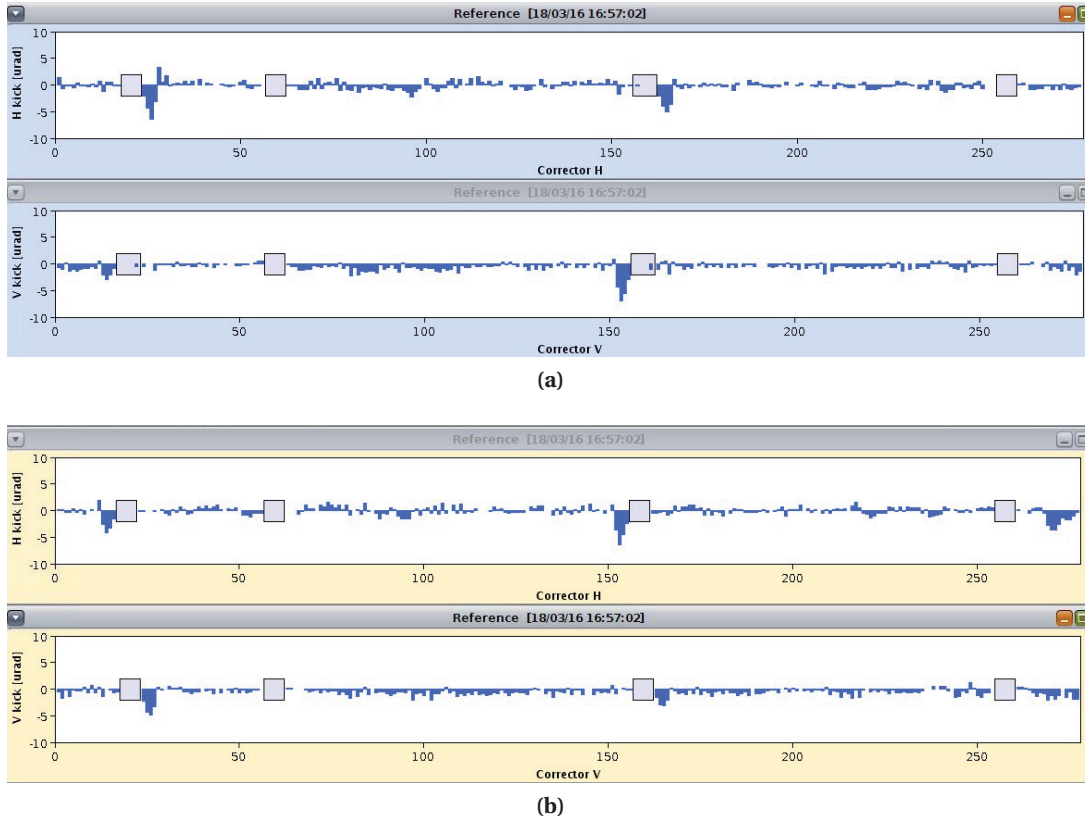


Figure 4.5 – Example of the correction patterns appearing in the OFB real time channel. (a) for Beam 1 and (b) Beam 2 during fill number 2994, unfolded with respect to the fill number 2980. An accumulation of strong deflections is visible around IR1 (corrector index $\approx 10\text{--}15$) and IR5 ($\approx 150\text{--}170$)

An analysis, based on pattern matching between occurrences (see Appendix A.3), **showed no systematic dependence on time nor with the position of appearance of those patterns**. An analysis of the structure of orbit corrections during the squeeze revealed however that the accumulation of the corrections around the IPs may be due to the sequential character of the correction during optics change in the betatron squeeze. The origin of the patterns is related to the fact that the feedback system has no access to the orbit correctors in the common region where the betatron functions are highest (more details see Chap. 5), therefore corrections must be done with correctors surrounding the source, most likely the triplet.

4.5 LHC orbit drifts during stable beams in 2015

4.5.1 The orbit drifts

When the machine commissioning period ended in 2015 and the higher intensity runs started, an instability of the horizontal beam orbit was identified during the periods of stable collisions. The perturbation in the form of a regular betatron oscillation in the horizontal plane of both beams was pointing to an element common to the two beams. The orbit perturbations affected the luminosity performance, mainly of the ATLAS experiment, by generating beam offsets at the IPs.

The following discussion and analysis is made for several LHC production fills whose details are listed in Tab. 4.3. An example for the drift analysis⁵, is presented in Fig. 4.6. This fill suffered

fill nb.	start time	end time	SB start	SB end	SB length [h]
4402	2015-09-21 18:43	2015-09-22 09:01	21:00	08:43	11.8
4479	2015-10-09 23:53	2015-10-11 01:46	09:30	01:37	16
4485	2015-10-11 13:39	2015-10-12 06:00	17:11	05:43	12.5
4538	2015-10-26 16:05	2015-10-27 18:52	18:25	18:44	24.5
4540	2015-10-28 00:00	2015-10-28 15:11	02:26	15:02	12.6

Table 4.3 – Details of selected LHC fills in 2015, used for further analysis. SB – Stable Beams.

from the largest perturbations in 2015 (fill 4402). The figure presents two time series with, the measured and the unfolded bare orbit r.m.s. versus time. The bare orbit is obtained by removing all corrections applied during the fill. On the bare orbit evolution one observes an increase of the r.m.s. with a sudden drop ≈ 6 hours after the start of the stable beam period. During that moment, a visible perturbation increase in the actual orbit is visible. The spikes and perturbations represents the moments when a significant orbit drifts in the IPs occurred.

4.5.2 Localization of the drift source

4.5.2.1 Orbit analysis

As described in Sec. 1.1.3 the MICADO algorithm provides a mean to localize the perturbation source. An analysis of all fills pointed consistently towards a source in the inner triplet right of point 8. In some cases the correction algorithm also pointed to a smaller source on the left side of point 1, but at the time this second source was never clearly confirmed.

⁵only fills of more than 6 hours in SB were taken into account

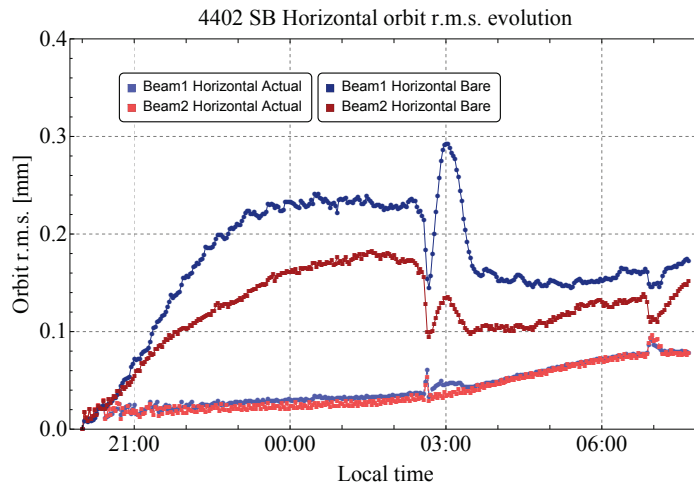


Figure 4.6 – Measured and bare orbit r.m.s. during fill 4402, the largest orbit perturbation observed in 2015. The two data series represent the measured orbit r.m.s. (light blue and red) and the bare orbit (blue and red) respectively for Beam 1 and Beam 2. A slow orbit feedback was active during the fill leading to the measured orbit change. The dip of the bare orbit just after 3 hours, corresponds to a fast change of the perturbation.

4.5.2.2 Triplet position monitoring system

For the reasons described in Sec. 4.1, the LHC inner triplet magnets are equipped with a special alignment monitoring system. For the alignment supervision, two systems, hydro–static [75, Sec. 3.4] and based on a stretched wire [75, Sec. 3.5], are installed along every inner triplets in the LHC machine. A system of stretched wires (WPS) covers the entire length of three triplet quadrupoles. A set of sensors records the evolution of both the radial and the vertical movements. The movement of the magnet cryostats can be monitored with a $1\ \mu\text{m}$ resolution (on a relative scale). The location of the sensors is indicated in Fig. 4.7.

The absolute values of the recorded cryostat positions are difficult to translate to real position of the magnet cold–mass. On the other hand relative position changes of up to **$30\ \mu\text{m}$** have been observed during the 2015 run on the IR8 triplet magnets. Figure 4.8 presents an example of the measurements on the left and right sides.

On the history of the WPS data, until 13 January 2015 no significant activity is observed on the IR8 triplet. On that day a position oscillation with a period of ≈ 8 hours started to appear on the right side triplet. The position changes were independent of the machine cycle (injection or high energy) and of any beam operation activity. The oscillations only stopped when the helium was removed from the cryostats (see Fig. 4.8). This observation clearly pointed to the cryogenics system as one of key "ingredients" for the position instability. For the entire 2015 run the mechanism driving the position change remained a mystery, no correlation with cryo conditions of the cold mass could be confirmed.

4.5. LHC orbit drifts during stable beams in 2015

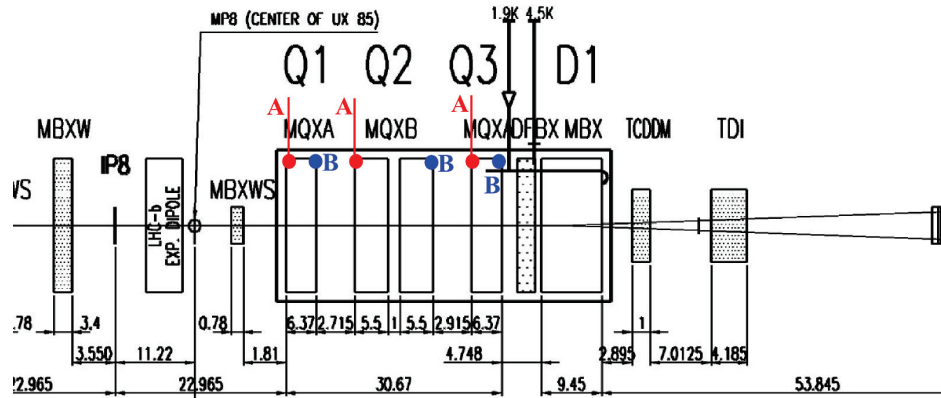


Figure 4.7 – The triplet layout on the right side of LHC point 8. The colored marks (A,B) represent the positions of the WPS sensors.

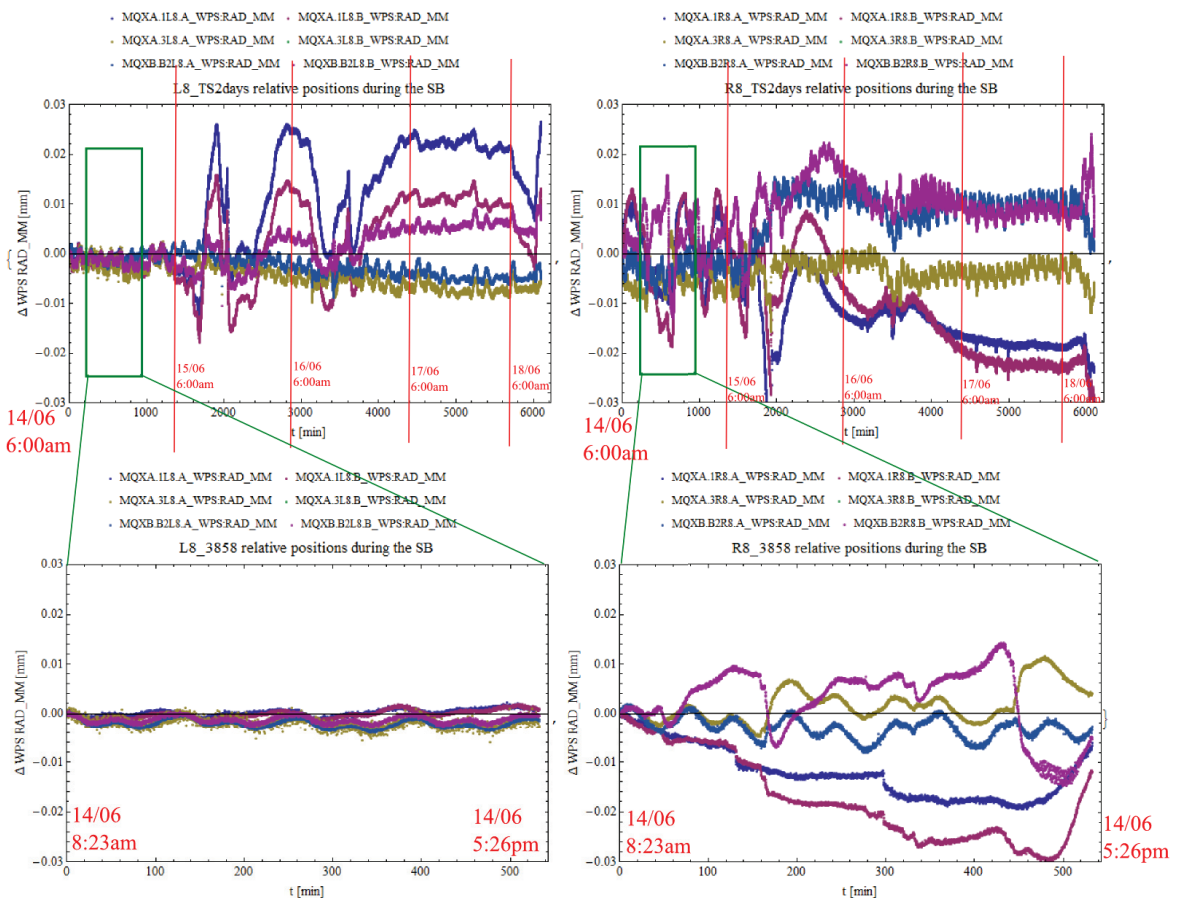


Figure 4.8 – The LHC triplet movement on the left and right side of points 8 (top row), during 24h period before the start of the Technical Stop 1 (15/06, 6:00am). A zoom for the period of stable beams during fill 3858 (bottom row) reveals the scale of the movement in R8 as compared to L8. On 15/06 after 6:00am the helium of the triplet magnet was emptied leading to large movements. The amplitude of the movements during SB and during emptying are similar for the right side.

4.5.3 Reconstruction of the orbit from the positioning system

In order to quantify the impact of the moving quadrupole, a tool was developed (inside the OrbitsFramework, see Appendix 8) **to feed the measured magnet movement to MADX and to extract the resulting orbit changes**. Figure 4.9 show the evolution of the misalignment and the simulated orbit response.

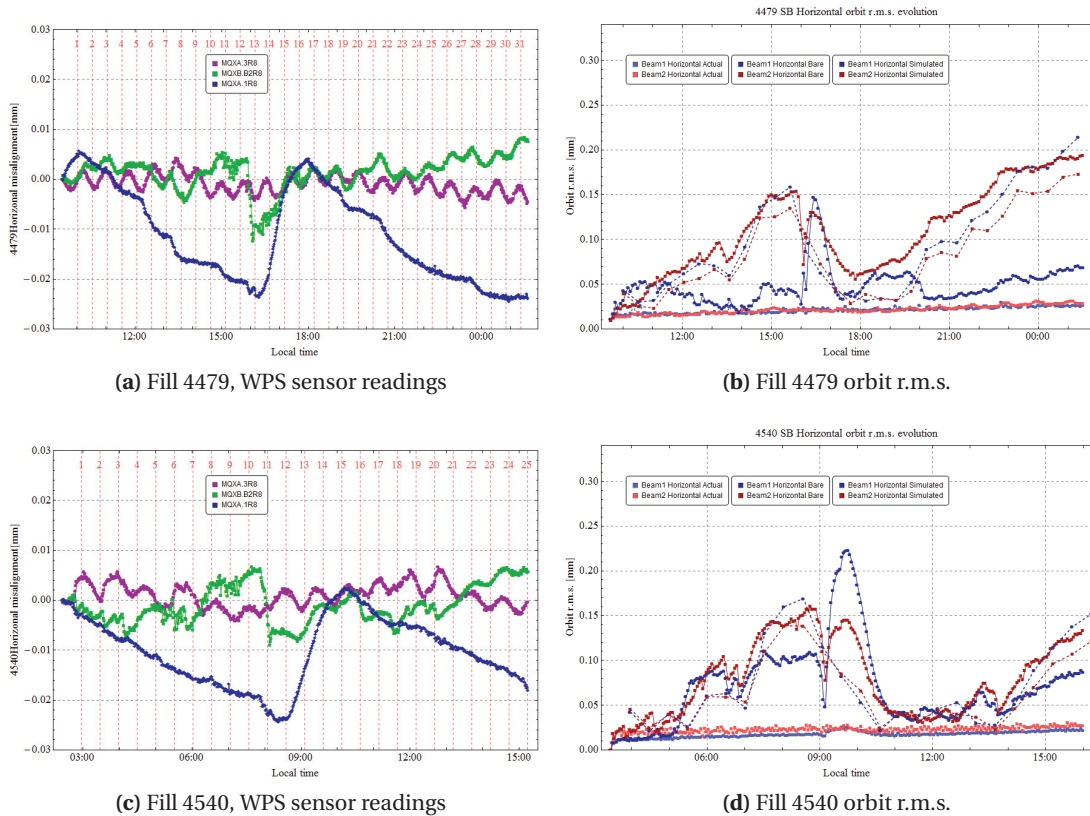


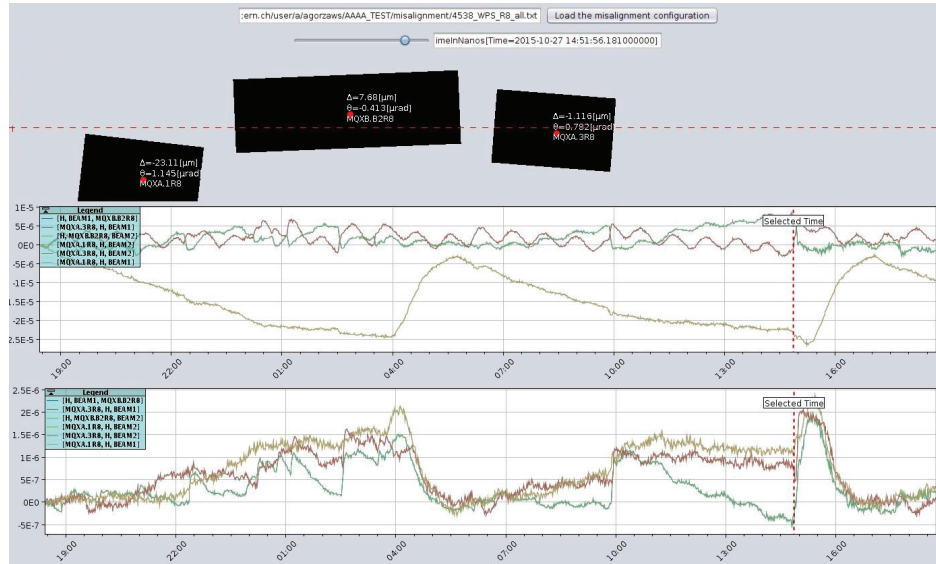
Figure 4.9 – Comparison of the observed bare orbit r.m.s. evolution (obtained from unfolding corrections) and the simulation based on the recorded triplet movements (right hand side). Simulation were run for the steps indicated by the dotted vertical lines on the left hand side figures. The simulation included only the three most active sensors as representative of the triplet assembly. No magnet tilt was included in this simulation.

Initially the readings on both magnet ends were averaged and used in the simulation as an offset. The results are shown in Fig. 4.9. Whereas the main perturbation followed the simulation rather well, the period with the largest and fastest orbit drift was **not properly reproduced** (see Fig. 4.9b around 16:00 and Fig. 4.9d around 9:00).

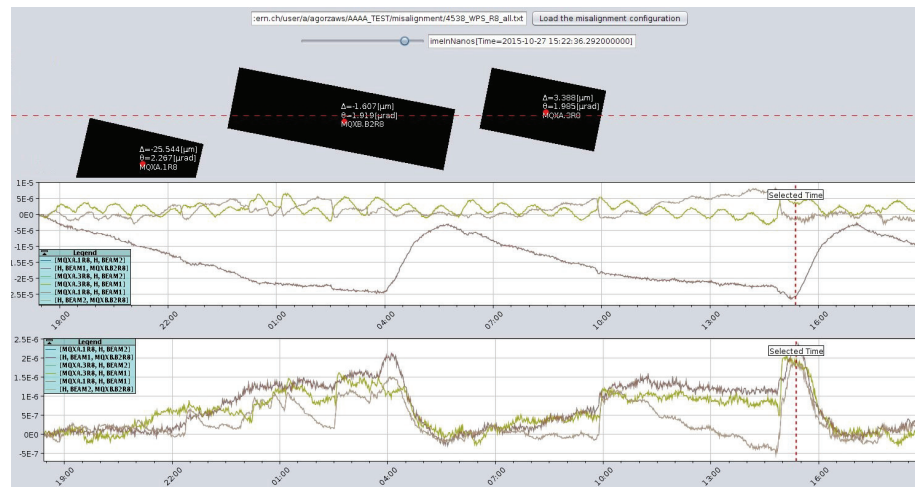
The next step in the simulation was to reproduce and include the tilt error. The longitudinal tilt was calculated from sensors A and B and the magnet lengths (see in Fig. 4.7). Figure 4.10 illustrates the position of the cryostat before and after the peak movement. One can see a

4.5. LHC orbit drifts during stable beams in 2015

significant change of the angle at the Q1 to Q2 transition.



(a) Fill 4538, before the peak perturbation



(b) Fill 4538, after the peak perturbation

Figure 4.10 – The triplet alignment before the main perturbation (a) and after the main perturbation (b). Top row of each figure presents the layout (offset and angle) of the triplet assembly, middle row illustrates the radial displacement of individual magnets while the bottom row is the angle of the magnets. There is clear change of the angle of the Q2 cryostat with a significant perturbation at the Q1 and Q2 transition.

The orbit response to displacements for fills 4540 (already shown in Fig. 4.9d) and 4538 is shown in Fig. 4.11. The result is in good agreement with observations both for, the shape with **a characteristic dip** and for the magnitude of the perturbation.

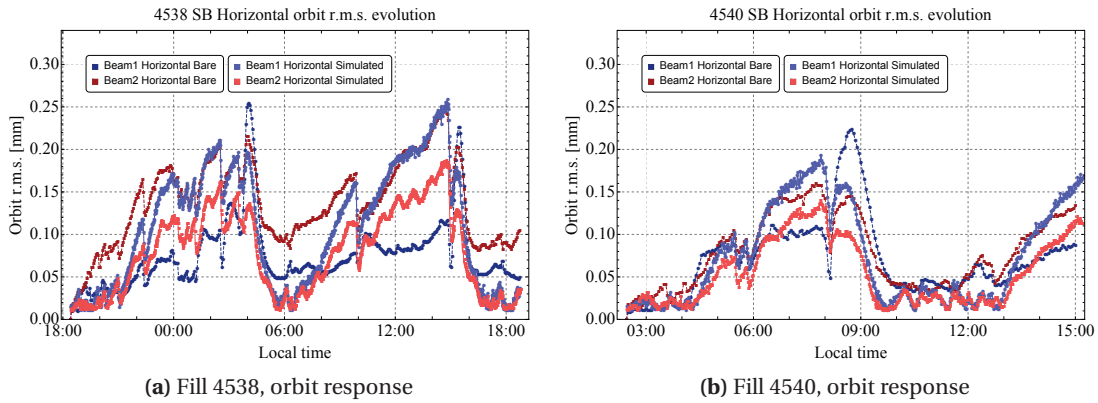


Figure 4.11 – Comparison of the simulation and the LHC bare orbit for fills 4538 and 4540.

Orbit response with ATS optics As an example the response was computed for the HL–LHC triplet using the wire positions as recorded during LHC fill 4540 (see Fig. 4.9c). The expected r.m.s. orbit perturbation with the collisions optics at $\beta^*=10$ cm ($\hat{\beta}_{IT} \approx 20$ km) is show in Fig.4.12. **The global r.m.s. reaches 1.2 mm for the original WPS traces (reaching in peak $30 \mu\text{m}$ of IT quadrupole displacement).** The same perturbation, as it was recorded for the LHC, of $w_{\text{rms}}^{\text{LHC}} \approx 150 \mu\text{m}$ (see e.g. in Fig. 4.9b) **is expected for the displacement of $3 \mu\text{m}$ in peak for Q1 or Q2 magnet.**

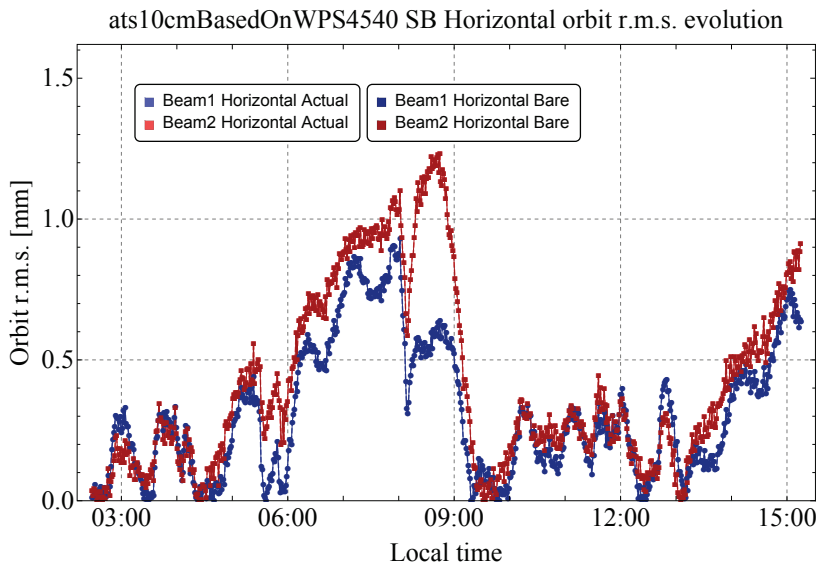


Figure 4.12 – HL–LHC response for the triplet movement as shown in Fig. 4.9c. The simulation was ran with collision optics with $\beta^*=10$ cm for original IP8 WPS recording reaching in peak $30 \mu\text{m}$ of displacement.

Triplet thermal shield

During the end of year technical stop (YETS) between 2015 and 2016 the origin of the position instability was finally localized in the IT thermal shield (Fig. 4.13). The radial position changes of the triplets was found to be strongly correlated to the temperature of the the thermal shield ($T_s \approx 50\text{--}100\text{ K}$). The temperature of the thermal shield also influences the temperature of the 3 cold mass feet inside the cryostat, and this seems to induce the radial position change of the cold-mass and cryostat.

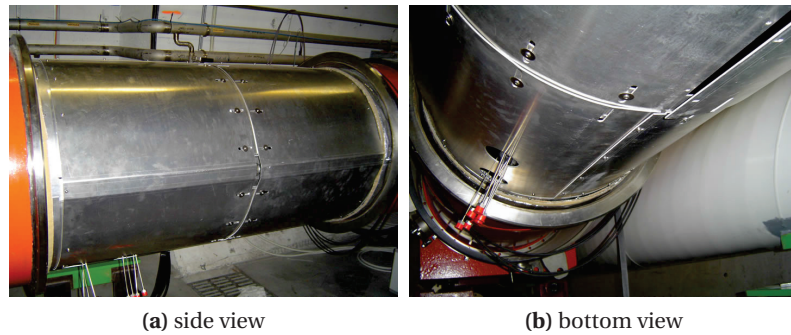


Figure 4.13 – LHC Triplet thermal shield, courtesy J-P. Tock [76].

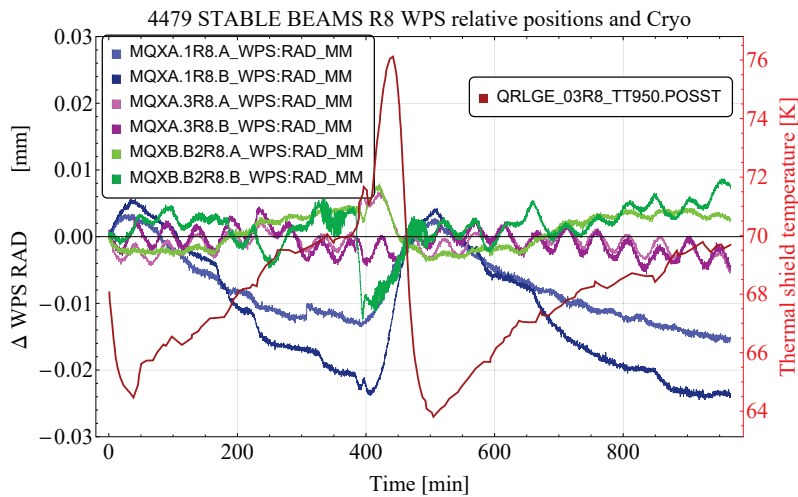


Figure 4.14 – The thermal shield temperature (QRLGE...) is shown together with the WPS recordings for IR8 right side. A defect regulation valve allowed the temperature to fluctuate with a range of 20 K. One can see a clear correlation between the peak temperature change with a cryostat movement activity.

This effect could be reproduced on other triplets assemblies. The root cause of the radial position change is not explained, in particular because at such temperatures the thermal

expansion is very small.

For the specific case of R8 triplet, a malfunctioning helium valve induced large temperature oscillations, leading to the subsequent orbit changes. The problem was solved for the 2016 run by modifying the reference temperature and the regulation of the R8 triplet thermal shield. Figure 4.14 presents the correlation of the shield temperature and WPS position for the R8 triplet.

4.6 Observations in 2016

In the first weeks of the 2016 LHC run, the triplet thermal shield issue reappeared on the R1 triplet around ATLAS. The orbit drifts were a factor 2–3 smaller than in 2015, and the rate of change was significantly slower. However, due to the very small beam sizes at the ATLAS IP, **the triplet movement induced beam separations leading to a loss of luminosity of up to a few % over periods of one hour**. The separations were difficult to correct with the orbit feedback, and required frequent re-optimization at the ATLAS IP [77]. The difficulty to regulate the temperature arises because the cryoplant⁶ is at a distance of 4 km [78]. Finally the cryogenics team, recognizing a general problem, changed all triplet thermal shield regulations. The temperatures are now stabilized to ≈ 2 K leading to a stable situation.

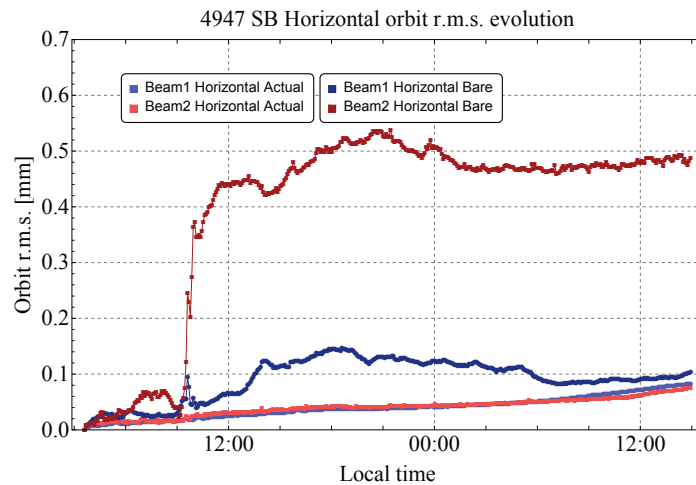


Figure 4.15 – Fill 4947 r.m.s. bare orbit evolution. The large orbit perturbation is caused by a ≈ 30 K temperature drop on the thermal shield of R1 as part of a cryoplant recovery.

During fill 4947 one of the final steps of the recovery of the point 2 cryoplant that had failed one day before, included a cool down of the R1 triplet thermal shield by ≈ 30 K causing large orbit perturbations. Figure 4.15 illustrates the bare orbit evolution with the peak activity around the temperature drop. The order of magnitude of this perturbation was much higher than anything else seen before and **would have led to a beam separation of 3 sigma at ATLAS**. A

⁶technical installation that allows to cool down recirculated helium

series of consecutive luminosity optimization was required to maintain the HO collisions.

4.7 Conclusions

As presented in the chapter opening, both environmental and mechanical sources were studied as causes of orbit changes. The **r.m.s. orbit perturbation was used to measure machine misalignment and its evolution** during regular production time for the LHC.

Based on the **2012 (Run 1) and 2015 (part of Run 2) data**, we derived estimates for the bare orbit evolution over time at injection and flat top. The underlying typical quadrupole position drift has been extracted from the data. Runs in 2012 show maximum misalignments change of $\delta_Q^{\text{rms}} = 0.3 \mu\text{m per day}$ whereas for Run 2 the situation was more stable with $\delta_Q^{\text{rms}} \approx 0.1 \mu\text{m per day}$. Part of the differences between Run 1 and Run 2 may be explained by better BPM reproducibility with improved temperature stabilization of the electronics in which case δ_Q^{rms} is overestimated for Run 1. A quantitative analysis of **influence of the BPM noise on the orbit quality** will be discussed in Chap. 5.

The **value of $\delta_Q^{\text{rms}} = 0.3 \mu\text{m per day}$** will be used for the analysis of the orbit stability at the IPs in the context of β^* leveling and collide and squeeze in Chap. 5.

During the 2015 run the horizontal orbit of the LHC was subject to large perturbations. As a consequence the LHC orbit FB had to be active also during the periods of collisions. We successfully correlated the problem to a cryostat movement. The origin was tracked down to cryogenics regulation problems, and highlighted the usefulness of the position monitoring system of the LHC triplets that could be used to explain the main features of the perturbations.

With the LHC high luminosity upgrade β^* will be pushed down further, from 40–50 cm in Run 2 to $\approx 10\text{--}15$ cm. The associated increase of β in the new triplet magnets will make the LHC even more sensitive to quadrupole misalignments as observed in IR8 in 2015. The same misalignment as recorded in IP8, but located in IP1 or IP5 would cause r.m.s. orbit to reach more than 1.5 mm. Therefore, **a similar peak orbit perturbations may be reached already with peak triplet quadrupole positions variations of $3 \mu\text{m}$. In case of a similar assembly for the future inner triplet a precise thermal regulation is needed to overcome this problem.**

5 Orbit perturbations during the squeeze

In this chapter we discuss the orbit stability during the betatron squeeze process. During a change of β^* the optics of the entire interaction region and long straight section is affected. We discuss the feed-down from the quadrupole misalignment to the beam separation at the IP for both the LHC and the HL-LHC case in view of β^* leveling. Options for tracking the beam position in the IP are presented for the squeeze beam process.

5.1 The squeeze process at the LHC

Once the beams are ramped, the β^* at the collision points are brought to their target values during the squeeze process. The squeeze consists of a set of matched optics that provide a stepwise transition between an initial and a final β^* . For the most commonly used squeeze, β^* is lowered. Figure 5.1 shows the evolution of the matching points and of β^* for the 2012

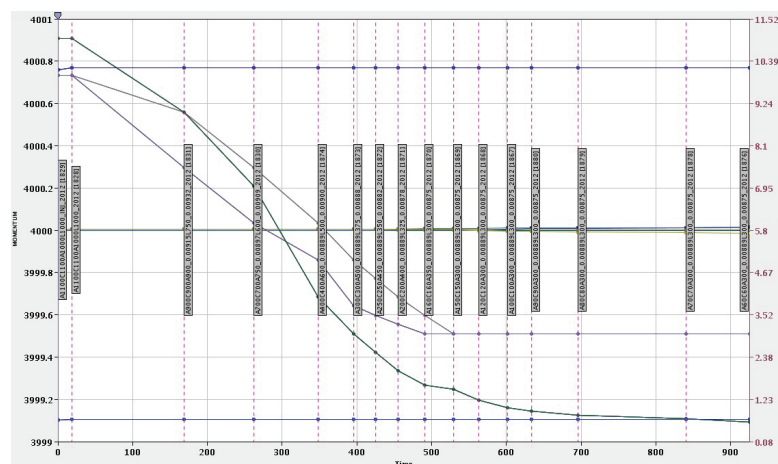


Figure 5.1 – The time evolution of the β^* in the LHC IPs (different color curves, scale on the right) during the Run 1 in 2012. The vertical marks represent the points where the optics is matched to given values of β^* at the IPs.

squeeze. This **2012 squeeze sequence will be used for the simulations presented in this document**. The initial β^* values are 10 m (IP1 and IP5) and 11 m (IP2 and IP8). The final β^* values are 0.65 m (IP1 and IP5) and 3 m (IP2 and IP8). The squeeze consists of 15 matched optic steps. Figure 5.2 illustrates how between 2 matched points the magnet strengths are interpolated. It is done using a parabolic, a linear and a second parabolic segment to ensure that the gradient and current derivations with time are zero at the matched points. The consistency of optics variation between matched points is ensured by imposing the same parabolic segment length for all magnetic circuits.

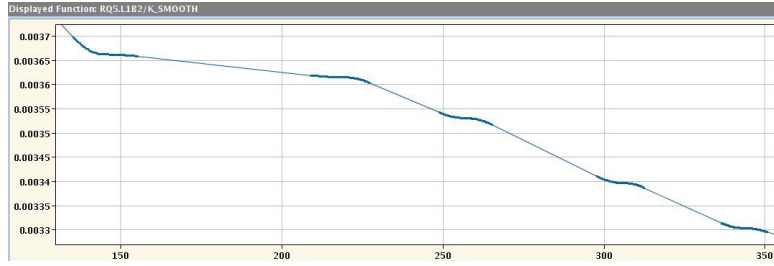


Figure 5.2 – Example of the parabolic segments in the functions to ensure that the gradient and current derivations with time are zero at the matched points.

5.2 Orbit perturbations

When, during the beam squeeze process, the strengths of the quadrupoles in the LHC matching sections change, the orbit response (related to the initial and evolving misalignment) changes as well following Eq. 1.21. Corrections are done to remove orbit perturbations at every optic step if required or continuously with the orbit feedback. The corrections are propagated towards the next optics steps where the impact on the beam orbit may change again.

The general form of the orbit perturbations during squeeze process, based on the initial misalignment and the step-wise corrections propagated through the process is given by [79]:

$$\vec{u}_{ct}^{(i)} = \Delta \mathbf{R}_Q^{(0 \rightarrow i)} \vec{\delta}_Q + \sum_{j=1}^i \Delta \mathbf{R}^{(j-1 \rightarrow j)} \vec{\theta}^{(j-1)} + \mathbf{R}^{(i)} \vec{\theta}^{(i)} \quad (5.1)$$

where the following symbols are used:

- \mathbf{R}^i – the response matrix at the i^{th} matched optics.
- $\vec{\theta}^i$ – the orbit corrector settings corresponding to the i^{th} optics.
- $\Delta \mathbf{R}_Q^{(i-1 \rightarrow i)} = \mathbf{R}_Q^{(i)} - \mathbf{R}_Q^{(i-1)}$ – the change of the quadrupole response matrix related to the gradient change between $(i-1)^{th}$ and i^{th} squeeze point.
- $\Delta \mathbf{R}^{(i-1 \rightarrow i)} = \mathbf{R}^{(i)} - \mathbf{R}^{(i-1)}$ – the change of the corrector response matrix related to the gradient change between $(i-1)^{th}$ and i^{th} squeeze point.

Algorithm and its verification The tool and its detailed calculation methods are described in [79]. To verify the implemented algorithm a series of known cases were computed and compared to MADX, details of the verification can be found in [79, Sec. 2].

5.2.1 Beam position and separation at the IP

For β^* leveling or collide and squeeze a key parameter is the offset between the beams at the IP. The beam position ($\delta_{IP}^{B1, B2}$) at the IP is therefore calculated at every squeeze step as:

$$\delta_{IP}^{Bi} = \frac{u_{BPM,R}^{Bi} + u_{BPM,L}^{Bi}}{2}. \quad (5.2)$$

The beam separation d_{IP} is calculated as shown in Fig. 5.3: is obtained from:

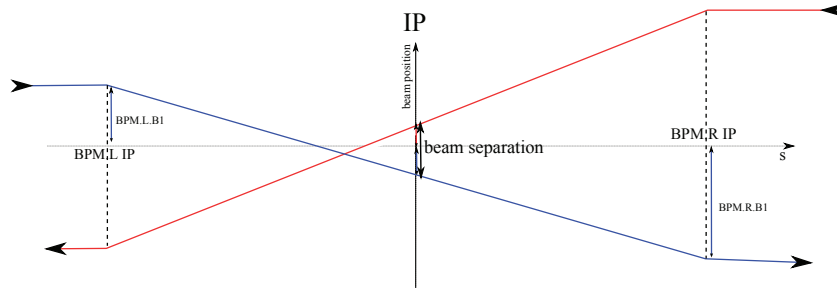


Figure 5.3 – The beam separation is calculated from the adjacent BPMs using equations 5.2 and 5.3.

$$d_{IP} = |\delta_{IP}^{B1} - \delta_{IP}^{B2}| \quad (5.3)$$

Simulation starting point

All the simulations concerning the LHC case presented in this chapter are done for a random misalignment of $\delta_Q^{rms} = 100 \mu\text{m}$. The same value, as used in Chap. 4 allows to compare and scale directly the computation results.

5.3 IP orbit drifts during the squeeze

As a first case and contrary to the LHC Run 1 OFB configuration, all CODs (including the common correctors MCBX) were used for the correction. We consider first the case with perfect BPMs. Figure 5.4a corresponds to a correction with 440 eigenvalues (EVs) and Fig. 5.4b to 501 eigenvalues. Appendix C.1 describes the meaning of the number of eigenvalues, as the calculations described in this chapter will vary depending on the selected eigenvalues. A clear reduction of the IP offsets are observed in Fig. 5.4a and Fig. 5.4b when the number of eigenvalues is increased from 440 to 501. The beam separation **drops from around 2σ** in the

first case to **less than 0.2σ** in the second case. This is logic since we have considered perfect BPMs, the situation can only improve when more eigenvalues are used to approach the best possible correction.

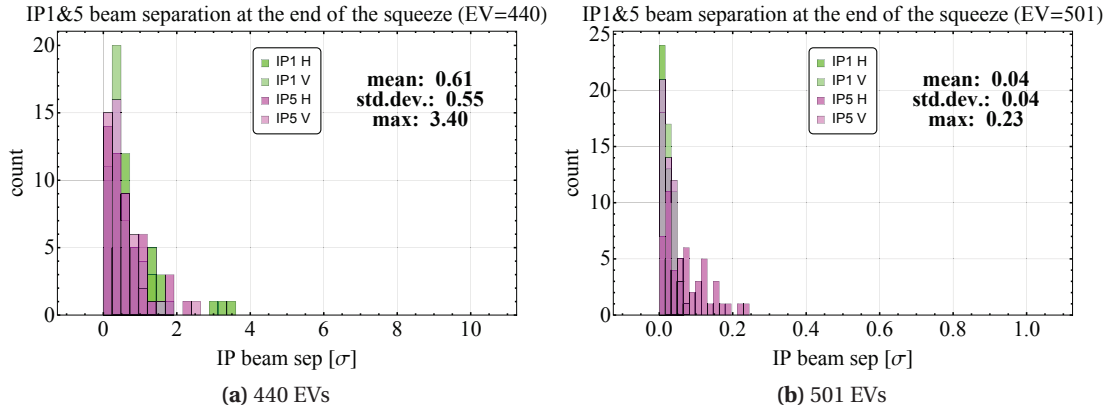


Figure 5.4 – The beam separation at the IPs at the final point of the squeeze for 50 misaligned machines. The four colours represent the horizontal and vertical plane in IP1 and IP5. Since the optics is symmetric (between H and V) and it is the same at both IPs, all values are plotted together. The correction algorithm used MCBX correctors and assumed ideal BPMs. The maximum separation is generally less than 2σ in case of 440 eigenvalues (Fig. 5.4a) and less than 0.2σ for a larger number of eigenvalues (Fig. 5.4b).

In the next step we consider more realistic BPM errors. For the standard LHC button BPMs [80], an overall reproducibility error of **$20 \mu\text{m}$** is assumed. Such an error could apply from one fill to the next. The absolute error between BPM reading and quadrupole magnetic center is larger than $100 \mu\text{m}$. This results in an error on the kicks that are applied to correct the perturbation along the squeeze. The under/over estimated kicks are causing small orbit perturbations that are propagated. In Fig. 5.5b one can observe that the beam separation in IP1 and IP5 (both planes) is increased w.r.t. the ideal BPM case (Fig. 5.4a).

The increase of the separation at the IP is roughly a factor 2 with 440 eigenvalues, from **$3\text{--}4 \sigma$** to around **$6\text{--}10 \sigma$** ¹.

The beam separation for 501 eigenvalues shows a much larger degradation (Fig. 5.5c). The separation of a maximum **0.2σ** with ideal BPMs is degraded to **15σ** . This can be explained by the fact that the inclusion of higher number of eigenvalues leads to a large propagation of the BPM errors on the beam position at the IPs.

Table 5.1 presents the results of the squeeze process analysis. A relation between the initial misalignment, BPM error and the beam offset at the IP (i.e. based on results shown in Fig. 5.5b) is estimated. The following estimates will be used as a reference for the observations and computations discussed later in this thesis.

¹The values correspond to the max value of the majority of cases, excluding the marginal outliers.

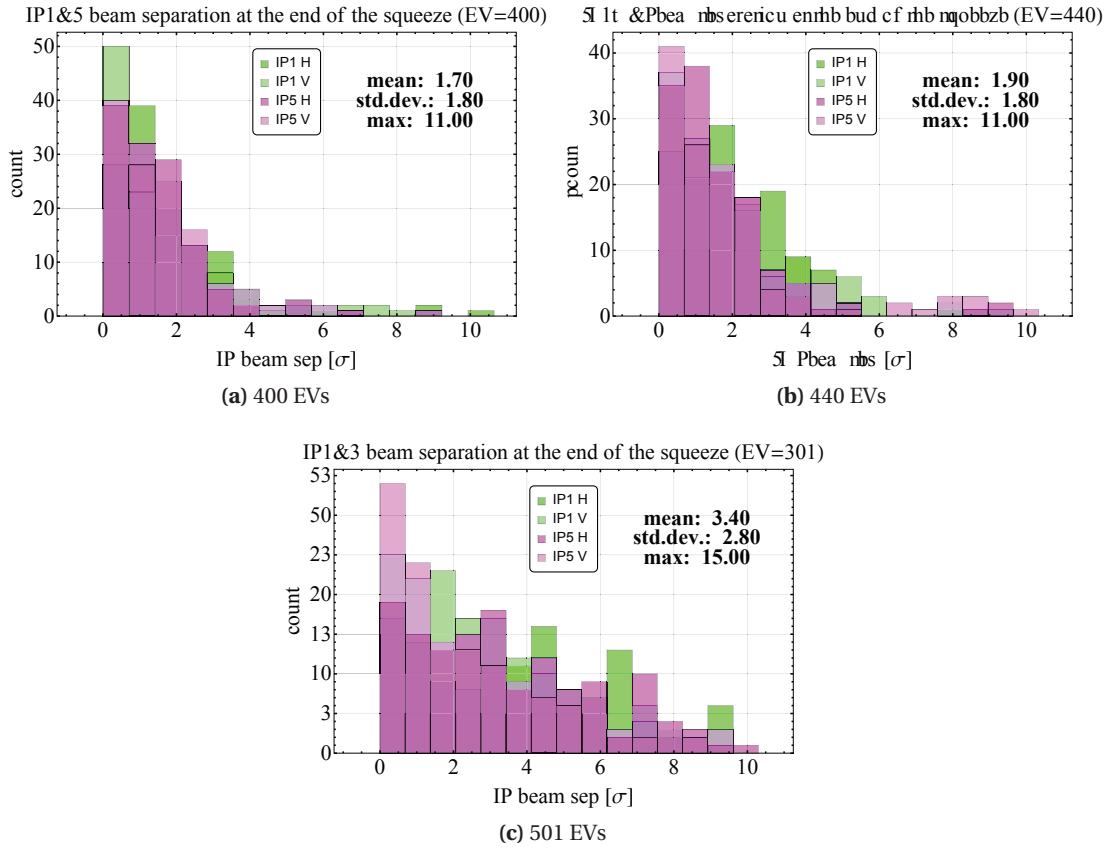


Figure 5.5 – Beam separation at the IPs at the final point of the squeeze for 140 misaligned machines. The four colours represent the horizontal and vertical plane in IP1 and IP5. Since the optics is symmetric (between H and V) and it is the same at both IPs, values are plotted on the same graph. The correction algorithm used all CODs (incl. MCBX) and assumed BPM errors of $20 \mu\text{m}$. The number of EVs used: 400 (a), 440 (b) and 501 (c). For the correction with 400 eigenvalues (Fig. (a)) the maximum separation is less than 11σ , but in most cases it does not exceed $\approx 6 \sigma$. A similar result is obtained when 440 EVs are used for correction (b). For the 501 EVs (c) the separation is increased compared to the previous cases (#400 and #440), reaching up to 15σ .

5.3.1 Impact of BPM errors on the corrections

In this section we discuss the influence of the BPM noise on the final IP beam separation. Noise with flat distribution and r.m.s. of 10,20,50,70 and $100 \mu\text{m}$ was generated for 150 seeds. Two cases of the calculation were performed: excluding the common correctors and including them for the correction, both cases are presented on Fig. 5.7. Calculations were done only using the collision optics ($\beta^* = 65 \text{ cm}$ for IP1 and IP5). One can notice the increase of the beam separation at the IP with increasing the number of eigenvalues used for the correction. Additionally, usage of the MCBXs further increases noise propagation to the IPs.

Figure 5.6 illustrates the distribution of the optimization done during LHC Run 1 in 2012 to

Chapter 5. Orbit perturbations during the squeeze

Initial misalignment δ_Q	BPM errors	Used MCBX	Max d_{IP} ($\sigma = 17 \mu\text{m}$)
100 μm	0 μm	no	5 σ
100 μm	0 μm	yes	2 σ^a
100 μm	20 μm	no	11 σ
100 μm	20 μm	yes	6 σ
100 μm	100 μm	yes	20 σ^b

^aMax value for the majority of cases

^bEstimate obtained only for a limited number of machines

Table 5.1 – The influence of the initial misalignment and BPM errors on the end of squeeze (collision optics) beam separation d_{IP} for the LHC. Different CODs configuration were used, **SVD was ran with 440 eigenvalues**. In bold the values that are used for separation compensations requirements presented later in this document.

bring the beams into collision. The histogram contains data from each **two consecutive fills with time difference less than 12 hours**. On such a small time scale, the impact from the ground motion may be neglected. Taking the spread from the distribution one gets **an average 0.75 σ of separation between two consecutive fills**. This value is highlighted in Fig. 5.7a and **allows us to assess the r.m.s. LHC BPM reproducibility at the level of $\approx 80 \mu\text{m}$** . The latter number is in reasonable agreement with the r.m.s. orbit change from one fill to the next.

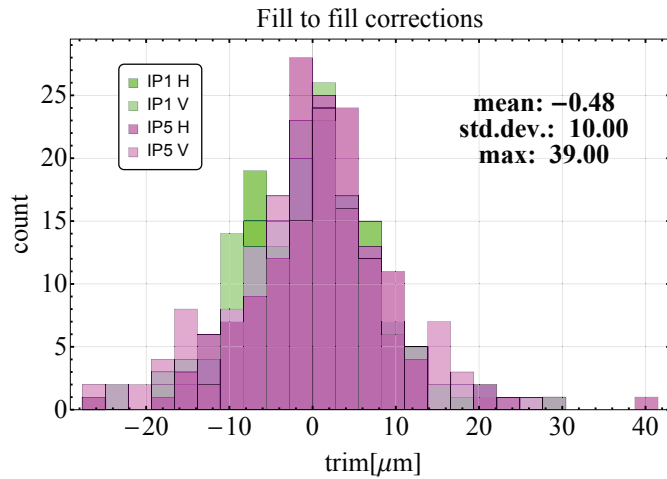


Figure 5.6 – Optimization trims for LHC fills in 2012 that started less than 12 h apart. The trim corresponds to the correction of the beam offsets at the IP.

5.3.2 Correction solutions patterns

The analysis of the orbit evolution throughout the squeeze revealed certain correction structures building up in IP1 and IP5. Figure 5.8 illustrates the corrections accumulated around IPs after squeeze process. The pattern matches the ones presented in Sec. 4.4.3.

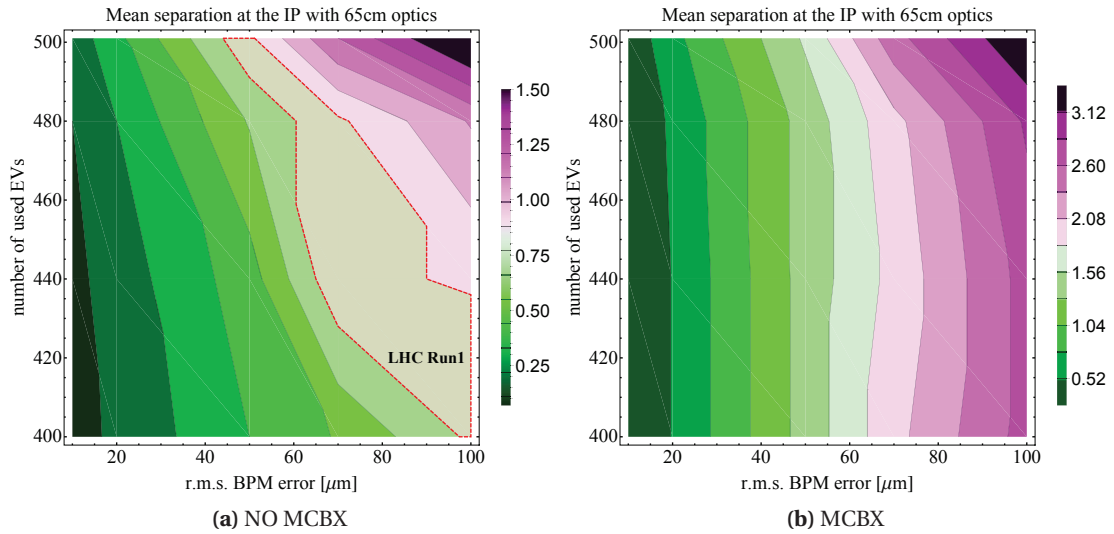


Figure 5.7 – Impact of the BPM errors on the beam separation in beam sigma at the IP as a function of the EV used in correction. (a) contains the marked area (red dotted line) and the label for the estimated LHC working point based on the optimization trims performed on fill to fill basis during LHC Run 1 in 2012.

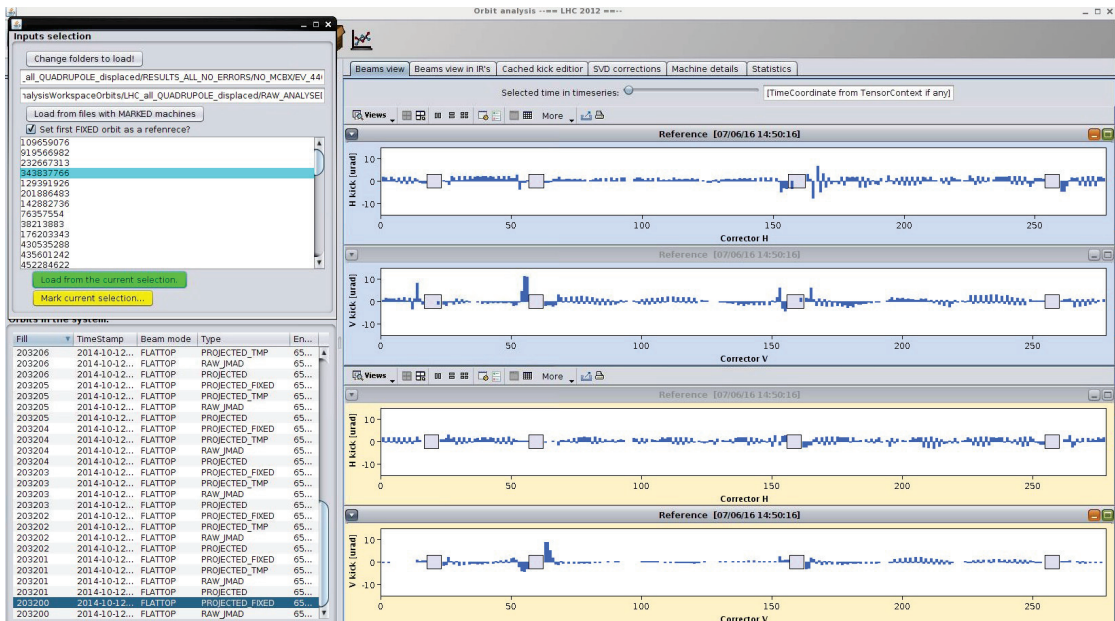


Figure 5.8 – Example of accumulated correction solutions obtained after 14 squeeze steps. Same structures build up as those that can be observed in Fig. 4.5. Calculation was done using no common correctors with 440 EV.

It is likely that the local combination of misalignments around the corresponding IPs generate such solutions. **This conclusion is derived from the fact that in the large set of simulation cases (and misaligned machines) only few of the configurations showed similar structures.**

5.4 LHC Orbit feedback configuration

To understand if the OFB configuration is adequate or if better corrections (w.r.t. beam separation) could be obtained, the simulations (of full squeeze sequence) were repeated by varying the number of eigenvalues. The results are shown in Fig. 5.9 with a rather wide minimum between ≈ 400 and 460 EVs. **The configuration of the OFB with ≈ 440 EVs matches well this minimum.**

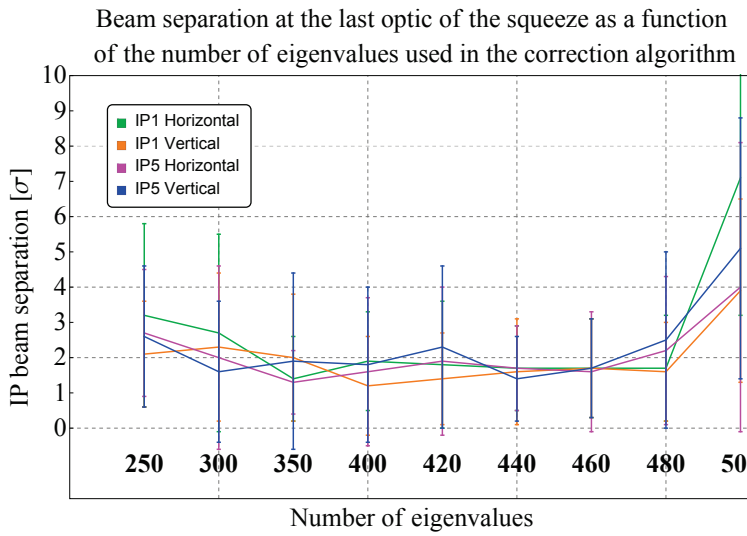


Figure 5.9 – Average separation at the IP at the end of the squeeze as a function of a number of eigenvalues used for correction (BPM errors of $20 \mu\text{m}$). A broad *minimum* is present around 440 values

5.5 IP orbit drifts at the HL-LHC machine

During the long shut down three (LS3, see Tab. 2.3) a complete replacement of the inner triplet magnets is foreseen. The new high field and larger aperture magnets will provide the means to further squeeze β^* by factor of four, resulting in a factor of four larger beta functions in the triplet area. Moreover, the final part of the squeeze is made with adjacent IR quadrupoles (see Sec. 3.6.2). Additionally, the HL-LHC sequence includes of few extra correctors in the interaction regions (one beam correctors) giving a chance for better local correction at the IP. **Therefore the impact on the beam separation at the IP needs to be validated.**

The same algorithms and calculations (as presented in the previous section) were applied to the HL-LHC squeeze. In order to estimate the influence of the correction (number of used EVs) propagation through the squeeze with the **ATS optics we selected 23 matched optics points²**. The **first 15 were regular squeeze points (similar to the current LHC) ranging from**

²we used the HLLHC v1.0 optics

$\beta^*=6\text{ m}$ to $\beta^*=44\text{ cm}$, and remaining **8** were the ATS squeeze points ranging from $\beta^*=44\text{ cm}$ to $\beta^*=10\text{ cm}$. All matched optics correspond to symmetric, round beams.

A set of 120 machines were simulated, with random misalignments for $\delta_Q^{\text{rms}} = 50\ \mu\text{m}$. It was not possible to use the same value as for the LHC ($\delta_Q^{\text{rms}} = 100\ \mu\text{m}$) due to numerical convergence issues for orbit calculations inside MADX.

As a first case, similarly to the LHC case, we simulated a situation with perfect BPMs. The results are shown in Fig. 5.10. We see again that increasing the number of eigenvalues provides

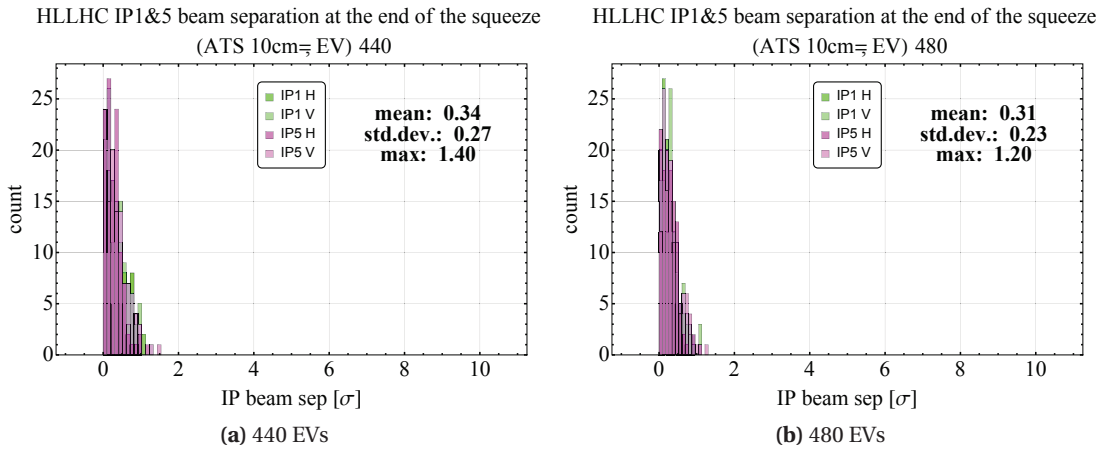


Figure 5.10 – The beam separation at the IPs at the final point of the squeeze for 120 misaligned machines (HL-LHC). The four colors represent horizontal and vertical plane in IP1 and IP5. Since the optics is symmetric (between H and V) and it is the same at both the IPs, all values are plotted together. The correction algorithm used MCBX correctors and assumed ideal BPMs.

better corrections, however, for the MCBX case, the mean of the obtained separation is far beyond values obtained for LHC and reached around $1.5\ \sigma$ for 440 EVs and $1.0\ \sigma$ for 480 EVs.

As for the LHC case, the next step was to include BPM errors in the calculation. Two cases were analysed. The results are presented in Fig. 5.11 for an r.m.s. noise of $20\ \mu\text{m}$.

Based on the simulations shown before, we derive the following relations between initial misalignment, BPM error and beam separation at the end of the squeeze. All the cases with extrapolation to compare with the LHC results (see Tab. 5.1) are listed in Tab. 5.2. **For the HL-LHC, the separation value is \approx four times larger than for the LHC case which actually corresponds to the β^* ratio between the HL-LHC optics and LHC optics.** While, the ATS results indicate the increased separation in a beam size scale, it does not contribute to the accumulated separation in micrometer measure. We can expect **no significant input for the absolute final beams separation is coming from the arc quadrupoles** that are used in the final part of the squeeze.

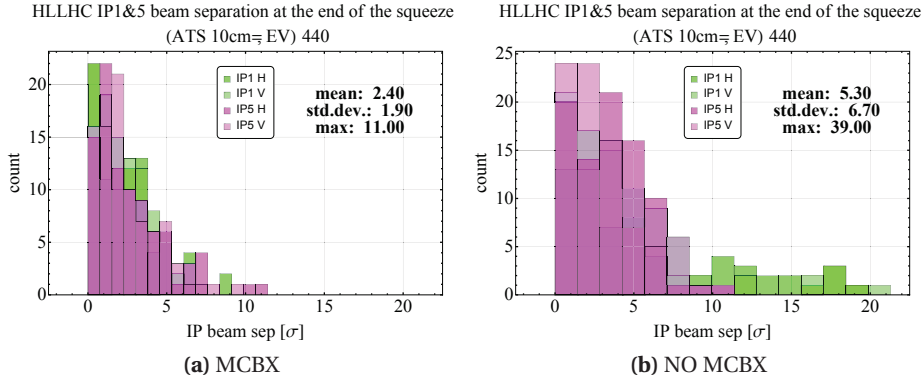


Figure 5.11 – The beam separation at the IPs at the final point of the squeeze for 120 misaligned machines (HL–LHC). The four colors represent horizontal and vertical plane in IP1 and IP5. Since the optics is symmetric (between H and V) and it is the same at both IPs, values are plotted on the same scale. The correction algorithm assumed BPMs with 20 μm error.

Initial misalignment δ_Q	BPM errors	Used MCBX	Max d_{IP} (no ATS) $\sigma = 14 \mu\text{m}$	Max d_{IP} (incl. ATS) $\sigma = 6 \mu\text{m}$
50 μm	20 μm	no	10* σ	25* σ
50 μm	20 μm	yes	5.5 σ	11 σ
50 μm	50 μm	no	14* σ	29* σ
50 μm	50 μm	yes	11 σ	22 σ
Scaled				
100 μm	20 μm	no	20 σ	50 σ
100 μm	20 μm	yes	11 σ	22 σ

Table 5.2 – The influence of the initial misalignment and BPM errors on the end of squeeze (collision optics) beam separation d_{IP} for the HL–LHC. Different CODs configuration were used, SVD was ran with 440 eigenvalues. (*) represents the majority of the data set.

5.5.1 Impact of BPM error on the correction

Figure 5.12 illustrates the impact of the number of eigenvalues for the correction for different BPM noise, here we used 5, 10, 20, 50 and 70 μm . The simulation was ran using the HL–LHC ATS optics with $\beta^*=10 \text{ cm}$. One can see that again, above a certain number of used eigenvalues the BPM error is strongly propagated to the IP separation. **The BPM reproducibility must remain below 10 μm to ensure small error propagation for optics with $\beta^*=10 \text{ cm}$.**

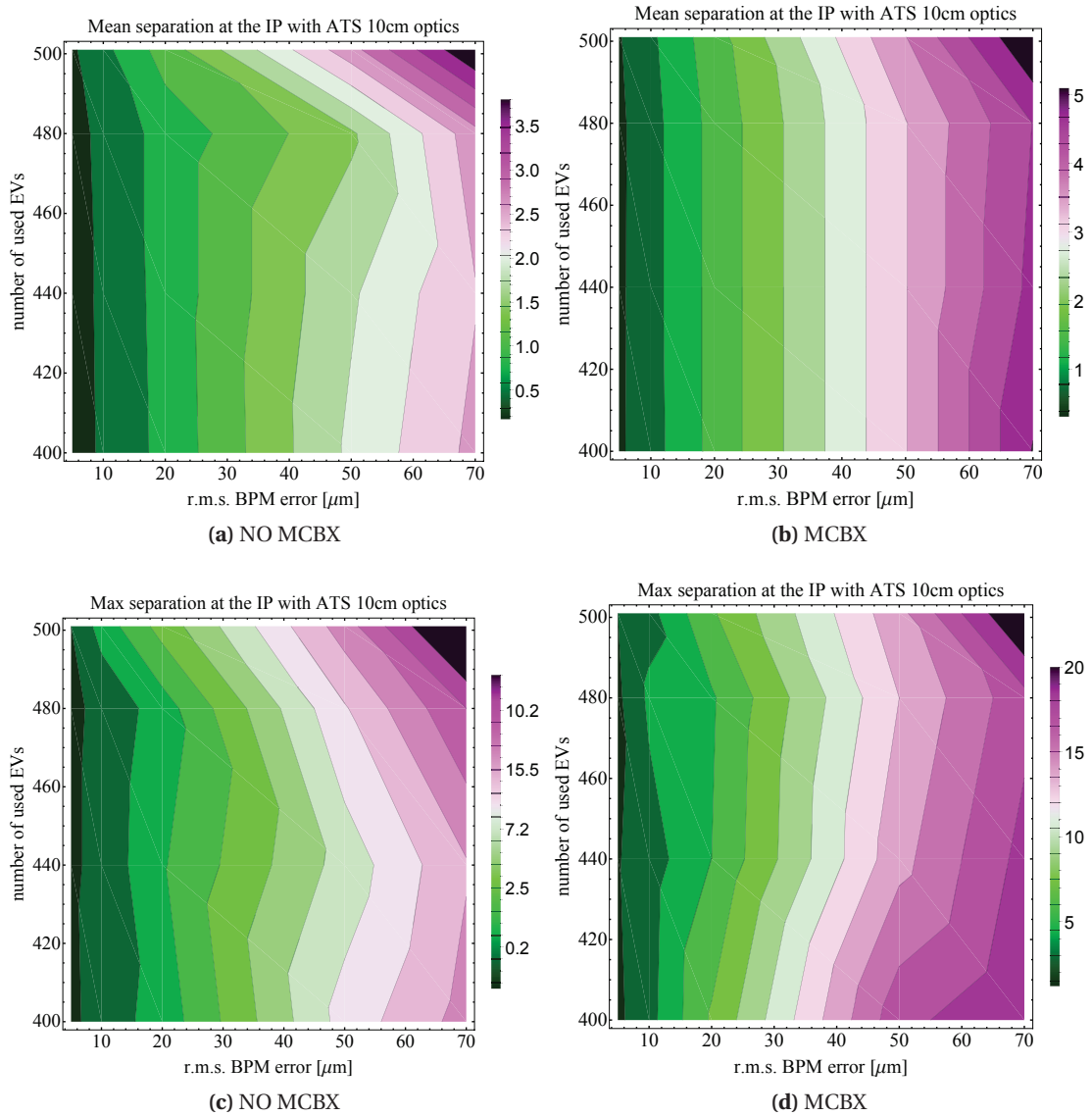


Figure 5.12 – Impact of the BPM errors on the beam separation in beam sigma at the IP as a function of the number of EVs used in the correction. The top row illustrates the mean values obtained in the calculations while the bottom shows the maximum values obtained. Simulations done for ATS optics with $\beta^*=10$ cm. (a) and (b) represent the mean value, (c) and (d) represent the max value

5.6 Conclusions

A model of the beam orbit perturbations occurring during the squeeze was put in place to better understand possible limitations for β^* leveling and collide and squeeze. From the simulations we conclude that:

- The influence of the initial misalignment during a betatron squeeze is important.
- The model for the LHC is in the good agreement with the data that was recorded during Run 1 in 2012. Based on the reconstructed ground motion of $\delta_Q \cong 0.3 \mu\text{m per day}$ (see Chap. 4), we can estimate that the orbit drifts in the squeeze from one fill to the next, should stay well below 0.1σ . **The fill to fill fluctuations of the beam positions at the IPs are dominated by the BPM reproducibility.**
- For the LHC collision optics ($\beta^*=65 \text{ cm}$) **beam offsets will remain below 1σ** for the current feedback configuration with no MCBX and ≈ 400 EVs or for a similar EVs configuration with MCBX, **as long as the BPMs r.m.s. error remains under $30 \mu\text{m}$.**
- For the HL-LHC collision optics ($\beta^*=10 \text{ cm}$) **beam separation larger than 1σ may be caused by BPM error propagation towards the IP if the error r.m.s. exceeds $\approx 10 \mu\text{m}$.**
- For the full HL-LHC ATS squeeze, the error propagation w.r.t. to misalignments will be more sensitive than for the LHC. Assuming a similar maximum ground movement **between the two consecutive fills of $\delta_Q \cong 0.3 \mu\text{m per day}$ the resulting beam separation at the IP reaches $\approx 1 \sigma$ at the end of squeeze.**
- **Including the common region MCBX correctors into the correction algorithm used by the OFB system could significantly reduce the local IR perturbations** when keeping beams colliding over longer periods, but BPM errors may spoil any gain if they exceed $\approx 20 \mu\text{m}$.
- Choosing a **limited number of a eigenvalues used for the OFB system (≈ 440) was a good choice**, regarding noise and BPM error propagation effects (less localized correction when limited number of EVs is used).
- To mitigate the orbit drifts at the IP as described in this chapter, besides using higher resolution BPMs (at the IPs), **a beam stabilization method based on luminosity feedback was proposed and developed.** Chapter 7 describes the concept and first tests of the method.

6 Experiments on collide and squeeze

In this chapter we discuss the results of recent experiments on a squeeze with colliding beams at the LHC. The data recorded during two dedicated machine development (MD) sessions is presented here. Predictions from Chap. 5 are compared to the experiments.

6.1 MD results and long term stability validation

Experiments overview The first MD took place on August 29th 2015. The MD started at 19:00 and finished on August 8th, 2015 at 05:00. Three machine cycles to 6.5 TeV were executed during this MD, corresponding to fills 4292, 4294 and 4295. In the first and the last fill, the beams were brought to the end of the squeeze with collisions in IR1, IR5 and IR8 [66].

The second MD was carried on 8th of November 2015. The development block started at 10:00 and ended at 19:00. Two fills, 4603 and 4604, were used to demonstrate and validate the long term stability with respect to the MD performed in August [67].

The last part of each fill was used to perform some measurements for experimental validation of the novel beam orbit stabilization method described in Chap. 7.

First experiment The first machine cycle of the August MD corresponding to fill 4292 was dedicated to setting up the standard LHC β^* squeeze with collisions in three points (IP1, IP5 and IP8). This setup fill is presented in Fig. 6.1a.

During this fill, the squeeze was executed in steps. At each step, the beam overlap was optimized in all three IPs and a precise reference orbit was recorded for subsequent fills.

For this fill collisions were maintained in all IPs (within 1.5σ) when stepping from one squeeze point to the next, except for one step in IP1 (β^* from 700 cm to 400 cm). That point coincides with an important local orbit correction that was made around IP1 at the time of the squeeze

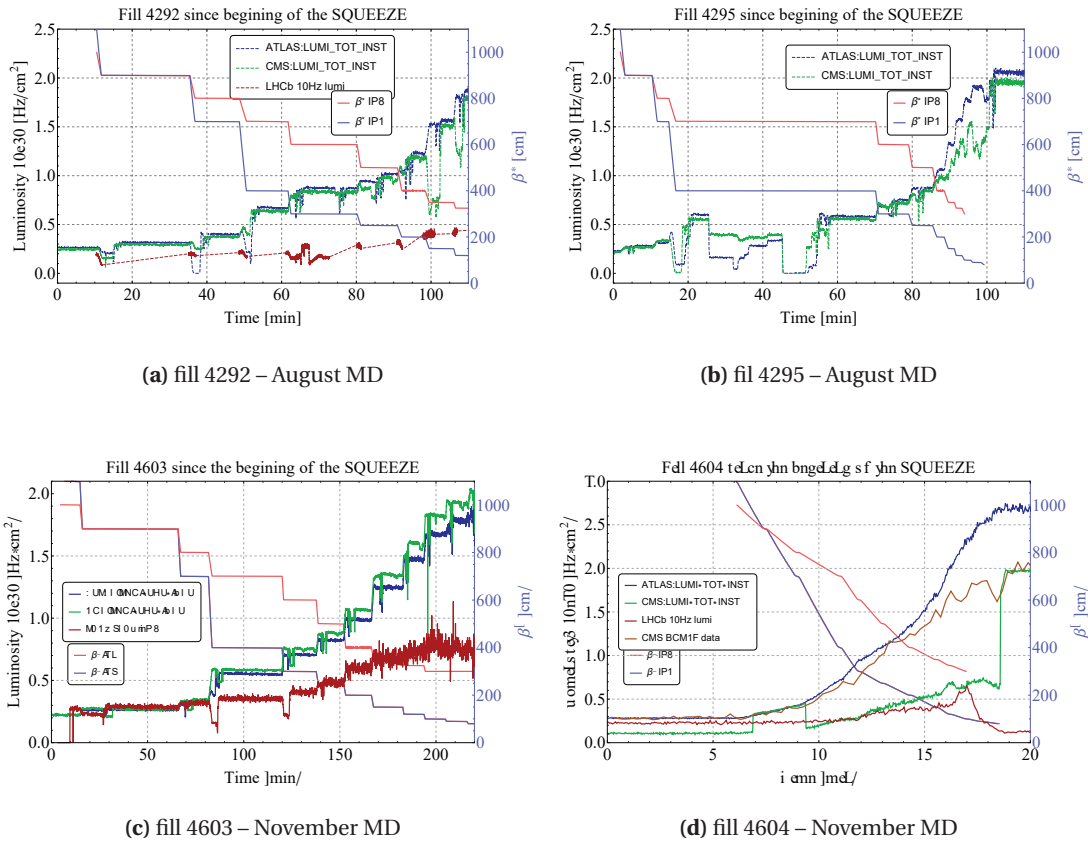


Figure 6.1 – The evolution of the luminosity and of β^* for the 3 colliding IPs. Fig. (a) shows the luminosity recorded during 4292 fill for IP1 and IP5. For IP8 the luminosity is reconstructed from data that was provided at higher sampling rate. Fig. (b) shows only IP1 and IP5 for fill 4295 data with a long stop at β^* of 4 m due to a settings issue[66]. Figs. (c) and (d) illustrate the second MD session on 8th November 2015.

commissioning in April 2015.

During the second fill (4295) the initial idea was to step again through the squeeze using the references established in the previous fill. In the first few steps, however, fine tuning of the reference orbit had to be done again. At the $\beta^*=4 \text{ m}$ step it was realized that an error was introduced in the IP1 settings during the first fill. This resulted in large differences between the reference orbit and the settings, leading to a partial re-separation and luminosity drop at that interaction point. After a short investigation, it was decided to revert all the settings changes that had been done and to restart from scratch (at $\beta^* = 4 \text{ m}$, see Fig. 6.1b). This eventually allowed to reconnect with the reference and settings established in fill 4292 for the other points. As a result the conditions of the first fill could be replayed nicely without significant re-tuning of the beam offsets from that point onwards.

Second experiment on collide and squeeze During the second MD session, the first fill was used to re-establish the reference orbits and validate the long term stability and reproducibility of the settings. As shown in Fig. 6.1c the first fill was only shortly disturbed at the $\beta^* = 9$ m point due to a problem with collimator functions [67].

Fill 4604 was used for demonstration of a collide and squeeze in a single step as time became too short for other studies. As shown in Fig. 6.1d the luminosity increased steadily along the squeeze in all points. The beams remained in HO collisions at IPs 1,5 and 8 within $0.2 \sigma^1$. This is clearly visible on the ATLAS and LHCb data. The CMS data was spoiled by the luminometer calibration that started at the time of the scheduled end the MD.

6.1.1 Orbit control

The initial tests of β^* leveling in 2012, although relatively successful, suffered from orbit reproducibility issues related to the definition of the orbit references [63, 64]. At each optics a new reference was recorded, but such a scheme was complex to maintain and to update, and impossible to move to an operational state.

For the experiments described here, a new approach was used. The reference orbit was defined as a common base orbit with in addition a superposition of bumps for crossing angles and for luminosity optimization. The concept is illustrated in Fig. 6.2.

6.1.2 Collimators and beam losses

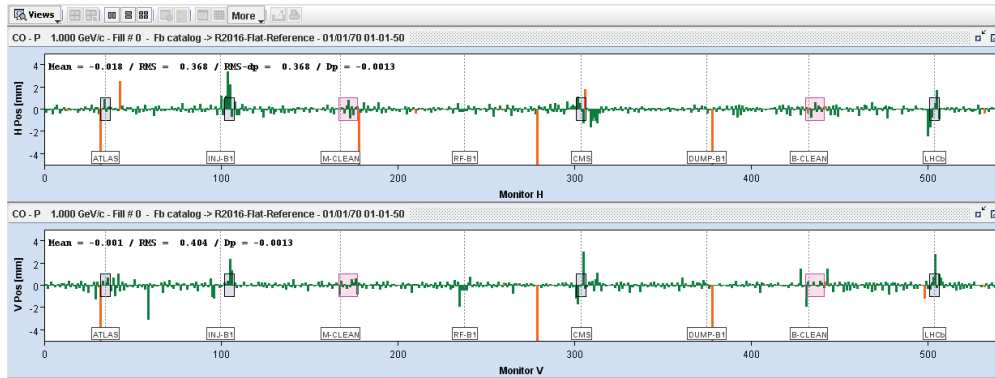
None of the fills of the August and of the November experiments showed any increase of beam losses around the tertiary collimators TCTs around the experiments. This was expected since the orbit deviations were modest and under control (see example in Fig. 6.3a). Regular wire scans (every 30 s) generated small loss spikes but, due to the low number of bunches, that did not have any impact [67]. During the first fill (4603) of the November MD, a mistake in the settings prevented to execute the TCT position functions in steps along the squeeze. Therefore, most of the MD was performed with collimators sitting at settings for 0.8 m. Another error in the settings generation was introduced for a Beam 2 horizontal TCT in IP5. As shown in Fig. 6.3b the beam moved by 1.6 mm w.r.t. the collimator center due to sign error in the programmed position center change.

6.1.3 Beam position at the IP

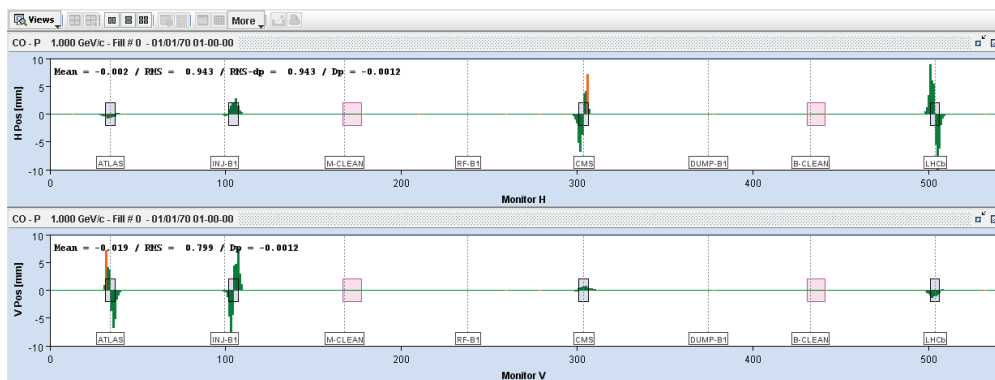
The data of DOROS beam position system [81] installed on the Q1 BPMs of IP1 and IP5 was analysed offline. The ultimate goal was to determine if tracking of the IP separation by interpolation to the IP would be good enough as input for a feedback on the beam offset during β^* leveling. Figure 6.4 presents the data for one of the β^* steps, here for IP5. Figure 6.4b

¹For IP1 and 8 0.2σ , IP5 finished with almost a 1σ separation

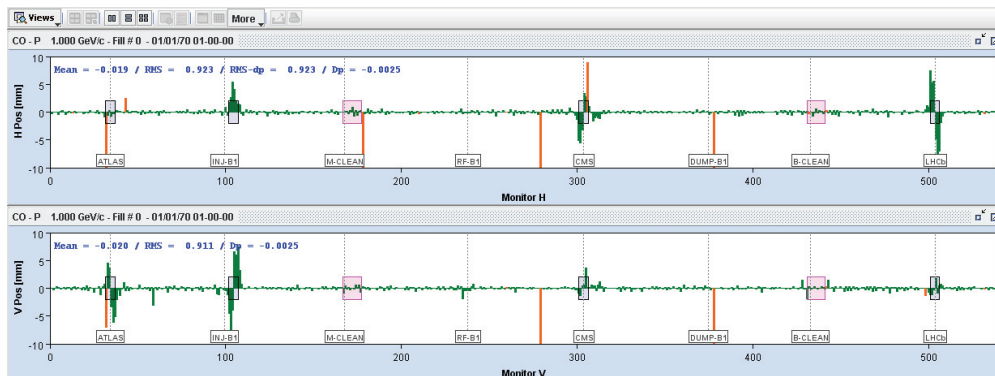
Chapter 6. Experiments on collide and squeeze



(a) Base orbit



(b) Crossing and luminosity optimization bumps



(c) Complete orbit

Figure 6.2 – The reference orbit concept with a base (a), bumps (b) and resulting full orbit (c).

shows the separation of the beams at the IP tracked by DOROS during a β^* change from 7 m to 4 m compared to the separation obtained from a luminosity optimization.

A similar analysis was performed for each step during both cycles. The result of the comparison is presented in Fig. 6.5. In four plots we can see the desired separation margin (1σ , with additional 0.5σ). There is a good agreement between the DOROS interpolation and the beam

6.1. MD results and long term stability validation

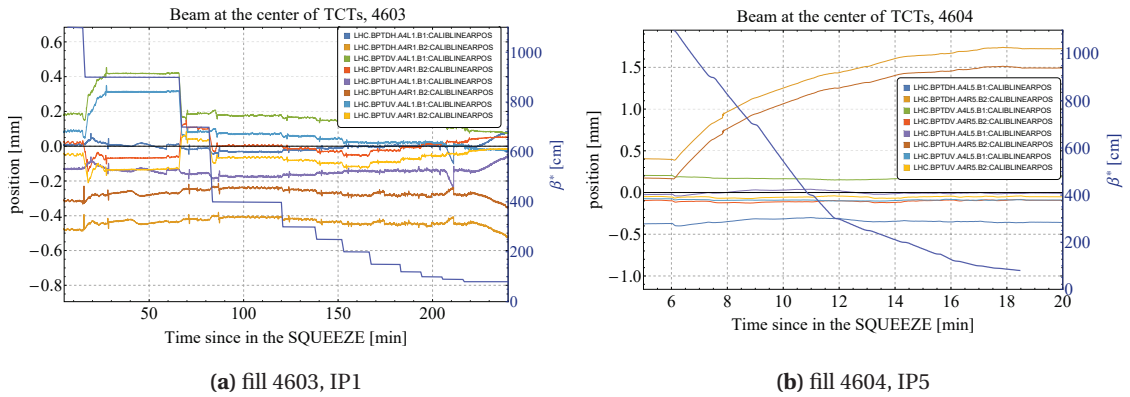


Figure 6.3 – The evolution of the beam position w.r.t. the center of the collimator for IP1 (a) and IP5 (b). The short position excursions (spike-like) visible on (a) correspond to the luminosity optimization scans at each β^* step of fill 4603. (b) The Beam 2 horizontal TCT in R5 developed a more than 1.5 mm beam offset due to incorrect settings generation (the collimators were moved in the wrong direction). The same mistake happened for collimators in IP1 but with much less impact.

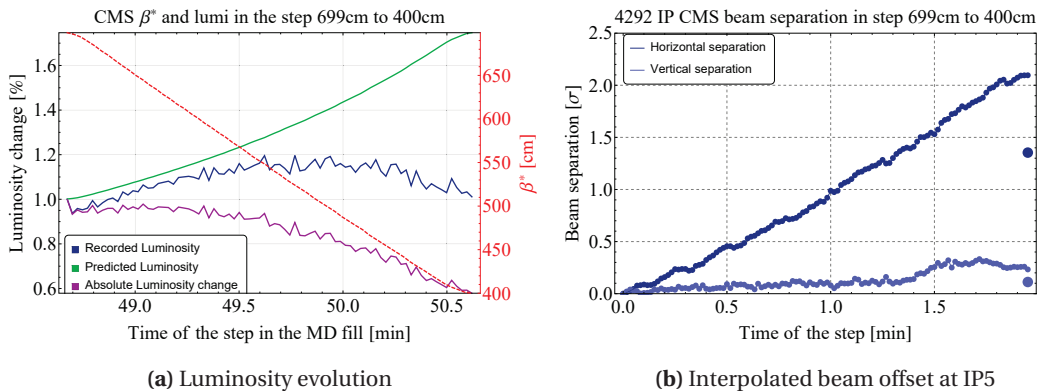


Figure 6.4 – Evolution of the luminosity (a) and of the beam offset at IP5 interpolated from the DOROS data (b) during the β^* step from 7 m to 4 m. Fig. (b) compares the interpolated offset with the result of the luminosity optimization done after the step (•). The DOROS interpolation agrees within 0.5 sigma with the optimization.

offset trims that were found by luminosity optimizations at each step.

The offset tracking comparison of the IP5 data (Figs. 6.5b and 6.5d) is biased by the fact that DOROS data for that IP had to be manually post-processed. This processing was necessary to recover all the data change channels, but it was using data from one BPM electrode instead of two. This could only be done because the relevant information is the relative change of the position

Chapter 6. Experiments on collide and squeeze

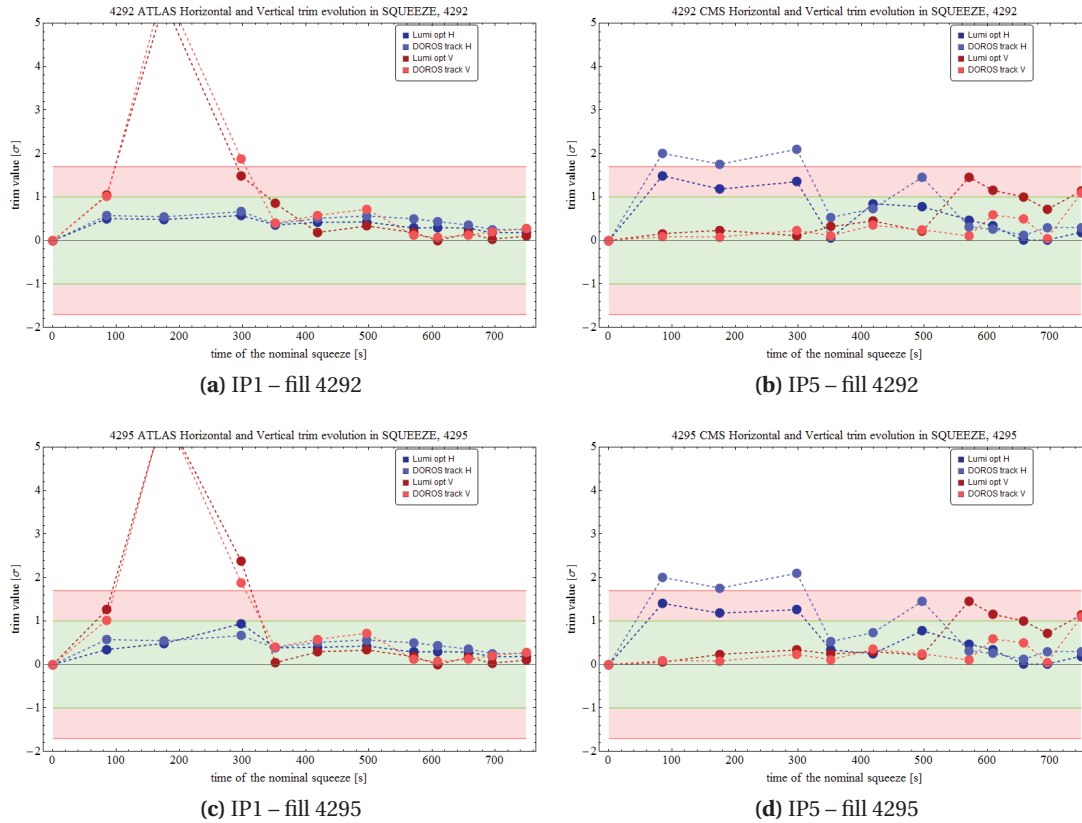


Figure 6.5 – Comparison of the evolution of the beam offsets tracked by DOROS with the offsets reconstructed from the luminosity optimization scans in IP1, (a) and (c), and in IP5, (b) and (d). The time scale refers to the time along the β^* squeeze. The green area corresponds to the 'safe' 1σ separation limit, while the red band corresponds to the more critical region up to 1.5σ [63]. The two cases off the visible scale (in vertical plane) corresponds to the mistake in the function incorporation.

and not its absolute value.

Figure 6.6 illustrates the evolution of beam position and the beam separation at the IPs as measured by DOROS, for the final test of Collide and Squeeze (fill 4604). We can see that at IP1 the separation stayed well below $8\mu\text{m}$ (0.5σ). At IP5, a drift that developed at the beginning of the process caused a significant separation of $>20\mu\text{m}$ ($>1\sigma$). As we will see in Sec. 6.2 the fact of having beams colliding HO (in IP1) will allow us to extract one of the operational parameters, namely the crossing angle. Figure 6.7 illustrates the absolute values of separation knobs that were used during the experiment.

6.1. MD results and long term stability validation

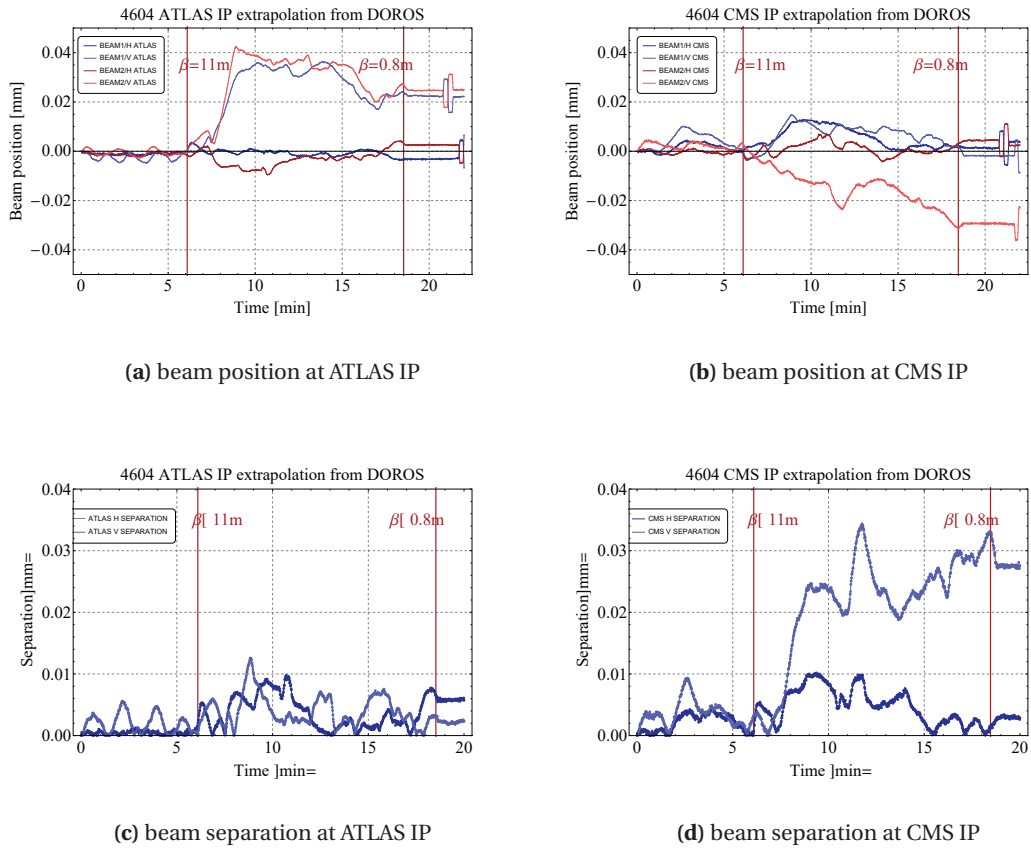


Figure 6.6 – Evolution of the beam positions at the ATLAS (bottom left) and CMS (bottom right) IPs obtained by extrapolation of the DOROS data for fill 4604. The squeeze corresponds to the time interval between the 7th and 18th minute of the plots. A clear separation (of about 1.5σ) developed in the CMS separation plane (d) close to the beginning of the squeeze, mainly driven by a Beam 2 vertical drift (see (b)).

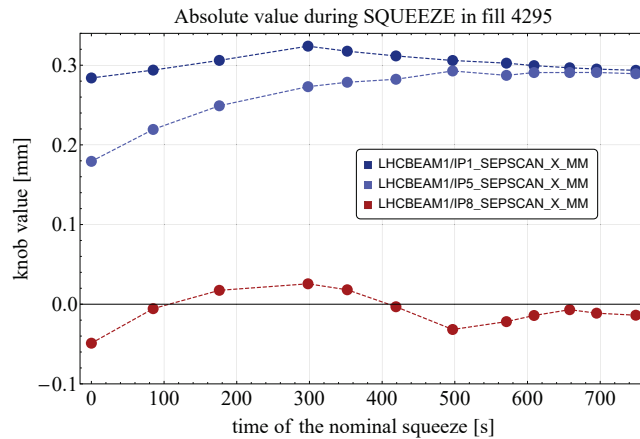


Figure 6.7 – The absolute value for the horizontal separation knob during the experiment in fill 4295.

6.1.4 Long term stability

Over the 70 days time interval between the 2 MDs, the expected maximum r.m.s. quadrupole alignment change² is $\delta_Q = 21 \mu\text{m}$. For such a modest change the beam separation (at the end of squeeze) should **not exceed** 1σ (see Tab. 5.1).

Figure 6.8 shows the relative change in beam separation corrections that were found and applied along the squeeze, with respect to the ones established in the previous August MD. For IP1 and IP5 the results agree well with the expectations. The excursions for IP8 may be related to residual issues with the settings.

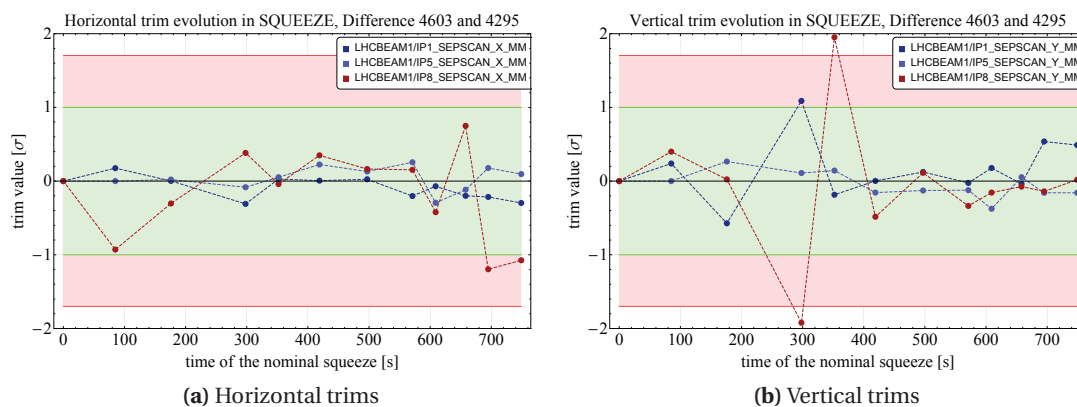


Figure 6.8 – The evolution of the beam separation trims as a function of the time along the squeeze w.r.t. the settings established in August (fill 4295).

²max value for the most active beam and plane, see Chap. 4

6.1.5 Beam emittance evolution

6.1.5.1 Measurement of the emittance

At the LHC two dedicated beam instrumentation devices are able to provide the emittance measurement. Both are installed in IR4, and provide measurements for Beam 1 and Beam 2. The two devices are cross-calibrated one with respect to other.

Wire scanner (WS) For a direct measurement of the beam size (and emittance see Sec. 1.1.1.4) a wire scanner [82] may be used at low intensity. At full energy the wire scanners can only be used with up to 12 nominal bunches to avoid quenching the downstream magnets due to the beam losses.

BSRT A Beam Synchrotron light Telescope (BSRT) [83, 84] is installed on each beam. The telescope images the light emitted by an undulator (low energy) or separation dipole (high energy). It provides a non-destructive measurement of each individual bunch. This instrument allows to track the beam size evolution continuously without any intensity limitations. It is calibrated with the WS at low intensity.

6.1.5.2 Emittance in the squeeze

Profiting from the small number of nominal bunches, a series of consecutive emittance measurements were performed with the wire scanners along the squeezes during the first experiment. The results are presented together with the BSRT measurement in Figs. 6.9a and 6.9b. Within the measurement fluctuations, no emittance growth was observed.

During the second experiment (Figs. 6.9c and 6.9d) no wire scanner measurements were performed during the squeeze. However a calibration of the BSRT was performed by beam instrumentation experts before the squeeze against the WS. Since no emittance growth was observed during the experiment, the emittance data was averaged (Table 6.1). The averaged values have been used for the analysis presented in Sec. 6.2.

	bunch id / slot	Plane	ε [μm]	σ_ε [μm]
Beam 1	#1 / 0	H	2.20	± 0.20
		V	1.90	± 0.06
	#2 / 1785	H	1.70	± 0.22
		V	1.69	± 0.06
Beam 2	#1 / 0	H	1.95	± 0.05
		V	1.85	± 0.04
	#2 / 891	H	1.55	± 0.05
		V	1.60	± 0.04

Table 6.1 – Measured normalized emittances for the squeeze of fill 4604.

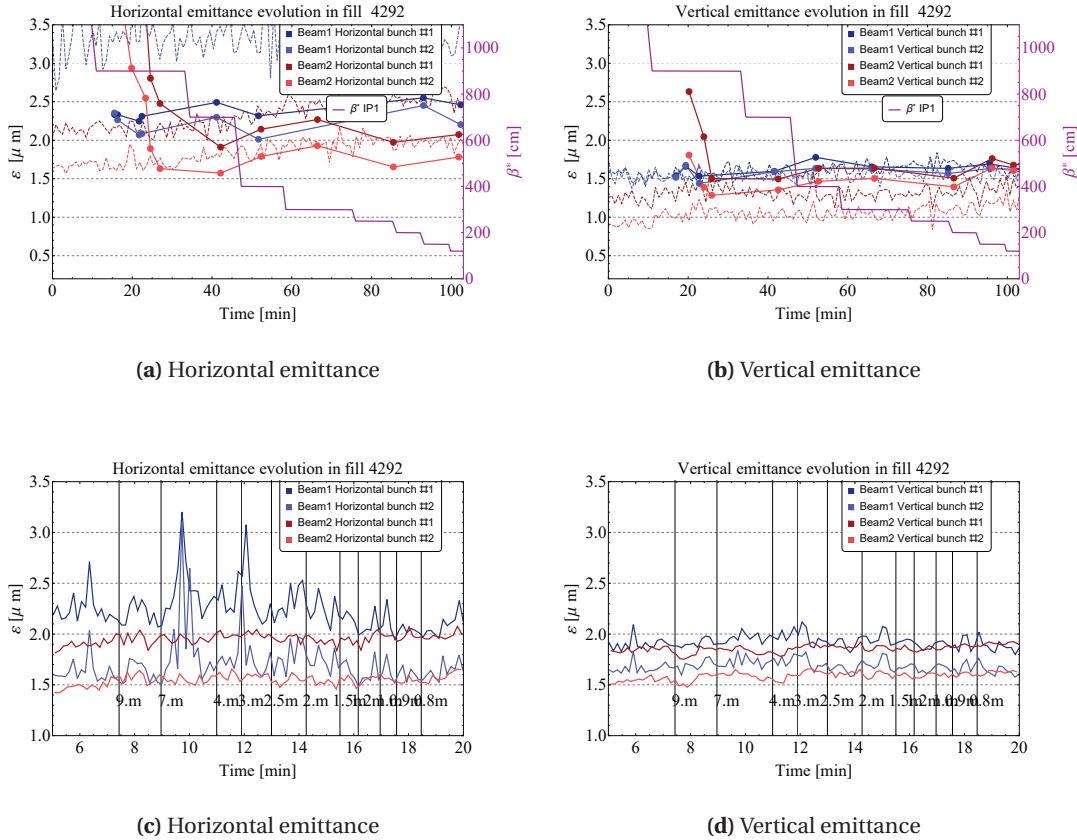


Figure 6.9 – The evolution of the emittance of the two bunches of each beam during the squeeze of fills 4292 and 4604. (a) and (b) compare the WS measurements (dots) with the BSRT data (dashed lines). For fill 4604 (c) and (d) only BSRT was available.

6.2 Measurement of the crossing angle

The fact that the beams were colliding perfectly HO along the squeeze at IP1 provided a possibility to measure the geometric luminosity reduction factor F (and therefore the crossing angle ϕ). Equation 1.36 shows the dependence of F on β^* and the crossing angle ϕ . Since IP1 operates with a vertical crossing angle the corresponding values for the Beam 1 and Beam 2 emittances (listed in Table 6.1) were used.

The actual beam intensity evolution (recorded by the BCT) was included into the analysis as well the betatron function waist shifts at the IPs. The dependence of β^* , the betatron function at the IP, as a function of the longitudinal waist shift is given by:

$$\beta^* = \beta_{nom}^* + \frac{L^2}{\beta_{nom}^*} \quad (6.1)$$

K-modulation measurements of the Q1 quadrupoles revealed that in 2015 the beam waist was systematically shifted by 20 cm with respect to the IP[85, 86]. These corrections were included in this analysis, systematically for all β^* .

For a constant emittance and crossing angle, the factor G :

$$G = \frac{\mathcal{L} * \beta^*}{F * N_1(t) * N_2(t)} = \text{const} \quad (6.2)$$

is expected to be constant. Deviations indicate possible errors of input parameters like ϕ . Figure 6.10 presents the result of the analysis for the ATLAS data that was very reliable. One can observe small deviations from the quasi constant value of the G factor if the betatron function waist shift is not included, especially at small β^* (see Fig. 6.10b).

The results for the estimates of the actual half-crossing angle are shown in Fig. 6.11 and are listed in Table 6.2. Due to the unreliable CMS luminosity it was impossible to reconstruct the crossing angle for IP5. The crossing angle is found to be around 10% larger than the nominal value. The discrepancy can be explained by a scale error of the IR BPMs.

IP	$\phi/2$ [μrad]			Range
	nominal	k-mod	C and S	
IP 1	145	160 ± 1	164 ± 5	$\beta^* < 5m$

Table 6.2 – The half-crossing angle estimate obtained from this collide and squeeze (C and S) MD are compared to the design values as well as to the values measured with K-Modulation [87]. No usable data was recorded in IP5.

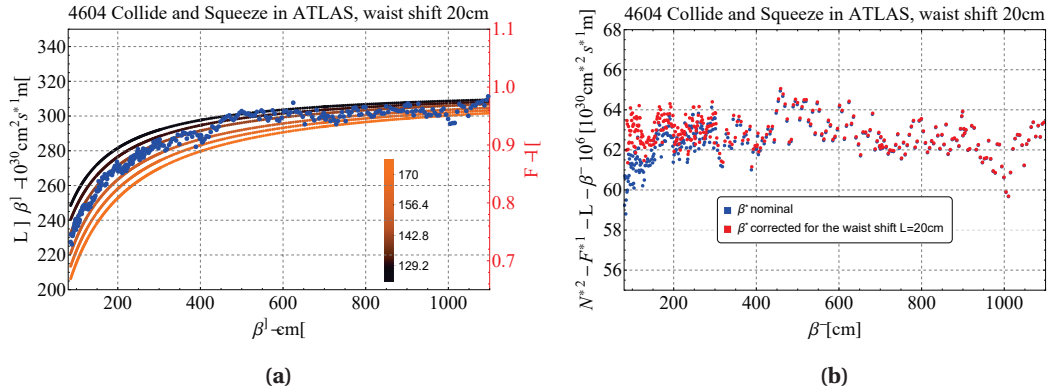


Figure 6.10 – Reconstructed geometric factor (F) in IP1 based on the recorded luminosity data along the squeeze. The data is compared to the model for different values of ϕ in Fig. (a). Figure (b) shows the G factor (Eq. 6.2) as a function of β^* with and without correction of the waist shifts for $\phi = 145 \mu\text{rad}$ [85, 86].

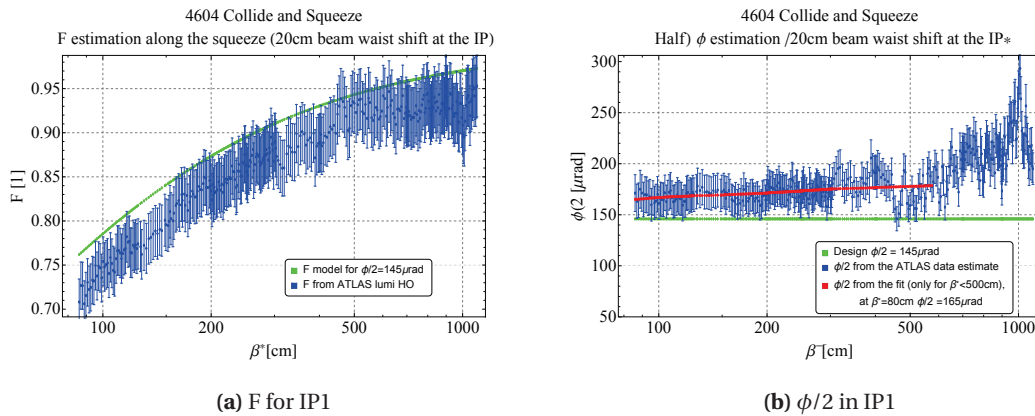


Figure 6.11 – (a) Estimate for the F factor at IP1 as a function of β^* . (b): the half crossing angle in IP1 derived from the F factor evolution. The error bars include 1% relative luminosity error and the errors of the emittance shown in Tab. 6.1 .

6.3 Conclusions

Following the first tests of β^* leveling in 2012 [88, 63] two new experiments were scheduled in 2015 to improve the technical aspects and demonstrate that the LHC control system is mature to operate with β^* leveling or collide and squeeze.

The experiments demonstrated that a collide and squeeze can be setup on the time scale of ten's of hours. A flexible reference orbit incorporating all local bumps required to maintain and reproduce the orbits was successfully tested. The system has been improved during 2015–2016 shutdown, leading also for regular operation to improved orbit control.

The experiments also **showed that the machine stability is sufficient to reproduce collide and squeeze over weeks** while remaining within the beam stability bounds without direct feedback on the beam separation. **The results are consistent with the corrections foreseen by the simulations.**

To ensure that a future collide and squeeze or β^* leveling is operationally robust, feedback on the IP separation must nevertheless be foreseen. The high precision DOROS BPM electronics installed on the BPMs around the IPs is one option and has been verified during the MDs. Another method will be presented in the next chapter.

Profiting from the excellent setup, we managed to reconstruct the crossing angle from the recorded luminosity as a function of β^* . The crossing angle obtained from the measurement is consistent with another measurement (K-modulation of the Q1 quadrupole).

7 IP orbit stabilization with luminosity

In this chapter we discuss a novel method for orbit stabilization at the interaction point with colliding beams. While it is expected that beams may separate by some amount during a β^* leveling step a deliberate modulation of the luminosity provides a means to track and correct the separation. First experimental results are presented. Since the method implies some additional transverse separation, the impact on the orbit effects due to the LR interactions is reviewed as a part of operational validation of the schemes.

7.1 Feedback on the special luminosity modulation

The principle of the method is based on the dependence of the luminosity on beam separation (see Eq. 1.34). It is not possible to deduce the separation from the luminosity itself, since this requires to know beam currents, emittances, optics etc. with very high accuracy. In addition there is an ambiguity on direction of the separation. If the separation is however changed **deliberately**, it is possible to obtain information on the separation by comparing the two luminosity values. This concept may be generalized to a smooth pre-programmed time-dependent separation for which the relative offset of the beams may be inferred in the x-y plane [89].

In order to determine the beam separation and its time evolution a rotation scan of one of the beams is proposed. The initial programmed separation from the other beam, e.g. $\delta = 0.4 \sigma$ is an input parameter of the procedure. The concept of the scan is presented in Fig. 7.1. The direction (α) and the average speed (v_Δ) of the drift ($\Delta(t)$) may be extracted from the recorded luminosity.

7.1.1 Scan phases

As shown in the Fig. 7.1 such a rotation scan involves the following phases:

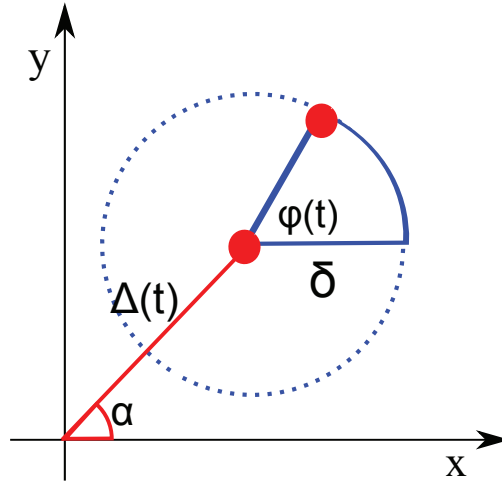


Figure 7.1 – Positions of the beams in the x-y plane. One beam is fixed at point (0,0). The initial position of the second beam corresponds to the point with coordinate α and $\Delta(0)$. The dotted circle represents a full scan of the moving beam around its central position that may drift away as a function of time. The scan properties are the phase $\phi(t)$ and the radius (δ). A possible drift is described by its evolution $\Delta(t)$ under certain angle $\alpha(t)$ in the transverse plane.

1. An initial unknown separation of the beams that may evolve with time $\Delta(t)$.
2. Application of a small initial separation (scan radius δ).
3. Scanning process (few full circles).
4. Removal of the separation (δ).

The recorded luminosity data must be carefully synchronized to the scan position.

7.1.2 Scan description and analysis

Let us consider the beam rotation angle $\phi(t)$ with frequency f and initial phase ϕ_0 as

$$\phi(t) = 2\pi f t + \phi_0 \quad (7.1)$$

The normalized¹ horizontal and vertical positions (at the IP center) may be parameterized as:

$$\begin{aligned} x(t) &= \Delta(t) \cos(\alpha) + \delta \cos(\phi(t)) \\ y(t) &= \Delta(t) \sin(\alpha) + \delta \sin(\phi(t)) \end{aligned} \quad (7.2)$$

where $\Delta(t)$ is the time dependent drift in the transverse plane, and α is the angle of that drift assumed to be fixed for the moment. The time evolution of various parameters is shown in Fig. 7.2a. Figure 7.2b shows the influence of the drift on the scan trajectories in the transverse plane. For the moment, we assume that the unknown drift depends linearly on time with the

¹to the beam size $\sigma(\beta(t))$ as is the case for β^* leveling

7.1. Feedback on the special luminosity modulation

initial separation $\Delta_0[\sigma]$ and drift speed $v_\Delta[\sigma/s]$:

$$\Delta(t) = \Delta_0 + v_\Delta t \quad (7.3)$$

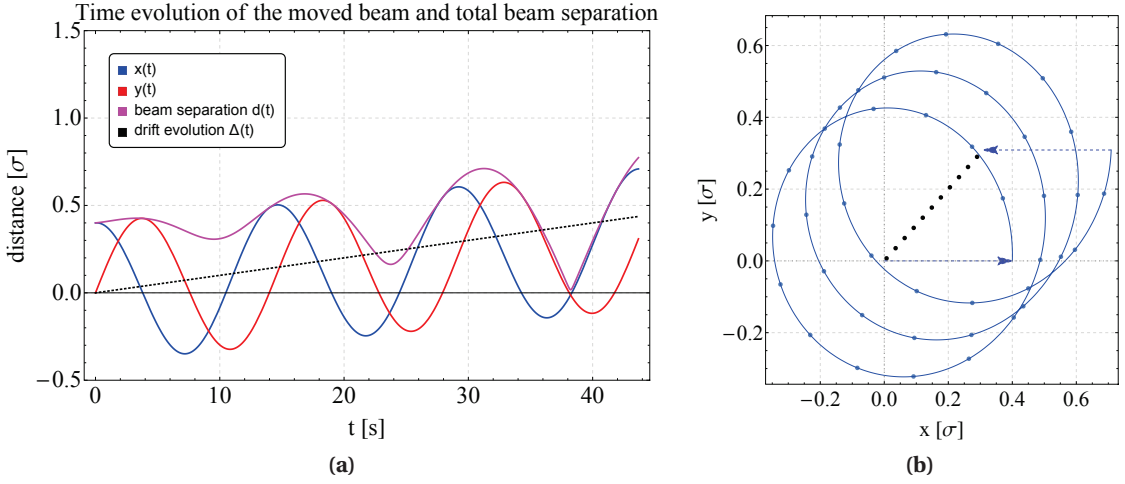


Figure 7.2 – (a) The time evolution of the trajectories (Eq. 7.2) for the horizontal (blue) and the vertical plane (red). The dotted black line illustrates the orbit drift (Eq. 7.3) while the magenta curve corresponds to the total beam separation as a function of time Eq.(7.4). (b) The rotating beam trajectory in x–y plane including the unknown drift (marked with black dots).

If we define as r_i the distance of the i -th beam from the center of the vacuum chamber then by changing the observation frame to the steady beam ($i=1$, as show in Fig. 7.1), the relative beam separation described by Eq. 7.4.

$$\begin{aligned} r_i(t)^2 &= x_i(t)^2 + y_i(t)^2, i = 1, 2 \Rightarrow \\ \vec{d}(t) &= (\vec{r}_1(t) - \vec{r}_2(t)), r_1 = 0 \Rightarrow \\ \boxed{d(t)^2} &= x(t)^2 + y(t)^2 \end{aligned} \quad (7.4)$$

The luminosity (Eq. 1.34) evolution may be expressed as:

$$\begin{aligned} \mathcal{L}(t) &= \mathcal{L}_0 \frac{\beta_0^*}{\beta^*(t)} \exp \left[-\frac{d(t)^2}{4\varepsilon\beta^*(t)} \right] \Rightarrow \\ \frac{\mathcal{L}(t)}{\mathcal{L}_0} &= \frac{\beta_0^*}{\beta^*(t)} \exp \left[-\frac{x(t)^2 + y(t)^2}{4\varepsilon\beta^*(t)} \right] \end{aligned} \quad (7.5)$$

Where we have considered that $\beta^*(t)$ may depend on the time as is the case for β^* leveling. For the next steps, to simplify the expression let us introduce the **normalized scan luminosity**

$\overline{\mathcal{L}_\phi(t)}$ as:

$$\overline{\mathcal{L}_\phi(t)} \equiv \log \left[\frac{\mathcal{L}(t)}{\mathcal{L}_0} \right] - \log \left[\frac{\beta_0^*}{\beta^*(t)} \right] \quad (7.6)$$

the normalized scan luminosity formula then becomes:

$$\overline{\mathcal{L}_\phi(t)} = \left[- \frac{x(t)^2 + y(t)^2}{4\epsilon\beta^*(t)} \right]. \quad (7.7)$$

7.1.2.1 Scan without initial separation

In a first step we consider the case where the initial separation is zero, i.e. $\Delta(0) = 0$. After simple substitution (Eq. 7.7, Eq. 7.2 and Eq. 7.1) and some element grouping we obtain the form:

$$\begin{aligned} \overline{\mathcal{L}_\phi(t)} &= - \frac{\Delta(t)^2 + \delta^2}{4\beta(t)\epsilon} + \frac{2\Delta(t)^2\delta}{4\beta(t)\epsilon} \cos(\alpha - 2\pi f t - \phi_0) \\ &\dots = - \frac{\nu_\Delta^2 t^2 (\delta^2 + 2\delta \cos(-\alpha + 2\pi f t + \phi_0) + 1)}{4\beta\epsilon} \end{aligned} \quad (7.8)$$

$$\boxed{\overline{\mathcal{L}_\phi(t)} = -t^2 \frac{\nu_\Delta^2 (\delta^2 + 1)}{4\beta\epsilon} + t^2 \frac{\nu_\Delta^2 \delta}{2\beta\epsilon} \cos(-\alpha + 2\pi f t + \phi_0)} \quad (7.9)$$

The functional form of the luminosity signal may be cast in the form:

$$f_{\text{fit}}(t) = \underbrace{a_{\text{fit}}}_{\text{offset}} t^2 + \underbrace{b_{\text{fit}} t^2}_{\text{modulation amplitude}} \times \overbrace{\cos(\phi(t) - c_{\text{fit}})}^{\text{modulation}} + d_{\text{fit}} \quad (7.10)$$

The proposed method assumes that n full scans will be performed such that $\phi(t) = 2\pi n$. The drift parameters α and ν_Δ can be extracted from the fit parameters of Eq. 7.10, namely from the amplitude modulation part that is:

$$\boxed{\begin{aligned} \nu_\Delta^2 &= \frac{2\epsilon\beta_0 b_{\text{fit}}}{\delta} \\ \alpha &= \phi_0 - c_{\text{fit}} \end{aligned}} \quad (7.11)$$

7.1. Feedback on the special luminosity modulation

7.1.2.2 Scan with initial beam separation

A generalized form of the luminosity evolution with arbitrary initial offset of the two beams is given by:

$$\overline{\mathcal{L}_\phi(t)} = -\frac{\delta \cos(\alpha) \Delta_x(t)^2 \cos(2\pi f t + \phi_0)}{2\beta\epsilon} - \frac{\delta^2 \Delta_x(t)^2 \cos^2(2\pi f t + \phi_0)}{4\beta\epsilon} - \frac{\delta \sin(\alpha) \Delta_y(t)^2 \sin(2\pi f t + \phi_0)}{2\beta\epsilon} - \frac{\delta^2 \Delta_y(t)^2 \sin^2(2\pi f t + \phi_0)}{4\beta\epsilon} - \frac{\cos^2(\alpha) \Delta_x(t)^2}{4\beta\epsilon} - \frac{\sin^2(\alpha) \Delta_y(t)^2}{4\beta\epsilon} \quad (7.12)$$

At this stage, we assume $\Delta_x(0) \approx \Delta_y(0) \approx d$, therefore the initial separation d becomes an additional free parameter. After expanding and regrouping terms, Eq. 7.12 becomes:

$$\overline{\mathcal{L}_\phi(t)} = -\frac{t^2 v_\Delta^2 (\delta^2 + 2\delta \cos(-\alpha + 2\pi f t + \phi_0) + 1)}{4\beta\epsilon} + \frac{t v_\Delta (x_0 (\cos(\alpha) + \delta \cos(2\pi f t + \phi_0))^2 + y_0 (\sin(\alpha) + \delta \sin(2\pi f t + \phi_0))^2)}{2\beta\epsilon} - \frac{2x_0^2 (\cos(\alpha) + \delta \cos(2\pi f t + \phi_0))^2 + 2y_0^2 (\sin(\alpha) + \delta \sin(2\pi f t + \phi_0))^2}{8\beta\epsilon} \quad (7.13)$$

The generalized form for the luminosity, including an initial separation (here simplified with $\Delta_x = d$ and $\Delta_y = d$) is given by:

$$\overline{\mathcal{L}_\phi(t)} = \frac{d^2(\delta^2 + 1)}{4\epsilon\beta} - t \frac{d v_\Delta (\delta^2 + 1)}{4\epsilon\beta} - t^2 \frac{v_\Delta^2 (\delta^2 + 1)}{4\epsilon\beta} + \left(\frac{2d^2 \delta^2}{4\epsilon\beta} - t \frac{4d v_\Delta \delta}{4\epsilon\beta} - t^2 \frac{v_\Delta^2 \delta^2}{2\epsilon\beta} \right) \cos(-\alpha + 2\pi f t + \phi_0) \quad (7.14)$$

Equation 7.14 is of the general form:

$$f_{\text{fit}}(t) = \underbrace{(a_{\text{fit}0} + a_{\text{fit}1} t + a_{\text{fit}2} t^2)}_{\text{offset}} + \underbrace{(b_{\text{fit}0} + b_{\text{fit}1} t + b_{\text{fit}2} t^2)}_{\text{modulation amplitude}} \times \overbrace{\cos(\phi(t) - c_{\text{fit}})}^{\text{modulation}} \quad (7.15)$$

The drift parameters α , v_Δ and d may be extracted from some of the fit parameters, for example:

$$\begin{aligned} v_\Delta^2 &= \frac{2\epsilon\beta_0 b_{\text{fit}2}}{\delta} \\ d &= \frac{4\epsilon\beta_0 a_{\text{fit}0}}{\delta^2 + 1} \\ \alpha &= \phi_0 - c_{\text{fit}} \end{aligned} \quad (7.16)$$

A global fit of Eq. 7.14 with free parameters v_Δ , d , α provides even better constraints. A simula-

tion of a scan and its analysis are presented in Fig. 7.3.

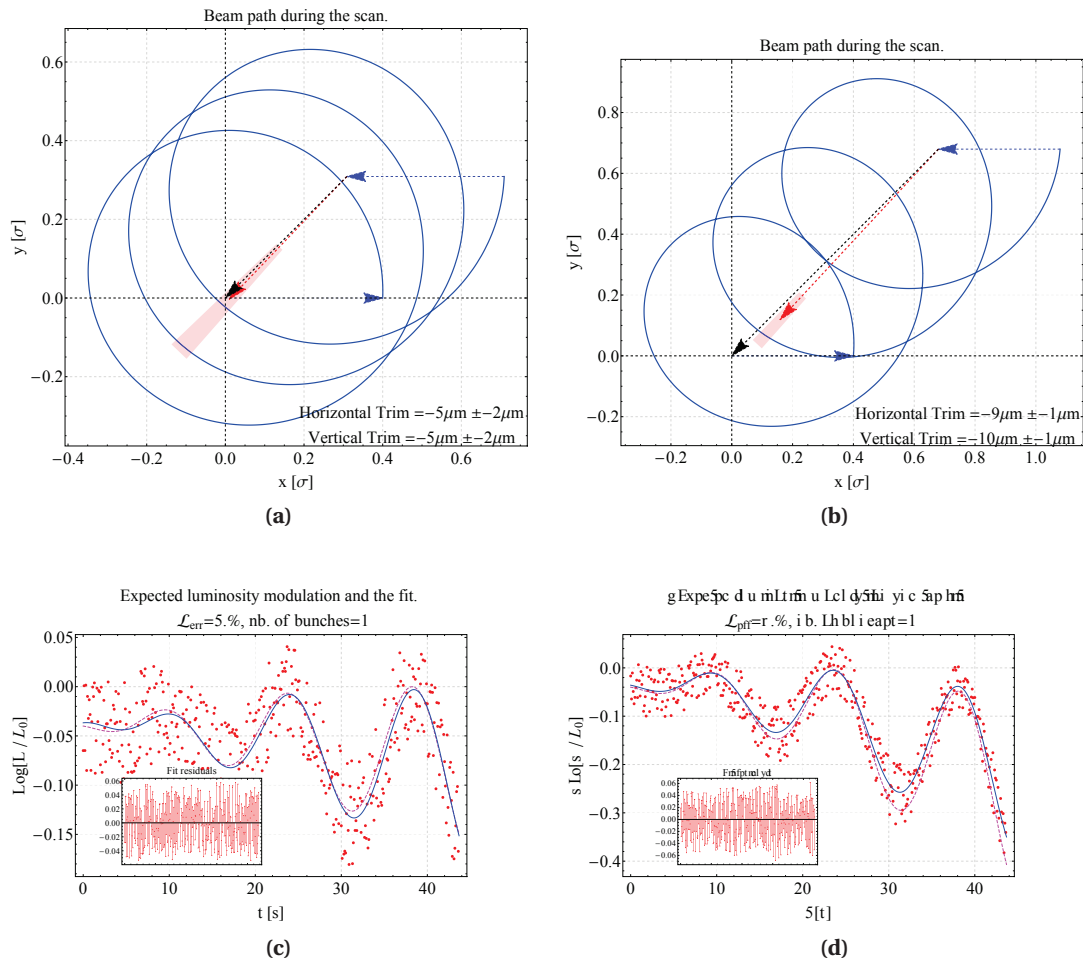


Figure 7.3 – Examples of simulated horizontal (x) and vertical (y) trajectories (top row) and simulated (noisy) luminosity measurements computed from the beam separation during the scans, assuming a statistical accuracy of 5% (bottom row) on the luminosity. The configurations correspond to test cases that were used during beam tests (see Table. 7.1 for: ST#2–left hand side (a) and (c) and for ST#4–right hand side (b) and (d)). The red arrows (top row) correspond to the reconstructed corrections (using eq. 7.11).

7.1.3 Luminosity rate and scan properties

To evaluate the parameters that are required for scans in real machine conditions, a number of cases were simulated with different number of rotations and for various luminosity measurement rates. For a one nominal bunch collision the statistical error on the luminosity is 15% corresponding to $\delta\mathcal{L}^{1b} = 1.5 \times 10^{29}$. The statistical error improves with a square root of the number of colliding bunches yielding an absolute value of $\delta\mathcal{L}^{1000b} = 8 \times 10^{30}$ for 1000 bunches. As shown in Fig. 7.4 **the luminosity rate has an impact on the final computation of the parameters with an optimal value above 5 Hz.**

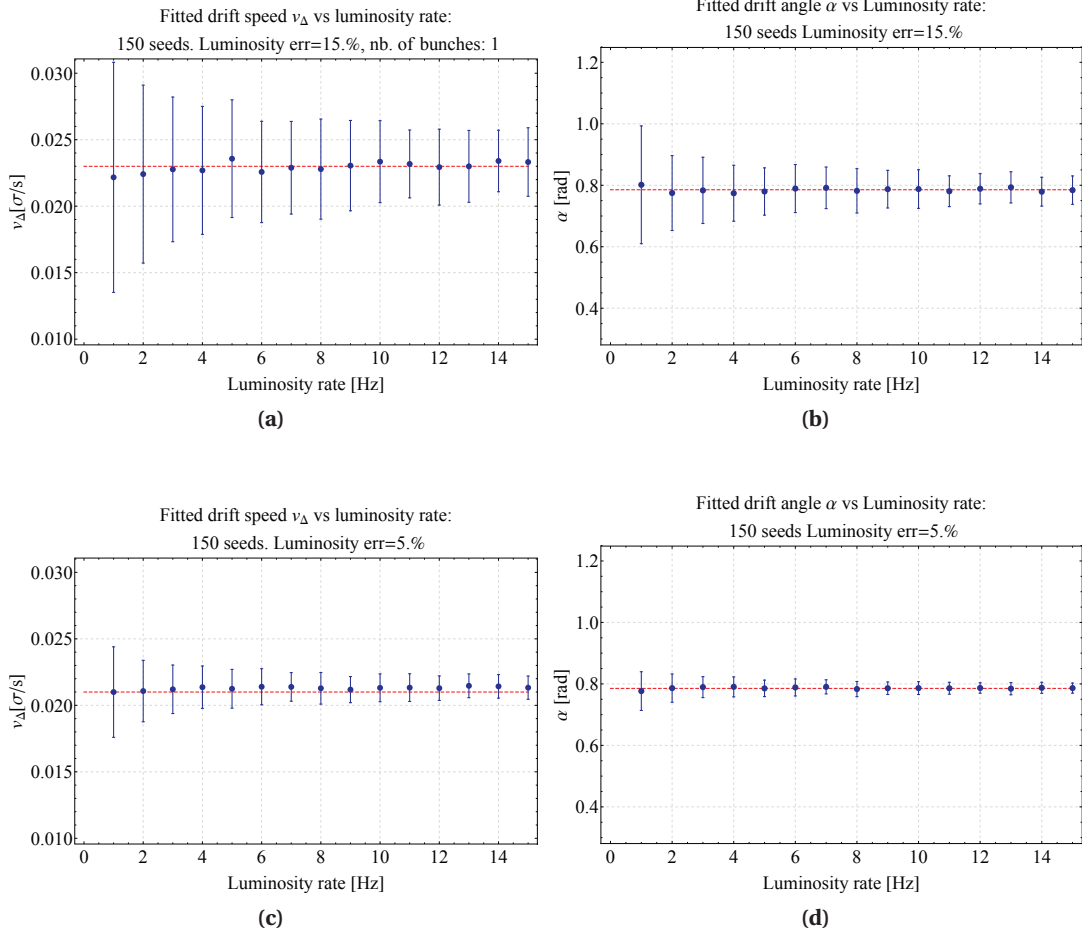


Figure 7.4 – Simulated fit result (for v_{Δ} and α) and its error as a function of the luminosity rate. Luminosity errors of $\frac{\delta\mathcal{L}}{\mathcal{L}} = 15\%$ (top row) and $\frac{\delta\mathcal{L}}{\mathcal{L}} = 5\%$ (bottom row) were assumed. 150 random seeds were used for a total scan time of 60 s (three rotations). Red lines represent the input values used in the simulation.

7.2 Experimental validation of the stabilization method

7.2.1 Validation scenarios and assumptions

To qualify the method for operation and understand the practical aspects, a series of measurements were carried in different MDs. To validate the method **a known drift was superimposed on the actual scan**. Functions combining increasing separation (known α and v_{Δ}) and the actual rotation (see. Eq. 7.2) were prepared and executed. Appendix C.3 describes the tool that was used for function generation and presents some examples. Table 7.1 lists all scans with their type id (ST) and the parameters that were used in 2015. The times when the scans were executed are shown in Table 7.2.

scan id	IP	nb of rotations	scan radius (δ)		frequency f [Hz]	total length [s]	drift X&Y	
			[σ]	[μm]			[σ]	[μm]
ST#1	IP8	3	0.4	16	1/20	55	0.05	3
			0.55			55	0.07	
ST#2	IP1		0.4	11	1/16	52	0.05	2
			0.55			52	0.07	
ST#3	IP8	3	0.4	16	1/20	60	0.3	13
			0.55			60	0.4	
ST#4	IP1		0.4	11	1/14	48	0.3	9
			0.55			48	0.4	
ST#5	IP5	2	0.4	11	1/10	36	0.8	15
			0.55			36	0.8	

Table 7.1 – The settings for IP1, IP5 and IP8 scans executed in the fills 4292, 4295, 4603 and 4604. The difference in the scan radius between the generated and used scan is due the fact that the actual emittance was much smaller than the value that was used for the generation. The last column represents the artificial separation at the end of the scan. Values in bold are normalized to the actual emittance.

To ease the experiments, the settings were prepared based on the following assumptions:

- The artificial drift that was superposed on the scans ranged from $0.5 \sigma / \text{min}$ to $1 \sigma / \text{min}$. The magnitude of the known drift was deduced from the simulations described in the Chap. 5 and ranged between $3 \mu\text{m}$ and $15 \mu\text{m}$, never exceeding 1σ of separation.
- It was assumed that at the start of the test the beams are colliding HO. A case with initial offset was however successfully handled as will be presented later.
- The maximum **duration for the step was set to 60 s^2** to be "compatible" with a collide and squeeze. For β^* leveling a step could be longer if needed since the duration of the leveling step is uncritical and may be stretched in time.

²see the squeeze steps description in Sec. 5.1

7.2. Experimental validation of the stabilization method

- A constant drift speed is assumed over the duration of a scan (during one scan - multiple rotations performed). The validity of this approximation was confirmed by the collide and squeeze experiments (see Sec. 6.1.3).
- The rotation speed and the initial scan radius were chosen such that the maximum beam separation (i.e. scan radius and the drift) would not exceed 1.4σ to match the Landau damping stability criterion (see Sec. 1.3.2).
- For the separation bump correctors, a maximum deflection rate of change of $1\ \mu\text{rad/s}$ was assumed for designing the scan and the superposed drift.

	fill nb	LHC Beam	Scan Type	Time from SB [min]	UTC Time
MD2 August	4292	Beam 1	ST#1	149.19	19:04:08.0
		Beam 2	ST#1	151.27	19:06:10.0
		Beam 1	ST#2	152.24	19:07:08.0
		Beam 2	ST#2	155.99	19:10:53.0
	4295	Beam 1	ST#2	110.9	02:16:18.0
		Beam 2	ST#2	112.3	02:18:30.0
MD3 November 8th	4603	Beam 1	ST#4	248.14	15:09:30.2
		Beam 1	ST#4	268.24	15:29:36.0
		Beam 1	ST#4	281.98	15:43:20.2
		Beam 1	ST#4	290.68	15:52:02.0
		Beam 2	ST#2	264.18	15:25:32.2
		Beam 2	ST#2	284.69	15:46:03.2
		Beam 1	ST#3	66.82	15:54:54.2
		Beam 2	ST#3	83.90	15:37:49.2
		Beam 2	ST#3	86.15	15:57:24.8
		4604	Beam 1	ST#4	33.04
	Beam 2		ST#2	34.44	19:06:29.4
	Beam 2		ST#5	36.24	19:08:17.5

Table 7.2 – List of scans performed during the MD blocks. SB – Stable Beams.

7.2.2 Tests without collisions

To evaluate the scan concepts a series of dry runs were performed without beam. Initially, power converters were set into the so-called *simulation mode* (no current is actually applied to the magnets) for the tests. This was done to verify that the LHC control system accepts the generated functions regarding operational limits (current acceleration and ramp rate limits).

In a second phase the scans were tested at injection energy (without collisions). The scan was tracked with the BPMs surrounding the IP. Figure 7.5 illustrates the results from the first beam rotations at the IP1. A significant noise is due to the BPMs used to interpolate the beam position to the IP center, as they are of standard type (BPMSW) with known $20\ \mu\text{m}$ precision.

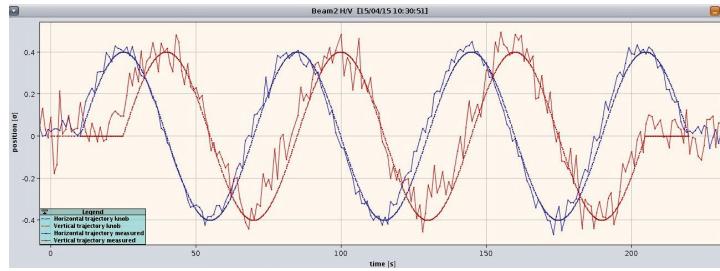


Figure 7.5 – Traces of the beam movement measured by the standard LHC BPMs installed next to the Q1 quadrupole, in blue the horizontal position and in red the vertical position.

7.2.3 First experimental tests

This section presents the results of all tests performed in a first session, corresponding to fills 4292 and 4295. The filling scheme consisted of 2 nominal bunches per beam with colliding pairs in IP1, IP2, IP5 and IP8 (one pair per IP). The normalized emittance was $\epsilon_n = 2.5 \mu\text{m}$. Table 7.3 presents the results of the experiments.

	fill nb	LHC Beam	Scan Type	Applied drift [H, V] [μm]	reconstructed drift [H, V] [μm]
MD2 August	4292	Beam 1	ST#1	[2, 2]	[3, 3I] \pm [n/a]
		Beam 2	ST#1	[2, 2]	[3I, 3I] \pm [n/a]
		Beam 1	ST#2	[2, 2]	[3, 5] \pm [2, 4]
		Beam 2	ST#2	[2, 2]	[5, 1] \pm [5, 1]
	4295	Beam 1	ST#2	[2, 2]	[6, 3] \pm [1, 1]
		Beam 2	ST#2	[2, 2]	[-1, 3] \pm [3, 1]

Table 7.3 – The scans performed during MD2 and their results. For IP8 data (ST#1) due to the noise on the recorded signal it was impossible to finalize the analysis.

7.2.3.1 Scans at IP1

Two sets of scans were performed during fills 4292 and 4295. The analysis was performed using the 3 Hz data provided by the ATLAS BCM group. The recorded luminosity is shown in Fig. 7.6 for the entire duration of each fill. The detailed fit result are shown in Fig. 7.7.

As can be seen on the figures, the luminosity data is very noisy, and the fit results differ substantially from the expectations.

7.2.3.2 Scans at IP8

For the scans of IP8, a direct 10 Hz luminosity transmission from the LHCb control room to the CCC was tested for the first time (see App. C.5). Figure 7.8 illustrates the results. One can see that the signal is too noisy to obtain reliable results.

7.2. Experimental validation of the stabilization method

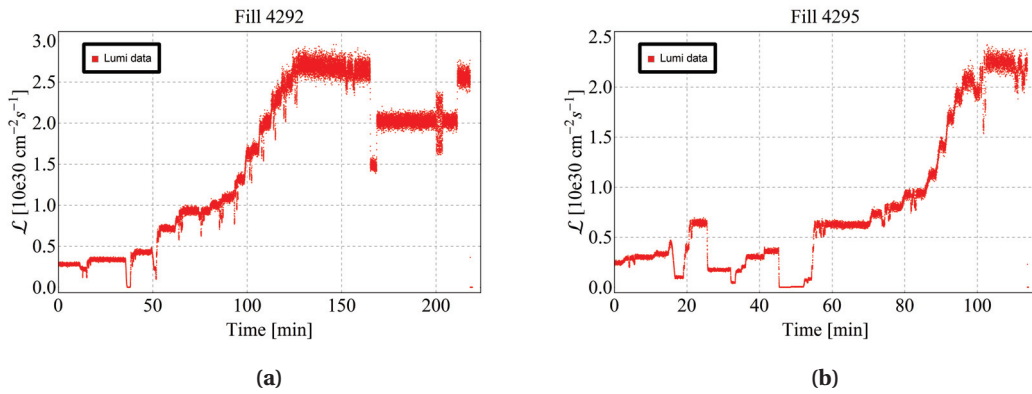
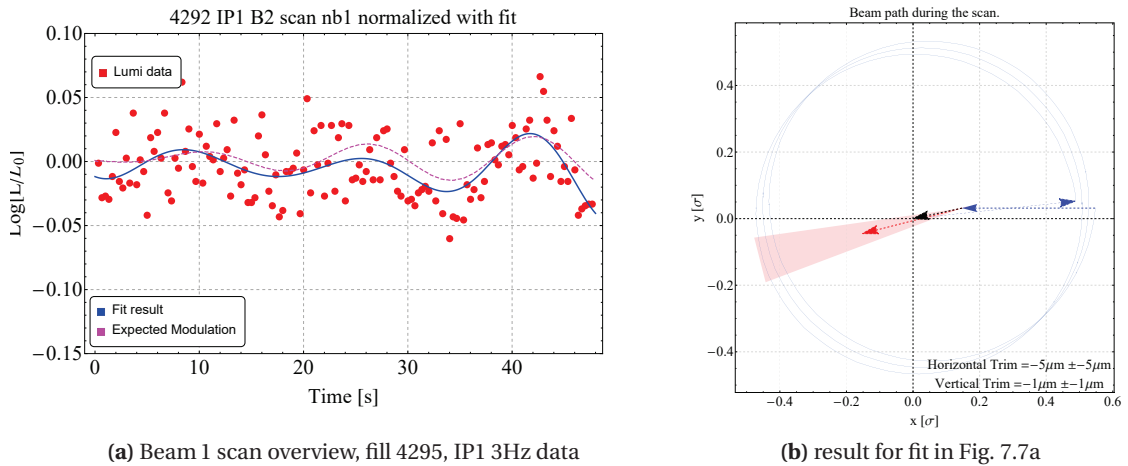


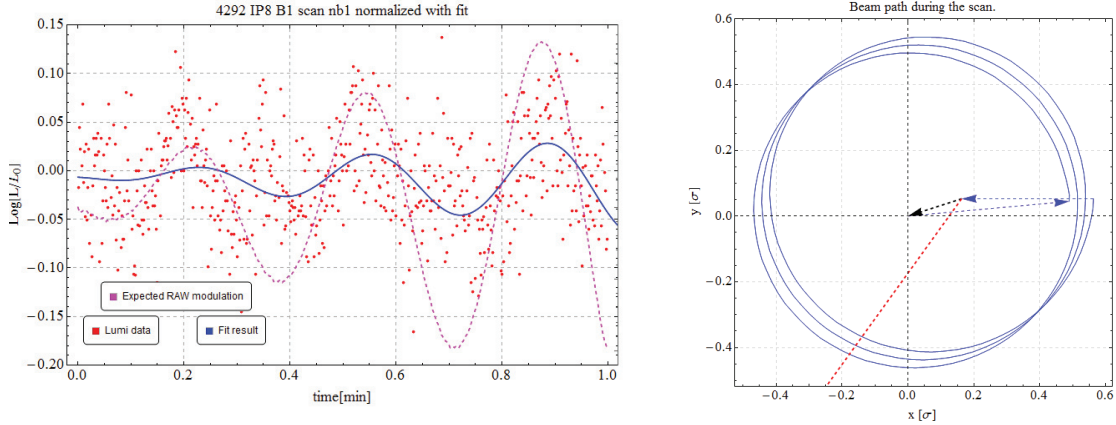
Figure 7.6 – Luminosity data recorded at 3 Hz in IP1 during fills 4292 (a) and 4295 (b).



(a) Beam 1 scan overview, fill 4295, IP1 3Hz data

(b) result for fit in Fig. 7.7a

Figure 7.7 – Examples of the scan test with Beam 1 (b) in IP1 with 3 Hz data. The blue curve represents the fit to the experimental points, the dotted magenta curve is the expected luminosity modulation. Right hand side shows the result of the fit.



(a) Beam 1 scan, fill 4292, IP8 10 Hz data

(b) result for fit in Fig. 7.8a

Figure 7.8 – Examples of the scan test results of Beam 1 (a) in IP8 with 10 Hz data. The blue curve represents the fit to the experimental points, the dotted magenta curve is the expected luminosity modulation. Right hand side plot shows the result of the fit. Due to the noise on the luminosity, the predicted corrections are not accurate.

7.2.4 Second experimental test

This section presents the results of all tests performed with beam scans during the second experiment. Table 7.4 lists the final results of the scans. The following subsections detail the experiments for the two IPs, the results as well as the test conditions. Section 7.4 presents an overview of the DOROS BPM electronics performance. The filling scheme consisted again of 2 nominal bunches per beam with colliding pairs in IP1, IP2, IP5 and IP8 (one pair per IP). In both fills the normalized emittance was $\varepsilon_n = 2.5 \mu\text{m}$, which resulted into slightly larger scan radii expressed in beam size.

	fill nb	LHC Beam	Scan Type	Applied drift [H, V] [μm]	Reconstructed drift [H, V] [μm]
MD3 November 8th	4603	Beam 1	ST#4	[9, 9]	[3, 7] \pm [2, 4]
		Beam 1	ST#4	[9, 9]	[4, 6] \pm [6, 4]
		Beam 1	ST#4	[9, 9]	[8, 6] \pm [4, 3]
		Beam 1	ST#4	[9, 9]	[3, -9] \pm [3, 1]
		Beam 2	ST#2	[2, 2]	[2, 4] \pm [2, 5]
		Beam 2	ST#2	[2, 2]	[1, 2] \pm [3, 9]
		Beam 1	ST#3	[13, 13]	<i>n/a</i>
		Beam 2	ST#3	[13, 13]	<i>n/a</i>
	Beam 2	ST#3	[13, 13]	<i>n/a</i>	
	4604	Beam 1	ST#4	[9, 9]	[8, 9] \pm [2, 2]
		Beam 2	ST#2	[2, 2]	[7, 1] \pm [3, 2]
		Beam 2	ST#5	[15, 15]	[8, 2] \pm [5, 5]

Table 7.4 – Scan parameters of second tests and results. (*n/a*) is for the scans disturbed by the orbit drifts that occurred in IP8, see details in Sec 7.2.4.2.

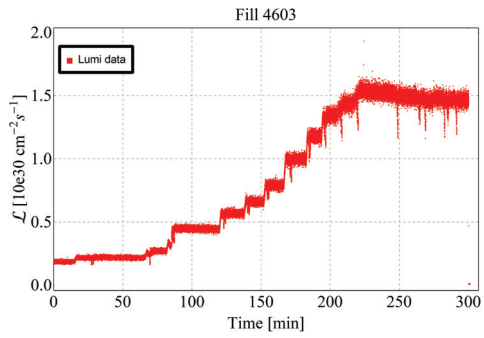
7.2.4.1 Scans at IP1

All the tests at IP1 used the 3 Hz luminosity data provided off-line by the ATLAS BCM group. Figure 7.9 illustrates the entire period with zooms on the selected scans for fills 4603 and 4604.

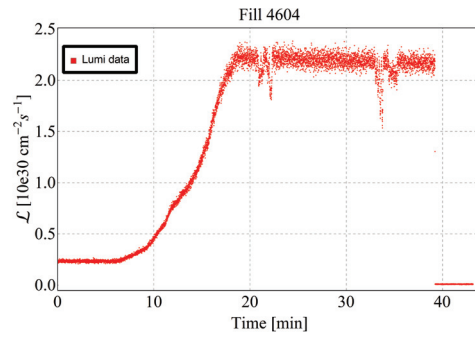
During the first attempt (fill 4603), after finishing the collide and squeeze we managed to perform multiple tests including Beam 1 and Beam 2 scans with different scan speeds and different imposed drifts. A series of promising scans was executed with Beam 1 (Figs.7.10a to 7.10d). Beam 2 tests were only executed with modest drifts (see later Fig. 7.10e) due to issues with some PC ramp rates. Consequently it is more difficult to extract the drift parameters given the very low luminosity.

A second set of scans (end of fill 4604) were only performed for Beam 1 since the problem of the generation limits for Beam 2 persisted. The results are illustrated in Fig. 7.11.

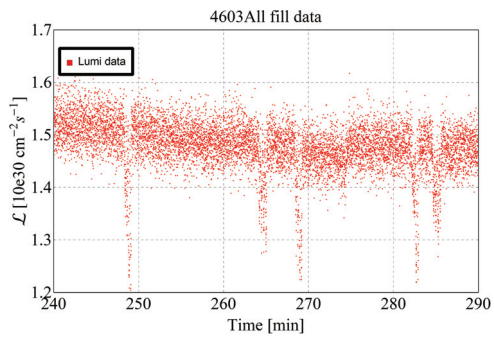
Chapter 7. IP orbit stabilization with luminosity



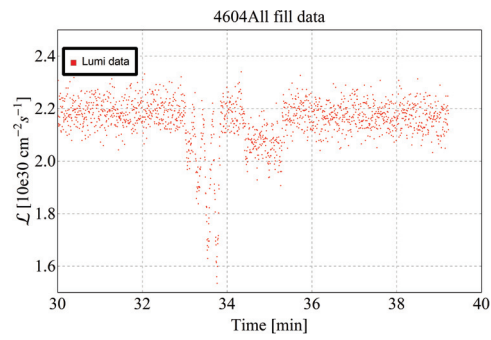
(a) Recorded luminosity during fill 4603



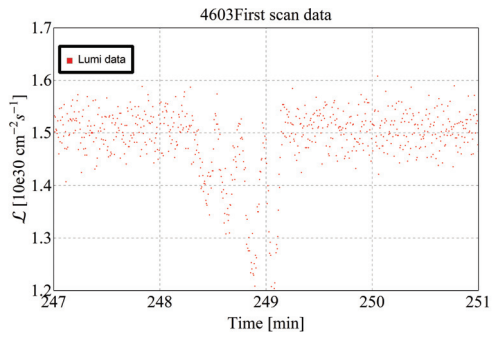
(b) Recorded luminosity during fill 4604



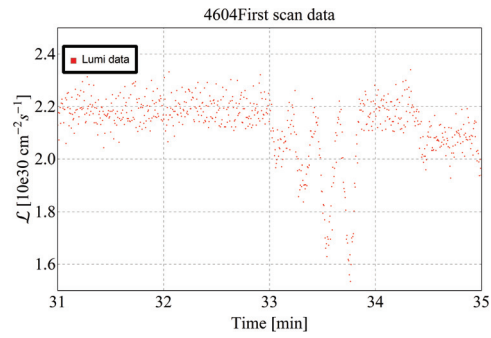
(c) Zoom of the luminosity, for scans in fill 4603



(d) Zoom of the luminosity, for scans in fill 4604



(e) Zoom of the 1st scan in fill 4603



(f) Zoom of the 1st scan in fill 4604

Figure 7.9 – The IP1 3 Hz luminosity data for fills 4603 (left) and 4604 (right).

7.2. Experimental validation of the stabilization method

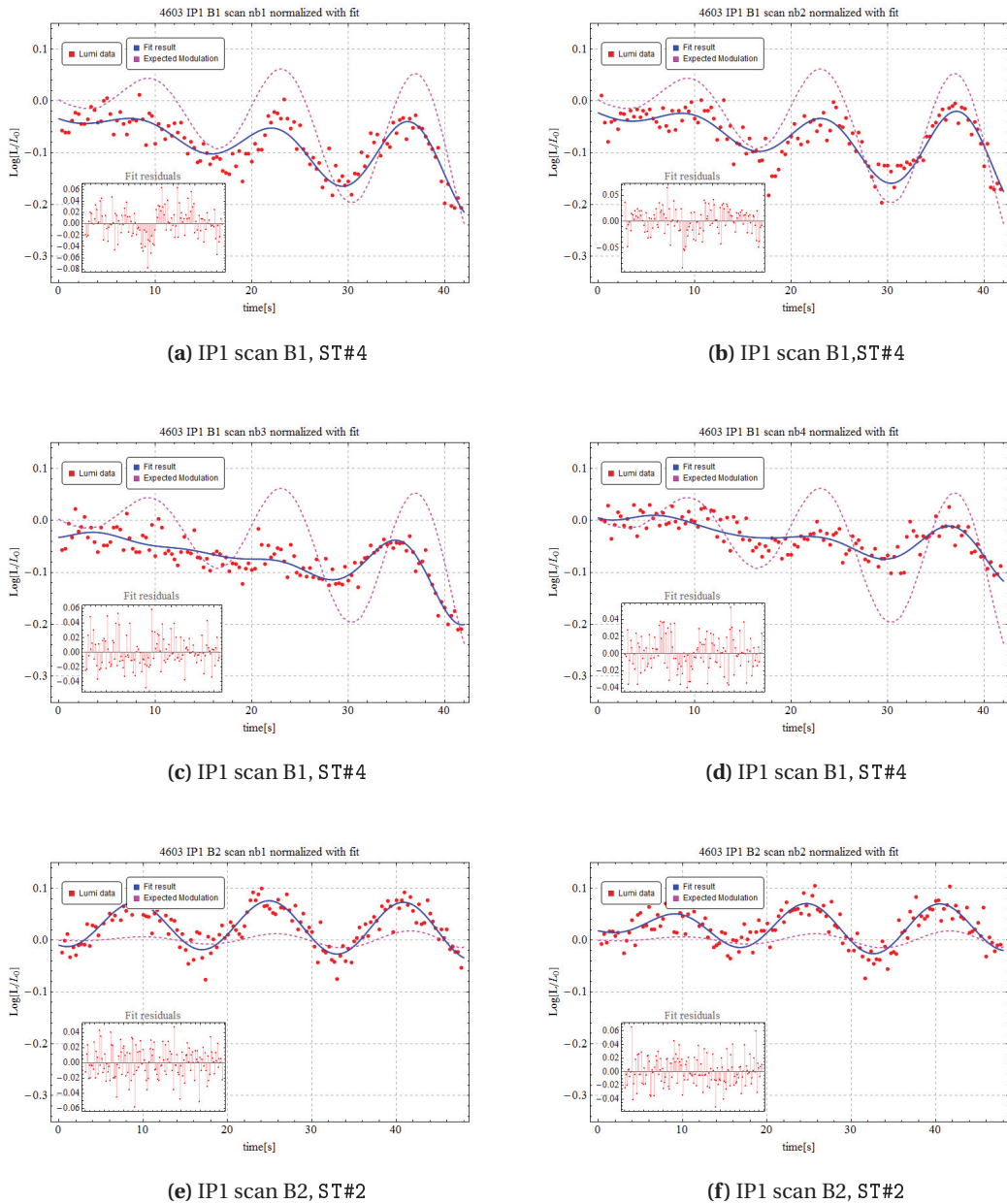


Figure 7.10 – IP1 scan results for fill 4603. The first four ((a) – (d)) figures show the results of Beam 1 scans with the drift configuration ST#4. The last two examples ((e) and (f)), with smaller luminosity drop, correspond to scan configuration ST#2. All cases present good correlation (phase) between the expected modulation (dotted magenta line) and data/fit. The amplitude do however deviate from the expectations, a sign that an initial offset may be present.

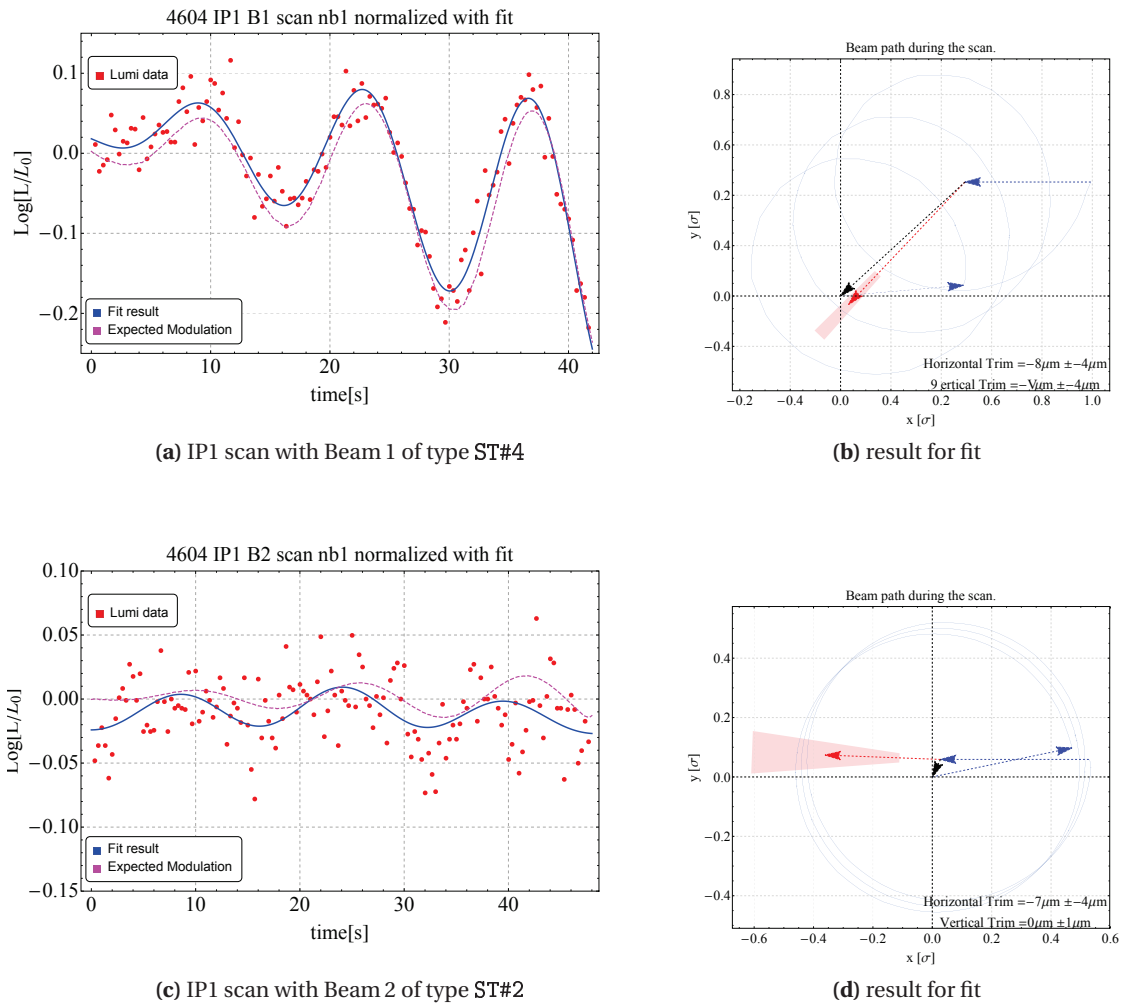


Figure 7.11 – IP1 scan results for fill 4604 (left hand side) and the corresponding fit results (right hand side). The Beam 1 scan (a), modulated with the same offset but larger artificial drift, provides a more distinct result than the Beam 2 scan with smaller drift (c). The applied drift (black arrow) and the reconstructed drift from the fit (red) are superposed to the scan shape. See Table 7.2 for details on the scan parameters.

7.2.4.2 Scans at IP8

The tests in IP8 were affected by very important orbit drifts due to the movement of the inner triplet magnet (see Sec. 4.5). Figure 7.12 shows the evolution of the luminosity during the experiment with a zoom on the moment when three test scans were performed. Despite the orbit drifts induced by the R8 triplet during experiment three scans were performed, see Fig. 7.12c.

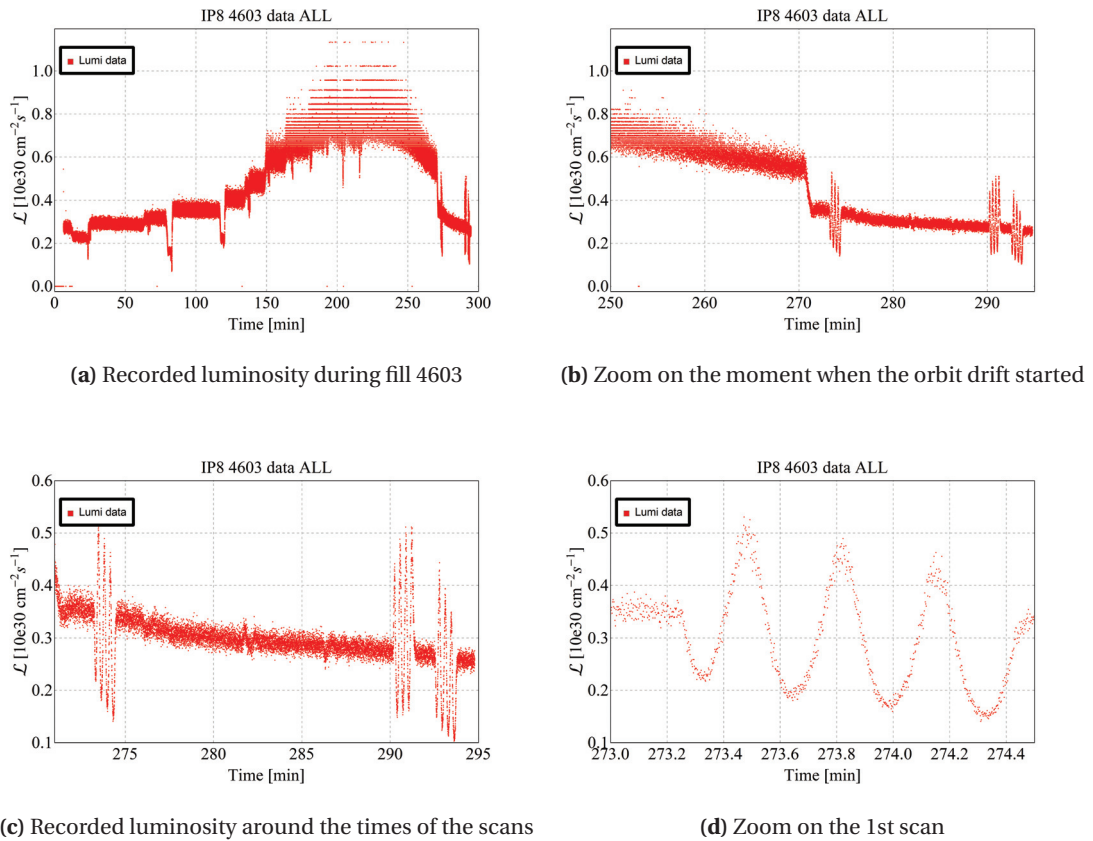


Figure 7.12 – IP8 high rate luminosity data during fill 4603. There is a visible quantization and very noisy period for the highest luminosity. Figure (b) illustrates the luminosity drops due to a sudden orbit drifts due to the R8 triplet. This resulted in a decay of the luminosity that lasted for the rest of the experiment.

Figure 7.12d shows the recorded luminosity modulation during the scan experiments. An offline analysis of the 10 Hz luminosity data showed that the predefined drift of the scans was almost completely compensating the drift coming from the perturbation due to the IR8 inner triplet. For a constant offset the modulation is of course static. During the IP8 scans an initial beam separation was present, which leads to larger than expected amplitudes for the modulations. The result of two tests are presented in Fig. 7.13. The scans have remarkable luminosity resolution (left hand side plots). On the right hand side, one observes that the

Chapter 7. IP orbit stabilization with luminosity

effective drifts were either very small (Fig. 7.13b) or doubled (Fig. 7.13d) depending on the relative sign of the programmed and "natural" drift (compensation or addition).

Unfortunately due to lack of time, it was not possible to repeat those scans at the end of fill 4604 in cleaner conditions (the orbit drifts from the triplet were stabilized).

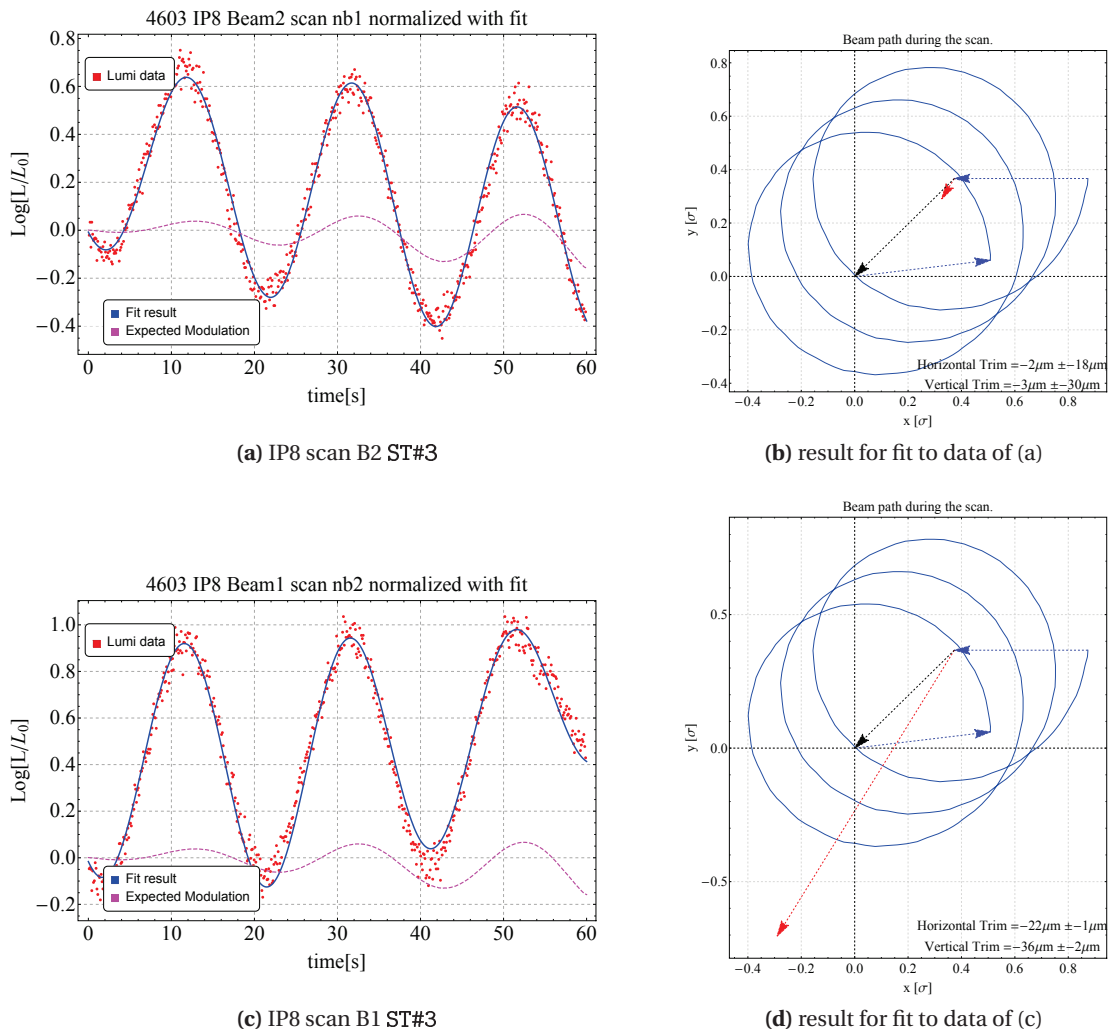


Figure 7.13 – The IP8 scan results. This test was affected by the R8 triplet movement. The large modulation indicates that a large initial offsets is present where the scans started.

Scans in IP5

Due to the absence of higher frequency luminosity data no useful scans could be performed in IP5.

7.2.5 Summary of the experiments and remarks for future tests

During both experimental sessions we demonstrated the feasibility of the proposed stabilization method. Despite the technical issues (problems with drifts and limited time) and the logistic issues (missing optimization steps) the overall results look promising for the operational application. The reconstructed drift parameters and their errors (see Tabs. 7.3 and 7.4) are mostly biased by initial beam offsets. Those two issues compromised the comparison between expectation and observation and need to be solved for the next iteration.

A series of optimization should be performed before each test in order to ensure well defined starting conditions. We have seen that the same test executed with larger initial offset gives cleaner luminosity signal and therefore, more accurate result.

The drift amplitude should be tuned (if possible) to the machine stability observed during the test.

Demonstrating the technique with low intensity beams and small superposed drifts is limited by the machine stability. We have seen that too modest drifts remain undetected due to the luminosity signal quality. The impact of higher luminosity is discussed in the next section.

7.3 Optimization scans with high luminosity

The examples and tests presented so far concerned only single bunch (low luminosity) beams. Both the simulations and the experiments highlighted the impact of the luminosity data accuracy. For an operational beam of ≈ 2000 bunches, the \mathcal{L} accuracy improves significantly providing higher accuracy on the reconstructed offsets. **At high luminosity it is possible to reduce the scan radius and short the scan time to 30 s or less.**

Figure 7.14 illustrates a simulation for 2000 bunches for luminosity recorded at 3 Hz and assuming a 15% of the error on the luminosity of one colliding bunch pair. In that case, the initial $\delta\mathcal{L}^{1b} = 1.5 \times 10^{29}$ (15%) drops down to an overall error of less than $\delta\mathcal{L}^{2000b} = 7 \times 10^{32}$ (1%). A radius of 0.2σ was used with a superposed drift of $0.75\sigma/\text{min}^3$. The drift of $4\mu\text{m}$ (0.3σ) is reconstructed in both direction with an accuracy of $\pm 1\mu\text{m}$.

Under such conditions, a scan of three rotations would last less than 25 s leading to a maximum separation of 0.5σ allowing to identify the optimal direction for correction with μm accuracy. The correction should be applied right after the scan is done allowing to correct the separation before it evolves further into the critical zone of $1-1.5\sigma^4$. For β^* leveling such a scan could be executed within a step while for the collide and squeeze, since no stops between β^* optics steps are foreseen, it would have to be integrated into the orbit feedback system.

³as seen in the experiments described in 6.1.3

⁴As required by HO Landau damping criterion, see Sec. 1.3.2

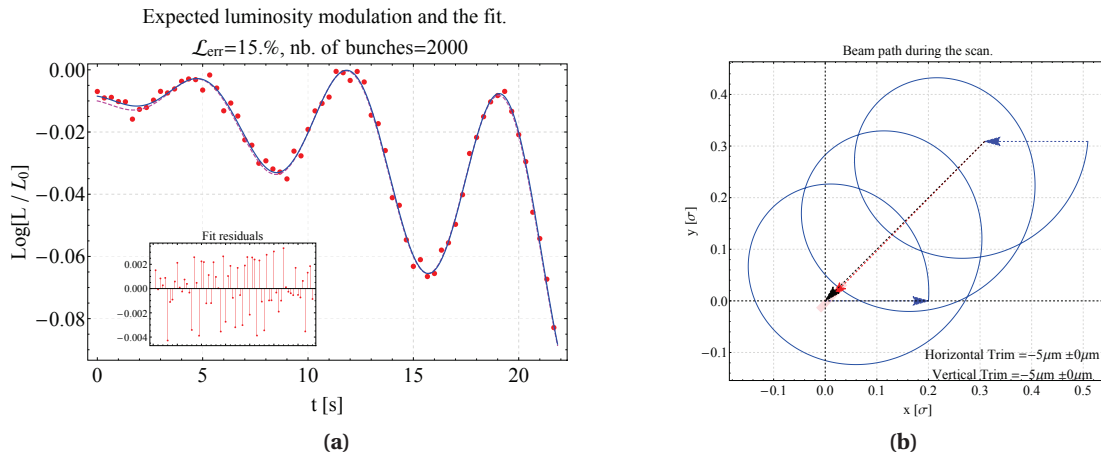


Figure 7.14 – Example of a scan at high luminosity with a reduced scan radius of $\delta = 0.2 \sigma$. The simulation assumes 2000 bunches in the machine. The relative error of $\frac{\delta \mathcal{L}}{\mathcal{L}} = 15\%$ on a single bunch drops down to overall error of less than 1%.

7.4 Beam position tracking during the scans

Taking advantage of the fact that a first DOROS test installation was available in IP1 and IP5, a parasitic measurement of the beam position at the IPs was possible by extrapolation from the BPMs installed next to the Q1 quadrupole. Figure 7.15 compares the expected and recorded movement of the beam (trim) at the IP and the recorded position. Figure 7.16 presents examples of scans for IP1 and IP5.

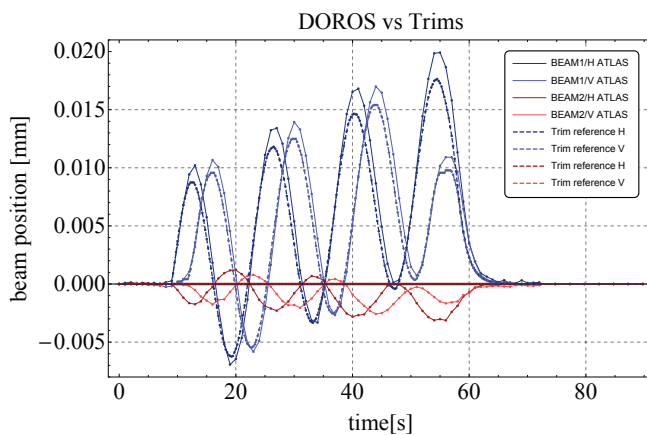


Figure 7.15 – The expected and recorded (DOROS extrapolation) beam movement at the IP.

7.4. Beam position tracking during the scans

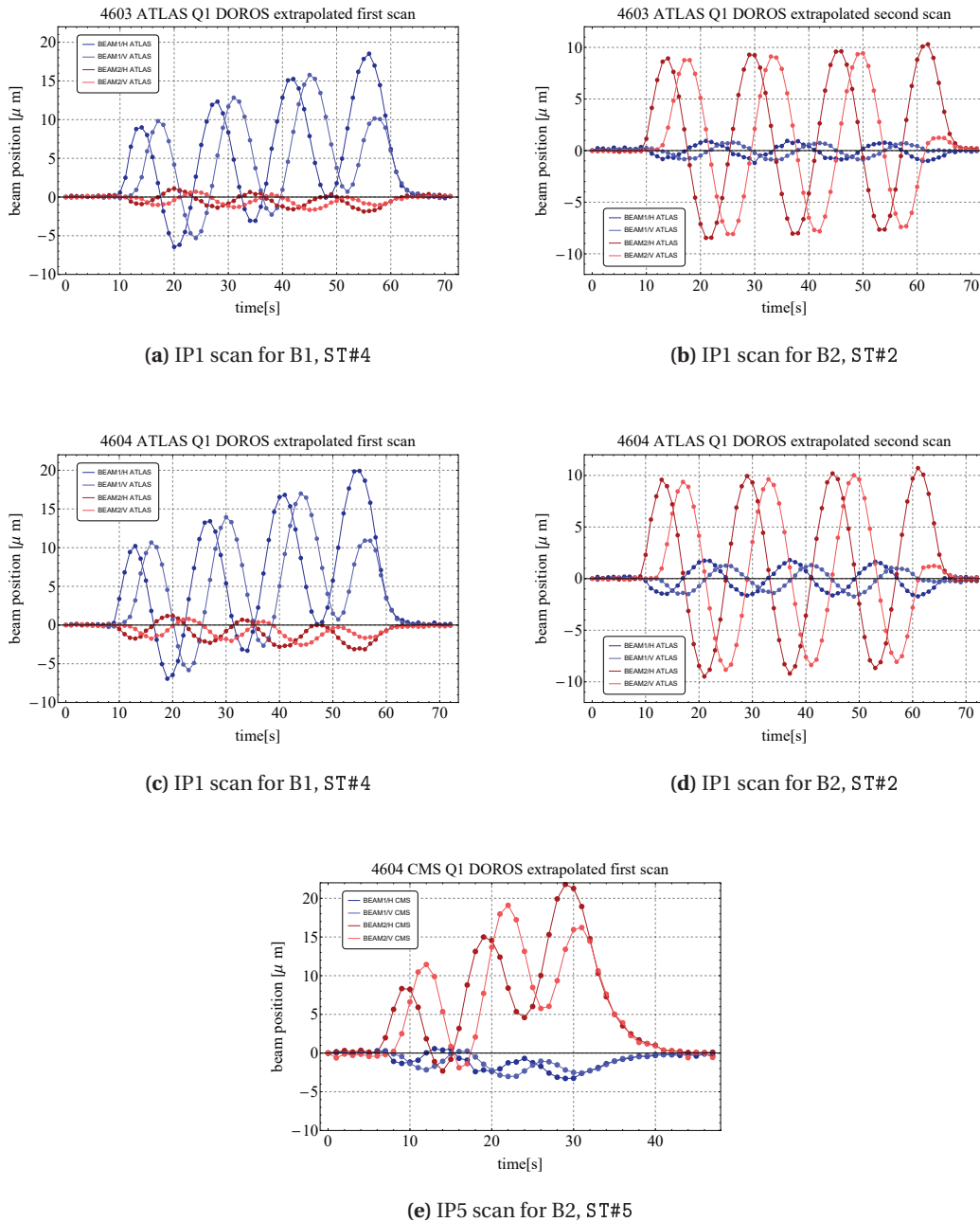


Figure 7.16 – Beam position at IP1 and IP5 during rotation scans. The position is extrapolated from the Q1 BPMs equipped with DOROS electronics. One can clearly observe an apparent movement of the nominally static beam.

Beam cross-talk seen by DOROS

As mentioned in Sec. 1.3.2 operation with beams separated by a fraction of a beam size leads to closed orbit shifts from the beam-beam deflection.

Chapter 7. IP orbit stabilization with luminosity

During the scans one can clearly observe an apparent movement of the nominally static beam, see Figs. 7.15 and 7.16. Figure 7.17 presents the beam–beam kick and the associated closed orbit shift expected at the IP. The expected kicks for selected beam properties are presented in Fig. 7.17 and listed in Table 7.5.

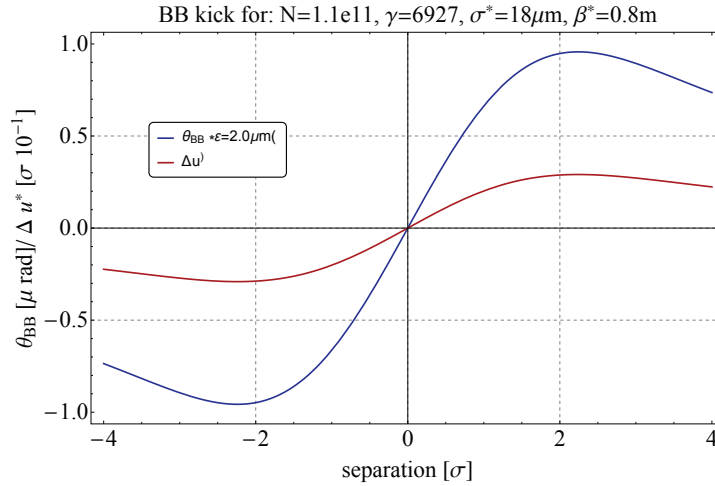


Figure 7.17 – The beam–beam kick and the associated closed orbit shift at the IP for the beam emittance of $2.5 \mu\text{m}$.

d [μm]/[σ]	θ_{bb} [μrad]	u_{bb} [μm]
5 / 0.3	0.27	0.08
10 / 0.6	0.52	0.14
25 / 1.2	0.9	0.25
31 / 2	1.0	0.28

Table 7.5 – Expected kicks (θ_{bb}) and orbit displacements (u_{bb}) at the IP due to the beam–beam effect for $\beta^* = 80 \text{ cm}$ at 6.5 TeV for a selection of beam separations and an emittance of $\epsilon = 2 \mu\text{m}$.

Figure 7.18 presents the observed beam position change of the nominally static beam together with the expected position due to the beam–beam kick for some examples of Fig. 7.16. **Since the beam–beam related displacements are expected to be much lower than the ones that were observed, it is suspected that the observed cross talk between beams is an artifact of the BPM electronics.** The "coupling" may be due to imperfect directivity of the coupler BPM installed at the Q1 quadrupole.

DOROS conclusions

We have seen that DOROS system provides valuable data at the very high resolution. Although some electronics cross–talk is visible it does not spoil the overall performance and resolution of the system. We observe a very good agreement (at the μm scale) over short time scales (tens

7.5. Bunch train behavior under stabilization scan

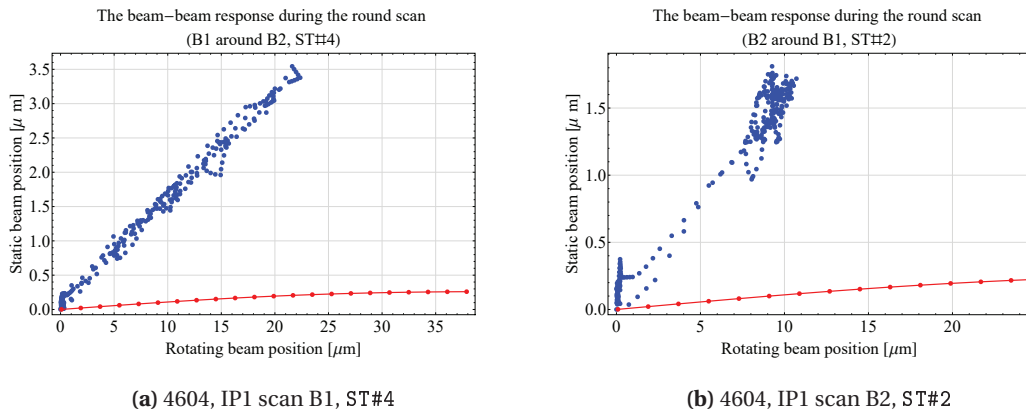


Figure 7.18 – The correlation between the moving and static beam during a scan. Blue points correspond to the extrapolated DOROS measurement shown in Fig. 7.16. The red line represents the expected beam-beam induced position shift (see Fig. 7.17).

of minutes) during the collide and squeeze experiment. Such coupling will however limit the performance of DOROS in view of possible IP position feedbacks.

Another aspect of the working DOROS is its longer term accuracy. For the measurements collected for those experiments we analysed only relative changes as the reference was frequently changed, but we have noticed systematic drifts on a long time scale. This issue was reported to the beam instrumentation group.

7.5 Bunch train behavior under stabilization scan

So far we did not discuss the influence of the LR interactions for bunch trains. The high intensity beams used for the luminosity production contain gaps of different lengths between consecutive trains. Most of the gaps correspond to the rise times of the SPS (225 ns) and the LHC (950 ns) injection kickers. Finally there is also the 3 μs gap for the LHC extraction kickers (to the LHC beam dump).

Due to the presence of such a gaps, LR interactions lead to slight orbit distortions for bunches at both ends of each train as described in Sec. 1.3.2.3.

Using the refurbished TRAIN code ([90], Appendix C.7) we studied the influence of the deliberate separation on the bunch by bunch offsets at the IP.

Figure 7.19 illustrates the validation step for the code. The impact of the HO and LR interactions for IP5 offsets when only IP1 and IP5 (in black) or for IP1, IP5 and IP8 (in red) are the colliding points, are compared to measurements (in green) done in 2015 during luminosity scans of the beams [91, 92] in IP5. There is a very good agreement in the separation plane. For

Chapter 7. IP orbit stabilization with luminosity

the crossing plane, some care in comparison needs to be taken as the luminosity scan affects the crossing configuration.

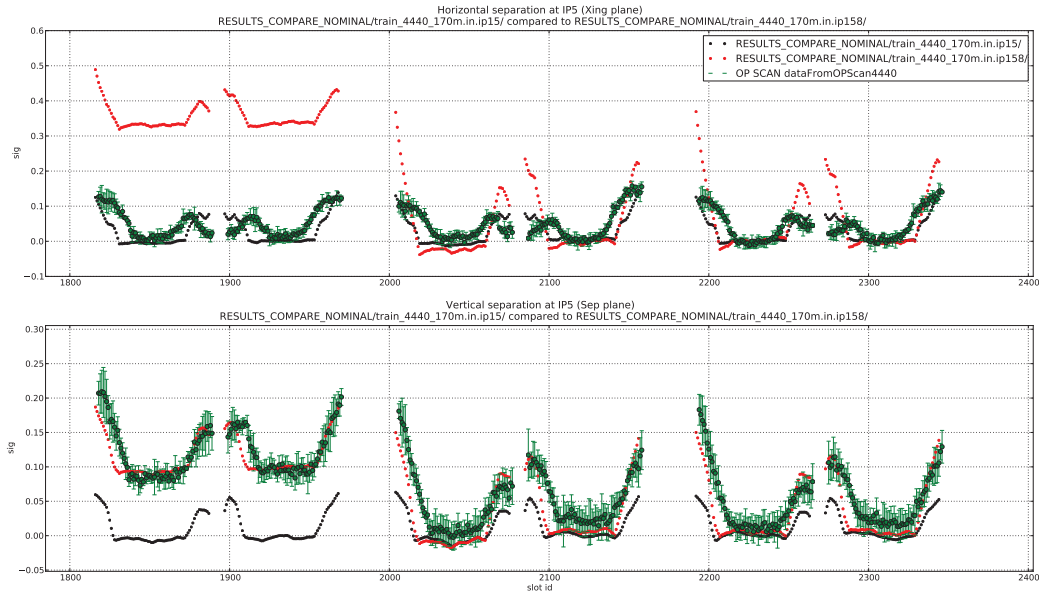


Figure 7.19 – Bunch by bunch offsets in the crossing plane (top row) and the separation plane (bottom) at IP5. The signatures of the different number of LR interactions are visible as a dependence of the transverse offset on the bunch slot. In black, offsets for bunches colliding only in IP1 and IP5, in red for collisions in IP1, IP5 and IP8. Trains located in the slots ≈ 1900 are without HO collision in IP8. In green results from the OP-scan campaign, courtesy M. Hostettler [92].

Figure 7.20 illustrates the simulation of the impact of the deliberate separation of the beams in one IP (red dots) on the other one with respect to the fully HO situation (black dots). From the simulations one can conclude that the **deliberate separation (i.e. $\delta = 0.4 \sigma$) does not perturb the beam separation beyond the level of $d = 0.01 \sigma$** . The impact of the LR interactions and beam offset at the scanned IP can therefore, be neglected when this method is used for reconstructing the beam offsets.

7.5. Bunch train behavior under stabilization scan

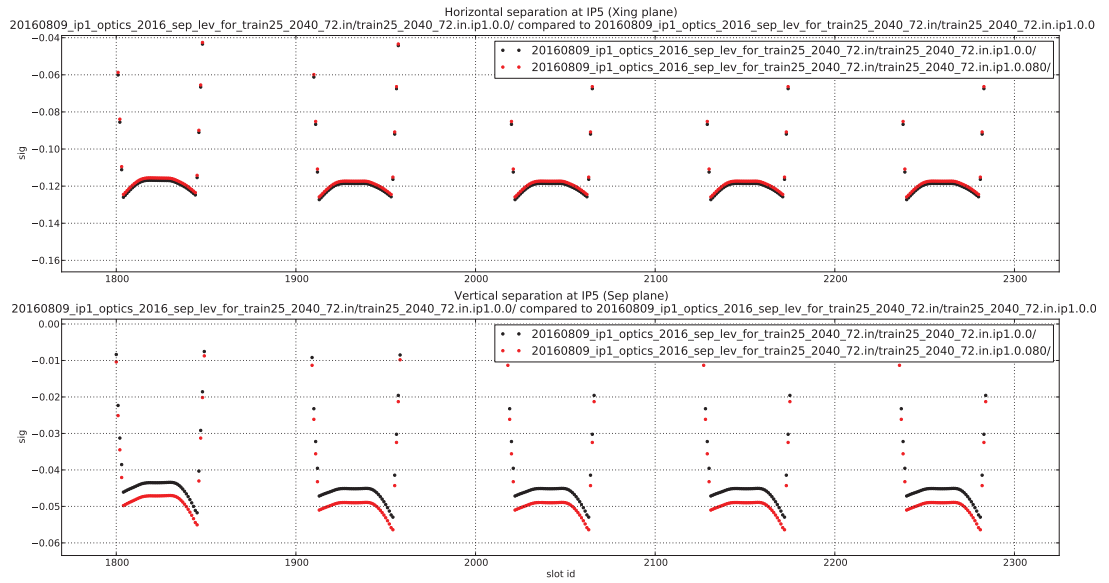


Figure 7.20 – Crossing plane offsets (top) and separation plane offsets (bottom) induced due to the deliberate separation introduced by a rotation scan (in IP1) on the beams separation. Plot contains selected trains in the LHC 2016 operational filling scheme. In black no separation applied in IP1 nor in IP5, in red separation of 2σ in IP1.

7.6 Conclusion and Outlook

We introduced a novel method for stabilizing the beam offsets at the IP. To determine and correct possible separation drifts (i.e. during the β^* leveling step and more importantly for a colliding and squeeze), one beam is rotated around the other beam at the collision point. The principle was introduced with formulas applicable to various initial simplified conditions.

This chapter summarized all the fruitful experiments with the new orbit stabilizing method for the IPs. **The proof of concept was experimentally demonstrated** with a series of measurements that were carried out during dedicated MD periods. We showed that we are able to reconstruct an artificial drift that was superposed with the scan as well as the real drift.

The following steps are required to move towards an operational implementation at the LHC:

1. A validation of the method for a real β^* step including the beam size change in the fit algorithm. This however requires a dedicated MD session, that was not attributed in 2015.
2. A test with more bunches to compare with simulations in order **to reduce the scanning radius and eventually shorten the scan duration.**
3. The scan configuration and analysis **must be automated to make this technique part of a fast-reacting feedback system to stabilize the beams at the IPs.**
4. An **operational link** for a fast real-time data transmission of the luminosity between the experiments and the control room.

The luminosity data must be provided with a frequency of at least 3 Hz and in real-time. A frequency of 10 Hz is recommended to ensure a good quality of the correction (reaching more than 90% of expected drift corrections). **Limitations of the experiments data acquisition systems may possibly limit the luminosity rates.**

Luminosity optimization It can be envisaged that the proposed method can be used to replace the existing optimization technique based on scanning each plane separately that is used for periodic adjustments of the beam offsets at the IP.

8 Summary and outlook

During Run 1 LHC operated mainly with 50 ns bunch spacing to avoid excessive problems of e-clouds. For 50 ns beams the bunch intensity could be pushed to $\approx 1.7 \times 10^{11}$ p/b for a transverse emittance of $\approx 2\text{-}2.5 \mu\text{m}$. This corresponds to a beam brightness more than a factor 2 above the nominal 25 ns beam. As a consequence operation was affected by instabilities, and the event pile-up in the experiments was very high. During 2012 the possible need for β^* leveling or collide and squeeze was considered for the first time for operation before HL-LHC.

When the LHC switched to operate with 25 ns beams at 6.5 TeV in 2015 the situation changed significantly. E-cloud together with intensity limitations on the injection protection device (TDI) and on the damaged SPS beam dump (2016) limited the number of bunches to around 2200. With a bunch brightness close to nominal, instabilities had a much reduced impact and the need for β^* leveling and collide and squeeze was no longer pressing, although it will be back on the table at the latest for Run 3 in 2021 when brighter beams will be available following the injector upgrades.

This thesis paved the way for operating LHC with β^* leveling and collide and squeeze in the future. Various leveling techniques were reviewed and possible operational scenarios for β^* leveling were established for LHC and HL-LHC. The critical issue of orbit stability was analysed and compared to the requirement of transverse beam stability established in other theses.

We attempted to quantify the impact of the quadrupole misalignment (i.e. ground motion, mechanical problems) on the reproducibility of the beam orbit and, what is the most important, the beam position at the IP during squeeze process and stable beams. We computed some estimates to predict the orbit r.m.s. behavior over time based on the data collected during LHC Run 1 and Run 2. We cross-checked the data against the measurements that we have done during dedicated experimental sessions. We highlighted that the performance of the feedback is highly dependent on the BPM reproducibility. Whereas for the LHC we are operating at the limit of the BPM noise that is allowable, for the HL-LHC a significant improvement in the BPM resolution will be required to not spoil the beam positions at the IPs. A series of computation

Chapter 8. Summary and outlook

were performed to characterize the limit for the BPMs reproducibility.

Within the time frame of this thesis, we were able to perform two experiments of collide and squeeze. With the experience from the first attempts (back in 2012) it was anticipated that beam orbit handling would be one of the key aspects. A very successful experiment conducted on November 2015, ultimately showed the LHC readiness for the β^* leveling. The upgrades of the orbit feedback controls (done during the winter shutdown in 2015/2016) allow now for much smoother operation, and would make schemes such as Collide and Squeeze or β^* leveling possible.

To overcome the issue of uncontrolled beam offset build-up during collisions and/or collisions while squeezing possible cures were assessed. The simplest way of tracking with beam position monitors was not usable with standard BPMs due to the systematic errors that spoil the position interpolation at the IP. The experiments we performed validated a new high resolution BPM electronics as a possible solution. Since the new system was not mature enough to reliably track the IP and to allow to feedback on the beam, we proposed a complementary method to stabilize beam offsets at the collision point.

A novel method was proposed to determine the beam offsets by a rotating scan and analysis of luminosity. We introduced the concept and a mathematical description supported by simulations of the process. Moreover, we conducted a series of experiments in the machine to establish validity of the method and propose the next steps. As this method involves some scans in the transverse planes at the collision point we used the simulation code to track the bunch by bunch behavior of trains and established that the scan technique has no detrimental side effects.

Outlook

Only when LHC will need the luminosity leveling, we will see most of the orbit effects described in this thesis. The issue of uncontrolled beam offset build-up needs to be revisited in the modeling with more wide approach, i.e. different corrections methods or different optics (*flat beams*).

The local IP orbit stabilization techniques require further development. We proposed and demonstrated the novel method for active stabilization, however, the completeness of the method will only be ensured after test in the real environment with changing optics. Dedicated MD time needs to be allocated to improve the technique and followed if possible, by bunch trains.

Operation (and setup) of the Tertiary collimators during *collide and squeeze* will require more time and development that was possible for this thesis. As we proved, there is no increase of losses with a stabilized orbit around the IP. However extended periods of validation will probably be required.

Other exciting ideas for further improvements are related to the spin-offs of this thesis namely, the computational tools *Tensorics* and *Multi-OrbitFramework*. Since a lot of attention was given to a sound design of these tools, they have the potential to evolve to powerful standard tools. Since *Tensorics* was made available as an open source project, it is constantly under development for different applications within LHC operations and LHC Machine Protection. For the *Multi-OrbitFramework*, an automated integration with operation would allow to diagnose bare orbit evolution on fill to fill basis.

Appendices

A Multi-orbit calculation framework

I have spent considerable time to develop tool dedicated to most of the calculations mentioned in the thesis. This part is a documentation for the software that was written throughout my doctoral appointment at CERN and was used at different moments of this thesis.

Since a number of different orbit calculations often require the same core functionality we introduced the idea of an extended-able platform to perform multi-orbit calculations. In this appendix, the overview of some technical aspects is presented together with examples that were used on a daily basis during the LHC 2015 operation.

A.1 Idea and main concepts

Existing and powerful orbit control software [93], in use since LHC started in 2008 is available to steer and analyze the orbit of CERN accelerators. However, a sequential, repetitive and the most important automated calculation for multi-orbit analysis was non implemented. A framework of adjustable and extendable modules was introduced to simplify all computation demands.

Work with the framework almost immediately triggered the need of special object to simplify all the operations, called *tensor* (see dedicated App. A.4). The code is written in JAVA to easily interface the LHC settings management system (LSA [42]). The following concepts are listed to simplify understanding of the later part:

1. An `Orbit` is an immutable, unchangeable combination of `OrbitReading` that represents the BPMs measurements and `OrbitCorrection` settings (for two channels) that represent the current corrector settings for a given orbit. The orbit `Context` holds an information on time, fill number, beam mode, optics etc...
2. The calculation result is a new, separate `Orbit` or it is an additional object (calculation

Appendix A. Multi-orbit calculation framework

result) to be accessed through dedicated Application Programming Interface (API) or Graphical User Interface (GUI).

3. A user can work with 1-N orbits in one calculation iteration.
4. There exist some predefined `Context` types to ease the orbits filtering of the calculation results. Among the all possible context types there are three main groups:
 - `ACTUAL` that is related with real measurements,
 - `RAW` that has no correction done or the ones that were just generated,
 - `PROJECTED` All the processed or touched objects with some analysis.
5. A predefined list of optics is available with the ID numbers ranging 0-M.
6. `fillNb` is an indicator of the real fill number when is set to less then 20000; All numbers above this value are associated to simulated orbits. In that case the last two digits represent the ID of the optics that was used for the generation.

A.2 Structure of the framework

For clarity of the software part, we introduce two groups of the components. The `internal components` include the mechanics of the framework and do not perform any calculations. They are meant to simplify input and output operations. The calculations, belong to the other group – `calculation strategies` perform an actual calculations with the help of some external libraries.

All of the work is stored in the central CERN SVN repository under the project names:

1. `accsoft-steering-domain`
2. `accsoft-steering-analysis`
3. `accsoft-steering-gui`

Architecture – core part The main `internal components` are:

1. `OrbitsManager` is the object where all complete orbits objects are kept. A complete orbit has a valid description of orbit reading (BPMs) and correction settings (CODs) and an associated context.
2. `ReferenceOrbitRegister` is the object where the actual reference orbit is kept (for a given optics). It keeps as well the cached `CorrectionSettings`. There is only one possible correction setting to keep at one time.
3. `OpticsManager` provides access to all optics information like `Twiss` parameters. Two implementations of this manager distinguish access to different optics sources:

- (a) `LsaOpticsManager` provides access the LHC optics definitions stored in the LSA control system.
 - (b) `JMadOpticsManager` interfaces to the JMad [94] based manager for any accelerator that have a JMad Model created. The model that is implemented is used for HLLHC calculations.
4. `OrbitGenerationManager` provides a service (in current implementation) to generate physical beam orbits using JMad. It uses the configuration provided by `AnalysisOptionsService` with the `JMadInputData`.
 5. `AbsolutePositionManager` and `MachineSurveyManager` are classes that distribute information about ordering of the elements in the current machine (physical layout) and its general configuration (i.e. actual misalignment configuration). It is needed since the orbit objects are deliberately unaware about any element order.
 6. `CalculationManager` and `CalculationStorage` are the places where the knowledge about the possible calculation modules – `CalculationStrategies` (manager) and additional results of their execution is stored (storage).
 7. `AnalysisOptionsService` stores some additional analysis information. An example of such an additional information can be: the SVD correction options or the options for orbit generation in JMad.
 8. `JMadModelHolder` References to the active accelerator model [94].

Multi-task calculations In the previous part we listed the mechanics of the framework. The calculations are implemented in the `Calculation Strategy` that may have access to the selected parts of the `framework core`. The strategy creator defines what type of calculations are performed. The main modules (`strategies`) to be distinguished in the framework are the grouped as following:

1. Orbit manipulation strategies are based on the concept of base orbit plus response to a given corrector settings like:
 - (a) `Real time kick unfolding` provides the orbit response obtained by unfolding the OFB real-time corrections.
 - (b) `Base kick unfolding` provides the orbit obtained by unfolding the non-real-time base corrections.
 - (c) `Orbit correction` performs a correction of the selected orbit (with respect to the selected reference) and applies the solution as a part of the real time channel correction. It uses the configuration provided by `AnalysisOptionsService` for the `SvdInputData`.

Appendix A. Multi-orbit calculation framework

- (d) `Kick from the cache` allows to check the orbit (any specified) response for the saved (cached) kicks settings.
2. `OrbitChangeDuringTheSqueeze` tracks the orbit change while changing the optics. This includes all applied corrections and all orbit differences with respect to the reference/source one. (see Chap. 5)
3. Beam position and separation at the IPs, including individual beam position at the IP as:
 - (a) `IP1 beam offsets`
 - (b) `IP2 beam offsets`
 - (c) `IP5 beam offsets`
 - (d) `IP8 beam offsets`
4. Empty orbit generation (for the analysis purposes):
 - (a) `EmptyOrbitGeneration` is generating the empty orbit based on the elements that are kept in the `MachineSurveyManager`
 - (b) `EmptyOrbitFromTheInputGeneration` is generating the empty orbit based actually selected orbit by putting zeros on reading and corrections.

Two more calculations, not directly related to the orbit but to the the data multi-set concept are accessible within a framework (see more in App. C.6):

1. `LuminosityCalculations` calculates the evolution of the delivered luminosity for a given type of leveling (β^* , offset) and for β^* leveling it also calculates the times of the steps to maintain the luminosity within the desired margin.
2. `EmittanceCalculations` allows to calculate an emittance based on the fill data (recorded luminosity and bunch intensities, stored in CALS [95]).

A.3 Symmetrical patterns in correction solutions

As it is described in Sec. 4.4.3 the dedicated search tool need to be made in order to find the regularities in the correction patters. Within the multi-orbit calculation framework a specific module for pattern matching and search was developed.

Figure A.1 illustrates the result of the search over more than 400 bare orbits for a pattern match. We can see that most of the structures are present in the fixed combinations, but no systematic dependence can be derived.

As it is later concluded in Sec. 5.3.2 those patterns are originating from the specific misalignment configuration.

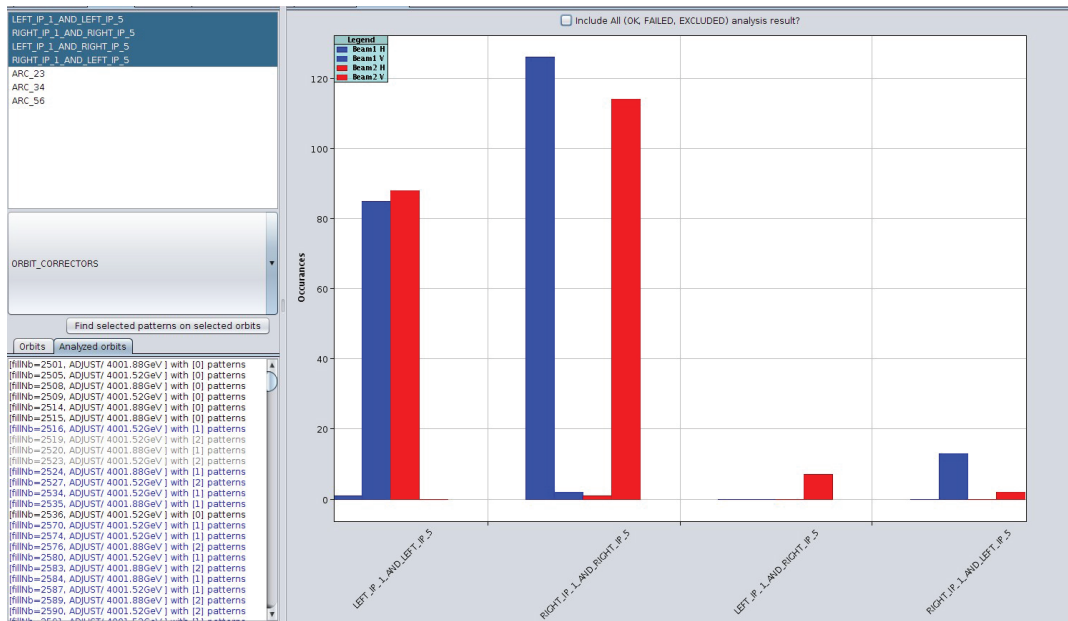


Figure A.1 – Result of the pattern search task. Most of the build structures appear in the same configuration that points to the static origin for this phenomena.

A.4 Orbits in squeeze calculation

Listing A.1 presents the algorithm used for the orbit tracking in the squeeze. The calculation that requires the most of the resources is the one used for computation how the orbit evolves during the squeeze after some misalignment was introduced.

Listing A.1 – Part of the main calculation loop

```

1 for (String changedOptic : opticsWithInjection()) {
2   OrbitDetailsContainer relativeResponseToKickWithNewOpticOrbit =
3     prepareOrbitResponseForOldKicks (orbitBPMs ,
4     orbitCorrection, orbitBPMsRef, orbitCorrectionRef, Optic.ofName (
5     changedOptic),
6     Optic.ofName (previousOptic), calculatedCorrectedOrbit ,
7     previousOpticContextFillNumber);
8   OrbitDetailsContainer correctedOrbitWithResponseOfTheNewOptic = new
9     ();
10
11   /* add all the inputs and prepare for the correction at new optic
12   */
13   OrbitReading sumOfRelatives = calculate (
14     relativeChangeInRawXingAndSep.getOrbit()).plus (
15     relativeChangeInRawJmadOrbit.getOrbit());
16   OrbitCorrectionSetting sumOfCorrectionRelatives = calculate (
17     relativeChangeInRawXingAndSep.getOrbitCorrection(RT)).plus (
18     relativeChangeInRawJmadOrbit.getOrbitCorrection(RT));
19

```

Appendix A. Multi-orbit calculation framework

```
15  OrbitDetailsContainer fullOrbitToCorrect = new
    OrbitDetailsContainerTensorsIn(contextForProjected,
16      orbitResponseToCorrect,
          correctedOrbitWithResponseOfTheNewOptic.
          getOrbitCorrection(TC),          calculate(
          correctedOrbitWithResponseOfTheNewOptic.
          getOrbitCorrection(RT)).plus(
          sumOfCorrectionRelatives));
17  saveIPDisplacement(fullOrbitToCorrect, calculationStorage);
18
19  calculatedCorrectedOrbit = orbitCorrectionCalcuationStrategy.
    calculate(fullOrbitToCorrect,
20      calculationStorage);
21
22  saveIPDisplacement(calculatedCorrectedOrbit, calculationStorage);
23  opticIndex++;
24  previousOptic = changedOptic;
25 }
```

B Tensorics

The need to unify domain specific objects in accelerator facilities is as old as attempts to analyse and hand over data. The constant need of adding new objects cause very often treating them as a raw arrays or facing the problem of re-implementing some mathematical operations for them like. Therefore we need to facilitate the creation of domain objects without having to re-implement the mathematical operations for them. That points to point that back bone for any of this object should fit into wide analysis framework that provides many down service features like i.e. mathematical calculations and manipulations. As well as their simplified usage in all applications given by so called fluent API (Application Programming Interface). This part will present an approach to represent those domain objects on example of LHC accelerator, especially focusing on beam orbit analysis with so called multi-key to value approach, called later - *tensor*.

The core part of the package is now open-sourced (GitHub) and publicly accessible through the link www.tensorics.org.

Nowadays, this package is widely used and simplifies some LHC controls and operation software products thanks to many contributions, mainly by K. Fuchsberger (co-founder), M. Hostettler and C. Aguilera Padilla.

B.1 The idea behind the need

As an example, we can consider an LHC orbit. The beam orbit is one of our main domain objects that has several implementations. They vary from simple arrays to very complex Java objects. All of them have a common start point, namely they are nothing else than a set of values that describe beam **position** at a monitor, for given **plane** and **beam** at given **time**. Complex accelerator systems, require data analysis across systems and tools, but for the time being it is almost impossible to reuse an orbit object between different systems (e.g. steering, feedback or calculated responses).

Depending on the type of analysis or data handling, the user one wants to access the values for one BPM over time, while for other cases the values for one point in time, but only for one beam and plane are of interest. The domain objects might even contain convenience methods, which allow the users to access data in a convenient way, which is natural for the respective domain. The main advantage of consistent domain objects within the accelerator controls environment is that of simplified data exchange and storage.

On the other hand, for mathematical operations, a generic approach is preferred (e.g. arrays) such that mathematical operations are only implemented in a generic way which improves code re-usage. Furthermore, it should be easy to add new domain objects, without having to reimplement the mathematical operations. Mathematical operations should be able to handle the remaining problems (i.e. data incompleteness, data invalidity, error propagation) in an elegant and transparent way.

Another requirement, which we added to this list, is that all object manipulations should be possible in two ways: One way, which would transform one object directly in another one, containing all the accessible data (like a real operation on two numbers in Java), and a second way, which would only allow to describe and chain the operations, but only would return place-holder objects (Nodes in the expression tree), which could be used in analysis scripts and would later be resolved during execution time of the analysis. Both invocation methods should provide the same operations and the same API.

The concept was prototyped during the development of a comprehensive LHC orbit study to identify orbit steering anomalies at the interaction points during LHC Run 1 see Chap. 4 and later to complete other calculations within scope of this thesis, see Chap. 5.

B.2 Tensors and their language

Our basic abstraction is a `Tensor`. One can see this object as a generalization of a tensor in the mathematical sense. The tensor object as we define it has the following properties:

- A tensor can be seen as an object which maps a set of coordinates to one value. The set of coordinates we call 'position' in the following.
- We always consider tensors as sparse objects, contrary to tensors in mathematical sense, which would have values for all coordinate combinations.
- The elements of the set of coordinates which define a position are constrained in that way, that exactly one coordinate which is an instance of distinct java class is allowed.
- The maximum dimensionality (rank, order) of the tensor is thus given by the number of classes defined in the position.
- The tensor object has access methods which allow to retrieve values at a certain position.

- Up to now, we only consider immutable tensors, so no put-like methods are provided.

Following this structure, it is possible to define operations on tensors and among them. A fluent API was chosen for this purpose. A minimal example of this small *eDSL* (embedded Domain Specific Language) is given in listing B.1 which creates an orbit tensor for one point in time (eg. now).

Listing B.1 – Tensor creation example

```
1
2 builder = Tensorics<Double>.builder(Plane.class, Beam.class, Element.
  class);
3 builder.putAt( 2.3, Plane.H, LhcBeam.B1, Element.of("BPM.B1.1"));
4 builder.putAt( 1.2, Plane.H, LhcBeam.B1, Element.of("BPM.B1.2"));
5 builder.putAt(-2.3, Plane.H, LhcBeam.B1, Element.of("BPM.B1.3"));
6 builder.putAt( 2.3, Plane.H, LhcBeam.B2, Element.of("BPM.B2.1"));
7 builder.putAt( 3.3, Plane.H, LhcBeam.B2, Element.of("BPM.B2.2"));
8 builder.putAt(-0.3, Plane.H, LhcBeam.B2, Element.of("BPM.B2.3"));
9 builder.setTensorContext(Context.of(Time.now()));
10 Tensor<Double> orbit = builder.build();
11
12 /* to get value at certain position */
13 double value = orbit.get(Plane.H, Beam.B1, Element.of("BPM.B1.2"));
```

To add even more flexibility and value to this concept, all operations in the language are not only defined for tensors. Following types are supported in the framework:

- `TensorBacked`: This interface is foreseen to be implemented by domain objects, which have a tensor as a backing container. It has one method (`tensor()`) which returns the backing tensor of the object. Together with factories for the domain objects registered to the language, it will be possible to apply all the language expressions directly to domain objects and e.g. transfer orbits into other orbits.
- `DeferredTensor`: This is an empty interface. If such objects are used with the language, then no real evaluation will be done, but only expression trees are produced, which can be used in analysis scripts for the framework.
- Even a combination of the above two interfaces could be envisaged: `DeferredTensorBacked` this would allow to use domain objects in analysis scripts.

B.3 Fields, operations and fluent API

Since our Tensors can be implemented for any chosen type framework has to provide the way for mathematical expressions. Concept of the `Field` of given type was introduced together with `FieldUsage`. Listing B.2 contains the example for instantiation and use of fields eg. obtaining an inverse (negative values) of given tensor or simply multiplying a tensor by a scalar value.

Appendix B. Tensorics

Listing B.2 – Tensors and Fields

```
1 /* here using real numbers field one can get negative of given tensor
   */
2 return Tensorics.using(Structures.doubles()).negativeOf(tensor);
3
4 /* to get tensor multiplied by a value one has to request appropriate
   field */
5 return Tensorics.using(Structures.doubles()).calculate(tensor).
   elementTimes(value);
```

The fluent API provides a "natural" operation/interaction with the programming language. In *Tensorics* we introduced this concept at all levels of the Tensors usage. Whether we create a new Tensor or manipulate an existing one, the start of the framework calls is the same and is self describing in the code line. Let us again consider the orbit tensor created in Listing B.1. To perform some calculations we simply call the `Tensorics` class and do some operation on it as shown in Listing B.3.

Listing B.3 – Fluent API

```
1
2 /* with one entry point, multiple calculations and operations are
   possible*/
3 double position = Tensorics.from(orbit).get(Plane.H, Beam.B1, Element.
   of("BPM.B1.2"));
4
5 /* A r.m.s. position in horizontal plane for beam 1 */
6 orbitForBeam1 = Tensorics.from(orbit).reduce(Beam.class).bySlicingAt(
   Beam.B1);
7 Tensor<Double> rmsValuesForBothPlanes = Tensorics.from(orbit).reduce(
   Plane.class).byRmsIn(Structures.doubles());
8 result = rmsValuesForBothPlanes.get(Plane.H);
9
10 /* To get the difference to any reference */
11 Tensor<Double> difference = Tensorics.using(Structures.doubles()).
   calculate(orbit).minus(refOrbit);
12
13 /* To get the time evolution, framework allows to merge tensors into
   one rank higher tensor with coordinate specified in their contexts
   */
14 Tensor<Double> orbits = Tensorics.merge(orbitsInOneTime);
```

A large part of *Tensorics* is still under development but the first implementations in the LHC analysis frameworks are operational since 2015. More detailed information can be found under the following link www.tensorics.org.

C LHC analysis and operation tools

During the time frame of that thesis, we developed many operational tools. Some of them are now integrated into the core part of the LHC control room tools. In this appendix we present some selected tools that were created or adapted as a part of the work for this thesis.

C.1 Orbit correction and eigenvalues

SVD is the main algorithm used for LHC orbit correction (see Sec. 1.1.4), in particular for the OFB. The spectrum of eigenvalues [96] is shown in Fig. C.1 for the LHC. In practice not all the eigenvalues are used for the corrections. The quality and locality of the correction and the required kick strengths can be controlled by limiting the correction to K eigenvalues ($K < M$). As K is increased, the correction becomes more and more local and the kick strengths increase. The correction also becomes more and more sensitive to measurement errors and noise. The singular values shown in Fig. C.1 (at the right side of the spectrum beyond ≈ 500) are normally excluded to prevent excessive measurement noise propagation on the correction (see Sec. 5.3.1).

C.2 Conceptual design for the leveling service

End of LS1, 2013 Towards the end of Long Shutdown 1 (see Tab. 2.3) β^* leveling was still considered as a possible option for operation in 2015 and beyond. We therefore developed a concept of a leveling service. To simplify the daily life of the LHC operation group a central service for luminosity optimization and control was proposed. That service could handle the leveling requests (either for the offset or for β^* see Sec. 3.1) and schedule their execution accordingly to the current luminosity production. Such a service should also track and protect the executed commands from being lost or overridden – the idea of an arbiter was introduced.

Since eventually the beam and machine parameters were such as not require β^* leveling, the

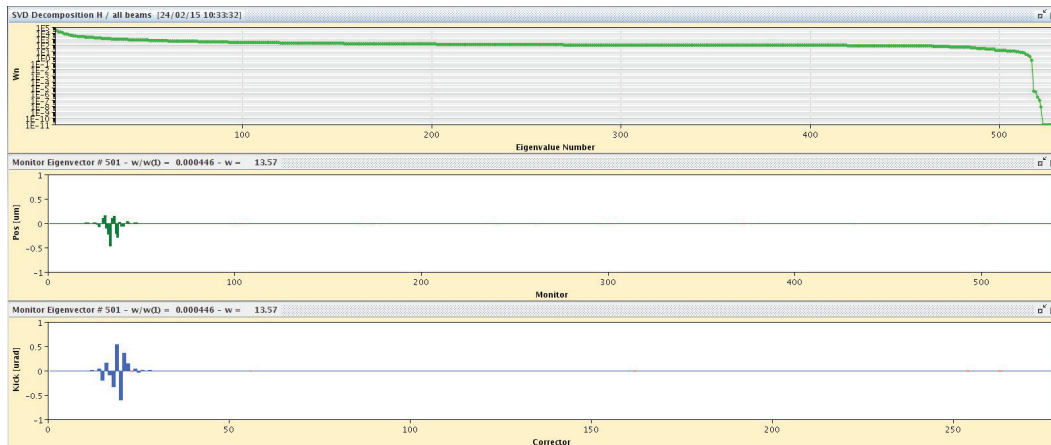


Figure C.1 – Eigenvalue spectrum for LHC Beam 2 based on the response matrix created for both beams (coupling via common correctors), ordered from the largest to the smallest eigenvalue. The spectrum has cut-off around EV#510 above which the values become very singular. The middle and bottom plots represent the orbit and corrector eigenvector for a $\lambda_{\#501}$

service remained in the conceptual phase with only little of it actually being implemented.

Luminosity Server 2015 With the LHC restart in 2015 new demands for luminosity optimization and calibration triggered a new effort to improve tools for luminosity control. The old tools in the form of an application were replaced with a server–client based on a "Luminosity Server" and client GUIs. The role of the server is to manage luminosity optimizations and calibration scan [97, 98], providing at the same time improved flexibility for beams control at the IPs. Many of the concepts (and first implementations) were kept from the first design (see previous paragraph).

Nowadays, except for the offset leveling in ALICE and LHCb part all the luminosity optimization and calibration tasks are executed by the new *Luminosity server*. Since it partially used the design form newly designed luminosity leveling service, it is ready to take over and include the luminosity leveling part in the future.

C.3 Generation of spiral scans

The spiral shape of the beam movement at the IP for the rotation scans was obtained by pre-generated orbit changes using LUMI -SCAN knobs. This knobs use four corrector bumps created around the IPs as shown in Fig. C.2. The complexity (and the requirement of pre-generation of the whole function) of the scan shape arises from the power converter limitations and response times . The requirements for the validation consist of superposition of the actual scan (described by the Eq.7.2) and the drift with a constant speed (Eq.7.3).

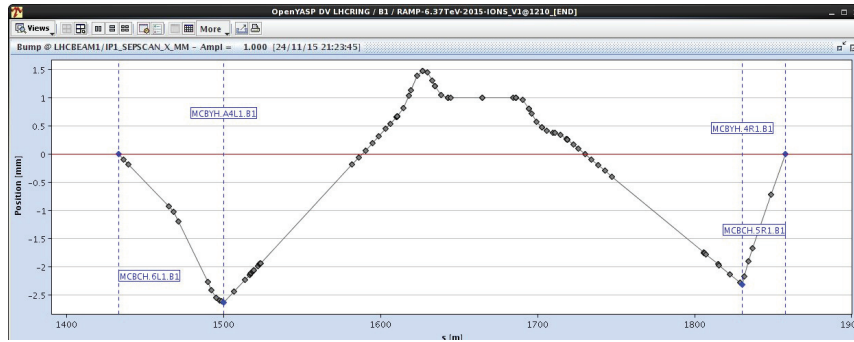


Figure C.2 – LUMI-SCAN Knob example for the Beam1 in IP1.

Generation Application A JAVA application was created to help with generation of such a scans. Figure C.3 shows the main panel of the application. To overcome issues with PC limitations, an automated algorithm was implemented to vary the parameters of the scan in case it does not fulfill the PC requirements. The algorithm is programmed to perform 20 attempts before giving up. User can track those actions and re-initialize for next iteration if needed. Figure C.4 illustrates the functions that were sent to the magnets.

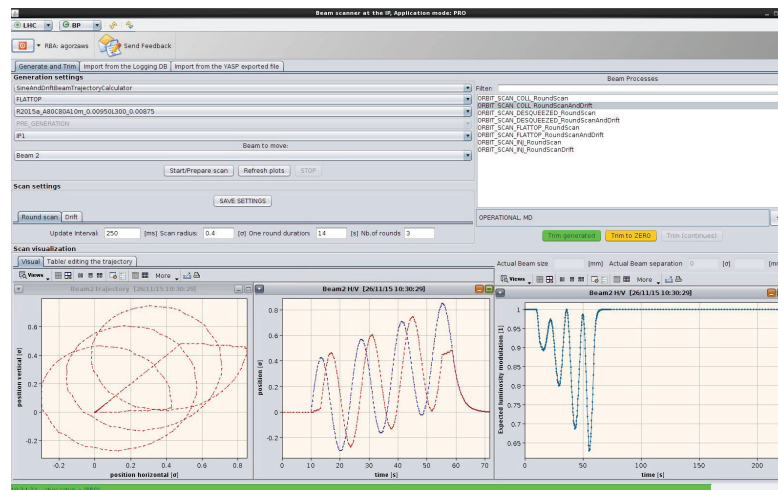


Figure C.3 – *Generation Application* main panel. The upper left part allows to set up the scan type and parameters like energy, IP and optics. The middle and bottom part defines scan properties like scan radius, number of scans, frequency etc. An additional part to overlay an artificial drift is accessible as well. The bottom part visualizes the scans. The top right hand side represents the LSA Beam Process selection box.

C.4 Initial finding of the collisions

A spin-of of the stabilization method (Chap. 7) based on the circular scans can be used to find first collisions after long machine stops, typically a winter stop.

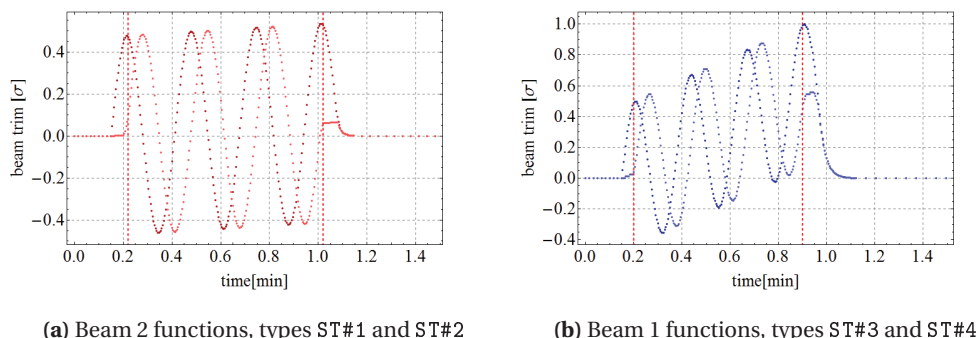


Figure C.4 – Example of actual functions expressed in beam sie at the IP (horizontal–darker and vertical–lighter) that were used for the tests. The circular scan radius was 0.56σ for those examples.

After a winter stop when the machine is realigned, elements are changed, the optics is modified, the 2 beams will not necessarily collide when the beam separation is collapsed. Due to the offsets between quadrupoles and BPMs, it is not possible to accurately predict the beam overlap at the IP. For the smallest beam sizes the beam offsets may exceed 10σ in each plane. A search in 2 directions must be performed to bring beams into collisions.

A modified rotation scan with a growing radius $\delta(t)$ can be used to generate a spiral motion of the beams around each other. Eventually signs of collisions may be observed when the beam tailtouch each other (see Figs. C.5a, C.5b). Ideally the scan is stopped as soon as significant luminosity signal is observed. Once some collisions occur, the final optimization can be preformed in a few minutes.

We demonstrated validity of the method on April 8th 2016. During the re-commissioning of the machine after the 2015–2016 winter stop, we attempted to establish head-on collisions (see Fig. C.6) in one IP with this technique. Unfortunately the beams were so far apart that a current limit on one orbit corrector stopped the scan. A re-steering of the beams had to be done, but principle of the method was demonstrated.

C.5 Luminosity data with higher rate

The stabilization scans should be performed during β^* leveling step that are usually ≈ 60 s long, the time for the scan should be limited to significantly less than for the tests. The standard 1 Hz luminosity data stream is not sufficient, a higher rate is required. For tests we managed to obtain 10 Hz data from the LHCb and 3 Hz data from ATLAS. The second was unfortunately accessible only offline but as it was a pilot test of this method this was acceptable. With the LHCb data group, thanks to R. Jacobsson, we managed to establish an on-line transmission that is illustrated in Fig. C.7 and to connect the data online during the experiment.

C.5. Luminosity data with higher rate

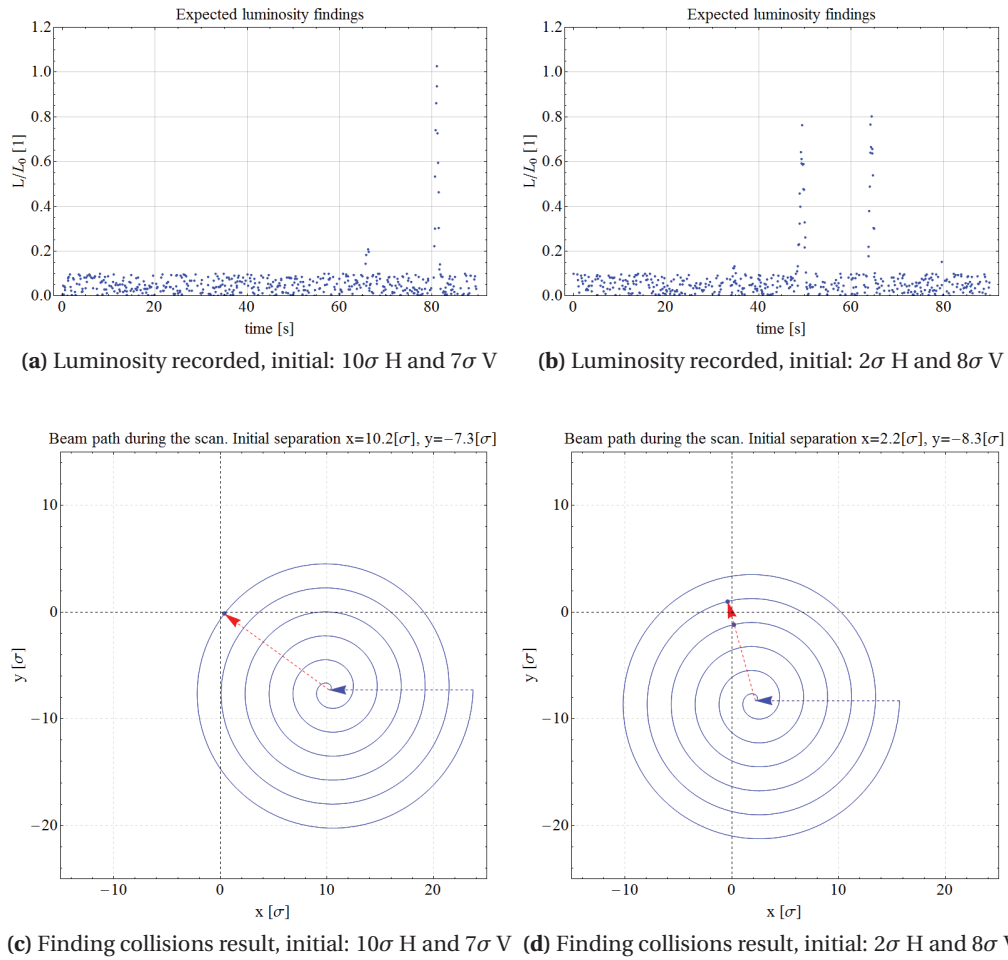


Figure C.5 – Example for finding collisions for a given initial separation based on a spiral scan. Example simulated for a beam size of $\sigma=18\ \mu\text{m}$ ($\beta^* 80\ \text{cm}$).

Appendix C. LHC analysis and operation tools



Figure C.6 – Finding collisions with a *spiral scan* (seen as a black line in the right bottom part, here in "rectangular form") on April 8th 2016 when establishing first collisions after the winter stop in 2015/2016.

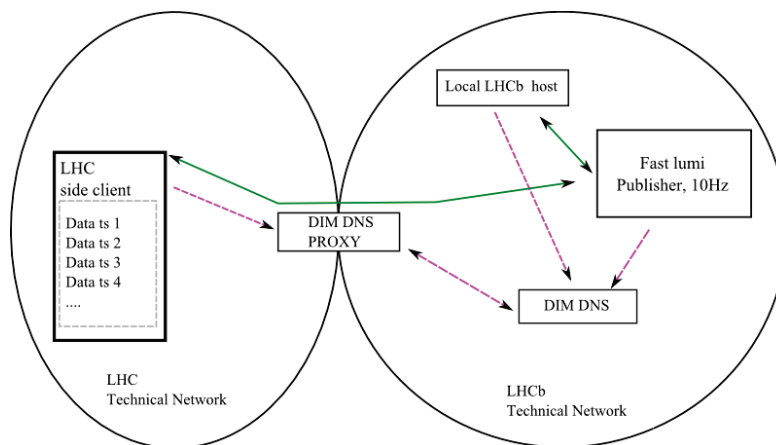


Figure C.7 – Principle of the LHCb luminosity data transmission. Unlike the local LHCb TN (Technical Network) host, the LHC TN host needs to communicate through the proxy for establishing the data connection (magenta channel). After connection is ensured by the proxy broker, the communication remains at the peer-to-peer level (green channel) [99].

C.6 Luminosity leveling predictor

A dedicated tool for luminosity leveling predictions was developed. Listing C.1 shows the simplest usage of the tool. Based on the beam properties the tool is able to construct the different operations such as leveling duration, leveling mixture need or β^* step granularity. Figure C.8 shows the graphical output of the tool that visualizes the optics, calculated luminosity as well as integrated luminosity for the optimal fill length.

Listing C.1 – Leveling code

```

1  LuminosityLevellingIP15ModelStrategy calc = new
    LuminosityLevellingIP15ModelStrategy();
2  BeamTypeEnum[] beamTypes = { BeamTypeEnum.BCMS_8b_4e,
    BeamTypeEnum.BCMS_25ns_PUSHED };
3  for (BeamType beamType : beamTypes) {
4      LHCLuminosityPerFillReadObjectContext context =
        ContextGenerator.simpleContext(beamType);
5      Collection<LHCLuminosityProjectionContext> calculatedData
        = calc.calculateProjectedLuminosity(context);
6      LHCLuminosityProjectionContext resultData = calculatedData
        .iterator().next();
7      printLevelingConditions(beamType, resultData, calc.
        getAcceptableMaxPileUp());
8      plotData(calculatedData, beamType);
9  }

```

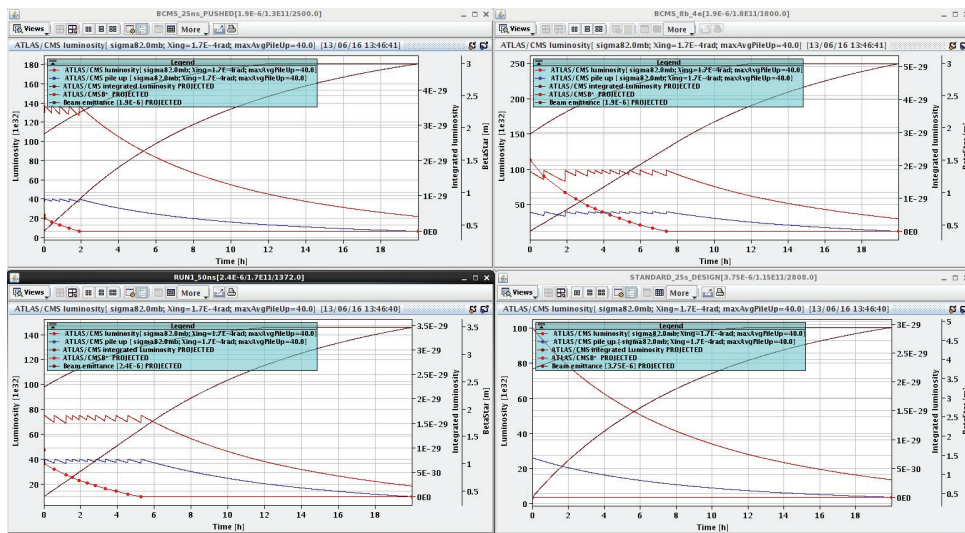


Figure C.8 – Result panel of the luminosity leveling tool.

C.7 Bunch by Bunch orbit with LR interactions: TRAIN

The TRAIN code [90] was refurbished to study the impact of the LR interactions on the rotation scan (see more in Sec. 7.5).

To improve, simplify and offer proper maintainability of the code the following changes were made (full list to be found under <https://gitlab.cern.ch/agorzaws/train>):

1. A versioning system for both optics and source code files was put in place (see Fig. C.9)
2. Optics input and source code was clearly separated (see Fig. C.10).
3. A general maintenance was made to simplify inputs such as filling schemes, correctness of the coherent beam–beam kicks calculation and the import of the optics file.
4. Improved and simplified result presentation using Python plotting scripts.

An attempt to generalize the TRAIN code for any collider was started. Since the amount of changes for such a generalization requires many man–weeks of work, we decided to focus on the LHC and simplified¹ HL–LHC cases [100].

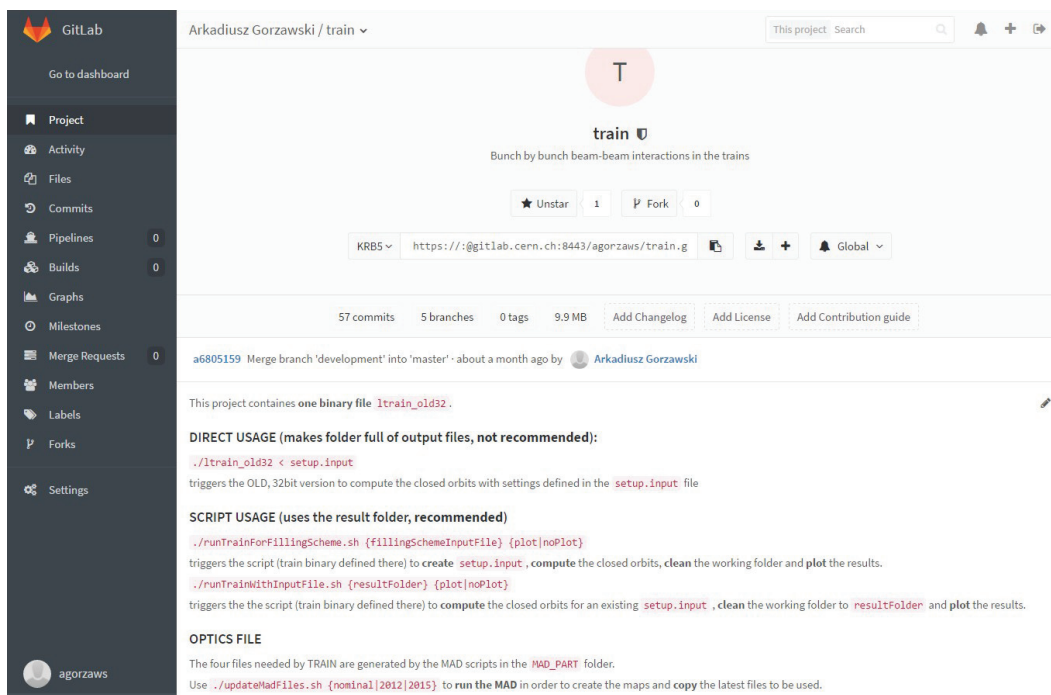


Figure C.9 – Cover page of the TRAIN repository <https://gitlab.cern.ch/agorzaws/train>.

¹number of LR encounters per IP side is still 15 not 17

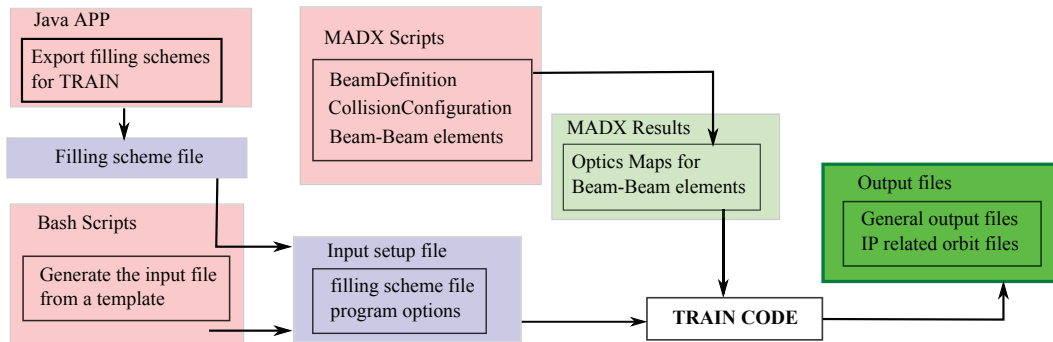


Figure C.10 – Structure of the TRAIN data flow. Input files marked in red. The middle state result/input files in blue.

Bibliography

- [1] K. Wille, *The physics of particle accelerators: an introduction*. Oxford: Oxford Univ. Press, 2000.
- [2] H. Wiedemann, *Particle accelerator physics; 3rd ed.* Berlin: Springer, 2007.
- [3] D. A. Edwards and M. J. Syphers, *An introduction to the Physics of High Energy Accelerators*. Wiley Beam Phys. Accel. Technol., New York, NY: Wiley, 1993.
- [4] A. W. Chao, *Physics of collective beam instabilities in high energy accelerators*. New York, NY: Wiley, 1993.
- [5] W. Magnus and S. Winkler, *Hill's equation*. Internat. Sci. Tracts Pure Appl. Math., New York, NY: Interscience, 1966.
- [6] E. D. Courant and H. S. Snyder, "Theory of the Alternating-Gradient Synchrotron," *Ann. Phys.*, vol. 3, pp. 1–48, 1958.
- [7] M. G. Minty and F. Zimmermann, *Measurement and control of charged particle beams*. Particle acceleration and detection, Berlin: Springer, 2003.
- [8] W. Press, B. Flannery, S. Teukolsky, and W. Vetterling, *Numerical Recipes*, vol. 1st. Cambridge University Press, Cambridge, 1987.
- [9] B. Autin and Y. Marti, "Closed orbit correction of A.G.machines using a small number of magnets," Tech. Rep. CERN-ISR-MA-73-17. ISR-MA-73-17. ISR-MA-73-17, CERN, Geneva, Mar 1973.
- [10] A. W. Chao, K. H. Mess, M. Tigner, and F. Zimmermann, *Handbook of accelerator physics and engineering; 2nd ed.* Singapore: World Scientific, 2013.
- [11] M. Benedikt, P. Collier, V. Mertens, J. Poole, and K. Schindl, *LHC Design Report*. Geneva: CERN, 2004.
- [12] W. Herr and B. Muratori, "Concept of luminosity," *CERN*, 1999.
- [13] M. Schaumann, J. M. Jowett, and R. Bruce, "Intra-beam Scattering and Luminosity Evolution for HL-LHC Proton Beams," Tech. Rep. CERN-ATS-2012-290, CERN, Geneva, Dec 2012.

Bibliography

- [14] A. W. Chao, “Beam dynamics with high intensity,” in *CAS Intensity Limitations in Particle Beams* (W. Herr, ed.), CERN, CERN, 2016.
- [15] G. Rumolo, G. Iadarola, O. Domínguez, G. Arduini, H. Bartosik, S. Claudet, J. Esteban-Müller, F. Roncarolo, E. Shaposhnikova, and L. Tavian, “LHC experience with different bunch spacings in 2011 (25, 50 and 75 ns),” in *Chamonix 2012 Workshop on LHC Performance*, pp. pp.89–98, Feb 2012.
- [16] K. S. B. Li and G. Rumolo, “Review of beam instabilities in the presence of electron clouds in the LHC,” *CERN Document Server*, p. 3 p, Sep 2011.
- [17] T. Pieloni, “Beam–Beam Effects in Hadron Colliders,” in *CAS Intensity Limitation in the particle beams*, (Geneva), CERN, CERN, 2016. Not yet published.
- [18] W. Höfle, “Transverse damper,” in *Chamonix 2012 Workshop on LHC Performance*, CERN, CERN, 2012. CERN-2012-006.157.
- [19] W. Hofle, G. Arduini, R. de Maria, G. Kotzian, D. Valuch, and V. Lebedev, “Suppression of emittance growth by excited magnet noise with the transverse damper in LHC in simulation and experiment,” in *Proc. of International Particle Accelerator Conference (IPAC’12), San Sebastian, Spain, 4 - 9 Sep 2011*, (Geneva, Switzerland), pp. 508–510, JACoW, Sep 2011. CERN-ATS-2011-038.
- [20] X. Buffat, W. Herr, N. Mounet, T. Pieloni, and S. White, “Stability diagrams of colliding beams in the large hadron collider,” *Phys. Rev. ST Accel. Beams*, vol. 17, p. 111002, Nov 2014.
- [21] W. Herr and T. Pieloni, “Beam–beam effects,” in *Proceedings of the CAS - CERN Accelerator School: Advanced Accelerator Physics Course*, p. 29 p, 2014. arXiv:1601.05235.
- [22] S. M. White, H. Burkhardt, and P. Puzo, *Determination of the Absolute Luminosity at the LHC*. PhD dissertation, Orsay, Université Paris-Sud 11, Orsay, 2010. Presented on 11 Oct 2010.
- [23] X. Buffat, L. Rivkin, and T. Pieloni, *Transverse beams stability studies at the Large Hadron Collider*. PhD dissertation, Ecole Polytechnique, Lausanne, Lausanne, Jan 2015. Presented 30 Jan 2015.
- [24] T. Pieloni, W. Herr, A. Bay, and L. Rivkin, *A study of beam-beam effects in hadron colliders with a large number of bunches*. PhD dissertation, Ecole Polytechnique, Lausanne, Milan U., 2008. Presented on 4 Dec 2008.
- [25] W. Herr, “Tune shifts and spreads due to short and long range beam-beam interactions in the LHC,” *CERN Document Server*, no. CERN-LHC-Note-119. CERN-SL-90-06-AP. LHC-NOTE-119, p. 26 p, 1990.

-
- [26] W. Herr, R. Calaga, E. Laface, G. Papotti, T. Pieloni, R. Alemany-Fernandez, R. Giachino, and M. Schaumann, “Observations of beam-beam effects at high intensities in the LHC,” *CERN Document Server*, p. 3 p, Sep 2011.
- [27] R. Bartoldus, “Online Determination of the LHC Luminous Region with the ATLAS High-Level Trigger,” Tech. Rep. ATL-DAQ-PROC-2011-028, CERN, Geneva, Oct 2011.
- [28] S. White, X. Buffat, N. Mounet, and T. Pieloni, “Transverse mode coupling instability of colliding beams,” *Phys. Rev. ST Accel. Beams*, vol. 17, p. 041002, Apr 2014.
- [29] C. De Melis, “The CERN accelerator complex. Complexe des accélérateurs du CERN,” *CERN Document Server*, Jan 2016. General Photo.
- [30] CERN, “CERN Document Server Photos.”
- [31] www.lhc.closer.es, “Web portal for the lhc facts.”
- [32] R. Bruce, “Collimator hierarchy limits: assumptions and impact on machine protection and performance,” in *MPP Workshop on LHC Machine Protection* (M. Jonker, ed.), <https://cds.cern.ch/record/1695409>, CERN, 2013.
- [33] CERN, *Proceedings of the CERN Accelerator School Beam Diagnostics*, (Geneva), CERN, 2009. In collaboration with Synchrotron SOLEIL, Gif-sur-Yvette, France.
- [34] A. Nosych, U. Iriso, A. Olmos, and M. Wendt, “Overview of the Geometrical Non-Linear Effects of Button BPMs and Methodology for Their Efficient Suppression,” in *Proc. 3rd International Beam Instrumentation Conference, Monterey, CA, USA*, (Geneva, Switzerland), pp. 298–302, JACoW, 2014.
- [35] A. Nosych, U. Iriso, and J. Olle, “Electrostatic Finite-element Code to Study Geometrical Nonlinear Effects of BPMs in 2D,” in *Proc. of International Beam Instrumentation Conference (IBIC2015), Melbourne, Australia, 13-17 September 2015* (A. Mark Boland (SLSA, Clayton, ed.), no. 4 in International Beam Instrumentation Conference, (Geneva, Switzerland), pp. 418–422, JACoW, JACoW, Jan 2016.
- [36] M. Gasior and R. Jones, “High Sensitivity Tune Measurement by Direct Diode Detection,” *CERN Document Server*, p. 3 p, Apr 2005.
- [37] E. Calvo Giraldo, J. L. Gonzalez, L. K. Jensen, O. R. Jones, T. Lefevre, J. J. Savioz, R. Steinhagen, and J. Wenninger, “The LHC Beam Position System: Performance during 2010 and Outlook for 2011,” *Conf. Proc.*, vol. C11-05-16.4, p. TUPD12. 3 p, May 2011.
- [38] M. Gasior, J. Olexa, and R. J. Steinhagen, “A High-resolution Diode-Based Orbit Measurement System - Prototype Results from the LHC,” *Conf. Proc.*, vol. C11-05-16.4, p. MOPD24. 3 p, May 2011.

Bibliography

- [39] G. Valentino *et al.*, “First Operational Experience with Embedded Collimator BPMs in the LHC,” in *Proc. of International Particle Accelerator Conference (IPAC’16), Busan, Korea, May 8-13, 2016*, no. 7 in International Particle Accelerator Conference, (Geneva, Switzerland), pp. 2510–2513, JACoW, June 2016. doi:10.18429/JACoW-IPAC2016-WEPMW034.
- [40] R. J. Steinhagen and J. Wenninger, *LHC Beam Stability and Feedback Control - Orbit and Energy* -. PhD dissertation, RWTH Aachen U., Aachen, 2007. Presented on 22 Jun 2007.
- [41] CERN, “HL-LHC project, <http://hilumilhc.web.cern.ch/about/hl-lhc-project>.” <http://hilumilhc.web.cern.ch/about/hl-lhc-project>, 2016. [Online; accessed 19-July-2016].
- [42] D. Jacquet, R. Gorbonosov, and G. Kruk, “LSA - the High Level Application Software of the LHC - and Its Performance During the First Three Years of Operation,” *CERN Document Server*, Mar 2014.
- [43] R. Jacobsson, “Future wishes and constraints from the experiments at the LHC for the proton-proton programme. LHC, Large Hadron Collider,” in *ICFA Mini-Workshop on Beam-Beam Effects in Hadron Colliders (BB2013), Cern, Switzerland, 18 - 22 Mar 2013*, p. 15 p, May 2013. arXiv:1410.3663. CERN-LHCb-PROC-2013-029. CERN-ATS-Note-2013-030 PERF LHCb-PROC-2013-029.
- [44] A. Vogel, “ATLAS Transition Radiation Tracker (TRT): Straw Tube Gaseous Detectors at High Rates,” Tech. Rep. ATL-INDET-PROC-2013-005, CERN, Geneva, Apr 2013.
- [45] X. Buffat, D. Banfi, G. R. Coombs, W. Herr, and T. Pieloni, “HL-LHC parameter space and scenarios,” in *Proc. of Chamonix 2012 Workshop on LHC Performance*, (Geneva), pp. 315–325, Feb 2012. CERN-ATS-2012-069.
- [46] P. Baudrenghien, J. Noirjean, and T. Mastoridis, “Cogging for 2-beam impedance MD,” tech. rep., CERN LHC Studies Working Group 25, 2012.
- [47] P. Baudrenghien, C. Bhat, T. Bohl, J. F. Esteban Müller, T. Mastoridis, J. Molendijk, G. Papotti, E. Shaposhnikova, H. Timko, and U. Wehrle, “Dependence of single beam lifetime on bunch length,” *CERN Document Server*, Sep 2011.
- [48] R. B. Palmer, “Energy scaling, crab crossing and the pair problem,” *CERN Document Server*, p. 7 p, Dec 1988.
- [49] R. Calaga, E. Jensen, G. Burt, and A. Ratti, “Crab Cavity Development,” *Adv. Ser. Dir. High Energy Phys.*, vol. 24, pp. 137–156, 2015.
- [50] S. Fartoukh, “Pile up management at the high-luminosity LHC and introduction to the crab-kissing concept,” *CERN Document Server*, Nov 2014.
- [51] X. Buffat, W. Herr, E. Métral, N. Mounet, and T. Pieloni, “Head-On and Long Range Beam-Beam Interactions in the LHC: Effective Tune Spread and Beam Stability Due to Landau Damping,” Tech. Rep. CERN-ACC-2013-0142, CERN, Geneva, May 2013.

-
- [52] A. Gorzawski, “Leveling options and strategy,” in *5th Evian Workshop on LHC beam operation* (B. Goddard and S. Dubourg, eds.), CERN, CERN, 2014. CERN-ACC-2014-0319.
- [53] X. Buffat, D. Banfi, G. R. Coombs, W. Herr, and T. Pieloni, “Beam-beam effects in different luminosity levelling scenarios for the LHC,” in *Proc. of International Particle Accelerator Conference (IPAC’14), Dresden, Germany, June 15-20, 2014*, no. CERN-ACC-2014-0101 in International Particle Accelerator Conference, (Geneva), Jun 2014.
- [54] R. Jacobsson, R. Alemany-Fernandez, and F. Follin, “The LHCb Online Luminosity Monitoring and Control,” *CERN Document Server*, Oct 2013.
- [55] E. Metral, “Review of the instabilities observed during the 2012 run and actions taken,” in *Proceedings Of The 2012 Evian Workshop on LHC Beam Operation*, pp. pp.87–95, Dec 2012.
- [56] T. Pieloni, “Observations of instabilities during OP scans,” tech. rep., CERN LHC Beam Operation Committee 49, 2015.
- [57] G. Arduini, R. Giachino, W. Herr, E. Metral, G. Papotti, T. Pieloni, X. Buffat, and N. Mounet, “Observations of Instabilities in the LHC Due to Missing Head-On Beam-Beam Interactions,” Tech. Rep. CERN-ACC-2013-0139, CERN, Geneva, May 2013.
- [58] G. Rumolo, “Electron Cloud I, II,” in *CAS Intensity Limitation in the particle beams*, (Geneva), CERN, CERN, 2016. Not yet published.
- [59] Y. Papaphilippou, H. Bartosik, G. Rumolo, and D. Manglunki, “Operational Beams for the LHC,” *CERN Document Server*, 2015.
- [60] A. Gorzawski, “Beta* leveling scenarios and implementation,” tech. rep., CERN LHC Beam Operation Committee 16, 2014.
- [61] J. Weninnger, “Private communication.” in 2013–2016.
- [62] T. Pieloni, “Beam stability with colliding beams at 6.5 TeV,” in *Proceedings Of The 2012 Evian Workshop on LHC Beam Operation*, pp. pp.101–109, Dec 2012.
- [63] X. Buffat, W. Herr, T. Pieloni, M. Lamont, S. Redaelli, and J. Weninnger, “Results of b* luminosity leveling,” *CERN MD Note*, 2012.
- [64] X. Buffat, W. Herr, T. Pieloni, L. Ponce, S. Redaelli, and J. Wenninger, “MD on squeeze with colliding beams,” *CERN Document Server*, Jan 2013.
- [65] X. Buffat, “Squeezing with colliding beams,” in *Proceedings Of The 2012 Evian Workshop on LHC Beam Operation*, pp. pp.27–33, Dec 2012.
- [66] A. Gorzawski, D. Mirarchi, G. Papotti, B. M. Salvachua Ferrando, T. Pieloni, and J. Wenninger, “Collide and Squeeze MD,” *CERN Document Server*, Dec 2015.

Bibliography

- [67] A. Gorzawski, D. Mirarchi, B. M. Salvachua Ferrando, and J. Wenninger, “MD 239 on Collide and Squeeze (part 2),” *CERN Document Server*, Jan 2016.
- [68] A. Gorzawski, D. Mirarchi, B. Salvachua, and J. Wenninger, “Experimental Demonstration of beta* Leveling at the LHC,” in *Proc. of International Particle Accelerator Conference (IPAC'16), Busan, Korea, May 8-13, 2016*, no. 7 in International Particle Accelerator Conference, (Geneva, Switzerland), pp. 1442–1445, JACoW, June 2016. doi:10.18429/JACoW-IPAC2016-TUPMW013.
- [69] L. Rossi and O. Brüning, “High Luminosity Large Hadron Collider A description for the European Strategy Preparatory Group,” Tech. Rep. CERN-ATS-2012-236, CERN, Geneva, Aug 2012.
- [70] S. Fartoukh, “Achromatic telescopic squeezing scheme and application to the LHC and its luminosity upgrade,” *Phys. Rev. Spec. Top. Accel. Beams*, vol. 16, p. 111002. 33 p, Dec 2013.
- [71] S. Fartoukh, “ATS MD experience for run I and perspective for run II,” tech. rep., CERN LHC Studies Working Group Day, 2015.
- [72] R. Alemany-Fernandez, E. Bravin, L. Drosdal, A. Gorzawski, V. Kain, M. Lamont, A. Macpherson, G. Papotti, M. Pojer, L. Ponce, S. Redaelli, G. Roy, M. Solfaroli Camillocci, W. Venturini, and J. Wenninger, “Operation and Configuration of the LHC in Run 1,” *CERN Document Server*, Nov 2013.
- [73] R. Steinhagen, “Real-Time Beam Control at the LHC,” *CERN Document Server*, p. 5 p, Mar 2011.
- [74] K. Fuchsberger, “LHC orbit system, performance and stability. Orbit system,” in *Proc. of Evian 2010 Workshop on LHC Commissioning*, pp. 45–51, Jan 2010. CERN-ATS-2010-028.
- [75] A. Herty, *Micron precision calibration methods for alignment sensors in particle accelerators*. Master thesis, Nottingham Trent University, March 2009.
- [76] J.-P. Tock, “Private communication.” in 2016.
- [77] J. Wenninger, “It movements, atlas luminosity and orbit,” tech. rep., CERN LHC Beam Operation Committee 62, 2016.
- [78] K. Brodzinski, “private communication.” in 2016, 2016.
- [79] A. Gorzawski and J. Wenninger, “Orbit drifts at the LHC interaction points during the squeeze,” *CERN Document Server*, May 2015.
- [80] E. Calvo, B. Araujo, J. L. Gonzalez, L. Jensen, O. R. Jones, T. Lefevre, J. J. Savioz, and R. Steinhagen, “BPM: status, measurement reliability and outlook for 2011,” *CERN Document Server*, 2010.

-
- [81] A. Gorzawski, “First experience with the Q1 DOROS BPMs,” tech. rep., CERN LHC Beam Operation Committee 48, Nov 2015.
- [82] J. Emery, B. Dehning, C. Morais Pereira, J. Sirvent Blasco, S. Cantin, M. Tognolini, B. Schneider, K. Henzer, and M. Starkier, “A fast and accurate wire scanner instrument for the CERN accelerators to cope with severe environmental constraints and an increased demand for availability,” *IEEE Nucl. Sci. Symp. Conf. Rec.*, pp. 1139–1145. 7 p, 2014.
- [83] R. Jung, P. A. Komorowski, L. Ponce, and D. Tommasini, “The LHC 450 GeV to 7 TeV Synchrotron Radiation Profile Monitor using a Superconducting Undulator,” *AIP Conf. Proc.*, vol. 648, pp. 220–228. 9 p, May 2002.
- [84] G. Trad, E. Bravin, A. Goldblatt, S. Mazzoni, T. Mitsuhashi, and F. Roncarolo, “Performance of the Upgraded Synchrotron Radiation Diagnostics at the LHC,” in *Proc. of International Particle Accelerator Conference (IPAC’16), Busan, Korea, May 8-13, 2016*, no. 7 in International Particle Accelerator Conference, (Geneva, Switzerland), pp. 306–309, JACoW, June 2016. doi:10.18429/JACoW-IPAC2016-MOPMR030.
- [85] M. Kuhn, “Updated results from triplet k-modulation,” tech. rep., CERN LHC Beam Operation Committee 52, 2015.
- [86] T. Persson, “Beta* corrections strategies,” tech. rep., CERN LHC Beam Operation Committee 52, 2015.
- [87] J. Weninger, “Update on crossing angles in IR1 and IR5,” tech. rep., CERN LHC Beam Operation Committee 51, Dec 2016.
- [88] X. Buffat, W. Herr, T. Pieloni, L. Ponce, S. Redaelli, and J. Weninger, “Squeeze with colliding beams,” *CERN MD Note*, 2012.
- [89] A. Gorzawski, R. Jacobsson, and J. Weninger, “Beam Offset Stabilization Techniques for the LHC Collision Points,” in *Proc. of International Particle Accelerator Conference (IPAC’16), Busan, Korea, May 8-13, 2016*, no. 7 in International Particle Accelerator Conference, (Geneva, Switzerland), pp. 1438–1441, JACoW, June 2016. doi:10.18429/JACoW-IPAC2016-TUPMW012.
- [90] H. Grote, “Self-consistent Orbits for Beam-beam Interactions in the LHC,” Tech. Rep. LHC-PROJECT-NOTE-216, CERN, Geneva, Feb 2000.
- [91] M. Hostettler, “Update on emittance measurements from OP scans,” tech. rep., CERN LHC Beam Operation Committee 49, Dec 2015.
- [92] M. Hostettler and G. Papotti, “Beam Size Estimation from Luminosity Scans at the LHC During 2015 Proton Physics Operation,” in *Proc. of International Particle Accelerator Conference (IPAC’16), Busan, Korea, May 8-13, 2016*, no. 7 in International Particle Accelerator Conference, (Geneva, Switzerland), pp. 290–292, JACoW, June 2016. doi:10.18429/JACoW-IPAC2016-MOPMR025.

Bibliography

- [93] J. Wenninger, "Yet Another Steering Program," 2008.
- [94] K. Fuchsberger, V. Baggiolini, R. Gorbonosov, W. Herr, V. Kain, G. Mueller, S. Redaelli, F. Schmidt, and J. Wenninger, "JMAD - Integration of MADX into the Java World," *CERN Document Server*, p. 4 p, May 2010.
- [95] C. Roderick, L. Burdzanowski, and G. Kruk, "The CERN Accelerator Logging Service- 10 Years in Operation: A Look at the Past, Present and Future," *CERN Document Server*, p. 3 p, Oct 2013.
- [96] R. W. Assmann, P. Raimondi, G. Roy, and J. Wenninger, "Emittance optimization with dispersion free steering at LEP," *Phys. Rev. Spec. Top. Accel. Beams*, vol. 3, p. 121001, Dec 2000.
- [97] M. Hostettler, A. Gorzawski, and R. Alemany, "The new luminosity-scan application: features, user interface, tests and dry runs," tech. rep., LHC Luminosity Calibration and Monitoring Working Group, Oct 2015.
- [98] M. Hostettler, "Update on emittance measurements from OP scans," tech. rep., CERN LHC Operation meeting, 2015.
- [99] R. Jacobsson, "Private communication." in 2015.
- [100] T. Pieloni, "Private communication." in 2016.

ARKADIUSZ ANDRZEJ GORZAWSKI

address	10 route des Collonges, 01550 Pougny, France
date and place of birth:	30.11.1982, Knurów, Poland
mob (FR, CH)	+33 771 265 101, +41 75 411 2358
e-mail	arkadiusz.gorzawski@cern.ch
social	www.linkedin.com/in/arekgorzawski

PHYSICIST & SOFTWARE ENGINEER

WORK EXPERIENCE

CERN - EUROPEAN ORGANIZATION FOR NUCLEAR RESEARCH IN GENEVA

01.07.2016 – 31.12.2016 POST: **Visiting Scientist in LHC Operation/Machine Protection Group**

UNDER THE SUPERVISION OF **Dr. Jörg Wenninger / Dr. Markus Zerlauth**

TASKS: Development for an operational software (PcInterlock, OrbitAnalysis) and beam dynamics tools (TRAIN) for the LHC and future accelerators.

01.07.2013 – 30.06.2016 POST: **CERN Doctoral Student in Beams Department, LHC Operation**

UNDER THE SUPERVISION OF **Dr. Jörg Wenninger**

TASKS: Research and development on the operational schema for the luminosity adjustment, called β^* leveling, needed for the High Luminosity upgrade of the LHC (using MADX, Mathematica, R) and finding the limits for the beam separation at the collision point. Paving the way for new stabilization techniques. Work with operational tools development PcInterlock, OrbitAnalysis and TRAIN. Participation in daily machine operation and dedicated machine development sessions.

01.07.2010 – 30.06.2013 POST: **CERN Fellow in Technology Department, Machine Protection Group**

UNDER THE SUPERVISION OF **Dr. Markus Zerlauth**

TASKS: Design and development of software for machine protection and accelerator testing concerning large projects for machine testing (AccTesting), protection (PcInterlock) and analysis purpose (AnalysisFramework, LHC PMAAnalysisModules). Leading a team of seven people within a section dedicated for a software development (Agile approach, Scrum Master/Product Owner, Crisis Management, Critical Thinker, TDD). Research and first implementations on new technologies for the future needs in automated analysis and large scale storage.

15.03.2006 – 31.03.2010 POST: **LHC Project Associate in Accelerator Technology Department,**

UNDER THE SUPERVISION OF **Knud Dahlerup-Petersen / Dr. Markus Zerlauth**

TASKS: Developing applications for operational tests of the protection systems for superconducting magnets of the LHC. Hardware commissioning team leader in the control room (Crisis Management, Critical Thinker). Developing software for an analysis framework.

AGH UNIVERSITY OF SCIENCE AND TECHNOLOGY IN CRACOW

JUNE 2005 POST: **Students Practice in Department of Process Engineering**

TASKS: Thermal radiation, heat and fluid transfer simulations.

EDUCATION

October 2016 PH.D. IN PHYSICS

Thesis directors Prof. Leonid Rivkin and Dr. Jörg Wenninger

Luminosity leveling and beam orbit stability with β^ leveling at LHC and HL-LHC.*

01.07.2013 – 30.11.2016 ÉCOLE POLYTECHNIQUE FÉDÉRALE DE LAUSANNE

Faculty of Physics, specialization: Accelerator physics, Doctorate school.

29.11.2006 M.SC. ENG. IN COMPUTER PHYSICS

01.10.2001 – 31.10.2006 AGH UNIVERSITY OF SCIENCE AND TECHNOLOGY IN CRACOW

Faculty of Physics and Applied Computer Science, Applied physics in computing

01.09.1997 – 05.06.2001 SECONDARY HIGH SCHOOL IN RYBNIK

ARKADIUSZ ANDRZEJ GORZAWSKI

address	10 route des Collonges, 01550 Pougny, France
date and place of birth:	30.11.1982, Knurów, Poland
mob (FR, CH)	+33 771 265 101, +41 75 411 2358
e-mail	arkadiusz.gorzawski@cern.ch
social	www.linkedin.com/in/arekgorzawski

PHYSICIST & SOFTWARE ENGINEER

Conference publications:

1. A.A. Gorzawski, R. Jacobsson, and J. Wenninger. Beam Offset Stabilization Techniques for the LHC Collision Points. In *Proc. of International Particle Accelerator Conference (IPAC'16), Busan, Korea, May 8-13, 2016*,
2. A.A. Gorzawski, D. Mirarchi, B. Salvachua, and J. Wenninger. Experimental Demonstration of beta* Leveling at the LHC. In *Proc. of International Particle Accelerator Conference (IPAC'16), Busan, Korea, May 8-13, 2016*
3. D. Anderson, M. Audrian, Z. Chaifoulline, M. Dragu, A.A. Gorzawski, S. Rowan, M. Dragu, K. Fuchsberger, M. Koza, K.H. Krol, K. Misiowiec, J.C. Garnier, K. Stamos, and M. Zerlauth. Testing quality and metrics for the LHC magnet powering system throughout past and future commissioning. In *Proc. of International Particle Accelerator Conference (IPAC'14), Dresden, Germany June 13-20, 2014*,
4. A.A. Gorzawski and J. Wenninger. Implementation of luminosity leveling by betatron function adjustment at the LHC interaction points. In *Proc. of International Particle Accelerator Conference (IPAC'14), Dresden, Germany, June 15-20, 2014*, number CERN-ACC-2014-0081 in International Particle Accelerator Conference, Geneva, Jun 2014.
5. J.C. Garnier, D. Anderson, M. Audrian, A.A. Gorzawski, M. Dragu, K. Fuchsberger, M. Koza, K.H. Krol, K. Misiowiec, K. Stamos, and M. Zerlauth. Reliable software development for machine protection systems. In *Proc. of International Particle Accelerator Conference (IPAC'14), Dresden, Germany June 13-20, 2014*
6. J.C. Garnier, B. Puccio, A. Moscatelli, D. Anderson, M. Audrian, A.A. Gorzawski, M. Dragu, K. Fuchsberger, M. Koza, K.H. Krol, K. Misiowiec, K. Stamos, and M. Zerlauth. Supervision software for the integration of the beam interlock system with the CERN accelerator complex. In *Proc. of International Particle Accelerator Conference (IPAC'14), Dresden, Germany June 13-20, 2014*
7. A.A. Gorzawski, D. Anderson, M. Audrian, A. Moscatelli, K. Fuchsberger, J.C. Garnier, E. Motesnitsalis, and J. Suchowski. The acctestng framework: An extensible framework for accelerator commissioning and systematic testing. In *Proc. of 14th International Conference on Accelerator & Large Experimental Physics Control Systems, San Francisco, CA, USA, Oct 6-11 2013*
8. K. Fuchsberger, A.A. Gorzawski, J.C. Garnier, and E. Motesnitsalis. Concept and prototype for a distributed analysis framework for the LHC machine data. In *Proc. of 14th International Conference on Accelerator & Large Experimental Physics Control Systems, San Francisco, CA, USA, Oct 6-11 2013*
9. J.C. Garnier, K. Fuchsberger, A.A. Gorzawski, J. Suchowski, P.C. Turku, and M. Zerlauth. System relation management and status tracking for CERN accelerator systems. In *Proc. of 14th International Conference on Accelerator & Large Experimental Physics Control Systems, San Francisco, CA, USA, Oct 6-11 2013*
10. M. Audrian, A.A. Gorzawski, D. Anderson, R. Gorbonosov, K. Fuchsberger, J.C. Garnier, and J. Suchowski. Using a JAVA embedded DSL for LHC test analysis. In *Proc. of 14th International Conference on Accelerator & Large Experimental Physics Control Systems, San Francisco, CA, USA, Oct 6-11 2013*
11. G. Papotti, A.A. Gorzawski, M. Hostettler, R. Schmidt. Beam Losses Through the LHC Operational Cycle in 2012. In *Proc. of 4th of the 4th International Particle Accelerator Conference, Shanghai, China, 12-17 May 2013*

Workshops / CERN internal notes:

1. A.A. Gorzawski and T. Pieloni. Long range beam-beam orbit effects in LHC – simulations and observations. *CERN Document Server*, Nov 2016 – to be published.
2. A.A. Gorzawski, D. Mirarchi, B.M. Salvachua Ferrando, and J. Wenninger. MD 239 on Collide and Squeeze (part 2). *CERN Document Server*, Jan 2016.
3. A.A. Gorzawski, D. Mirarchi, G. Papotti, B. M. Salvachua Ferrando, Tatiana Pieloni, and Jorg Wenninger. Collide and Squeeze MD. *CERN Document Server*, Dec 2015.
4. M. Hostettler, A.A. Gorzawski, and R. Alemany. The new luminosity-scan application: features, user interface, tests and dry runs. Technical report, LHC Luminosity Calibration and Monitoring Working Group, Oct 2015.
- 160 5. A.A. Gorzawski and J. Wenninger. Orbit drifts at the LHC interaction points during the squeeze. *CERN Document Server*, May 2015.
6. A.A. Gorzawski. Leveling options and strategy. In *Proc. of 5th Evian Workshop on LHC beam operation*. CERN, CERN, 2014. CERN-ACC-2014-0319.
7. R. Alemany-Fernandez, et al. Operation and Configuration of the LHC in Run 1. *CERN Document Server*, Nov 2013.

ARKADIUSZ ANDRZEJ GORZAWSKI

address	10 route des Collonges, 01550 Pougny, France
date and place of birth:	30.11.1982, Knurów, Poland
mob (FR, CH)	+33 771 265 101, +41 75 411 2358
e-mail	arkadiusz.gorzawski@cern.ch
social	www.linkedin.com/in/arekgorzawski

PHYSICIST & SOFTWARE ENGINEER

SPECIALIZATION COURSES AND TECHNICAL TRAININGS

03.11.2015 – 14.11.2015	CAS: Intensity Limitations in the Particle Beams
27.09.2015 – 09.10.2015	CAS: Advanced Accelerator Physics
06.11.2014 – 13.11.2014	JAS: Beam Loss and Accelerator Protection
20.06.2014 – 26.06.2014	Using <i>Mathematica</i> with experimental data
27.01.2014 – 02.02.2014	USPAS: Control Room Accelerator Physics
20.01.2014 – 26.01.2014	USPAS: System Safety and Safety Systems for Accelerators
29.10.2012	SPRING Core
17.01.2011	Java Advanced Level

SKILLS AND COMPETENCES

LANGUAGES:

Native Polish
 Highly proficient in spoken and written English (C1)
 Very good command in French (B2)

BEHAVIOURAL AND SOCIAL:

Open minded, End-oriented work capacity, Problem-solving attitude
 Responsibility, self-respect and self-reliance
 Natural ability in team work
 Strong referential values of fairness, equity and dignity
 Ability to establish and maintain good working relations with people of different nationality and cultural backgrounds
 Open source attitude (co-founder of www.tensorics.org)

IT SKILLS:

Programming: JAVA EE (with SPRING framework), JUnit/Mockito, LABVIEW, PHP, C/C++, HTML, Python
 Numerical simulation and analysis: MATHEMATICA, MADX, TRAIN, R
 Data services: SQL (MySQL, Oracle), XML, CSS
 OS's: WINDOWS 10,7,VISTA,XP,2000,NT,9X, GNU LINUX, MACOS X
 Office: L^AT_EX, MS Office, OpenOffice, AutoCAD, Corel Suite, Inkscape
 Other: Eclipse, SubVersion/Git, Agile Methodology/SCRUM
 Continuous integration: Bamboo/Travis, JIRA, Ant/Gradle/Maven

OTHERS:

SINCE MARCH 2014	Official FFS Ski Instructor for Ski Touring
SINCE JULY 2013	CERN First Aider
SINCE JANUARY 2010	Official CERN Guide
SINCE NOVEMBER 2000	Driving License B Category
SINCE OCTOBER 1999	INLAND SKIPPER with Certificate of Competency
SINCE MAY 1999	POLISH RED CROSS Certificate of First Aid Competency

ACTIVITIES AND INTERESTS

OUTDOOR

ski touring, hiking, mountaineering, rock climbing, sailing and photography

INDOOR

playing guitar and bass guitar (in a band since 2009), board games and cooking